



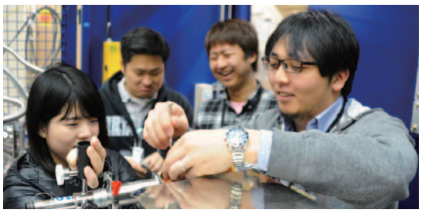


J-PARC

ANNUAL REPORT 2016

Vol.2: Materials and Life Science Experimental Facility

MLF ANNUAL REPORT

J-PARC MLF
Materials and Life Science Division
J-PARC Center
http://j-parc.jp/MatLife/en/

J-PARC was jointly constructed and is now operated by the High Energy Accelerator Research Organization (KEK) and the Japan Atomic Energy Agency (JAEA).

Comprehensive Research Organization for Science and Society
http://www.cross-tokai.jp/

J-PARC 17-07

Preface

Toshiji Kanaya
Division Head of Materials and Life Science Division, MLF

In 2016, the operation of the Material and Life Science Experimental Facility (MLF) was rather stable, thanks to the dedicated work of all the scientists and engineers involved in the facility. The availability of the scheduled beam time reached over 90 percent. The stable operation was very important for conducting the user programs. However, in 2016, the power of the delivered beam was not as high as in the previous years, because of the following problems. In November 2015, the neutron target vessel (#7) had a water leak as reported in MLF Annual Report 2015. In January 2016, a target vessel (#2) was installed, which has an older design without helium bubbling system. As a resul, the beam power was reduced to 200 kW, and later in the autumn period of 2016 - to 150 kW. In addition, before the summer of 2016, the neutron source had a problem with the helium refrigerator of the cryogenic hydrogen circulation system. We were forced to shut it down for 6 days for helium purification after a 3-week operation of the beam. The operation of the muon production target, replaced by a target with a rotating design in 2014, continued without a major problem. The scientific results from the delivered beam of neutrons and muons, as well as the status report of the beamlines, spectrometers and the research environment will be found in this Annual Report. In the coming years, we will make efforts to achieve the beam power of 1 MW, while keeping the operations stable.

Many scientific and collaborating meetings were held at MLF in 2016. An important one was the European Spallation Source (ESS) - J-PARC collaboration meeting, held at the J-PARC Center on June 1 and 2, 2016. The meeting was carried out under the agreement on cooperation in the field of spallation neutron related development between ESS and J-PARC. Sixteen delegates from ESS visited the J-PARC Center and we exchanged information about the management of the organization, radiation and general safety issues, accelerator technology, neutron sources, and neutron instruments. A complete list of the meetings can be found in this Annual Report.

The education of a new generation and invitation of new users are crucial for the sustainable development and research activities of the facility in the future. The Neutron and Muon School was held from November 22 to 26. Ten host organizations and societies took part in organizing the school. Twenty nine young researchers and graduate students from Japan, Korea, Australia, Indonesia, India, Hong Kong, Taiwan, and the United Kingdom, participated in the school. They enjoyed nine neutron and four muon lectures, a site tour to J-PARC and JRR-3, hands-experiments with eight neutron beamlines and one muon instrument at MLF, and a science seminar.

I would like to introduce the reader to the research highlights and status reports of MLF in fiscal year 2016. A new framework of collaboration may be found in the national projects, such as the Element Strategy Initiative and the Photon and Quantum Basic Research Coordinated Development Program, in addition to the individual research programs.

Materials and Life Science Division, Japan Proton Accelerator Research Complex
http://j-parc.jp/MatLife/en/

Preface

Hideaki Yokomizo
Director, CROSS

CROSS has served as a Registered Institution of specific neutron beam Facilities of J-PARC, appointed by the Government in 2011. We have been supporting the appropriate user program operations of the Public Beamlines at Materials and Life Science Experimental Facility (MLF). We have also been engaged in facility promotion activities, such as operating a fair and open proposal selection system for the MLF Public Beamlines, providing high-quality user support and promoting facility utilization for both academic and industrial researchers. CROSS increased the number of science coordinators in order to encourage the industrial use and to help the management of the Industrial Users Society for Neutron Application, so, we have three science coordinators in 2016.

CROSS supported the user programs at seven fully-operational Public Beamlines: BL01 *4SEASONS*, BL02 *DNA*, BL11 *PLANET*, BL15 *TAIKAN*, BL17 *SHARAKU,* BL18 *SENJU and* BL22 *RADEN*. In 2016, we accomplished a stable and highly reliable machine operation, which reached over 90% of the original operation plan. However, the beam power had to be reduced to 150-200 kW, because we used a spare target vessel, which had no protection from the pitting damage on the beam window.

A special program for new user promotion (NUP) started in 2016 to invite scientists new to the neutron research. NUP has a preferential beam time allocation and provides courteous support to first-time or novice users from both the industrial and academic sectors. NUP is expected to create a new science by conducting the cooperative research between industrial and academic scientists. The special program of Element Strategy Initiative has also proceeded successfully this year. Element Strategy Initiative is an integrated strategic research program of the Japanese Government that promotes the development of innovative materials and alternative technologies in the research areas of permanent magnets, catalysis and batteries, and electronic and structural materials. Complementary Use is a program that encourages and facilitates the complementary and collaborative use of pulsed neutrons (J-PARC MLF), synchrotron radiation (SPring-8), and supercomputer (K computer).

I hope this Annual Report would serve as a useful information source for anyone wishing to know more about the current status of MLF, its recent scientific achievements, the technical R&D projects that support the science program, and the operational details of our facility.

On behalf of the team at Neutron Science and Technology Center, CROSS, I extend a warm welcome to all researchers who wish to use the Public Beamlines at J-PARC MLF.

Contents

Research and Development Highlights

Neutron Source

Neutron Science

Muon Science

MLF Safety

MLF Operations in 2016

Organization Chart

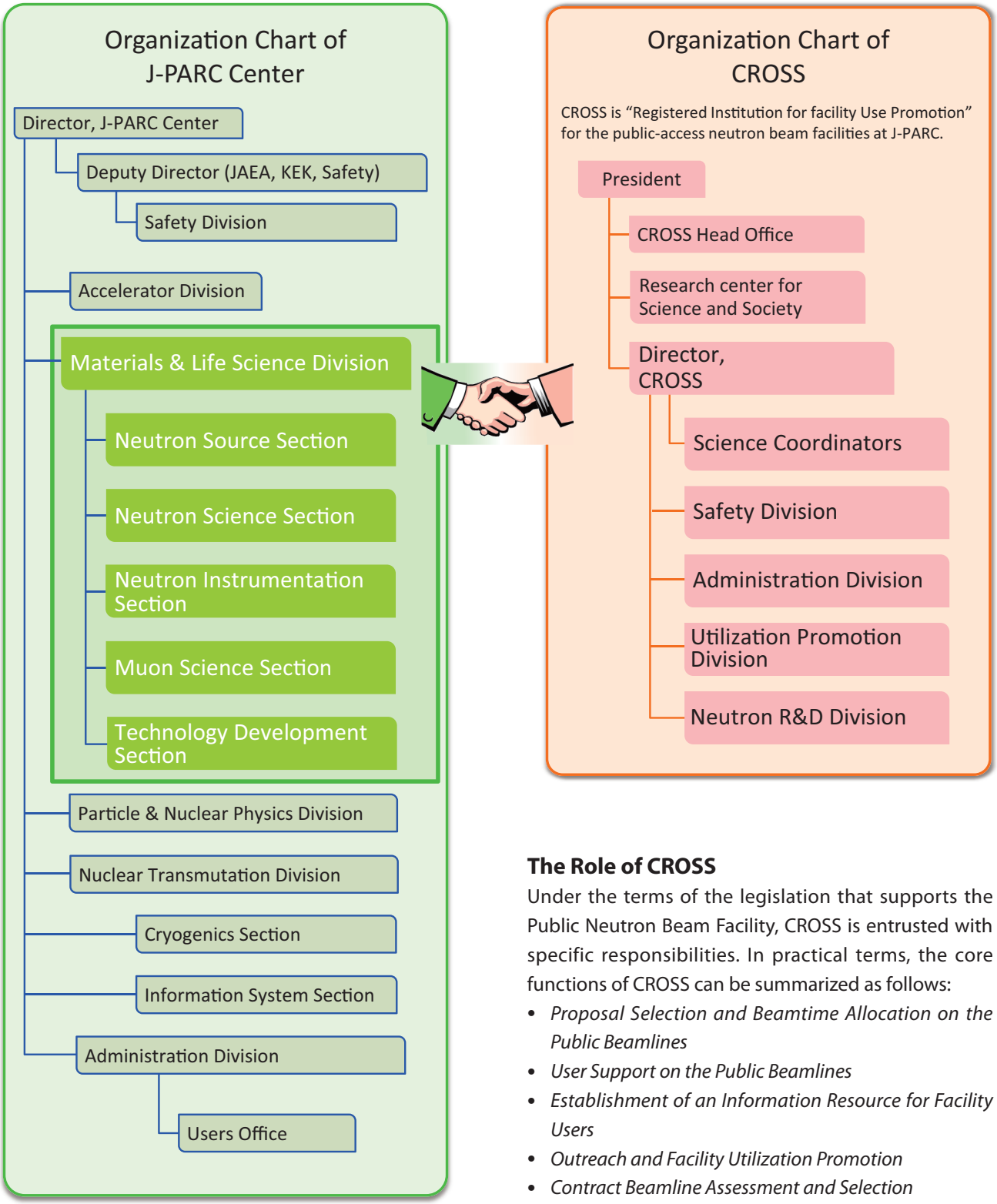

The Role of CROSS

Under the terms of the legislation that supports the Public Neutron Beam Facility, CROSS is entrusted with specific responsibilities. In practical terms, the core functions of CROSS can be summarized as follows:

- *Proposal Selection and Beamtime Allocation on the Public Beamlines*
- *User Support on the Public Beamlines*
- *Establishment of an Information Resource for Facility Users*
- *Outreach and Facility Utilization Promotion*
- *Contract Beamline Assessment and Selection*

J-PARC Map

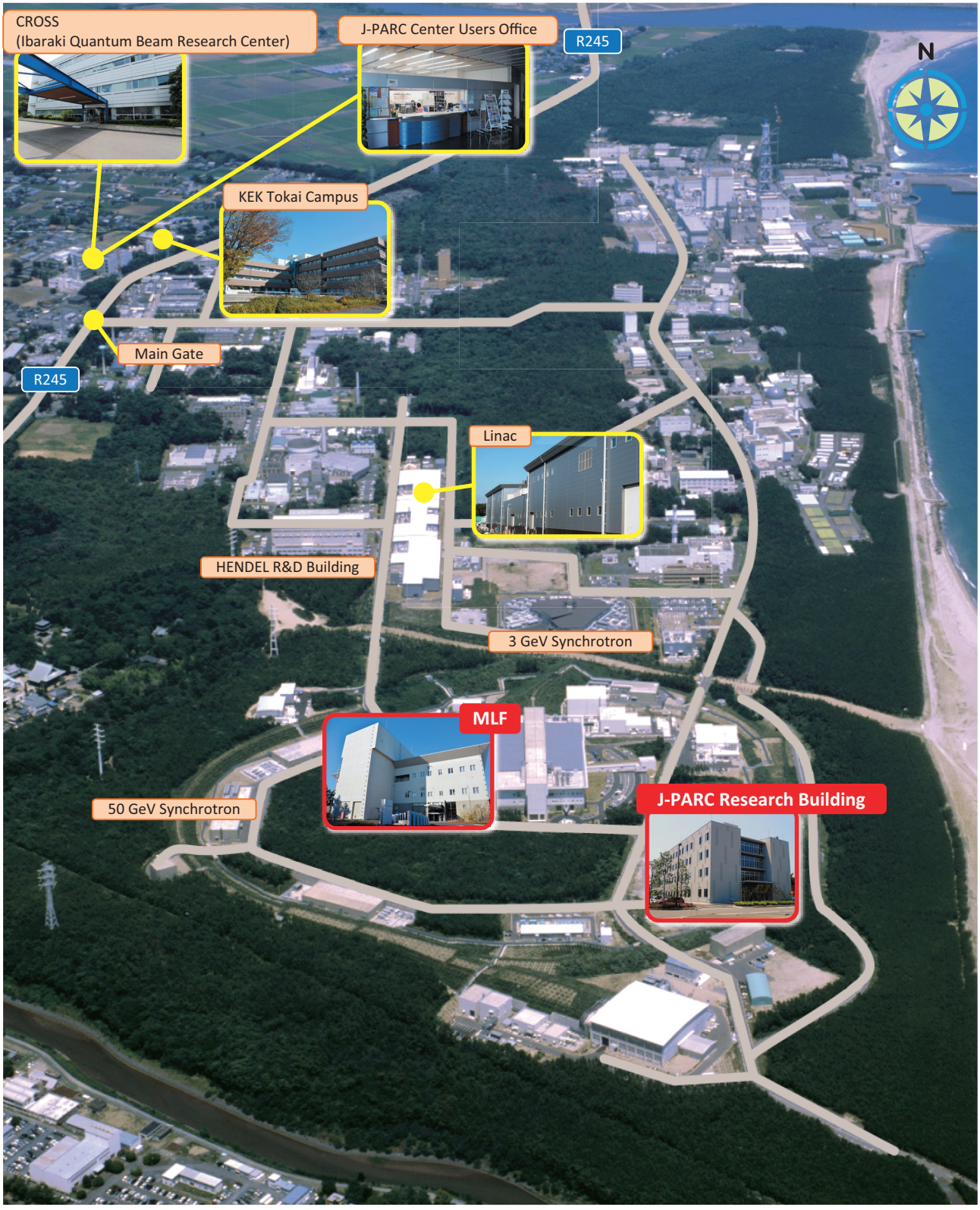
CROSS
(Ibaraki Quantum Beam Research Center)
J-PARC Center Users Office
R245
N
KEK Tokai Campus
Main Gate
R245
Linac
HENDEL R&D Building
3 GeV Synchrotron
MLF
50 GeV Synchrotron
J-PARC Research Building

Muon and Neutron Instruments

Muon Source

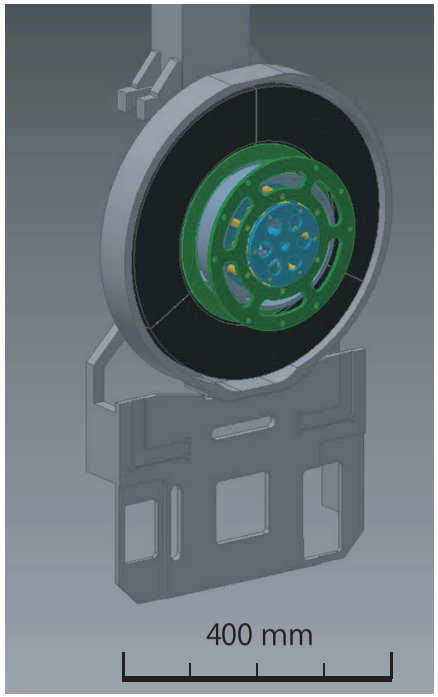

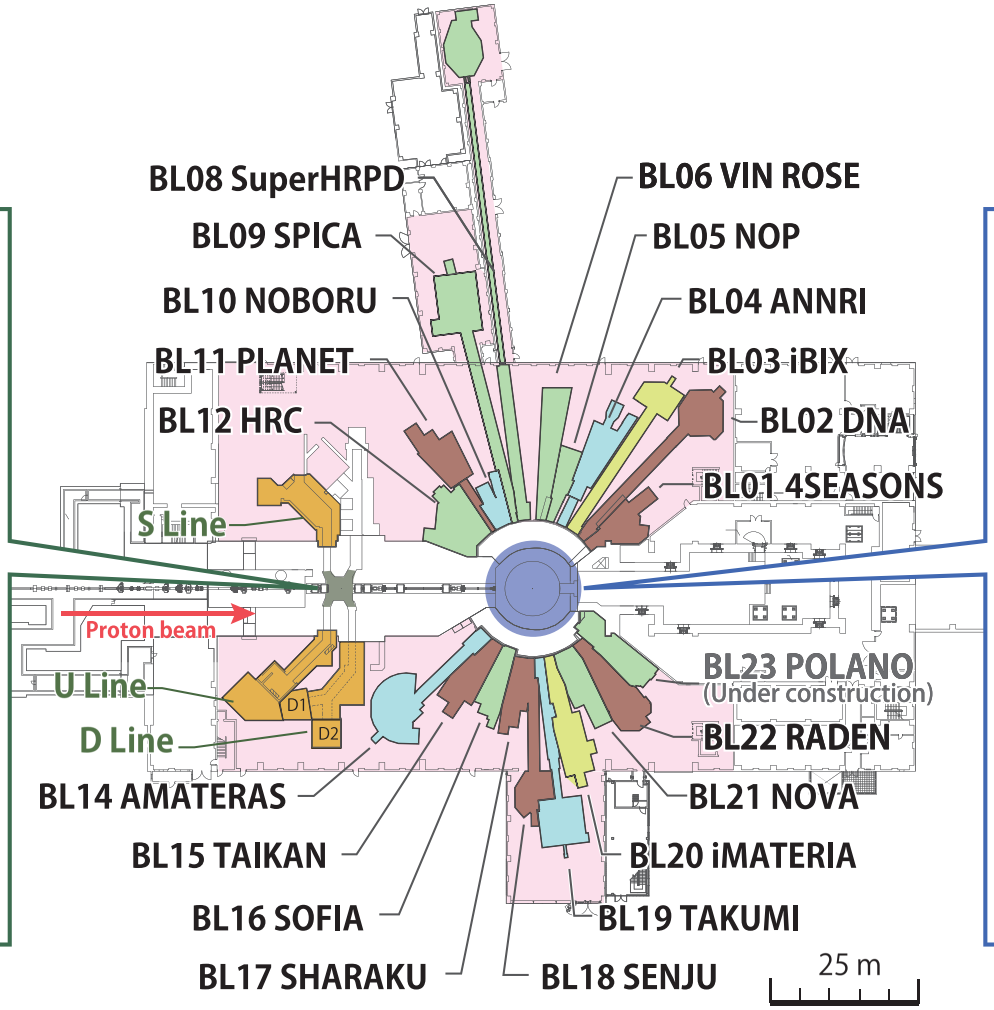

Neutron Source

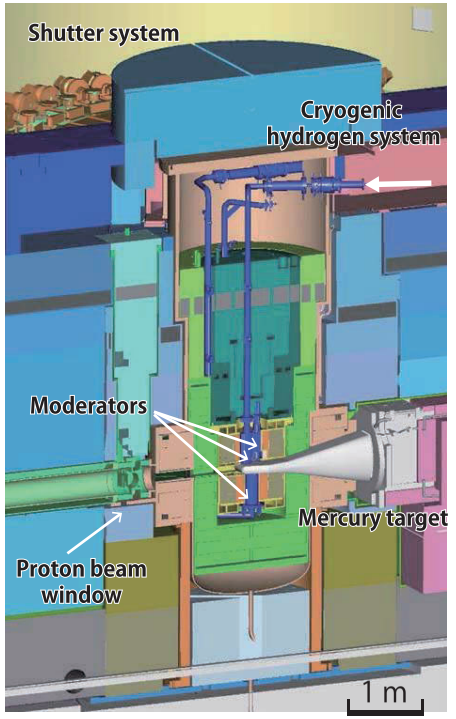

Muon Instruments

Neutron Instruments

JAEA

KEK

Public beam lines

Ibaraki Pref.

As of March 2017

Research and Development Highlights

Reconsidering Partially Ordered States of Ice XV

1. Introduction

Water freezes below 0°C. This is considered a common fact, but it is valid only in our world at a pressure of 1 atm. The melting temperature of ice drops when pressure increases, and reaches its minimum at 0.21 GPa (Fig. 1). This fact was discovered by G. Tammann in 1900 [1], he also found two new high pressure polymorphs, ice II and III, after observing the melting point and density of ice. Even over 100 years after the after the discovery of the ice polymorphs, the exploration of new polymorphs of ice still continues, leading to the recent discovery of ice XVII [2].

Why do the ice structures display such rich varieties? One of the reasons could be the order-disorder phenomena of the hydrogen bonds in ices. Even a single water molecule in an ice structure has four hydrogen bonds to the adjacent water molecules, yielding ${}_4C_2 = 6$ different hydrogen positions and the number of possible configurations will be exponentially increased with multiplying the number of molecules. The degree of freedom for these hydrogen configurations contributes to the rich variety of ice structures, and in fact, most ice polymorphs have disorder-order "pairs" in terms of hydrogen positions. Ice VI-XV, which is one of the "pairs", is the target of our study.

Ice XV, the ordered form of ice VI, was identified by Salzmann et al. [3], from their observation of neutron diffraction for sample prepared from ice VI by slow cooling from 250 to 80 K. Prior to the identification of ice XV by Salzmann et al., the phenomena suggesting hydrogen ordering in ice VI had been reported in a number of studies (see references in [4]). However, as Salzmann et al., noted in their review paper [5], there was an inconsistency among the various experiments and calculations for ice XV, i.e., neutron diffraction observations suggested antiferroelectrically ordered structures, which disagreed with the dielectric measurement and theoretical studies, implying ferroelectrically ordered structures. Here we re-investigate the in-situ neutron diffraction measurements and density's functional theory calculations to revisit the structure and stability of ice XV.

2. Stability of ice XV

In a previous neutron study, detailed structure and stability investigations were carried out on a sample recovered at ambient pressure; they showed that the phase boundary between ice VI and ice XV is about 130 K, regardless of the pressure, because the volume change (ΔV) accompanying the transition was so small that the phase boundary could be flat in terms of pressure based on the Clausius-Clapeyron relation ($dT/dP = \Delta V/\Delta S$). We noted that the entropy change (ΔS) would also be rather small; it should be less than the Pauling entropy ($R\ln(3/2) \cong 3.37$ J mol^{-1} K^{-1}) as the hydrogen ordering is incomplete and occurs only partially.

In our neutron study, the ordering process from ice VI to ice XV was clearly observed as appearing additional peaks (e.g., 003) or a c/a axial ratio (Fig. 2), and the

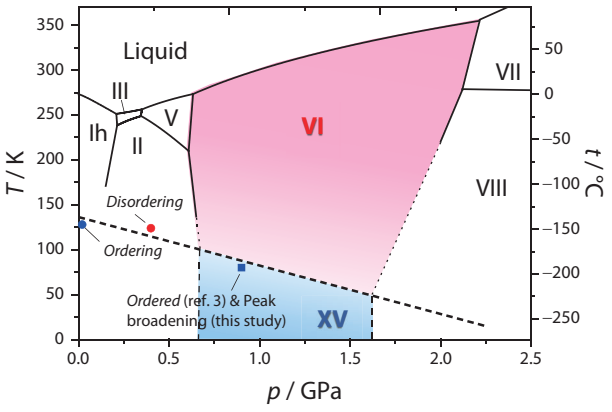

Figure 1. Phase boundary between ice VI and XV, proposed in [4]. The phase boundary of ice VI and XV has a slightly negative slope, which is constrained by the results from our neutron diffraction experiments denoted as blue (ordering) and red (disordering) circles.

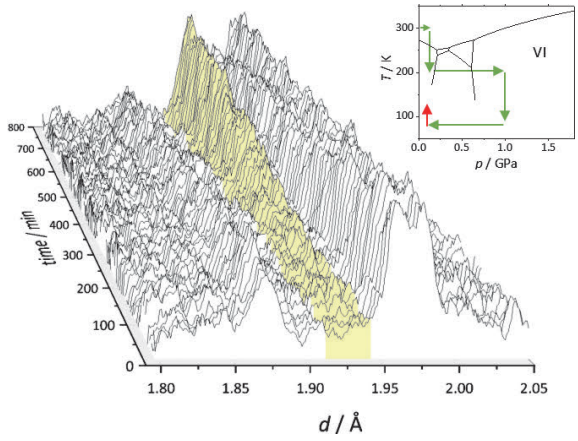

Figure 2. Selected area of neutron diffraction patterns showing the growth of the 003 peak (yellow shaded area) as a function of time, indicating hydrogen ordering process from ice VI to XV for the sample recovered from 1.0 to 0 GPa with increasing and then maintaining the temperature constant. The detailed p-T path is shown in the inset as arrows.

additional peak intensities or c/a ratio were still being grown after nearly 10 h at a constant temperature of 128 K. The corresponding run at approximately 0.4 GPa shows the disappearing of the additional peaks and a decreasing c/a ratio, displaying a trend toward disordering. These observations clearly showed that the phase boundary between ice VI and XV has a slightly negative slope, as shown in Fig. 1.

3. Partially ordered structure of ice XV

A neutron diffraction pattern, which was registered at 80 K and ambient pressure after recovering at 80 K from high pressure, and subsequently annealed at 130 K, was analyzed by the Rietveld refinement. We first analyzed it through 45 completely ordered structure models derived from ice VI by using graph and group theories, and found that none of the completely ordered configurations was particularly favored. In other words, several configurations, for example four configurations 39-42, shown in Fig. 3, have the lowest R factors with quite similar consistency among the 45 symmetry distinct configurations. Our DFT calculations also support the phenomenon that a particular single completely ordered configuration is not favorably established, but several configurations may coexist at finite temperatures, as our investigations have shown.

Next, we tried to refine the structure based on partially ordered *Pmmn* model (Fig. 3b), which was derived from the reflection conditions and had been already proposed as the hydrogen ordered form of ice VI, called ice VI′, by Kamb more than 40 years ago [6]. The result shows good consistency in the observed data, especially the better fit compared to all completely ordered models. Although we do not insist that the noted consistency shows the *Pmmn* partial ordered model as the true structure of ice XV, i.e., other possibilities like $Pm2_1n$, $P2_1mn$ or even lower symmetry could not be excluded from our observations, but we can at least conclude that a completely ordered structure could not be established and the mixture of locally ordered motifs apparently produces the reflection conditions. Although the space group *Pmmn* itself suggests an antiferroelectrically ordered state because of the presence of a center of symmetry, this does not mean that the crystal physically possesses antiferroelectricity. Even ferroelectricity may appear due to the locally ordered motifs and its presence does not conflict with the previous dielectric measurement.

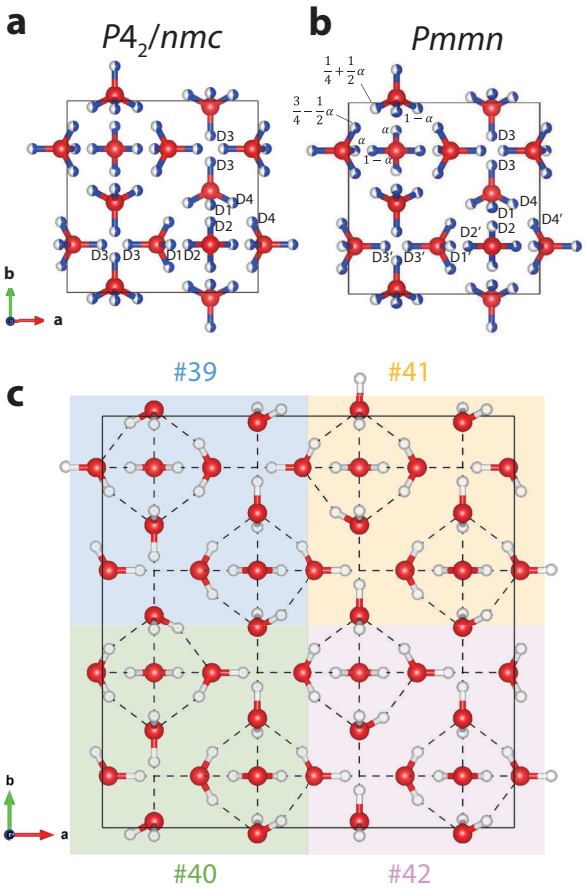

Figure 3. Structure models of (a) ice VI, (b) ice XV, and (c) four seamlessly adjacent ordered configurations 39-42 formed without breaking ice rules. Of the 45 symmetry distinct configurations, the four configurations shown here have the lowest R factors and the highest phase fractions obtained from Rietveld analysis of the neutron diffraction pattern.

4. The issue is still debated

Finally, we should note that the structure of ice XV is still under debate; a more recent neutron diffraction study [7] stated that the ice XV structure should be derived from a completely ordered structure model. The key issue to recognize, is how we treat the partially ordered structure model, which may also be related to a more fundamental problem in physics, that is how neutrons located apart can interact coherently. Further experimental and theoretical approaches describing partially ordered structure will be required for a complete understanding.

References

[1] G. Tammann, Annaleu der Physik, 2, 1 (1900).
[2] L. del Rosso, M. Celli and L. Ulivi, Nature Communications, 7, 13394 (2016).
[3] C. G. Salzmann, P. G. Radaelli, E. Mayer and J. L.

Finney, Physical Review Letters, 103, 105701 (2009).
[4] K. Komatsu, F. Noritake, S. Machida, A. Sano-Furukawa, T. Hattori, R. Yamane and H. Kagi, Scientific Reports, 6, 28920 (2016).
[5] C. G. Salzmann, P. G. Radaelli, B. Slater and J. L. Finney, Physical Chemistry Chemical Physics, 13, 18468-18480 (2011).
[6] B. Kamb, in Physics and chemistry of ice, edited by E. Whalley, S. J. Jones and L. W. Gold (Royal Society of Canada, Ottawa, 1973), pp. 28-41.
[7] C. G. Salzmann, B. Slater, P. G. Radaelli, J. L. Finney, J. J. Shephard, M. Rosillo-Lopez and J. Hindley, The Journal of Chemical Physics, 145, 204501 (2016).

K. Komatsu[1], F. Noritake[1,†], S. Machida[2], A. Sano-Furukawa[3], T. Hattori[3], R. Yamane[1], and H. Kagi[1]

[1]Geochemical Research Center, Graduate School of Science, The University of Tokyo; [2]CROSS, Research Center for Neutron Science and Technology; [3]J-PARC Center, Japan Atomic Energy Agency; [†]Present address: Faculty of Engineering, Graduate Faculty of Interdisciplinary Research, University of Yamanashi

Composite Behavior of Lath-Martensite Steels Induced by Plastic Deformation, a New Paradigm for the Elastic-Plastic Response of Martensitic Steels

1. Introduction

Lath martensite steels are widely used iron base alloys with outstanding mechanical properties. Their strength is due to phase transformation of fcc structure into lamellar bcc plates during fast cooling. Coherency strains induce large dislocation densities which are the source of the alloy's strength. Though this alloy has been used since the existence of steel, the way its microstructure functions is still unclarified. High resolution neutron diffraction peak profiles revealed that there is a load redistribution between martensitic laths oriented differently relative to the applied stress direction. Based on characteristically asymmetric neutron diffraction profiles, we showed that the initially homogeneous microstructure becomes heterogeneous during plastic deformation [1-3]. We also showed that lath packets soften when the active Burgers vectors are parallel to the lath planes, but harden when they are not parallel. We found that in lath packets that soften, the annihilation distance and the mean free path of active dislocations are two orders of magnitude larger than in those which harden. Knowledge of load partitioning during plastic deformation in martensitic steels will open new options for developing iron base structural materials with several improved mechanical properties. Typical martensite steels consists of blocks of lamellar plates, where the blocks are forming packets [4]. The blocks are subdivided into sub-blocks, where the smallest constituents are lamellar plates called martensite-laths. The hierarchy of packets, blocks, sub-blocks and laths is shown schematically in Fig. 1. Within the packets the crystallographic orientation is the same. The 110 oriented lath planes align coherently with one of the 111 type planes of prior austenite. Within the prior austenite grain boundary several packets of different crystallographic orientations can coexist, as shown in Fig. 1a.

2. Experimental

Neutron diffraction patterns were collected in-situ during tensile deformation of a martensitic steel specimen with a small amount of retained austenite at the TAKUMI beamline of the Materials and Life Science Facility of the Japan Proton Accelerator Research Complex, J-PARC [1-3]. The beamline was operated with the high resolution and medium intensity time-of-flight (TOF) method. The schematic outline of the TOF diffractometer and the specimen geometry is shown in Fig. 2. The instrumental peak width was tuned to 0.3% and the strain rate was 10^{-5} s^{-1}. The loading direction and the diffraction vectors are parallel or perpendicular for the +90° or the −90° detector, i.e. for the 'axial' or the 'side' directions, relative to the applied stress, σ. In order to improve the counting statistics the deformation was interrupted at 9 consecutive strain values as shown in the stress-strain curve in Fig. 3.

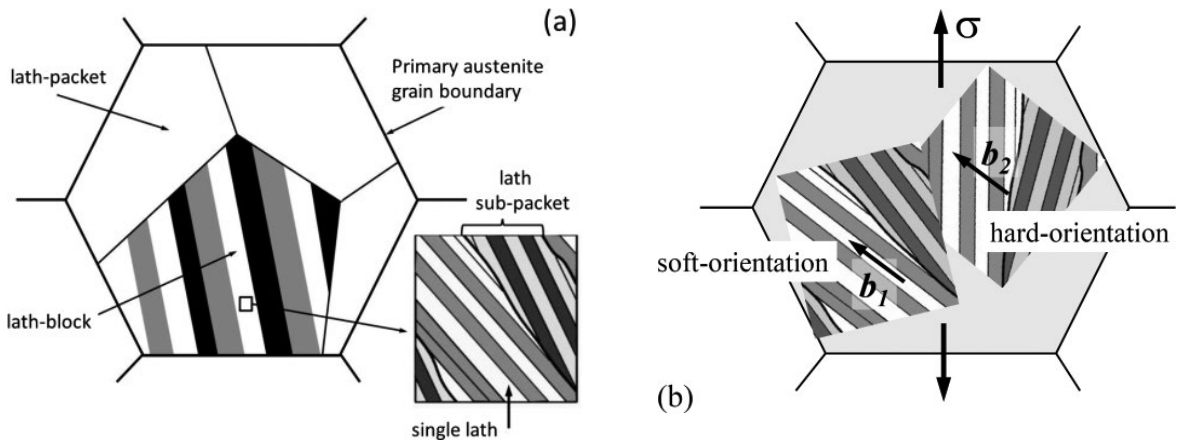

Figure 1. Schematic illustration of the hierarchical structure of lath martensite with the active Burgers vectors. (a) Lath packets consisting of parallel blocks in three different packet. (b) Two packets oriented with the active Burgers vectors either in- or out-of-lath-plane relative to the direction of the applied stress, σ.

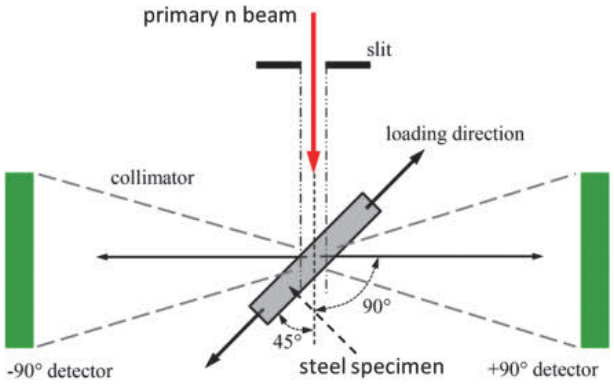

Figure 2. Schematic drawing of the in-situ neutron diffraction experiment at the TAKUMI beamline using two detector banks at scattering angles of ±90°.

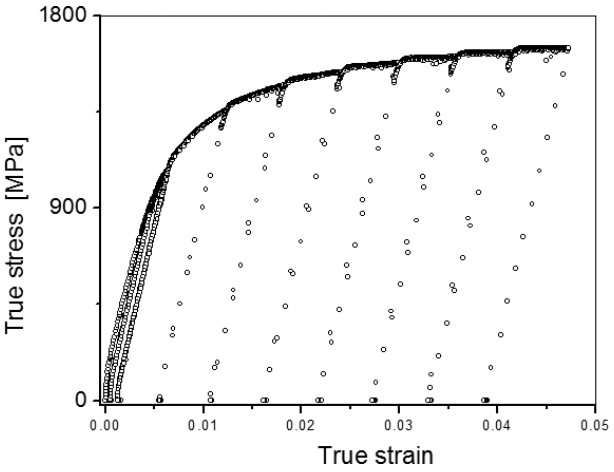

Figure 3. Stress-strain curve with step by step loading followed by unloading at several strain values to improve counting statistics.

3. Results and discussion

A typical axial diffraction pattern is shown in Fig. 4 for the $\varepsilon = 0.042$ tensile deformed state. In the initial state the diffraction peaks were perfectly symmetric, whereas they have become asymmetric in the tensile deformed states, as shown for the 200 axial and side diffraction peak profiles in Fig. 5. The figure shows that the asymmetries of the axial and side case peaks are in opposite direction. The diffraction patterns were evaluated by the Convolutional-Multiple-Whole-Profile (CMWP) fitting procedure based on physically modelled profile functions for dislocations, crystallite size and planar defects [5]. The CMWP fitting was performed for all diffraction peaks from 110 to 330 simultaneously, as shown in Fig. 4. The asymmetric profiles were handled by the sum of two dislocation profile functions shifted to smaller or larger K values around the center of gravity of the measured peaks, where K is the reciprocal space coordinate. The shifts, $\Delta d^* = \Delta K$, are evaluated in terms

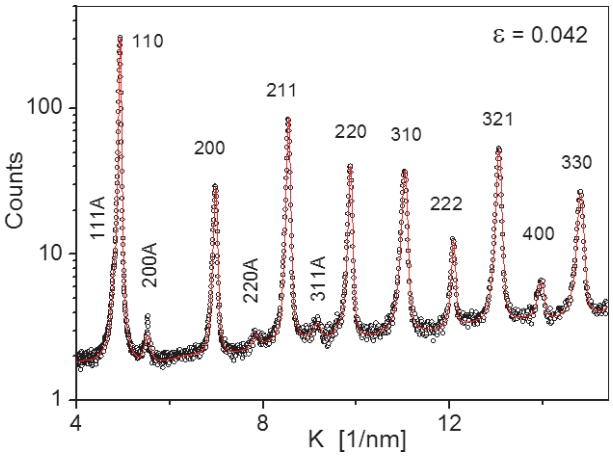

Figure 4. Typical diffraction pattern of observed (black-circles) and CMWP evaluated (red line) neutron diffraction patterns for $\varepsilon = 0.042$ tensiled state.

of residual internal stresses, $\Delta\sigma$, corresponding to the forward and backward stresses acting in the hard-orientation (HO) or soft-orientation (SO) packets, respectively. The two shifted dislocation profile functions were evaluated for the dislocation densities in the HO and SO packet components and the results are shown in Fig. 6a as a function of strain.

The average flow stress, σ_{av} or τ_{av}, and the local flow stress values acting in the HO and SO packets, σ_{HO} or τ_{HO} and σ_{SO} or τ_{SO}, were calculated by the Taylor equation:

$$\sigma_i = \sigma_0 + \alpha G M_T b\sqrt{\rho_i}, \quad \tau_i = \tau_0 + \alpha G b\sqrt{\rho_i}, \qquad (1)$$

where i stands for, HO or SO, α is a free parameter usually between zero and unity, G is the shear modulus, b is the absolute value of the Burgers vector of dislocations and ρ_i is the total average dislocation density or the local average dislocation density in the hard or soft packets, respectively. The flow stress values, σ_i, calculated by equation (1) are shown in Fig. 6b. *vs*. the measured applied stress, $\sigma_{applied}$. The schematic microscopic model of stress redistribution is based on the composite model [6, 7] and is shown in Fig. 7. After unloading forward and backward residual stresses will remain in the HO and SO packets respectively. Stress and strain compatibility between the SO and HO packets is guaranteed by the geometrically necessary dislocations (GNDs) lined up along the interfaces of the differently oriented packets shown schematically in Fig. 7a. The forward and backward local residual stresses are shown schematically in Fig. 7b. During loading the weighted spatial average of the local stresses are adding up for the applied stress:

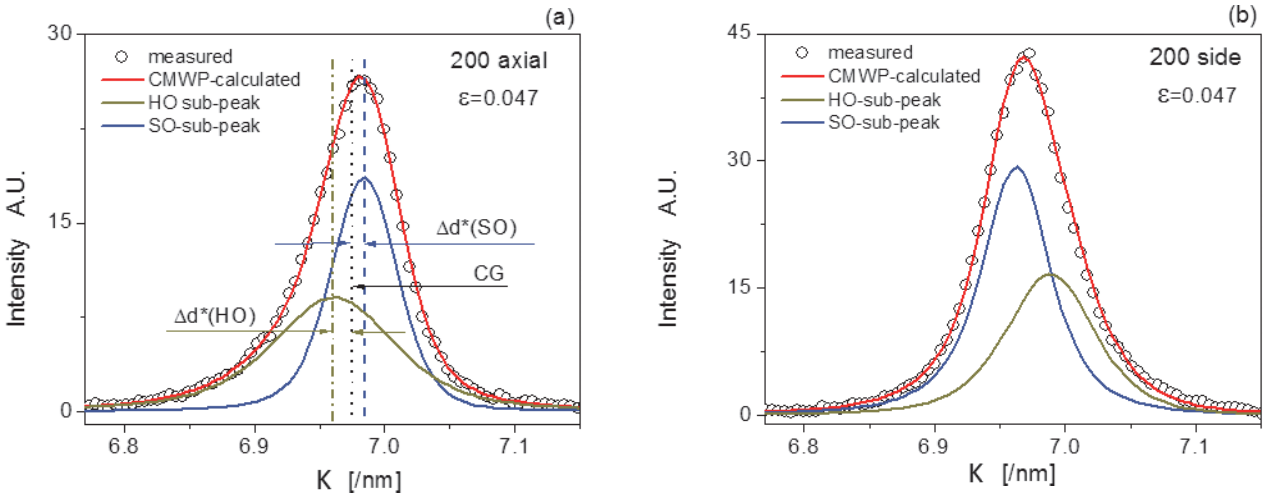

Figure 5. (a) The CMWP calculated sub-profiles corresponding to the HO (dark green line) and the SO (blue line) packets in the axial direction, along with the measured data (open circles) and the CMWP calculated total profile (red line). The center of gravity of the measured profile and the positions of the sub-peaks are indicated as dotted, dashed and dash-dot lines, respectively. (b) The measured (open circle), the CMWP calculated total profile (red line) and the CMWP calculated sub-profiles corresponding to the HO (dark green line) and the SO (blue line) packets in the side direction.

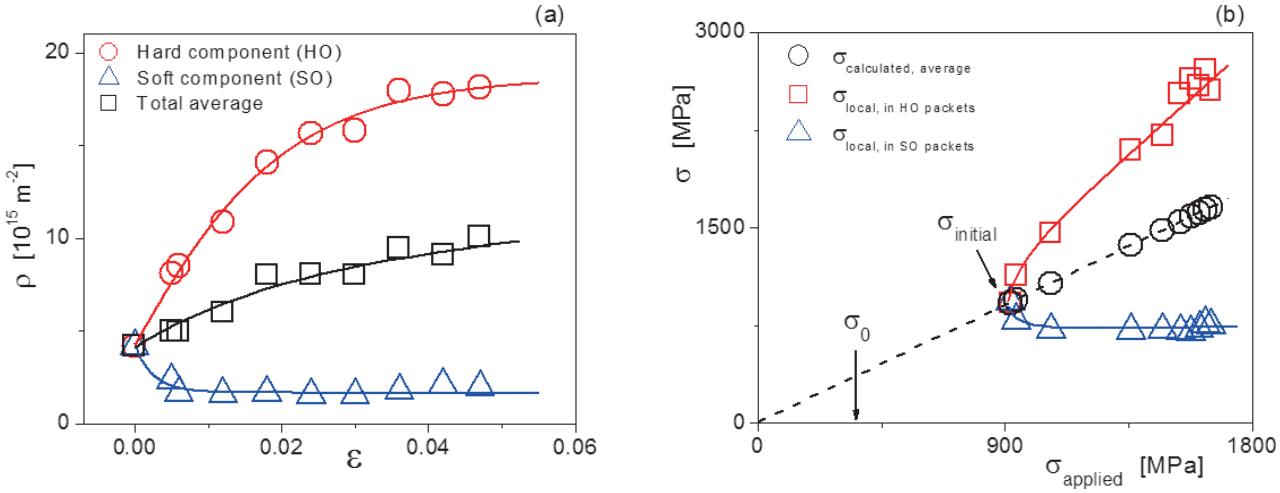

Figure 6. (a) Dislocation densities in the HO (red symbols) and the SO packets (blue symbols), and the volume fraction weighted average dislocation densities (black symbols). (b) Local stresses in the HO (red symbols) and the SO packets (blue symbols) calculated from the dislocation densities according to Taylor's equation.

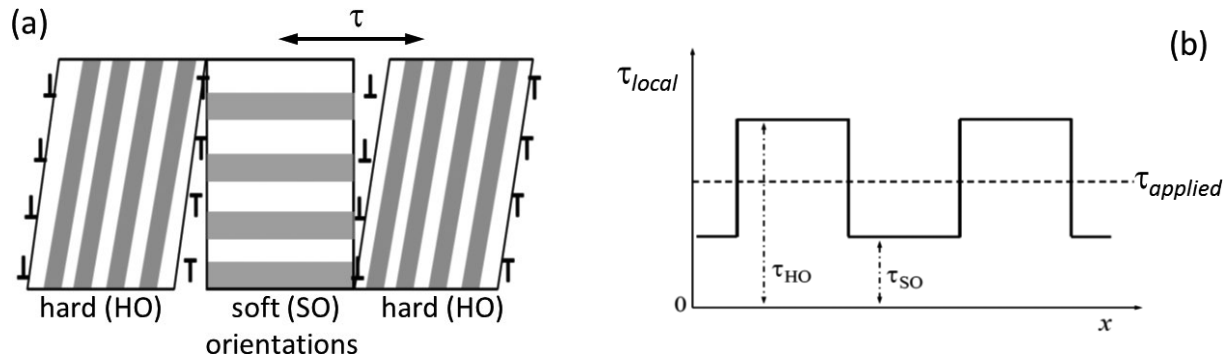

Figure 7. (a) Schematic illustration of the GNDs lined up along the interfaces of the differently oriented packets. (b) Spatial distribution of the local long-range-internal-stresses in the HO and SO packets under the action of the applied stress.

$$\tau_{applied} = f_{HO}\tau_{HO} + (1 - f_{HO})\tau_{SO} . \quad (2)$$

After unloading the residual internal stresses in the HO and SO packets are:

$$\Delta\tau_{HO} = \tau_{HO} - \tau_{applied} , \Delta\tau_{SO} = \tau_{SO} - \tau_{applied} ,$$
$$\text{where } f_{HO}\Delta\tau_{HO} + (1 - f_{HO})\Delta\tau_{SO} = 0. \quad (3)$$

During plastic deformation the backward stresses in the SO and the forward stresses in the HO packets hamper and assist dislocation motion in such a manner that the entire material flows simultaneously. The backward and forward stresses ensure that macroscopic flow takes place irrespective of the packet being soft or hard. The experiments in [1-3] proved the existence of the long range internal stresses between the softened and hardened lath packets and indicate the evolution of load redistribution between the differently oriented packets in lath martensite.

4. Future plans

The recognition of load redistribution in low-alloy high-strength ferritic steels opens new perspectives to develop new ferritic steel base structural materials for various applications. The beamline TAKUMI will be used to reveal the mechanical elastic-plastic response along with the load partitioning microstructure in many different ferritic steels for developing new high performance structural materials.

References

[1] T. Ungár, S. Harjo, T. Kawasaki, Y. Tomota, G. Ribárik, Z. Shi, Met. Mat. Transact., A48, 159-167 (2017).
[2] S. Harjo, T. Kawasaki, Y. Tomota, W. Gong, K. Aizawa, G. Tichy, T. Ungár, Met. Mat. Transact., A48, 4080-4092 (2017).
[3] Y. Wang, T. Ohnuki, Y. Tomota, S. Harjo, T. Ohmura, Scripta Mater., 140 45-49 (2017).
[4] H. Kitahara, R. Ueji, N. Tsuji, Y. Minamino, *Acta Mater*. **54**, 1279-1288 (2006).
[5] G. Ribárik, T. Ungár, *Mater. Sci. Eng*. **A528**, 112-121 (2010).
[6] T. Ungár, H. Mughrabi, D. Rönnpagel, M. Wilkens, *Acta Metall*. **32**, 333-342 (1984).
[7] H. Mughrabi, T. Ungár, W. Kienle, M. Wilkens, *Philos. Mag*. **A53**, 793-813 (1986).

T. Ungár[1], S. Harjo[2], T. Kawasaki[2], Y. Tomota[3], G. Ribárik[4], and Z. Shi[5]
[1]*Materials Performance Centre, School of Materials, The University of Manchester, Manchester, M13 9PL, UK;* [2]*J-PARC Center, Japan Atomic Energy Agency;* [3]*National Institute for Materials Science, 1-2-1 Sengen, Tsukuba, Ibaraki, 305-0047, Japan;* [4]*Department of Materials Physics, Eötvös University, Budapest, PO Box 32, H-1518, Hungary;* [5]*College of Materials and Chemical Engineering, China Three Gorges University, Yichang 443002, PR China*

Crystal Structure and Electrode Performance of $Li_{1.2-x}Ti_{0.4}Mn_{0.4}O_2$

1. Introduction

During the past two decades, the technology of rechargeable lithium-ion batteries (LIBs) has become highly sophisticated and contributed to the development of today's convenient modern society with versatile portable electronic devices. However, due to the ever-increasing demand for energy density, there is a need to develop positive electrode materials with higher energy density. The energy density of commercial LIBs is currently limited by positive electrode materials. Lithium-excess positive electrode materials such as Li_2MnO_3 and their derivatives have been studied extensively in the past decade. In this system, the oxidation state of manganese ions is tetravalent, and therefore further oxidation of manganese ions is difficult on charge. Instead, oxide ions as anions contribute in the charge compensation process. However, oxidation of oxide ions for Li_2MnO_3-based electrode materials causes oxygen loss as an irreversible process [1].

To use effectively the charge compensation of oxide ions, several lithium-excess positive electrode materials have been reported. Recently, our group successfully synthesized new niobium- and titanium-based high-capacity positive electrode materials, which use effectively the solid-state redox reaction of oxide ions [2, 3]. In this study, a detailed crystal structure of a binary system of Li_2TiO_3-$LiMnO_2$ is examined by neutron diffraction, and possibility of reversible solid-state redox of oxide ions for the high-capacity positive electrode materials is discussed.

2. Crystal structure of $Li_{1.2}Ti_{0.4}Mn_{0.4}O_2$

A binary system of Li_2TiO_3-$LiMnO_2$ has been systematically examined as electrode materials. Both end-members, Li_2TiO_3 and $LiMnO_2$, crystallize into different cation-ordered rocksalt-type structures. Li_2TiO_3 is expected to be a high capacity electrode material with anion redox if all lithium ions are reversibly extracted from the host structure. However, Li_2TiO_3 has no d electrons in a conduction band, leading to an insulating character as electrode materials. Therefore, pure Li_2TiO_3 is electrochemically inactive. Substitution of 3d transition metal ions for Ti/Li ions effectively induces conductive electrons, and color of samples is also changed from white for Li_2TiO_3 to black for substituted samples with Mn^{3+}. Such 3d transition metals can accept electrons from oxide ions. However, a change in the crystal structure is also unavoidable, and formation of a cation-disordered rocksalt-type structure is noted. A neutron diffraction pattern of the sample with the one to one composition between Li_2TiO_3 and $LiMnO_2$, which is reformulated as $Li_{1.2}Ti_{0.4}Mn_{0.4}O_2$, is shown in Fig. 1. The neutron diffraction pattern was collected at BL09 (SPICA) in MLF. Rietveld analysis of the neutron diffraction pattern revealed that the sample contains 1% vacancy at 4*a* site (cation sites). Moreover, no evidence is found for the formation of oxygen vacancy.

3. Electrode performance of $Li_{1.2}Ti_{0.4}Mn_{0.4}O_2$

Historically, such cation-disordered rocksalt phase had been regarded as electrochemically inactive as electrode materials because of a lack of the Li migration

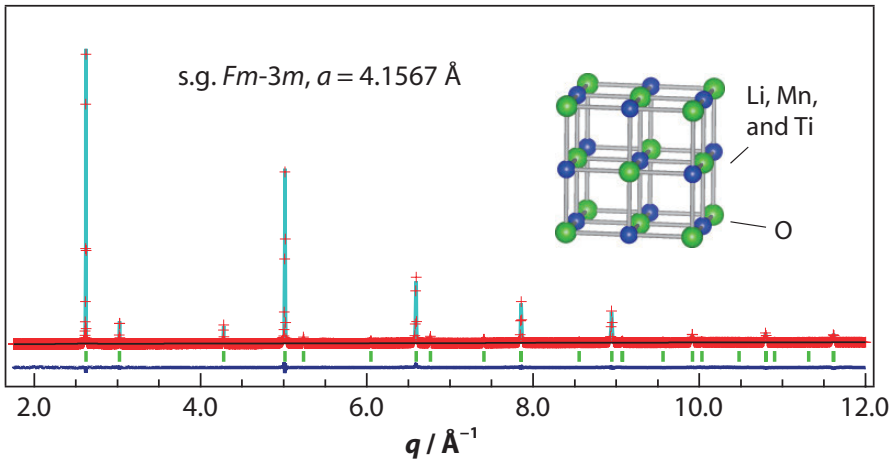

Figure 1. A neutron diffraction pattern of as-prepared $Li_{1.2}Ti_{0.4}Mn_{0.4}O_2$. Refined structural parameters are found in Table 1.

Table 1. Results of Rietveld analysis on the neutron diffraction pattern of $Li_{1.2}Ti_{0.4}Mn_{0.4}O_2$. The fitting result is shown in Fig. 1.

Atom	site	g	x	y	z	B(Å^2)
Li(1)	4a	0.625(3)	0	0	0	0.946(16)^a
Mn(1)	4a	0.198(2)	$=x$(Li(1))	$=y$(Li(1))	$=z$(Li(1))	$=B$(Li(1))
Ti(1)	4a	1-g(Li(1))-g(Mn(1))-g(Vacancy)	$=x$(Li(1))	$=y$(Li(1))	$=z$(Li(1))	$=B$(Li(1))
Vacancy	4a	0.012(2)	$=x$(Li(1))	$=y$(Li(1))	$=z$(Li(1))	$=B$(Li(1))
O(1)	4b	1	1/2	1/2	1/2	1.41(3)^a

Space group $Fm\bar{3}m$ (No. 225), a = 4.156745(4) Å
Histogram A:
R_{wp} = 5.57, R_p = 4.31, $S = R_{wp}/R_e$ = 2.74, R_B = 3.13, R_F = 11.89.
[a] Equivalent isotropic thermal parameter, B_{eq}.

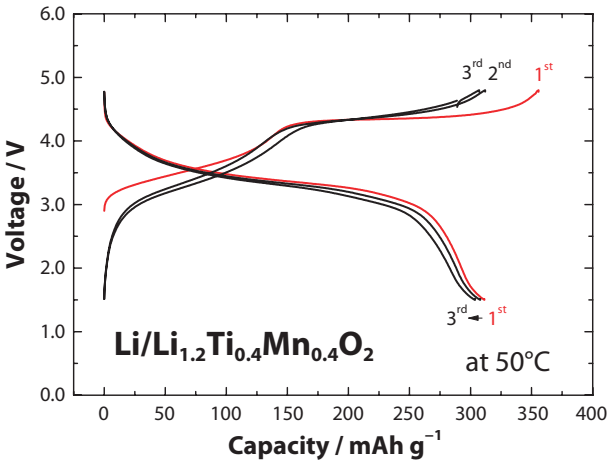

Figure 2. Charge/discharge curves of $Li_{1.2}Ti_{0.4}Mn_{0.4}O_2$ in a Li cell at a rate of 5 mA g^{-1} at 50°C.

path in a bulk structure. Nevertheless, formation of percolating network for the Li-excess system ($Li_{1+x}Me_{1-x}O_2$) opens the path for Li migration in the cation-disordered rocksalt-type structure [4].

$Li_{1.2}Ti_{0.4}Mn_{0.4}O_2$ was mixed with 10 wt% acetylene black and ball milled to enhance the electrode performance. Thus prepared sample shows a large reversible capacity in a Li cell, as shown in Fig. 2, and the sample delivers more than 300 mAh g^{-1} at 50°C. Available energy density of $Li_{1.2-x}Ti_{0.4}Mn_{0.4}O_2$ exceeds 1,000 mWh g^{-1} as a positive electrode material. Moreover, capacity retention is much better than that of pure Li_2MnO_3.

To examine whether oxide ions are oxidized and stabilized in $Li_{1.2-x}Ti_{0.4}Mn_{0.4}O_2$, reaction mechanisms were examined by soft X-ray absorption spectroscopy. A study by soft X-ray absorption spectroscopy revealed that, on the initial charge, Mn^{3+} is oxidized to Mn^{4+} for the slope region to 4 V, and oxide ions are oxidized at the plateau region around 4.2 V. Moreover, this process is highly reversible. Solid-state redox reaction of oxide ions is effectively stabilized by the presence of relatively less covalent character of Mn^{4+} with oxide ions without the sacrifice of electronic conductivity [3]. This finding opens a path to develop a new series of high-capacity positive electrode materials on the basis of oxide ion redox for rechargeable high-energy battery applications.

4. Summary

The use of solid-state redox reaction of oxide ions is an effective strategy to further increase energy density of rechargeable lithium batteries. We have demonstrated that the stabilization of redox reaction for oxide ions is possible using a combination of only 3d transition metals as the metallic constituents. Now, we are not restricted any more by the conventional and classical concept of transition metal redox, which totally limited the materials design and theoretical capacity of positive electrode materials as used in the past three decades. We expect that many new positive electrode materials with high capacity will appear, such as $Li_{1.2}Ti_{0.4}Mn_{0.4}O_2$.

References

[1] N. Yabuuchi, Chemistry Letters 46 (2017) 412.
[2] N. Yabuuchi, M. Takeuchi, M. Nakayama, H. Shiiba, M. Ogawa, K. Nakayama, T. Ohta, D. Endo, T. Ozaki, T. Inamasu, K. Sato and S. Komaba, PNAS 112 (2015) 7650.
[3] N. Yabuuchi, M. Nakayama, M. Takeuchi, S. Komaba, Y. Hashimoto, T. Mukai, H. Shiiba, K. Sato, Y. Kobayashi, A. Nakao, M. Yonemura, K. Yamanaka, K. Mitsuhara and T. Ohta, Nature Communications 7 (2016) 13814.
[4] J. Lee, A. Urban, X. Li, D. Su, G. Hautier, G. Ceder, Science 343 (2014) 519.

N. Yabuuchi[1] and M. Yonemura[2,3]
[1]Department of Applied Chemistry, Tokyo Denki University; [2]Institute of Materials Structure Science (IMSS), High Energy Accelerator Research Organization (KEK); [3]Department of Materials Structure Science, Sokendai (The Graduate University for Advanced Studies)

Nanometer-Size Effect on Hydrogen Sites in Palladium Lattice

1. Introduction

Palladium hydride (PdH_x, $0 < x < 1$) is the best known classical metal hydride, which has been investigated by many physicists and chemists. It has been remarked also from industrial points of view, *e.g.*, hydrogen storage, filters, sensors, catalysts, etc. In the hydrogen adsorption process, a hydrogen molecule (H_2) dissociates into two hydrogen atoms (2H), and the H atoms occupy the interstitial sites of the Pd lattice. In the H concentration region higher than $x = 0.6$, the hydride crystal takes the β phase with an fcc (NaCl-type) structure as shown in Fig. 1(a). In the β phase, it is known that the H atoms are located only at the octahedral (O) sites (1/2, 1/2, 1/2) at ambient temperature and H_2 pressure [1]. In other transition metals with the fcc lattice, H atoms also preferentially occupy the O sites. In high-temperature or high-pressure conditions, however, the tetrahedral (T) sites (1/4, 1/4, 1/4) are partially occupied, for example in PdD_x [2] and fcc-FeD_x [3].

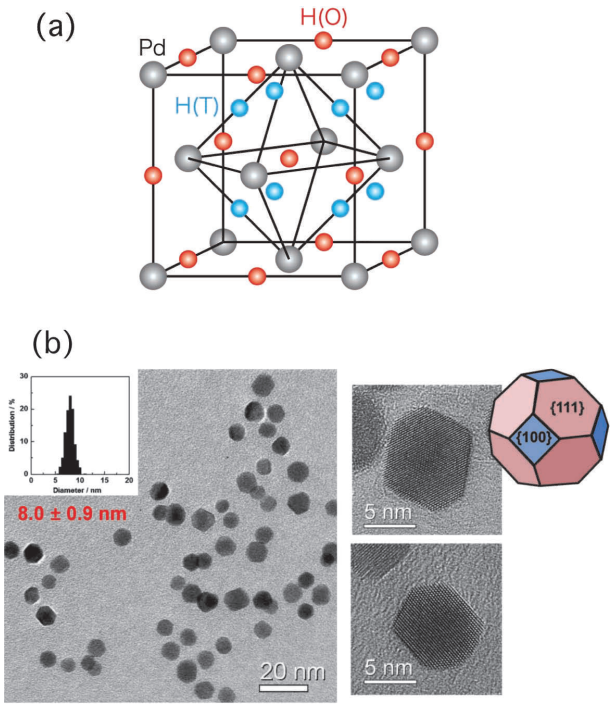

Figure 1. (a) Structure of the β phase of Pd hydrides. The red and blue spheres show the possible octahedral and tetrahedral sites for hydrogen atoms, respectively. The gray spheres show the Pd fcc lattice. (b) Photographs of the transmission electron microscope (TEM) for Pd nanoparticles [5]. The size distribution of the nanoparticles and the schematic drawing of an edge-cut octahedron are also shown.

The physical and chemical properties of nanometer-sized materials are of interest, since they are often different from the bulk properties. As for the nanoparticles of palladium hydrides, there are drastic changes of the H_2 pressure-composition phase diagram [4] and heat capacity [5]. To understand the characteristic properties of PdH nanoparticles from microscopic point of view, it is first necessary to investigate their structure, including the location of hydrogen atoms. In this work, therefore, we have performed *in situ* neutron powder diffraction (NPD) experiments [6] for high-quality Pd nanoparticles, as shown in Fig. 1(b). The nanoparticles have a well-defined shape of an edge-cut octahedron with diameter of 8.0 ± 0.9 nm. The nanoparticles are covered with a protective polymer polyvinylpyrrolidone (PVP) to avoid adhesion between the nanoparticles. The NPD measurements were performed using a high-intensity total diffractometer (NOVA) installed at J-PARC.

2. Results and discussion

Figure 2 shows the neutron diffraction pattern of $PdD_{0.363}$ nanoparticles measured at 300 K under 0.11 MPa of D_2 gas. The amount of the D atoms absorbed into Pd nanoparticles was precisely determined by the hydrogen gas control system installed on NOVA. The data shown in Fig. 2 were obtained after subtracting the large contribution of the incoherent scattering from PVP. This is the first neutron diffraction data for nanoparticles of metal hydrides.

The crystal structure of $PdD_{0.363}$ has been refined by the Rietveld analysis using the Z-Rietveld software [7]. We have examined the following structural models: (model 1) the O sites are occupied by the D atoms homogeneously; (model 2) the O sites in the shell part (a few layers near the surface) are occupied; (model 3) both the O and T sites are occupied homogeneously; (model 4) the O and T sites in the shell part and the O sites in the core part are occupied. In models 2 and 4, the hypothetical phase separation between the shell and core part was assumed to incorporate the surface effect of the nanoparticles. The best fit result was obtained with model 4. The obtained fitting parameters are as follows: lattice constants of the shell and core parts a(shell) = 4.0177(4) Å, a(core) = 4.0027(2) Å, Pd atomic fraction of the shell part f_S = 0.24 (fixed),

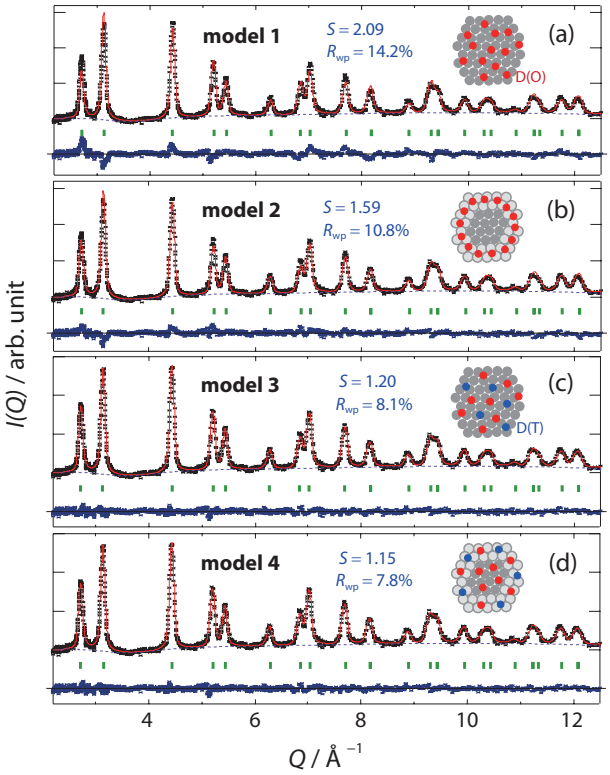

Figure 2. Observed (black crosses) and calculated (red curves) diffraction patterns of the nanoparticles of $PdD_{0.363}$ at 300 K. The Rietveld analyses were performed assuming structural models 1-4 shown schematically in the insets. The gray circles represent the Pd atoms, and the red and blue circles show the D atoms at the O and T sites, respectively.

isotropic atomic displacements B_{Pd} = 0.280(5) Å^2, $B_{D(O)}$ = 1.99(6) Å^2, $B_{D(T)}$ = 14.1(5) Å^2, occupancies of the O and T sites $g_{D(O)}$(shell) = $g_{D(O)}$(core) = 0.251(2) and $g_{D(T)}$(shell) = 0.234(3) under the constraints $g_{D(O)}$(shell) = $g_{D(O)}$(core), $x = (1 - f_S)\, g_{D(O)}(\text{core}) + f_S[g_{D(O)}(\text{shell}) + 2g_{D(T)}(\text{shell})] = 0.363$. Our Rietveld analysis revealed that 30% of the D atoms are located at the T sites and 70% at the O sites in the Pd nanoparticles. This contrasts with the result that only the O sites are occupied in bulk PdD_x. We guess that the T site occupation can be due to the change in potential energy caused by the surface and/or distortion effects of the nanoparticles. The T site occupation is associated with the drastic changes in the diffusional and vibrational motions of the H atoms in Pd nanoparticles revealed in our recent quasielastic [8] and inelastic [9] neutron scattering investigations. Furthermore, the present work will become a foundation for future research in the nanoparticles of other metal and alloy hydrides.

3. Acknowledgments

The experiment in the MLF at J-PARC was performed with the approval of J-PARC (Proposal No. 2012B0246, 2014A0228). This work is financially supported by CREST, Japan Science and Technology Agency.

References

[1] H. E. Worsham, M. K. Wilkinson and C. G. Shull, J. Phys. Chem. Solids **3**, 303-310 (1957).
[2] K. G. Mclennan, E. M. Gray and J. F. Dobson, Phys. Rev. B **78**, 014104 (2008).
[3] A. Machida, H. Saitoh, H. Sugimoto, T. Hattori, A. Sano-Furukawa, N. Endo, Y. Katayama, R. Iizuka, T. Sato, M. Matsuo, S. Orimo and K. Aoki, Nat. Commun. **5**, 5063 (2014).
[4] M. Yamauchi, R. Ikeda, H. Kitagawa and M. Takata, J. Phys. Chem. C **112**, 3294-3299 (2008).
[5] H. Akiba, H. Kobayashi, H. Kitagawa, M. Kofu and O. Yamamuro, Phys. Rev. B **92**, 064202 (2015).
[6] H. Akiba, M. Kofu, H. Kobayashi, H. Kitagawa, K. Ikeda, T. Otomo and O. Yamamuro, J. Am. Chem. Soc. **138**, 10238-10243 (2016).
[7] R. Oishi, M. Yonemura, Y. Nishimaki, S. Torii, A. Hoshikawa, T. Ishigaki, T. Morishima, K. Mori and T. Kamiyama, Nucl. Instrum. Methods Phys. Res. Sect. A **600**, 94-96 (2009).
[8] M. Kofu, N. Hashimoto, H. Akiba, H. Kobayashi, H. Kitagawa, M. Tyagi, A. Faraone, J. R. D. Copley, W Lohstroh and O. Yamamuro, Phys. Rev. B **94**, 064303 (2016).
[9] M. Kofu, N. Hashimoto, H. Akiba, H. Kobayashi, H. Kitagawa, K. Iida, M. Nakamura and O. Yamamuro, Phys. Rev. B **96**, 054304 (2017).

H. Akiba[1], M. Kofu[1], H. Kobayashi[2], H. Kitagawa[2], K. Ikeda[3,4], T. Otomo[3,4], and O. Yamamuro[1]
[1]Institute for Solid State Physics, University of Tokyo; [2]Department of Chemistry, Graduate School of Science, Kyoto University; [3]Institute of Particle and Nuclear Studies, KEK; [4]Neutron Science Section, Materials and Life Science Division, J-PARC Center

Deficient 5 Coordination Li^+ in Solvate Ionic Liquid toward Electrolytes for Next Generation Li Batteries

1. Introduction

Solvate ionic liquids (SIL) are a new category of room-temperature ionic liquids [1] that have novel applications as electrolytes in the next generation lithium secondary batteries. Watanabe and Dokko et al. demonstrated that SILs composed of an equimolar mixture of LiTFSA salt (TFSA: bis-(trifluoromethanesulfonyl) amide) and oligo-ether glymes such as triglyme (G3: $CH_3O–(CH_2CH_2O)_3–CH_3$) and tetraglyme (G4: $CH_3O–(CH_2CH_2O)_4–CH_3$), can be utilized as electrolytes for Li secondary batteries [2], particularly Li-sulfur ones, due to the rather small solubility of the electrode active species lithium polysulfide Li_2S_n [3]. In addition, the electrode reactions and the Li_2S_n solubility should be governed by the liquid structure and/or the Li^+ local structure, because it is crucial to maintain the glyme solvate complex of Li^+ $[Li(glyme)]^+$ structure [4].

Recently, the molecular level properties of the SILs have been probed using the NMR diffusion coefficients, Raman spectra analysis, and theoretical calculations, such as ab initio molecular orbital calculations and molecular dynamics simulations. These studies clarified that the Li^+ was coordinated with almost all of the glyme to form $[Li(glyme)]^+$ in the SIL.

Quite recently, the Atkin's group performed neutron scattering experiments with empirical potential and structure refinement (EPSR) analysis to elucidate the bulk nanostructure of various solvate ionic liquids like [Li(G4)][TFSA] and [Li(G4)][NO_3] [5]. However, the Li^+ local structure in the SILs is still needed from an experimental perspective as this structure is critical for the Li^+ ionic conduction mechanism in the bulk and the reduction/oxidization mechanisms at the SIL electrolyte/electrode interface. For that purpose, neutron scattering experiments with the $^{6/7}$Li isotopic substitution technique are one of the most powerful tools and have successfully revealed Li^+ solvation structures in aqueous and non-aqueous solvent solutions.

Here, the Li^+ local structure in [Li(G4)][TFSA] SIL is determined using neutron total scattering experiments with the $^{6/7}$Li isotopic substitution technique. We found the unique deficient 5 coordination structure of Li^+ in the SIL.

2. Experimental

The sample solution was introduced into a thin-walled cylindrical V-Ni null alloy cell (6.0 mm in inner diameter and 0.1 mm in wall thickness) and sealed by an indium seal. Neutron scattering measurements were carried out at 25°C using the NOVA total scattering spectrometer installed at BL21 of the MLF pulsed neutron source in J-PARC, Tokai, Japan. The incident beam power of the proton accelerator was 300 kW. Scattered neutrons (neutron wave band of $0.1 \leq \lambda \leq 8.7$ Å) were detected by ca. 900 of 20 atm ^{3}He position sensitive proportional counters (1/2 inch ϕ, 800 mm in active length with 5 mm in positional resolution) installed at 20°(13.1° – 27.9°), 45°(33.6° – 54.9°), 90°(72.7° – 107.4°) and back scattering (136.5° – 169.0°) detector banks. The data accumulation time was ca. 6 h for each sample. Measurements were made in advance for a 6 mm in diameter vanadium rod, empty cell and instrumental background. The observed scattering intensities for the sample were corrected for instrumental background, absorption of sample and cell, multiple and incoherent scatterings. The wavelength dependence of the total cross sections for H nucleus was estimated from the observed total cross sections for H_2O. Since the attenuation coefficients calculated for the absorption correction exhibit significant neutron wavelength (λ) dependence for the sample with large absorption cross section, the attenuation coefficients, $A_{s,sc}(2\theta, \lambda)$ and $A_{c,sc}(2\theta, \lambda)$, were successfully approximated by fitting them in the form of exponential of the 7th polynomial of λ by the following equation,

$$A(2\theta, \lambda) = \exp(\Sigma\, \alpha_i \lambda_{i-1}). \quad (1)$$

The first-order difference function, $\Delta_{Li}(Q)$, ($Q = 4\pi\sin\theta/\lambda$ is a scattering vector, where θ and λ are the scattering angle and neutron wave length, respectively) is derived from the numerical difference between scattering cross sections observed for two solutions that are identical compositions except for the scattering length of Li. The $\Delta_{Li}(Q)$ normalized for stoichiometric units, $(LiTFSA)_x(G4)_{1-x}$ can be written as linear combination of partial structure factors, $a_{Lij}(Q)$, involving correlations form the Li - j pair:

$$\begin{aligned}\Delta_{Li}(Q) = {} & A[a_{LiO}(Q) - 1] + B[a_{LiC}(Q) - 1] + C[a_{LiH}(Q) - 1] \\ & + D[a_{LiF}(Q) - 1] + E[a_{LiS}(Q) - 1] + F[a_{LiN}(Q) - 1] \\ & + G[a_{LiLi}(Q) - 1] \quad (2)\end{aligned}$$

where, $A = 2x(5 - x)(b^{6}\mathrm{Li} - b^{\mathrm{nat}}\mathrm{Li})b\mathrm{O}$, $B = 4x(5 - 4x)(b^{6}\mathrm{Li} - b^{\mathrm{nat}}\mathrm{Li})b\mathrm{C}$, $C = 44x(1 - x)(b^{6}\mathrm{Li} - b^{\mathrm{nat}}\mathrm{Li})b\mathrm{H}$, $D = 12x^{2}(b^{6}\mathrm{Li} - b^{\mathrm{nat}}\mathrm{Li})b\mathrm{F}$, $E = 4x^{2}(b^{6}\mathrm{Li} - b^{\mathrm{nat}}\mathrm{Li})b\mathrm{S}$, $F = 2x^{2}(b^{6}\mathrm{Li} - b^{\mathrm{nat}}\mathrm{Li})b\mathrm{N}$, and $G = x^{2}(b^{2\,6}\mathrm{Li} - b^{2\mathrm{nat}}\mathrm{Li})$. Since the observed $\Delta_{\mathrm{Li}}(Q)$ from forward angle detector pixels located at $13.1 \leq 2\theta \leq 27.9°$ agree well within the statistical uncertainties, they were combined at the Q-interval of 0.1 Å^{-1} and used for subsequent analyses.

The distribution function around Li^{+}, $G_{\mathrm{Li}}(r)$, was deduced from the Fourier transform of $\Delta_{\mathrm{Li}}(Q)$:

$$\begin{aligned} G_{\mathrm{Li}}(r) &= 1 + (A + B + C + D + E + F + G)^{-1}(2\pi^{2}\rho_{0}r)^{-1} \\ &\quad \int Q\Delta_{\mathrm{Li}}(Q)\sin(Qr)\,dQ \\ &= [Ag_{\mathrm{LiO}}(r) + Bg_{\mathrm{LiC}}(r) + Cg_{\mathrm{LiH}}(r) + Dg_{\mathrm{LiF}}(r) + Eg_{\mathrm{LiS}}(r) \\ &\quad + Fg_{\mathrm{LiN}}(r) + Gg_{\mathrm{LiLi}}(r)] \times (A + B + C + D + E + F \\ &\quad + G)^{-1} \end{aligned} \tag{3}$$

The upper limit of the integral was set to 20 Å^{-1} in the present study.

3. Results and discussion

The interference functions $i(Q)$ were successfully obtained in the $0 < Q/\text{Å}^{-1} < 26$ range for sample solutions of [*Li(G4)][TFSA] (* stands for both ^{6}Li enriched and natural abundance) solvate ionic liquids. Consequently, $\Delta_{\mathrm{Li}}(Q)$ was also adequately determined in the $0 < Q/\text{Å}^{-1} < 20$ range. The radial distribution function $G_{\mathrm{Li}}(r)$ obtained by Fourier transformation of the $\Delta_{\mathrm{Li}}(Q)$ is shown in Fig. 1. The first and the second peaks of $G_{\mathrm{Li}}(r)$ can be assigned to the positions of atoms close to the Li^{+} cations.

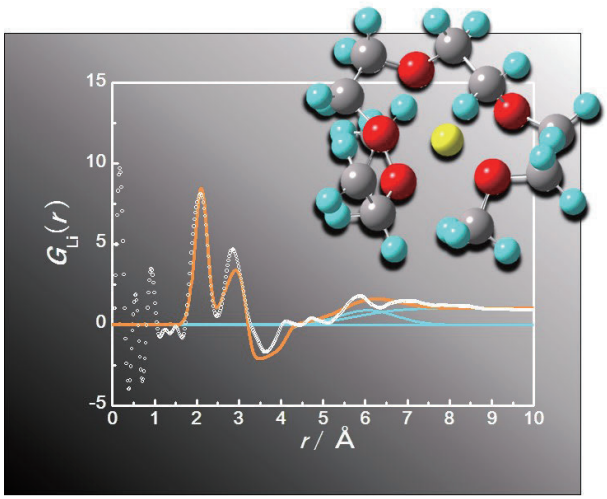

Figure 1. The partial radial distribution functions $G_{\mathrm{Li}}(r)$ for the solvate ionic liquid [Li(G4)][TFSA]. Dots and solid lines represent experimental and calculated based on the model structure shown in the figure, respectively.

Such close neighbors can be unambiguously found at about 2 and 3 Å, respectively. It should be noted that the broad valley found in the $G_{\mathrm{Li}}(r)$ at around 3.5 Å can be ascribed to the solvated G4 hydrogen atoms of the negative neutron scattering length. The presence of the valley in the $G_{\mathrm{Li}}(r)$ suggests that most of the Li^{+} in the SIL is solvated by G4 molecules, which is consistent with the previous NMR and Raman studies.

We performed a quantitative analysis of the neutron scattering data based on a local structure model. In the case of the G4 molecule, 5 oxygen atoms can potentially coordinate to the Li^{+} ion (although in solution the Li^{+} prefers a 4-atom coordinated structure). Therefore, the fitting parameters considered here were the Li^{+} – G4 coordination number, the Li^{+}–O bond lengths, their thermal factors, the Li^{+}–O–C bond angles, also twelve significant torsion angles along the backbone of the G4 molecule. The $G_{\mathrm{Li}}(r)$, calculated based on the obtained structural parameters of the model structure, is shown in Fig. 1 as a solid line. As shown in the figure, the model agrees with the experimental results. An atomistic depiction of the model structure is shown in Fig. 1.

In the least squared model structure, the Li^{+} is coordinated by five oxygen atoms in G4 that have their own characteristic distances, 2.06, 2.09, 2.13, 1.93 and 2.24 Å, respectively. Clearly, 2.24 Å is significantly larger than the others. The average distance of 2.05 Å, except the longest one, is still significantly larger than the values of 1.95 – 1.97 Å usually found in aqueous solutions. However, the distances are similar to the values for cyclic and acyclic carbonates (2.04 – 2.08 Å) and for the polyethyleneoxide solutions (2.07 – 2.1 Å). According to Shannon and Bondi, the ionic radius for the 4-coordinated Li^{+} and van der Waals radius for the oxygen atom are 0.59 and 1.52 Å, respectively. The sum of these two values, 2.11 Å, is close to the Li^{+} – O average distance of 2.05 Å. On the other hand, the 2.24 Å distance is considerably larger than 2.11 Å.

To obtain further insights, classic MD simulations were performed. Figure 2 compares the MD-derived $G_{\mathrm{Li}}(r)$ with that from the experiments. This figure reveals good agreement between them. In the MD simulations, the Li^{+} is on average a 5-coordinated structure: 4 oxygen atoms from the G4 molecule and 1 from the TFSA anion, respectively. Figure 3 shows pair correlation functions $g(r)$ and their integral curves $N(r)$ for the Li^{+} – O (G4) in the simulated [Li(G4)][TFSA] SIL. As shown in the figure, the first peak in $g(r)$ for the central oxygen atom in G4 is the shortest and sharpest, which suggests that the central oxygen inertly coordinates to the Li^{+}. As

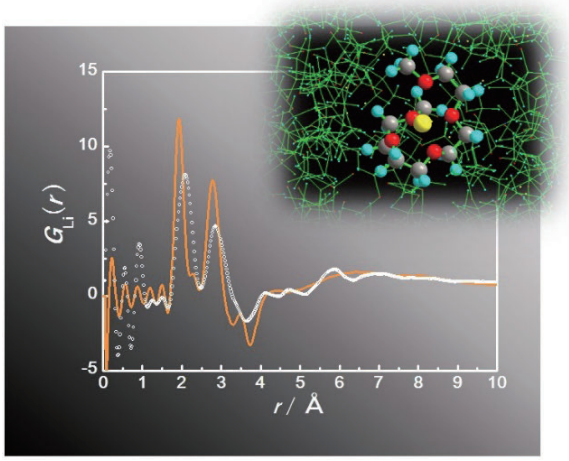

Figure 2. The partial radial distribution functions $G_{Li}(r)$ for the solvate ionic liquid [Li(G4)][TFSA]. Dots and a solid line represent experimental and calculated based on MD simulations, respectively.

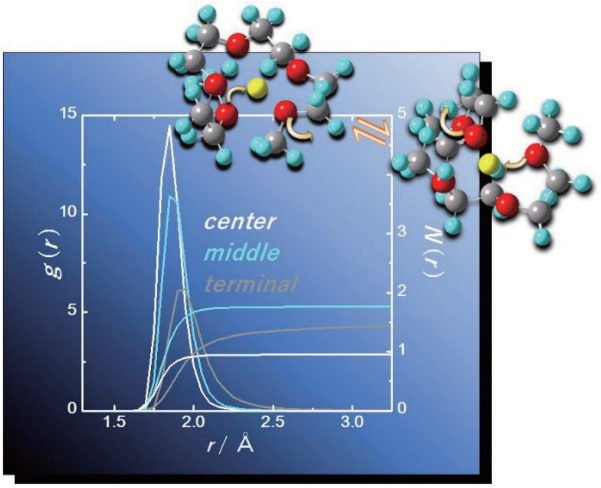

Figure 3. The pair correlation functions and its integral curves for the Li^+ - O (G4) in the solvate ionic liquid [Li(G4)][TFSA].

the oxygen atoms locate closer to the terminal, the first peaks in $g(r)$ shift further with broadening. The smallest coordination number of about 1.4 for the terminal oxygen atoms with the longest position and the broadest width is consistent with the present neutron experiments. This means that on average one of the terminal oxygen atoms in the G4 is not fully coordinated to the Li^+, which supports the longer 2.24 Å distance predicted by the model. Our MD simulations suggested that the terminal oxygen atoms never fully coordinate to the Li^+ but rather undergo successive coordination/uncoordination stages.

4. Future

Here, we demonstrated that the neutron scattering with the $^{6/7}$Li isotopic substitution technique evidently reveals the Li^+ local structure in much complicated solution systems as the SIL for the next generation Li secondary batteries. To build electrochemical devices, including Li batteries with much higher performance, innovative electrolytes, which have new ionic conduction mechanisms and/or redox reactions at the electrode/electrolyte interface, are being discovered one after another. It is expected that the neutron scattering techniques will strongly support further development of science and technology in this field.

References

[1] C. A. Angell, Y. Ansaria, Z. Zhaoa, Faraday Discuss,154, 9-27, (2012).

[2] T. Tamura, T. Hachida, K. Yoshida, N. Tachikawa, K. Dokko, M. Watanabe, J. Power Sources, 195, 6095-6100, (2010).

[3] K. Dokko, N. Tachikawa, K. Yamauchi, M. Tsuchiya, A. Yamazaki, E. Takashima, J-W. Park, K. Ueno, S. Seki, N. Serizawa, M. Watanabe, J. Electrochem. Soc. 160, A1304-A1310, (2013).

[4] K. Ueno, R. Tatara, S. Tsuzuki, S. Saito, H. Doi, K. Yoshida, T. Mandai, M. Matsugami, Y. Umebayashi, K. Dokko, M. Watanabe, Phys. Chem. Chem. Phys. 17, 8248-8257, (2015).

[5] T. Murphy, S. K. Callear, N. Yepuri, K. Shimizu, M. Watanabe, J. N. C. Lopes, T. Darwish, G. G. Warr, R. Atkin, Phys. Chem. Chem. Phys. 18, 17224-17236, (2016).

Y. Umebayashi[1], H. Watanabe[1], S. Saito[1], K. Dokko[2], M. Watanabe[2], and Y. Kameda[3]

[1]Graduate School of Science and Technology, Niigata University; [2]Department of Chemistry and Biotechnology, Yokohama National University; [3]Department of Material and Biological Chemistry, Faculty of Science, Yamagata University

Contrast Variation by Dynamic Nuclear Polarization and Time-of-Flight Small-Angle Neutron Scattering

1. Introduction

Contrast variation for small-angle neutron scattering (SANS) is a very useful technique in investigating multi-component systems. For contrast variation studies, deuterium substitution has been conventionally used, which takes advantage of the difference in the neutron scattering length between protons and deuterons. The deuterium substitution technique can be easily applied to solutions or gels, due to reasonable availability of deuterated solvent, whereas the synthesis of deuterated polymer is costlier and requires significant efforts. Hence, alternative methods are needed. Besides deuterium substitution, contrast variation can also be achieved by controlling both spin states of neutrons and protons. The coherent scattering length ($b_{coh,H}$) of a proton against a fully polarized neutron are given by the following equation [1]:

$$b_{coh,H} = (-0.374 + 1.456\, P_H) \times 10^{-12}\ [\mathrm{cm}] \quad (1)$$

where P_H denotes the proton spin polarization. Polarization means the difference in populations between up and down spins. Figure 1 shows the P_H dependence of $b_{coh,H}$. Note that the variation of $b_{coh,H}$ is about 2.5 times larger than the one caused only by deuterium substitution. As for $P_H = 0$, the coherent scattering length of hydrogen is -0.374×10^{-12} cm, whereas that for a deuteron is 0.667×10^{-12} cm.

At room temperature, up and down proton spins are almost equally populated. With decreasing temperature and increasing magnetic field, the proton spin polarization increases. However, even at 3.3 Tesla and 1.2 K, the proton spin is polarized up to only 0.3%. In contrast, the electron spin is largely polarized up to 95% under the same conditions (at 3.3 Tesla and 1.2 K). This is because of a large difference in the gyromagnetic ratio between the electron spin and the proton spin ($|\gamma_e|/\gamma_H = 658$). The large polarization of an electron spin can be transferred to the proton spins by microwave irradiation with energy equal to the simultaneous flipping of electron and proton spins. Consequently, high proton spin polarization is achieved. This is called dynamic nuclear polarization (DNP) and requires electron spin doping, magnetic field, low temperature, and microwave irradiation.

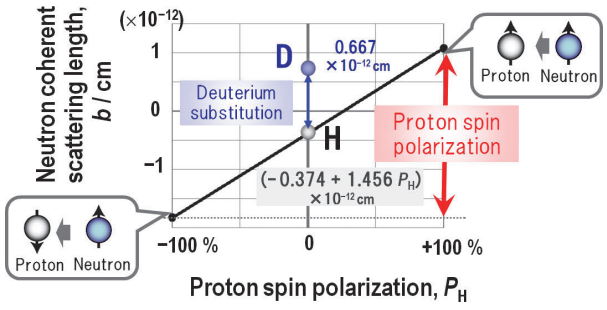

Figure 1. Coherent scattering length of a proton against a fully polarized neutron beam as a function of proton spin polarization, P_H.

A stable organic free radical, TEMPO [(2,2,6,6-tetramethylpiperidine-1-yl)oxy] can be used as an electron spin source. TEMPO is sublimable around room temperature. Vaporized TEMPO permeates spontaneously the rubbery phase of solid polymer samples (Fig. 2). Based on this vapor sorption technique, we prepared polymer systems for SANS studies after the construction of a DNP cryostat [2] and polarized neutron ultra-small-angle scattering spectrometer (SANS-J-II) [3] at research reactor JRR-3, Tokai, Japan. We investigated the polyethylene film [4] and the di-block copolymer to evaluate precisely the inhomogeneity of proton polarization around doped TEMPO molecules [5]. Subsequently, the vapor sorption technique was successfully applied to silica-filled rubber, which is used for fuel-efficient tires [6]. The vapor sorption technique can be applied to industrial rubber products after a manufacturing process.

A tire is a multi-component nanocomposite and an attractive target for contrast variation SANS with DNP. To improve tear and wear resistance, filler particles, such as carbon black (CB) and silica particles (SP), are mixed into the rubbery matrix. The spatial distribution of filler particles in rubbery matrix determines not only the tires' reinforcement but also the energy loss performance. According to the empirical knowledge that the homogeneous dispersion of filler particles lowers the energy loss, various attempts to achieve dispersion

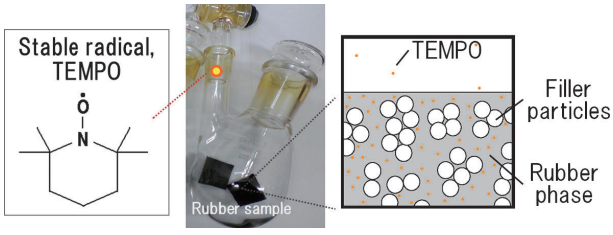

Figure 2. TEMPO vapor sorption technique for rubber sample.

control have been conducted. A reliable methodology for evaluating the filler particle dispersion is critical for optimizing the tire rubber performance.

The combination of CB and SP is frequently used in tire manufacturing. In addition to the above-mentioned effects, CB is useful for specific UV resistance and electric discharge. For precise structural analyses, we need to decompose the observed SANS profiles into individual partial scattering functions of CB and SP.

2. DNP experiment setup

As a model system for industrial tires, we prepared a ternary mixture of SBR (styrene-butadiene random copolymer) with SP and CB particles (SBR/SP/CP). The sample consisted of solution-SBR, silica particles, CB, silane-coupling agent and other additives. In the mixture, the volume fractions of CB and SP were 2% and 10%, respectively. After cure process (170°C for 20 min), the rubbery mixture was placed with TEMPO inside a sealed container at 40°C for 1 week. Consequently, the vaporized TEMPO spontaneously permeated the rubbery matrix. By ESR measurement, the TEMPO concentration was determined to be 35 mM. It was close enough to the empirically-known optimum value (30 mM) for DNP.

Figure 3 shows the schematic picture of the DNP-SANS experiment performed at TAIKAN (BL15) in J-PARC MLF. TAIKAN is equipped with a magnetic super-mirror polarizer, composed of Fe/Si multilayer ($4Q_c$) to polarize neutron beams [7].

The top roof of the shield room has a slide hatch covering over the sample stage. Through this slide hatch, the DNP cryostat was introduced onto the sample stage. The DNP cryostat was originally designed for SANS-J-II at JRR-3 and cannot fully cover the detectors of TAIKAN, which has detectors for neutrons with wider-scattering-angles ($2\theta > 15°$).

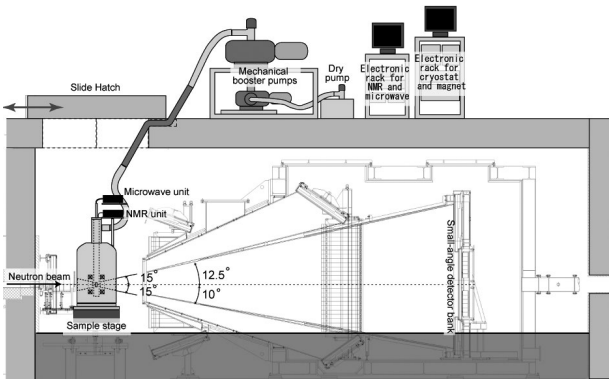

Figure 3. Schematic view of the experimental setup for DNP in BL15.

The TEMPO doped rubber specimen was placed into a chamber filled with liquid ^{4}He. By evaporating the liquid ^{4}He, the specimen was cooled down to 1.2 K during continuous irradiation of microwave (94 GHz). The superconducting magnet generated a magnetic field up to 3.5 Tesla at the sample position. The inhomogeneity of the magnetic field ($\Delta B/B0$) was designed to be less than 10^{-4}. The neutron beam passed along the central axis of the magnet coils. The windows through which the neutron beam passed were formed by thin aluminium plates, which caused less background scattering.

The top roof of the shield room had two trenches under the slide hatch. Through these trenches, pipes and cables were pulled out. The pipes were necessary to evaporate liquid ^{4}He. The cables were used for energizing the superconducting magnet, monitoring the signals from the liquid helium level meter and the pressure and temperature sensors, measuring the NMR signals, and supplying voltage to the microwave generator. The mechanical booster pump unit and the two electronic racks were placed on the roof of the shield room. Consequently, we controlled remotely the magnetic field, sample temperature, NMR measurements and microwave irradiation.

3. Contrast variation SANS results

Figure 4a shows the SANS results obtained for the ternary mixture system (SBR/SP/CP). We employed the limited wavelength range of $4 < \lambda < 7.6$ Å, where the neutron polarization was high ($P_N > 97\%$). The q-dependence of the SANS profile varied as changing P_H; the scattering maxima due to silica particles were observed for $P_H = 0\%$ and $P_H = -34\%$, whereas the scattering maxima disappeared for $P_H = +38\%$. As shown in Fig. 4b, the scattering length densities of silica and SBR match at $P_H = +30\%$. Around the matching point, the CB contribution was observed more obviously.

SANS for the ternary mixture is given by a sum of three partial scattering functions ($S_{SP\text{-}SP}(q)$, $S_{CP\text{-}CP}(q)$ and $S_{SP\text{-}CP}(q)$), as follows

$$I(q; P_H) = [\rho_{SP} - \rho_{SBR}(P_H)]^2 S_{SP\text{-}SP}(q) + [\rho_{CP} - \rho_{SBR}(P_H)]^2 S_{CP\text{-}CP}(q) + 2[\rho_{SP} - \rho_{SBR}(P_H)][\rho_{CP} - \rho_{SBR}(P_H)] S_{SP\text{-}CP}(q), \quad (2)$$

where the partial scattering functions are weighted by contrast factors. In the above equation, ρ_{SP}, ρ_{CP}, and ρ_{SBR} correspond to the neutron scattering-length density of SP, CP and SBR phases: $\rho_{SP} = 3.08 \times 10^{10}$ cm^{-2}, $\rho_{CP} = 6.50 \times 10^{10}$ cm^{-2}, and $\rho_{SBR} = (0.62 + 8.39\ P_H) \times 10^{10}$ cm^{-2}. Only ρ_{SBR} depends on P_H, because SBR contains hydrogen (Fig. 4b).

Figure 5 shows the separated partial scattering functions calculated by applying singular value decomposition to the observed SANS profiles with various P_H. The partial scattering function of silica, $S_{SP\text{-}SP}$, agreed well with the spherical form factor with the radius of 610 ± 40 Å. The same profile was observed for the silica-filled SBR rubber sample (not shown here). The partial scattering function of CB, $S_{CP\text{-}CP}$, indicated a power-law function of $q^{-3.6}$, deviating from the Porod-law (q^{-4}). This originated from the surface structure of CB. The result agreed with the reports for CB-filled rubber specimens [8]. The decomposition into partial scattering functions was successfully achieved. The cross-correlation term between silica and CB, $S_{SP\text{-}CP}$, was also determined. $S_{SP\text{-}CP}$ is negligibly small as compared to $S_{SP\text{-}SP}$ and $S_{CP\text{-}CP}$.

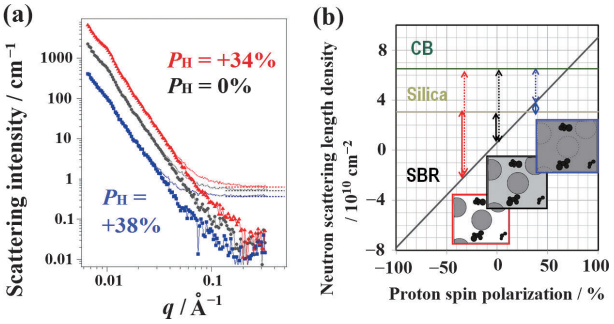

Figure 4. (a) SANS profile for the SBR/SP/CP mixture at various P_H. (b) Neutron scattering length density of each domains of the sample as a function of proton spin polarization. The grey scale of the microscopic view corresponds to the neutron scattering length density.

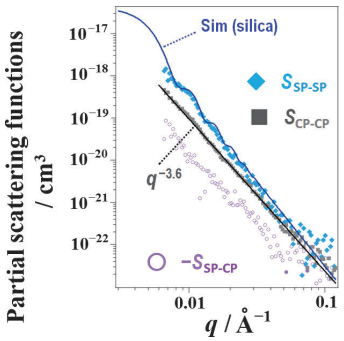

Figure 5. Separated partial scattering functions for the ternary mixture (SBR/SP/CP).

4. Conclusion

In this article, we report the first attempt of DNP and contrast variation SANS experiments on the model mixtures for industrial tire conducted at the MLF of the J-PARC [9]. We performed TOF-SANS experiments using neutrons with a wide λ-range, which caused imperfect neutron polarization and variations of coherent and incoherent scattering lengths. By carefully circumventing the effect from the imperfect neutron polarization, the partial scattering function separation was successfully demonstrated for the ternary system (SBR/SP/CP).

Finally, the neutron scattering experiment at the MLF of the J-PARC was performed under the user program (Proposal No. 2016A0160). We appreciate the help of the MLF instrument safety team and the sample environment team. This study was financially supported by a Grant-in-Aid for Young Scientist (A) (Grant No. 25706033) of the Japan Society for the Promotion of Science.

References

[1] V. F. Sears, Neutron News, 3(3), 26-37 (1992).
[2] T. Kumada, Y. Noda, T. Hashimoto and S. koizumi, Phys. B, 404, 2637-2639 (2009).
[3] S. Koizumi, H. Iwase, J. Suzuki, T. Oku, R. Motokawa, H. Sasao, H. Tanaka, D. Yamaguchi, H. M. Shimizu and T. Hashimoto, J. Appl. Cryst. 40, s474-s479 (2007).
[4] Y. Noda, T. Kumada, T. Hashimoto and S. Koizumi, Phys. B, 404, 2572-2574 (2009).
[5] Y. Noda, T. Kumada, T. Hashimoto and S. Koizumi, J. Appl. Cryst. 44, 503-513 (2011).
[6] Y. Noda, D. Yamaguchi, T. Hashimoto, T. Shamoto, S. Koizumi, T. Yuasa, T. Tominaga and T. Sone, Phys. Procedia, 42, 52-57 (2013).
[7] T. Shinohara, J. Suzuki, T. Oku, S. Takata, H. Kira, K. Suzuya, K. Aizawa, M. Arai, T. Otomo, and M. Sugiyama, Phys. B. 404, 2640-2642 (2009).
[8] T. Koga, T. Hashimoto, M. Takenaka, K. Aizawa, N. Amino, M. Nakamura, D. Yamaguchi, and S. Koizumi, Macromolecules, 41, 453-464 (2008).
[9] Y. Noda, S. Koizumi, T. Masui, R. Mashita, H. Kishimoto, D. Yamaguchi, T. Kumada, S. Takata, K. Ohishi and J. Suzuki: J. Appl. Cryst., 49 2036-2045 (2016).

Y. Noda[1], S. Koizumi[1], T. Masui[2], R. Mashita[2], H. Kishimoto[2], D. Yamaguchi[3], T. Kumada[3], S. Takata[4], K. Ohishi[5], and J. Suzuki[5]
[1]Institute of Quantum Beam Science, Ibaraki University; [2]Sumitomo Rubber Industries Ltd; [3]Material Science Research Center, Japan Atomic Energy Agency; [4]J-PARC Center, Japan Atomic Energy Agency; [5]Neutron Science and Technology Center, Comprehensive Research Organization for Science and Society (CROSS)

A Contrast Variation Study of Nanogels by Small-Angle Neutron Scattering

1. Introduction

Partially hydrophobic groups-bearing polysaccharides spontaneously form stable nanogel of 20–30 nm diameter in aqueous solution due to hydrophobic interactions (Fig. 1) [1, 2]. Because the nanogel possesses a high loading capacity for proteins and drugs mainly through the hydrophobic interactions, they have been applied in drug delivery systems [3]. Although the nanoscopic structure of the nanogels would be strongly related to their properties, no clear structural information has been obtained so far due to their complex multicomponent structure. We investigated the structure of the cholesterol (as a hydrophobic group) -bearing pullulan (as a polysaccharide) (CHP) nanogels by using as means of contrast variation small-angle neutron scattering (CV-SANS), which enables us to determine quantitative complex structure at nanometer scale.

CV-SANS is a powerful tool to investigate multicomponent structures with nanometer resolution [4]. Because the components (pullulan, cholesterol, and water) in the CHP nanogel possess different scattering length densities, as shown in Fig. 2(a), the scattering intensities are affected by the deuterium and hydrogen ratio in the water. We determined the polymer network structures and cross-linking points in the nanogels individually.

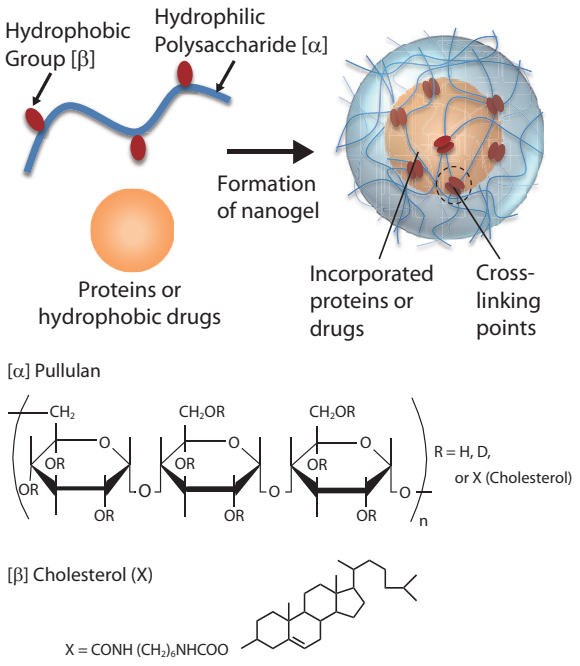

Figure 1. Schematic of a nanogel that is formed by self-associating partially hydrophobic modified polysaccharides.

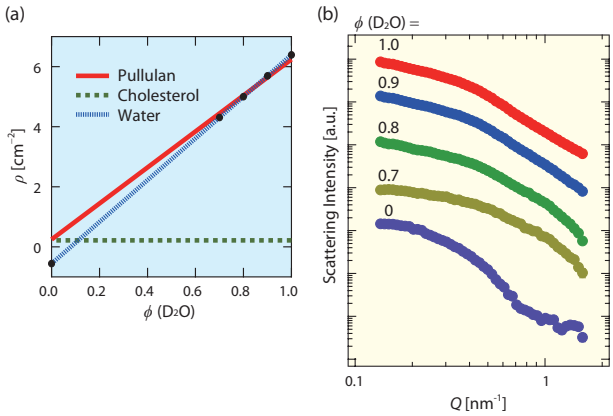

Figure 2. (a) Scattering length density of pullulan, cholesterol, and water as a function of the D_2O volume fraction in the water. The experimental conditions are marked by black filled circles on the dotted line. (b) Scattering intensities of CHP nanogels dispersed in solvents with a deuterium oxide (D_2O) fraction, ϕ_{D2O} = 1.0, 0.9, 0.8, 0.7, and 0.

2. Partial Scattering Functions and Contrast Variation

The CHP nanogel consists of pullulan, cholesterol, and water. Therefore, the scattering intensities of the CHP nanogel can be described using partial scattering functions $S_{ij}(Q)$, as follows:

$$I(Q) = \Delta\rho_p^2 S_{pp}(Q) + 2\Delta\rho_p\Delta\rho_c S_{cp}(Q) + \Delta\rho_c^2 S_{cc}(Q) \qquad (1)$$

Here, $\Delta\rho_i$ (with $i = p$ and c for pullulan and cholesterol, respectively) is the difference in scattering length densities between component i and Q is the momentum transfer defined as $Q = 4\pi \sin(\theta/2)/\lambda$ with scattering angle θ and neutron wavelength λ. $S_{pp}(Q)$ and $S_{cc}(Q)$ are the self-terms, which represent the self-correlations of pullulan and cholesterol, respectively. $S_{cp}(Q)$ is the cross-term, which represents the cross-correlation between pullulan and cholesterol. The partial scattering function possesses a volume dimension. In order to extract these three partial scattering functions, we tuned the scattering length density of the solvents by mixing deuterated and protonated water. The detailed procedure is described elsewhere [1, 4].

3. Scattering Intensity of the CHP Nanogel

The SANS experiments were performed using TAIKAN [5] at J-PARC. For CV-SANS, we measured a series of CHP nanogel samples dispersed in water with a deuterium oxide (D_2O) volume fraction, ϕ_{D2O} = 1.0, 0.9, 0.8, 0.7, and 0. Fig. 2(a) shows the variation of the scattering length density of pullulan, cholesterol, and water as a function of ϕ_{D2O}, which was calculated on the basis of their chemical structures and mass densities. Fig. 2(b) shows the scattering intensities of the nanogels. The scattering intensities vary with the D_2O volume fraction in the water. This is characteristic of multicomponent systems because the contrast matching points for pullulan and cholesterol against water are different as shown in Fig. 2 (a). The partial scattering function for each component was extracted individually by the singular value decomposition [4], then the pullulan network structure and the cholesterol distribution in the nanogels were evaluated.

4. Structures of the Polysaccharide Chains and the Cross-Linking Points in the CHP Nanogel

Figure 3 shows the partial scattering functions of pullulan, $S_{pp}(Q)$, choleterol, $S_{cc}(Q)$, and the pullulan-cholesterol cross-term, $S_{cp}(Q)$, which reflect the spatial correlations of each component. At first, the partial scattering function of pullulan, $S_{pp}(Q)$ was evaluated by the sphere model with the Percus-Yevick (PY) structure factor. This model can reproduce $S_{pp}(Q)$ shown by the blue solid curve in Fig. 3 with two tuning parameters, that is, the radius of the pullulan chain aggregate, R_p, found to be 8.1 ± 0.3 nm and the standard distribution of R_p, σ_R, which is 1.1 ± 0.1 nm. The result indicates that the pullulan chains forms a CHP nanogel skeleton and the nanogel particles can exist stably in water solution. Next, we analyzed the partially scattering function of cholesterol, $S_{cc}(Q)$, which reflects the distribution and the individual volume of the cross-linking points in the CHP nanogel. The spatial configuration of the cross-linking points was evaluated by the fractal dimension, d_f and the upper-cutoff length, ξ. The red solid curve in

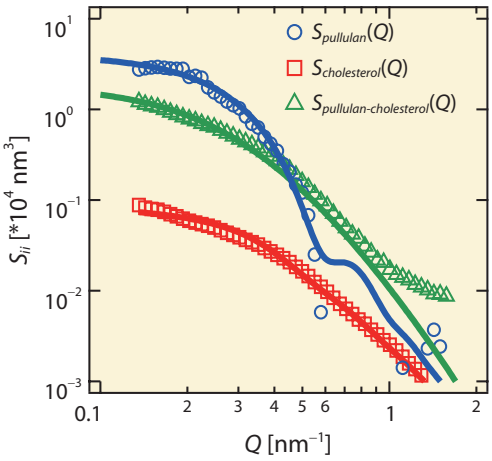

Figure 3. Partial scattering functions of pullulan, $S_{pp}(Q)$, cholesterol, $S_{cc}(Q)$, and pullulan-cholesterol cross-term, $S_{cp}(Q)$.

Fig. 3 shows the fitting result for $S_{cc}(Q)$. From the analysis, a mean radius of the cross-linkers, R_c and fractal dimension, d_f of the cholesterol molecules were obtained as R_c = 0.5 ± 0.1 nm and d_f = 2.6 ± 0.1 with ξ = 3.7 ± 0.1 nm. Because the volume of the single cross-linking point could also be evaluated by R_c, the aggregation number of cholesterol molecules in a cross-linking point was calculated to be 3.4. In conclusion, we found that the cross-linking points consisting of 3.4 cholesterol molecules dispersed inhomogeneously within the interior space of the nanogel, which may be represented by a mass fractal distribution with a dimension of 2.6. The unique internal space of the nanometer-scaled CHP nanogel may contribute to the specific functions of the nanogel, such as chaperone-like activity. The details are described in paper [1].

References

[1] Y. Sekine, et. al., J. Chem. Phys. B, 120, 11996-12002 (2016).
[2] T. Nishikawa, K. Akiyoshi, J. Sunamoto, J. Am. Chem. Soc., 118, 6110-6115 (1996).
[3] Y. Sasaki, K. Akiyoshi, Chem. Rec. 10. 366-376 (2010).
[4] H. Endo, Physica B, 385-386, 682-684 (2006).
[5] S. Takara, et. al., JPS Conf. Proc., 8. 036020 (2015).

Y. Sekine[1] and H. Endo[2]
[1]*Materials Sciences Research Center, JAEA;* [2]*Neutron Science Section, Materials and Life Science Division, J-PARC Center*

Neutron Brillouin Scattering of Liquid Methanol

1. Introduction

The structure and dynamics of liquids at molecular level reflect their macroscopic properties. In fact, some transport properties of liquids were calculated from time-space correlation functions by the mode coupling theory [1]. Molecular dynamics (MD) simulation is a common tool to explain the physicochemical properties of liquids at molecular level. However, the outcome of the simulation is very sensitive to the intermolecular potentials used in the simulations, and the potential parameters are somewhat ambiguous. Therefore, the experimental investigation of liquid's dynamics is highly needed to verify the potential parameters. Particularity, collective dynamics is important, since it contains structural information. Its comparison with the liquid's static structure would provide more detailed knowledge of the liquid.

We focus on the "fast sound" of liquids [2]. It has been found that the dispersion relation obtained through inelastic scattering experiments deviates positively from the line predicted by the adiabatic sound velocity. The fast sound for liquid water was found by MD, inelastic neutron (INS), and inelastic X-ray scattering (IXS) [2-4]. The velocity of the fast sound of liquid water is about twice higher than the adiabatic sound's velocity (positive dispersion ~100%) and similar to that of ice. On the other hand, those for noble gas and other molecular liquids, such as carbon tetrachloride, are much lower (~30%) than that for water. Although the origin of the high positive dispersion of water has been discussed ever since it was first discovered [2], its nature is still not clear.

Methanol has been used as an appropriate reference to water in discussing the liquid structure. A methanol molecule can be thought of as replacing one hydrogen-bonding site of water with a methyl group. Hence, methanol molecules possess a hydrogen-bonding chain-like structure, whereas water has a hydrogen-bonding three-dimensional network structure. A comparison of collective dynamics of methanol with that of water would clarify a relation between the static structure formed via hydrogen bonding interactions and the dynamics, which reflects these interactions.

So far, for collective dynamics measurements, IXS has an advantage over INS because of the availability of high-flux X-ray beams. However, a pulsed neutron source, such as J-PARC, is desirable to observe the dynamics because observations over a wide energy-momentum space are possible using a time-of-flight spectrometer. Moreover, high-flux neutron beams are now available there. We measured the collective dynamics of D_2O down to Q values of 0.2 $Å^{-1}$ at 300 K with the High-Resolution Chopper Spectrometer (HRC) at J-PARC MLF [5, 6]. Data with higher incident neutron energy, higher energy resolution, and lower momentum transfer are obtained, compared with those in Ref. [3].

In the present study [7], collective dynamics of liquid deuterated methanol at room temperature was measured with the HRC spectrometer at J-PARC/MLF. The dispersion relation of liquid methanol was compared with that obtained using the IXS result to investigate collective dynamics of liquid methanol in more detail.

2. Experimental

Deuterated methanol-d_4 (CD_3OD) was purchased from Sigma Aldrich and used without further purification. An aluminum flat container with inner dimensions of $40 \times 40 \times 10$ mm^3 was manufactured.

The sample container was installed into the vacuum chamber of the HRC spectrometer. Measurements were performed at room temperature. The energy of the incident neutron beam was $E_i = 102$ meV and the resolution was $\Delta E = 2.0$ meV. The proton beam power of the accelerator was 200 kW. The data were accumulated for 2 days.

3. Results

Figure 1 shows the scattering intensity of methanol at 298 K. The spectra showed shoulders due to symmetrical excitation peaks and a resolution-limited elastic peak. The excitation peaks were fitted with a damped harmonic oscillator scattering function convoluted with resolution width multiplied by a temperature factor (Bose-Einstein factor). The peak positions $E(Q)$ were determined as a function of Q. The present analysis is identical to that for D_2O measured at HRC previously [5].

Figure 2 shows that the Q dependence of the excited peak positions $E(Q)$ down to $Q = 0.7$ $Å^{-1}$ was well fitted to a straight line, equivalent to 1770 ± 30 m s^{-1}. The dispersion relation obtained from IXS is also depicted. This value is almost identical to that (1700 m s^{-1}) from IXS [8]. The adiabatic sound velocity of liquid methanol is 1094 m s^{-1} [9]. Hence, the positive dispersion is ~60%. It is an intermediate value between those

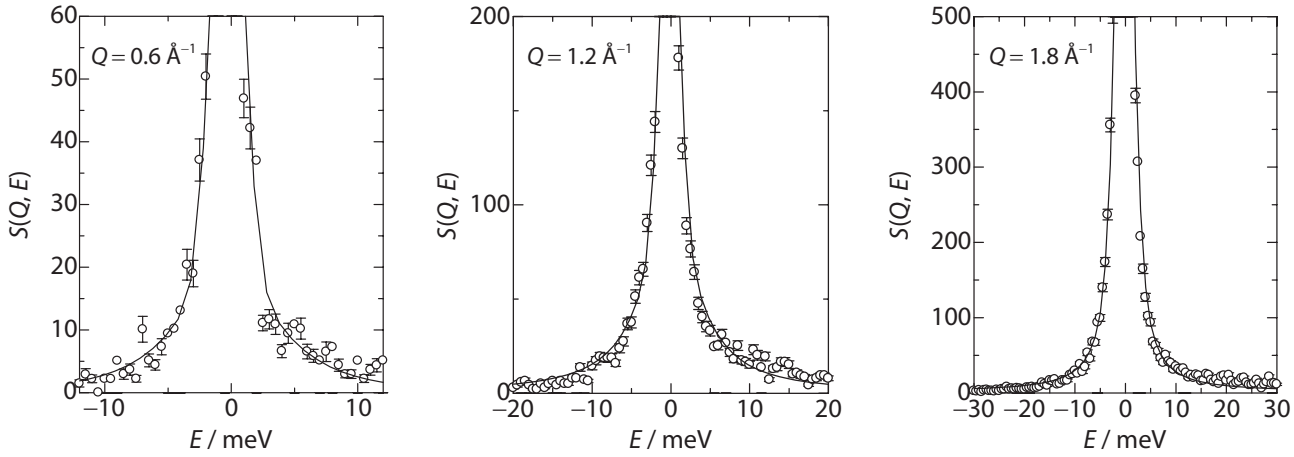

Figure 1. Dynamics structure factor of liquid methanol at room temperature. The solid lines indicate the fitting results by the DHO model [7].

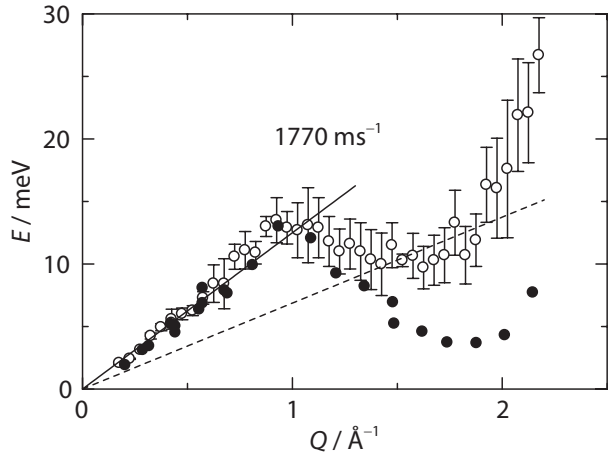

Figure 2. Dispersion relation of liquid deuterated methanol at room temperature. Open symbols are the results by INS and closed ones are those by IXS. The dashed line corresponds to the adiabatic sound velocity of liquid methanol [7].

of water and carbon tetrachloride [10]. It could be associated with the extent of hydrogen bonding. Moreover, in the Q range, above the first peak in $S(Q)$, at 1.7 Å^{-1}, the excitation energy of neutron increased more significantly than that of IXS. This was caused by another excitation in the collective dynamics. Although it is not yet to define the mode of the dynamics, it seems to be internal vibration involving the methyl groups of methanol. This is because the scattering factor of the deuterons is dominant in INS.

4. Future Plans

The present results indicate the importance of complementary use of X-ray scattering to investigate the collective dynamics of liquids. That collective dynamics could be measured through coherent scattering performed with high-flux neutron beams, which would provide more information about both the structure and the dynamics.

References

[1] T. Yamaguchi, et al., J. Chem. Phys. 2016, 144, 124514.
[2] A. Rahman, et al., Phys. Rev. A 1 (1974) 368.
[3] J. Teixeira, et al., Phys. Rev. Lett. 54 (1985) 2681.
[4] F. Sette, et al., Phys. Rev. Lett. 75 (1995) 850.
[5] S. Itoh, et al., J. Phys. Conf. Ser. 502 (2014) 012043.
[6] S. Itoh, et al., J. Phys. Soc. Jpn. 82 (2013) 043001.
[7] K. Yoshida, et al., J. Mol. Liquids 222 (2016) 395–397.
[8] K. Yoshida, et al., Chem. Phys. Lett. 440 (2006) 210.
[9] A. Kumar, Acoust. Lett. 20 (1997) 203–212.
[10] T. Kamiyama, et al., J. Phys. Soc. Jpn. 73 (2004) 1615–1618.

K. Yoshida[1], T. Yamaguchi[1], T. Yokoo[2,3], and S. Itoh[2,3]
[1]Facluty of Science, Fukuoka University; [2]Neutron Science Section, Materials and Life Science Division, J-PARC center; [3]Institute of Materials Structure Science, KEK

Dynamics Changes of Human Hemoglobin Detected by Quasielastic Neutron Scattering

1. Introduction

Hemoglobin (Hb) is a tetrameric hemoprotein that transports O_2 from lungs to tissues. Hb consists of two α and two β subunits, each containing one heme group to which O_2 can bind reversibly. Binding of an O_2 molecule to the heme of one subunit increases the O_2 affinity of other subunits and thereby that of the whole molecule. This cooperative behavior (allosteric regulation) makes efficient O_2 transport by Hb possible. Allosteric regulation is found in many proteins as a regulatory mechanism of their functions, and thus elucidation of the mechanism of allosteric regulation is important. Hb has long served as a prototypical system for the study of allosteric regulation, and its structures and function have been extensively studied. The standard description, based on the structures of the fully-unliganded tense (T) and fully-liganded relaxed (R) states, was that Hb switches between a low-affinity T conformation and a high-affinity R conformation upon ligand binding.

The recent identification of various intermediate structures [1] and the finding that Hb in solution is in a rapid equilibrium between the distinct structural states [2], however, cast doubts on this rather simple picture of allosteric regulation. Furthermore, as it is evident from the structure of Hb, in which the heme groups are buried deep inside the protein, conformational flexibility is required for the proper function of Hb. The information on the dynamics of Hb is thus important to elucidate the mechanism of allosteric regulation of Hb.

Compared to the wealth of structural data, much less is known about their dynamics. While proteins have a hierarchy of dynamics ranging from picosecond thermal fluctuations of atoms within a protein, through submillisecond diffusive motions of polypeptide chains and domains, to conformational changes that occur at millisecond or slower time scales [3], the dynamics at the picosecond time scale is known to work as a lubricant for the slower motions, without which the structural changes of the proteins do not occur [4]. Characterization of the dynamics at the picosecond time scale is thus important as an elementary process of the hierarchy of protein dynamics.

Quasielastic neutron scattering (QENS) provides a unique tool to measure directly the dynamics at the picosecond time scale of proteins. We thus carried out the QENS measurements on the T and R states of human hemoglobin to extract the dynamics changes upon ligation [5].

2. Materials and methods

The solution samples of human adult Hb were prepared in D_2O for the unliganded deoxy form (deoxyHb) and the fully CO-liganded form (COHb), which correspond to the T and R states respectively, at concentrations of 100 mg/ml. The QENS experiments were carried out using the near-backscattering spectrometer, BL02 (*DNA*), at MLF/J-PARC. The measurements were done at several temperatures between 280 K and 300 K, at energy resolution of 12 μeV.

3. Results

Figure 1 shows examples of the QENS spectra of deoxyHb and COHb. The spectra, $S(Q,\omega)$, can be fit with the equation,

$$S(Q,\omega) = \{A_0(Q)\delta(\omega) + (1 - A_0(Q))\, L_{local}(Q,\omega)\} \otimes L_{global}(Q,\omega) \otimes RF(Q) + BG. \quad (1)$$

Here, Q is the momentum transfer, $\hbar\omega$ is the energy transfer, $A_0(Q)$ is the elastic incoherent structure factor (EISF) that characterizes geometry of atomic motions, $L_{local}(Q,\omega)$ and $L_{global}(Q,\omega)$ are the Lorentzian functions that characterize the local motions within the protein and the global motions of the entire protein, respectively, and $\otimes$ denotes the convolution operation. By fitting the spectra with this phenomenological equation, the global and local motions can be separated.

The Q-dependence of the width of $L_{global}(Q,\omega)$ provides information on diffusive motions of the entire molecules. Figure 2 shows the apparent diffusion coefficients (D_{app}) of deoxyHB and COHb obtained from the analysis of these widths. Significant differences are observed between deoxyHb and COHb. To investigate the origin of these differences, D_{app} was simulated from the translational and rotational diffusion coefficients calculated from the crystal structures. As shown in Fig. 2, the simulated D_{app} values of deoxyHb agree with the experimental values, while those of COHb do not. This indicates that while deoxyHb behaves like a rigid body, COHb has additional internal motions. The test simulation of D_{app} based on the translational diffusion coefficient of the entire COHb and the rotational diffusion of the $\alpha\beta$ dimer in COHb shows agreement with the experimental values, suggesting that the additional motions are the rotation of the $\alpha\beta$ dimers within the protein.

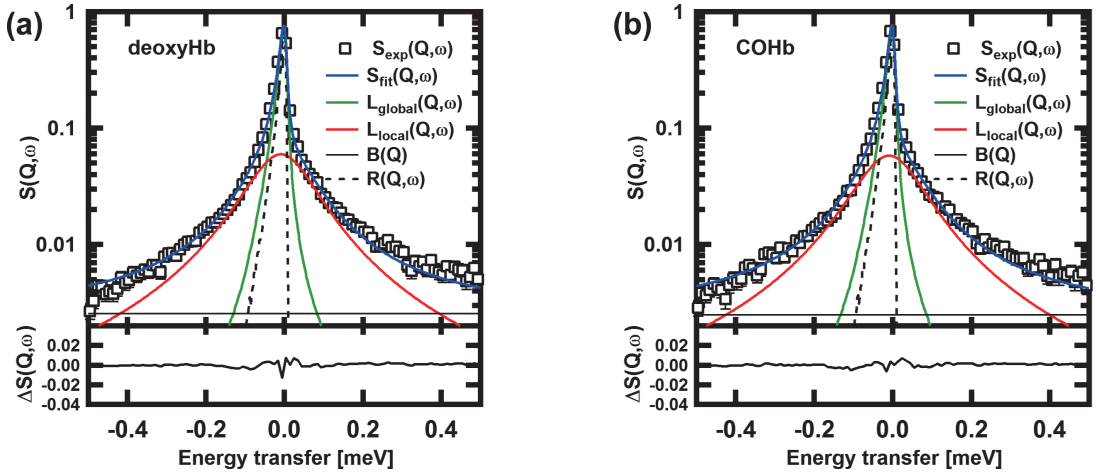

Figure 1. Examples of quasielastic neutron scattering spectra, S(Q,ω). The spectra of (a) deoxyHb and (b) COHb at Q = 1.05 Å^{-1} and at 280 K, are shown along with the results of the fits using Eq. 1. In the upper panels, open squares denote the data, thick solid lines in blue denote the total fits, solid lines in green and red denote $L_{global}(Q,\omega)$ and $L_{local}(Q,\omega)$, respectively, thin solid lines in blue show the background, and dashed lines in black show the resolution functions. The lower panels show the residuals of the fits.

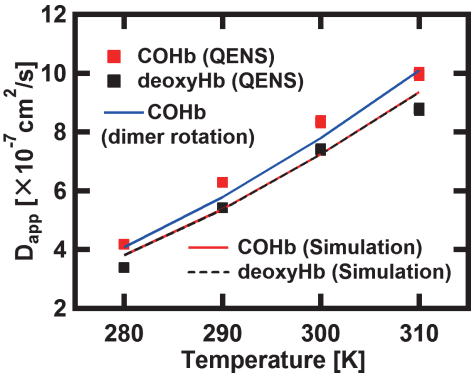

Figure 2. Summary of D_{app} of deoxyHb (■) and COHb (■) obtained from the QENS spectra and the simulated values of deoxyHb (dashed line) and COHb (solid line in red) based on the crystal structures. The simulated values for COHb assuming the dimer rotations are also shown (solid line in blue). Errors bars for the experimental data are within the symbols.

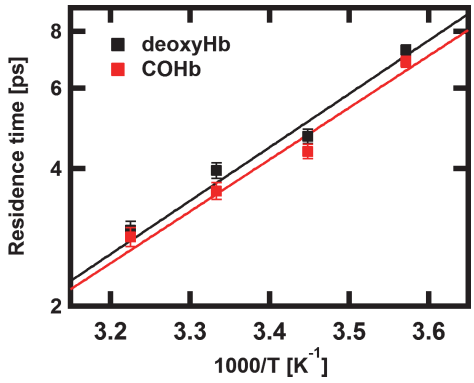

Figure 3. The Arrhenius plot of the residence times of deoxyHb (■) and COHb (■), estimated according to the jump diffusion model.

The Q-dependence of the width of $L_{local}(Q,\omega)$ provides information on the rates of the local atomic motions within the protein. Figure 3 shows the Arrhenius plot of the residence times of deoxyHb and COHb. Differences in the residence time suggest that the frequency of the local motions is a little lower in deoxyHb than in COHb. On the other hand, analysis of the EISF curves showed that the amplitudes of the local motions are similar between deoxyHB and COHb (data not shown).

The QENS measurements on deoxyHb and COHb thus show that the dynamics changes occur according to the changes in the ligation states. In particular, the significant motions at the quaternary structure level occur at the ligation, suggesting the important role of the dynamics in allosteric regulation of the function of Hb.

References

[1] N. Shibayama et al., J. Am. Chem. Soc. 136 (2014) 5097.
[2] J. A. Lukin et al., Proc. Natl. Acad. Sci. U. S .A. 100 (2003) 517.
[3] K. Henzler-Wildman and D. Kern, Nature 450 (2007) 964.
[4] G. Zaccai, Science 288 (2000) 1604.
[5] S. Fujiwara et. al., J. Phys. Chem. B 121 (2017) 8069.

S. Fujiwara[1], T. Chatake[2], T. Matsuo[1], F. Kono[1], T. Tominaga[3], K. Shibata[4], A. Sato-Tomita[5], and N. Shibayama[5]
[1]Quantum Beam Science Research Directorate, QST; [2]RRI, Kyoto Univ.; [3]Neutron Science and Technology Center, CROSS; [4]Neutron Science Section, Materials and Life Science Division, J-PARC Center; [5]Div. Biophysics., Dept. Physiology, Jichi Medical Univ.

Magnetic Structure and Excitations in $La_5Mo_4O_{16}$

1. Introduction

Magnetic insulators with 4*d* electrons have attracted research interest in condensed matter physics, since they exhibit various magnetic phenomenaocaused by the intermediate scale of the spin-orbit interaction (SOI). $La_5Mo_4O_{16}$ is a layered perovskite compound with localized 4*d* electrons, which shows fascinating bulk magnetic properties, as described below.

$La_5Mo_4O_{16}$ consists of corner-sharing $Mo(1)O_6$ and $Mo(2)O_6$ octahedra forming a quasi-square checkerboard lattice. Mo(1) and Mo(2) sites have spins $S = 1/2$ ($4d^1$) and $S = 1$ ($4d^2$). $Mo(2)O_6$ is connected by nonmagnetic $Mo_2(3)O_{10}$ pillar, whichocreates a very weak interlayer exchange coupling. $La_5Mo_4O_{16}$ undergoes antifferomagnetic phase below $T_N = 190$ K. Recently, $La_5Mo_4O_{16}$ shows intriguing magnetic phenomena: high-temperature magnetoresistance [1] and long-time magnetization decay [2]. To uncover their microscopic origin and the effect of the spin-orbit coupling in $La_5Mo_4O_{16}$, we performed time-of-flight (TOF) elastic and inelastic neutron scattering measurements using iMATERIA, HRC, and 4SEASONS [3].

2. Experimental

Neutron powder diffraction (NPD) was performed at $T = 4$, 40, and 220 K using iMATERIA. Inelastic neutron scattering (INS) measurements at HRC were performed using $E_i = 102.4$ meV with a Fermi chopper rotating at a frequency of 400 Hz. INS measurements were also performed using $E_i = 15.3$ meV with 250 Hz at 4SEASONS. Both INS experiments were conducted at 4 and 224 K.

3. Results and discussion

Figure 1(a) shows a NPD pattern at $T = 4$ K ($< T_N$). Below T_N, magnetic Bragg peaks evolve at momentum transfers (*Q*s) of 1.138(2), 1.174(2), 1.400(6), and 1.486(8) Å^{-1}. The peak positions correspond to (–1, 1, 1/2), (1, 1, 1/2), (–1, 1, 3/2), and (1, 1, 3/2) in *C*2/*m* notation, and the magnetic propagation vector can be indexed by **k** = (0, 0, 1/2). The magnetic structure, where Mo(1) and Mo(2) show collinear antiferromagnetic coupling within the layers, the latter being also antifferomagnetically coupled along the *c* axis, as described in Fig. 1(b), was indicated by the magnetic propagation vector and single-crystal bulk measurements. As shown in Fig. 1(a), the observed NPD pattern was well fitted by the magnetic structure with magnetic moments of μ_1 = 0.54(2)μ_B and μ_2 = 1.07(3)μ_B where μ_1 and μ_2 were the magnetic moments of Mo(1) and Mo(2) sites. The ordered magnetic moments were about half of the spin-only values.

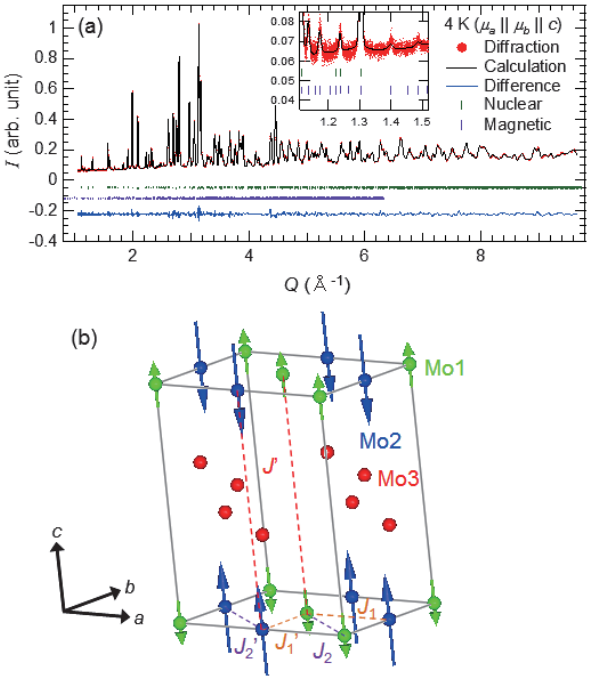

Figure 1. (a) NPD pattern in $La_5Mo_4O_{16}$ at $T = 4$ K measured by iMATERIA and the Rietveld refinement result [3]. The inset shows a magnified view. (b) Magnetic structure of $La_5Mo_4O_{16}$ with the magnetic propagation vector **k** = (0, 0, 1/2) [3]. Dashed lines represent exchange interactions.

The INS intensity (*I*) map in $La_5Mo_4O_{16}$ at $T = 4$ K as a function of *Q* and energy transfer ($\hbar\omega$) is shown in Fig. 2(a). Broad-energy bands were observed around $\hbar\omega$ = 10 and 20 meV. The *Q* and *T* dependences of both excitations revealed that the excitations originate in spin wave excitations. To quantitatively understand the spin wave excitations, we calculated the linear spin wave excitation assuming the magnetic structure shown in Fig. 1(b) and found out that the spin Hamiltonian consisted of in-plane anisotropic exchange interactions, interlayer exchange interaction, and easy-axis single-ion anisotropy. The calculated LSW intensity was fitted to the experimental spin wave excitations, and the spin Hamiltonian was determined. The calculated LSW intensity, using the optimum parameters, is shown in Fig. 2(b), which can explain the experiment well. The estimated interlayer exchange interaction (*J*′) was very weak compared to the nearest-neighbor exchange interaction ($J'/J_1 < 0.01$).

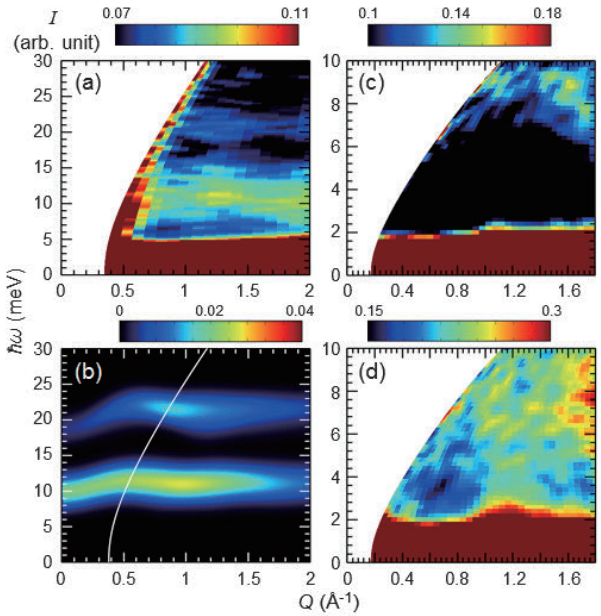

Figure 2. (a) $I(Q, \hbar\omega)$ map in $La_5Mo_4O_{16}$ at T = 4 K measured by HRC with E_i = 102.4 meV [3]. (b) $I(Q, \hbar\omega)$ map at 4 K calculated by LSW theory [3]. (c) and (d) $I(Q, \hbar\omega)$ maps measured by 4SEASONS with E_i = 15.3 meV at 4 and 224 K [3].

To gain insight on the spin-orbit coupling in $La_5Mo_4O_{16}$, the INS maps using lower E_i (15.3 meV) are shown in Figs. 2(c) and 2(d) (below and above T_N). Above T_N, a gapless quasielastic excitation centered around the magnetic zone centers ($Q \sim 1.2$ Å^{-1}) was observed [Fig. 2(d)]. On the other hand, although Goldstome modes of the spin wave excitations are expected to evolve in the vicinity of the magnetic zone centers below T_N, the $I(Q, \hbar\omega)$ map with better energy resolution clearly shows the absence of the Goldstone mode [Fig. 2(c)]. The observed spin gap at the magnetic zone center is direct evidence of the strong magnetic anisotropy due to the strong SOI in $La_5Mo_4O_{16}$.

As reported above, the ordered magnetic moments at Mo(1) and Mo(2) are reduced to about half of the spin-only values. Since the valences of the Mo(1) and Mo(2) sites are about +5 and +4, respectively, at all temperatures measured by our bond valence sum method, anomalous charge disproportionation of the Mo 4*d* electrons between Mo(1) and Mo(2) sites in the long-range magnetic ordered state is ruled out. Instead, our INS study suggests that fluctuations induced by low dimensionality and J_2 bond frustration [$J'/J_1 << 1$ and $J_2 > 0$ in Fig. 1(b)] are the origin of the reduced magnetic moments. The quantum fluctuation effect due to the spin S = 1/2 (and 1) may alsoecause reduced moments. The small magnetic moments at Mo(1) and Mo(2) and the large spin gap suggest that the SOI in $La_5Mo_4O_{16}$ induces a strong easy-axis magnetic anisotropy instead of the total momentum number **J** (= **S** + **L**). Therefore, our results indicate that the SOI in $La_5Mo_4O_{16}$ is similar to that in 3*d* electron systems, rather than that in 5*d* and 4*f* electron systems.

4. Summary

The magnetic structure and spin dynamics in the localized 4*d* electron layered perovskite antiferromagnet $La_5Mo_4O_{16}$ have been studied by TOF powder neutron measurements [3]. Our NPD refinement revealed a magnetic structure, where Mo(1) and Mo(2) are coupled antiferromagnetically within the layers and the layers are also coupled antiferromagnetically along the *c* axis with reduced magnetic moments. The INS results were analyzed using a model Hamiltonian, including the easy-axis anisotropy and weak interlayer exchange interaction using the semiclassical LSW theory. The spin gap at the magnetic zone center was explained by Ising anisotropy due to the intermediate scale of the SOI. The microscopic spin structure, strong easy-axis anisotropy, and very weak interlayer exchange interaction, compared with the intralayer exchange interactions determined by our TOF elastic and inelastic neutron scattering measurements, support the microscopic models proposed for the high-temperature magnetoresistance and long-time magnetization decay in $La_5Mo_4O_{16}$.

References

[1] K. Kobayashi and T. Katsufuji, Phys. Rev. B **83**, 100411(R) (2011).

[2] T. Konishi, K. Kobayashi, and T. Katsufuji, Phys. Rev. B **92**, 020419(R) (2015).

[3] K. Iida, R. Kajimoto, Y. Mizuno, K. Kamazawa, Y. Inamura, A. Hoshikawa, Y. Yoshida, T. Matsukawa, T. Ishigaki, Y. Kawamura, S. Ibuka, T. Yokoo, S. Itoh, and T. Katsufuji, J. Phys. Soc. Jpn. **86**, 064803 (2017).

K. Iida[1], R. Kajimoto[2], S. Itoh[2,3], and T. Ishigaki[4]

[1]Neutron Science and Technology Center, Comprehensive Research Organization for Science and Society (CROSS); [2]Neutron Science Section, Materials and Life Science Division, J-PARC center; [3]Institute of Materials Structure Science, KEK; [4]Frontier Research Center for Applied Atomic Sciences, Ibaraki University

Structure of the Magnetic Excitations in the Spin-1/2 Triangular-Lattice Heisenberg Antiferromagnet $Ba_3CoSb_2O_9$

1. Introduction

A spin-1/2 triangular-lattice Heisenberg antiferromagnet (TLHAF) with a spatially isotropic lattice is a prototypical frustrated quantum magnet, which exhibits remarkable quantum effects that arise from the synergy between spin frustration and quantum fluctuation. In 1973, Anderson proposed a resonating-valence-bond (RVB) state without a long-range magnetic ordering as the ground state of the spin-1/2 TLHAFs [1]. A prolonged theoretical debate, which started from the RVB theory, reached a consensus that the ground state is an ordered state of the 120° spin structure with an extremely small sublattice magnetization [2]. Nevertheless, a remarkable quantum effect emerges in magnetic fields. An up-up-down spin state is stabilized in a finite magnetic field range by the quantum fluctuation, which gives the magnetization curve a plateau at one-third of the saturation magnetization [3]. The 1/3-magnetization-plateau was quantitatively verified by high-field magnetization measurements on $Ba_3CoSb_2O_9$ [4], which demonstrates that this compound closely approximates the spin-1/2 TLHAF.

Although the ground state properties of a spin-1/2 TLHAF with a uniform triangular lattice are well understood both theoretically and experimentally, the magnetic excitations are less well understood. The theoretical consensus is limited only to single-magnon excitations [5, 6]. There is no theoretical consensus for the excitation continuum. According to the theory, the dispersion relation of low-energy excitations near the K point is described by linear spin wave theory (LSWT). However, in a large area of the Brillouin zone, the excitation energy is substantially renormalized downward, which leads to the flat dispersion curve. Recently, the magnetic excitations in $Ba_3CoSb_2O_9$ were investigated by inelastic neutron scattering [7]. However, the energy range was limited below 3 meV and the excitation spectrum appeared to be indistinct, although flat dispersion was observed.

In this study [8], we investigated magnetic excitations of $Ba_3CoSb_2O_9$ by inelastic neutron scattering. We observed well-defined excitation spectra, which provide the whole picture of magnetic excitations in a spin-1/2 TLHAF. From the previous high-field magnetization and ESR measurements on $Ba_3CoSb_2O_9$, the predominant intralayer exchange interaction and its anisotropy were obtained as $J = 1.67$ meV and $\Delta J/J = 0.046$ [4].

2. Experiment

$Ba_3CoSb_2O_9$ single crystal of $10 \times 8 \times 4$ mm^3 size was grown from the melt, using a Pt crucible. The mosaicity of the crystal was found to be 0.5°. The magnetic excitations in a wide momentum-energy range were measured using the cold-neutron disk chopper spectrometer AMATERAS [9] installed in the MLF at J-PARC. The sample was mounted in a cryostat with its (1,1,0) and (0,0,1) directions in the horizontal plane. The sample was cooled to 1.0 K using a ^{3}He refrigerator. Scattering data were collected by rotating the sample around the (-1,1,0) direction. All the data were analyzed using the software suite Utsusemi [10].

3. Results and discussion

Figures 1(a)-(d) show energy-momentum maps of the scattering intensity along two high-symmetry directions parallel to $\boldsymbol{Q} = (H, H)$ and $(-K, K)$ measured at 1.0 K ($< T_N = 3.8$ K) with incident neutron energies of $E_i = 3.14$ and 7.74 meV. At 10 K, excitation spectra shown in Fig. 1 are considerably smeared and the intensities decrease. This result verified their magnetic origin. The scattering intensities in Fig. 1 were integrated over L to obtain the statistics, assuming good two-dimensionality (2D), which was confirmed from the dispersion relation along the c^* direction. The low-energy excitations for $\boldsymbol{Q} = (1/3, 1/3, L)$ are dispersive, while those for $\boldsymbol{Q} = (1/2, 1/2, L)$ are almost dispersionless. This indicates that the interlayer exchange interaction is small and does not affect the excitations above 1 meV. The low-energy excitations near the K point can be described by LSWT, as shown in Fig. 1a. Thus, by applying LSWT to the dispersion curves of the single-magnon excitations for $\boldsymbol{Q} = (1/3, 1/3, L)$, we evaluated the interlayer exchange interaction as $J' = 0.080$ meV, which is less than 5% of J. Thus, we can deduce that all the excitations, except the low-energy excitations near the K point, can be attributed to the 2D spin-1/2 TLHAF.

The most noteworthy feature of the excitation spectrum is its three-stage energy structure. The lowest

stage is composed of two distinct branches of single-magnon excitations, which rise from the K point. The middle and highest stages are dispersive continua. This structure of magnetic excitations is significantly different from the theoretical results. The solid lines in Figs. 1(a) and (c) are dispersion curves calculated by LSWT with $J = 1.67$ meV and $\Delta J/J = 0.046$ based on the 2D model. Near the K point, the lower bound of the spectrum, which closely approximates the spectrum at the 2D limit, coincides with the LSWT result. However, the further the wave vector moves away from the K point, the more rapidly the excitation energy deviates downwards from the LSWT dispersion. This result is qualitatively consistent with the theory [5, 6]. Both single-magnon branches show distinct rotonlike minima at the M point, although the theory predicts that only the lowest branch shows a minimum [6]. The rotonlike minimum is interpreted in terms of pairs of spin-1/2 fractionalized excitations, spinons, characteristic of the RVB state [6].

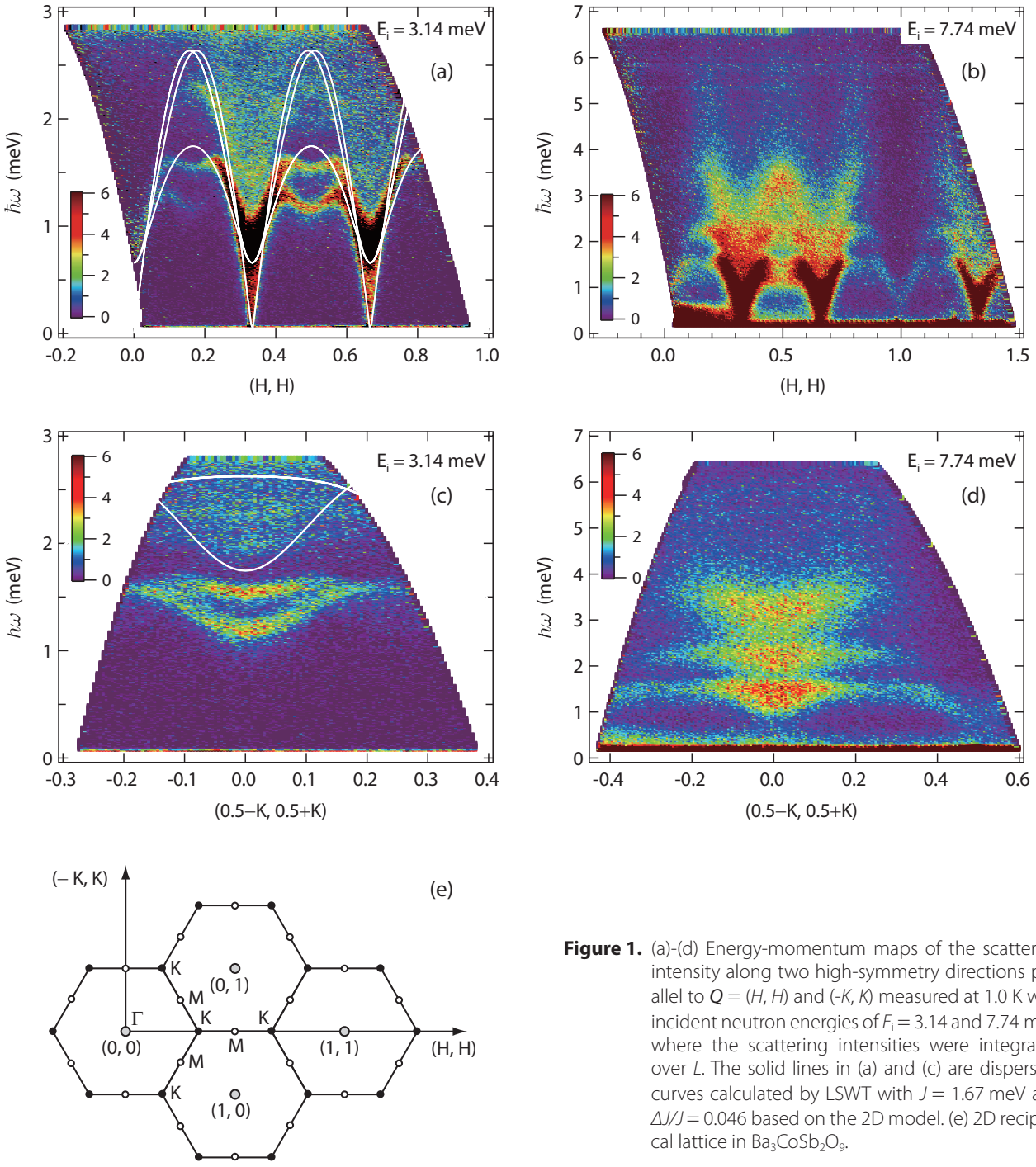

Figure 1. (a)-(d) Energy-momentum maps of the scattering intensity along two high-symmetry directions parallel to $\boldsymbol{Q} = (H, H)$ and $(-K, K)$ measured at 1.0 K with incident neutron energies of $E_i = 3.14$ and 7.74 meV, where the scattering intensities were integrated over L. The solid lines in (a) and (c) are dispersion curves calculated by LSWT with $J = 1.67$ meV and $\Delta J/J = 0.046$ based on the 2D model. (e) 2D reciprocal lattice in $Ba_3CoSb_2O_9$.

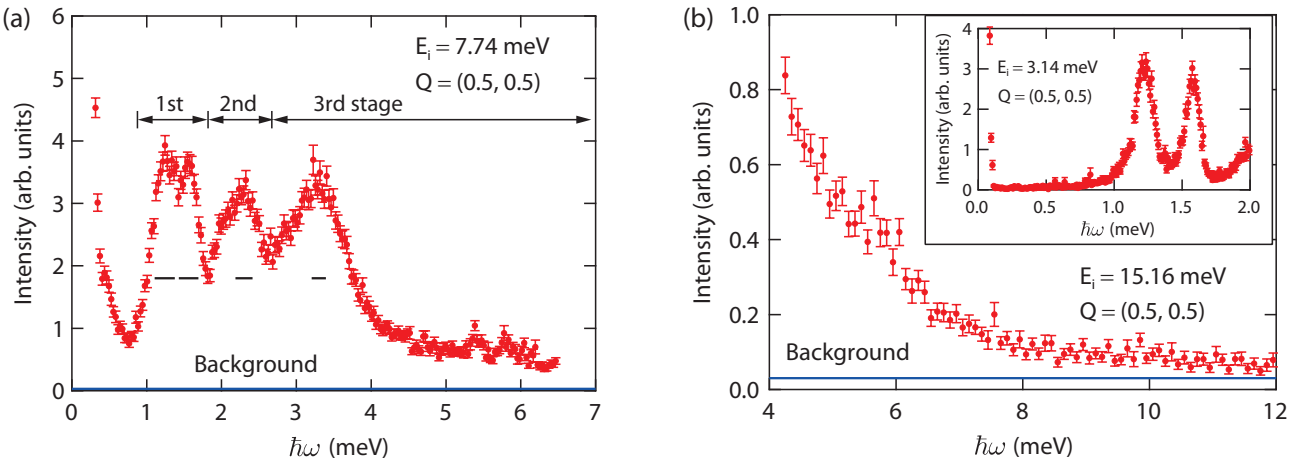

Figure 2. Scattering intensity at M point for Q = (1/2, 1/2) as a function of energy measured at 1.0 K (a) with E_i = 7.74 and (b) 15.16 meV. The horizontal blue lines in (a) and (b) are background level, which was estimated from the scattering intensity between 0.12 and 0.5 meV measured with E_i = 3.14 meV as shown in the inset of (b).

A significant feature of the magnetic excitations is the two strong dispersive continua that form the middle and third stages of the excitation spectrum. The highest third stage is accompanied by a columnar continuum extending to at least 6 meV. Figures 2(a) and (b) show the energy dependence of the excitation spectrum at the M point for $\boldsymbol{Q}$ = (1/2, 1/2) measured with E_i = 7.74 and 15.16 meV, respectively, where the scattering intensity was integrated over L. The horizontal bars in Fig. 2(a) are the energy resolution. The inset of Fig. 2(b) shows the energy dependence of the excitation spectrum for $\boldsymbol{Q}$ = (1/2, 1/2) measured with E_i = 3.14 meV. The horizontal blue lines in Figs. 2(a) and (b) are background level, which was estimated from the scattering intensity between 0.12 and 0.5 meV measured with E_i = 3.14 meV. A three-stage energy structure composed of two single-magnon excitations and two excitation continua is clearly observed. The third stage has a long energy tail of excitation continuum. The energy tail continues to over 10 meV, which is six times larger than the exchange interaction J. Because the highest energy of single-magnon excitation is approximately equal to J =1.67 meV, as shown in Figs. 1(a) and (c), the observed excitation continuum cannot be explained in terms of conventional two-magnon excitations [5]. Recently, magnetic excitations in a spin-1/2 TLHAF were discussed from the standpoint of spinon, using mean field Schwinger boson approach [6]. However, it is difficult to describe the observed high-energy excitation continuum in terms of a two-spinon continuum, because the highest upper bound of the continuum is approximately 2J at most. At present, no theory describes the structure of the excitation continua observed in this experiment, and thus, a new theoretical framework is required.

References

[1] P. W. Anderson, Mater. Res. Bull. **8,** 153 (1973).
[2] B. Bernu et al., Phys. Rev. B **50,** 10048 (1994), S. R. White and A. L. Chernyshev, Phys. Rev. Lett. **99,** 127004 (2007), and references therein.
[3] D. J. J. Farnell et al., J. Phys.: Condens. Matter **21,** 406002 (2009), T. Sakai and H. Nakano, Phys. Rev. B **83,** 100405 (2011), and references therein.
[4] Y. Shirata et al., Phys. Rev. Lett. **108,** 057205 (2012), T. Susuki et al., Phys. Rev. Lett. **110,** 267201 (2013).
[5] M. Mourigal et al., Phys. Rev. B **88,** 094407 (2013), and references therein.
[6] E. A. Ghioldi et al., Phys. Rev. B **91,** 134423 (2015), and references therein.
[7] H. D. Zhou et al., Phys. Rev. Lett. **109,** 267206 (2012), J. Ma et al., Phys. Rev. Lett. **116,** 087201 (2016).
[8] S. Ito et al., Nat. Commun. **8**, 235 (2017).
[9] K. Nakajima et al., J. Phys. Soc. Jpn. **80,** SB028 (2013).
[10] Y. Inamura et al., J. Phys. Soc. Jpn. **82,** SA031 (2013).

S. Ito[1], N. Kurita[1], H. Tanaka[1], S. Ohira-Kawamura[2], K. Nakajima[2], S. Itoh[3], K. Kuwahara[4], and K. Kakurai[5]
[1]Department of Physics, Tokyo Institute of Technology; [2]Materials and Life Science division, J-PARC Center; [3]Neutron Science Division, Institute of Materials Structure Science, KEK; [4]Institute of Quantum Beam Science, Ibaragi University; [5]Science Coordination Section, CROSS-Tokai

Rotational Modes and Phonons of $CH_3NH_3PbI_3$

1. Introduction

Over the last few years, the inorganic-organic hybrid perovskite solar cells have taken the worldwide research community by storm [1]. These hybrid compounds exhibit physical properties distinct from those in conventional semiconductors. Their hot-phonon bottleneck effect of energetic carriers is obviously stronger than that of GaAs and other inorganic perovskites, which has been attributed to the acoustic-optical phonon up-conversion [2, 3]. The mobility of charge carriers is relatively smaller compared with classical semiconductors and the scattering mechanism is still under debate [4, 5]. Resembling the charge transport, the thermal transport is unusual as well. The thermal conductivity is surprisingly low, about 0.5 $Wm^{-1}K^{-1}$ for single crystals at room temperature [6], which is tenfold lower than that of GaAs [7]. It is evident that atomic dynamics underlies these peculiarities. However, the atomic-level description of $CH_3NH_3PbI_3$ is complicated by its hybrid nature, where both molecular jumping rotations and phonon excitations have to be taken into account. Moreover, these two components also interact via hydrogen bonds between H and I [8]. Here, we present the complete atomic pictures established using the high-resolution quasi-elastic neutron scattering (QENS) and inelastic neutron scattering (INS) on a large single crystal [9].

2. Experiments

The high-resolution QENS and INS measurements were performed at the inverse-geometry time-of-flight chopper spectrometer BL02 DNA with E_i = 2.084 meV and at the direct-geometry time-of-flight chopper spectrometer BL14 AMATERAS with E_i of 54, 16, 7 and 4 meV of J-PARC in Japan. The crystal was aligned at room temperature at DNA. It took 12 hours to cool down to 140 K from room temperature at which it crystallizes in the tetragonal structure. The four-dimension $S(\mathbf{q},E)$ data were reduced and visualized by using Utsusemi suite, along [hh0], [00l] and [$k\bar{k}$0] based on a tetragonal unit cell (a = 8.80625 Å, c = 12.712 Å).

3. Results and discussion

- **Jumping rotational modes of $[CH_3NH_3]^+$**

$CH_3NH_3PbI_3$ crystallizes in the common perovskite structure, where the organic cation $[CH_3NH_3]^+$ occupies the center of the PbI_6 octahedral cage, as shown in Fig. 1a. It undergoes successive phase transitions, from cubic ($Pm\bar{3}m$) to tetragonal ($I4/mcm$) at 330 K, and then to orthorhombic ($Pnma$) at 165 K. While it is believed that this transition is coupled with the orientation of $[CH_3NH_3]^+$, the current reports on rotational dynamics are contradictory [10, 11], probably owing to the lack of results on single crystals. Here, the accurate jumping rotational dynamics of molecules is obtained by performing ultrahigh energy resolution QENS measurements on the large single crystal at the backscattering neutron spectrometer, DNA, as summarized in Fig. 1b. At about 80 K, the C_3 rotational mode is activated, where the protons of CH_3 and NH_3 groups are subjected to a 120° jumping rotation with respect to the C-N axis. As temperature increases up to about 165 K, the whole molecule undergoes a C_4 rotation with respect to the fourfold axis of the tetragonal unit cell. At 180 K, their relaxation times are 0.71(3) and 64(2) ps, respectively.

- **Optical phonons**

The longitudinal optical phonons are shown in the dynamic structure factor $S(\mathbf{q},E)$ at 5 K in the direction of [00l] (Fig. 2a-c). With E_i of 54 meV, the full view of $S(\mathbf{q},E)$ is provided, indicating six prominent modes located at

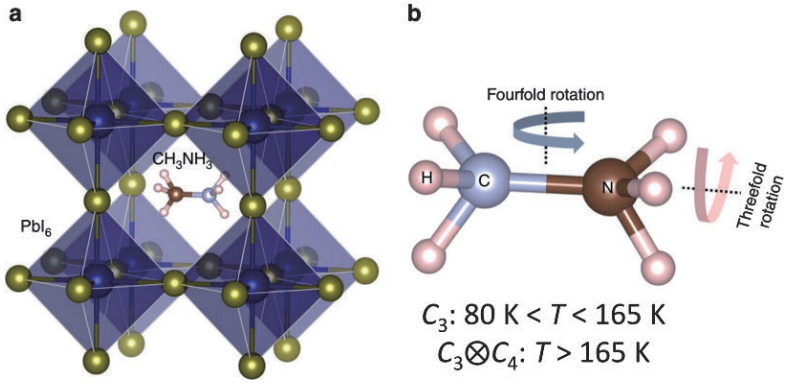

Figure 1. a. Crystal structure of $CH_3NH_3PbI_3$. **b.** The molecular rotational modes (taken from Ref [9]).

11.3, 15.3, 18.3, 22.6, 26.0, and 37.6 meV, respectively. With smaller E_i, more details are revealed. We found the peak at 11.3 meV to be actually a superposition of three peaks at 10.6, 11.5, and 12.6 meV (Figs. 2b). It seems that a gap appears between 6 and 10 meV, but several weaker modes can be roughly identified. The data with E_i of 7 meV (Figs. 2c) suggest four low-energy modes at 2.28, 3.11, 3.79 and 4.35 meV. Thanks to the high-resolution, we were able to identify several modes that were overlooked in the previous Raman scattering [12] and INS measurements [13].

- **Acoustic phonons**

The detailed acoustic phonons of the Brillouin zone (220) were examined with E_i of 4 meV. Shown in Fig. 3a-d are the longitudinal and transverse phonons at 5 and 180 K, respectively. Even though the background level is high, the dispersions can be seen in both directions. At 5 K, the dispersion curve of longitudinal acoustic (LA) phonon emanates from zone center of (220), undergoes a steep increase and finally approaches the top in the middle of zone centers and zone boundary (h ~ 0.2), where it overlaps with longitudinal optical (LO) phonons. The dispersion of transverse acoustic (TA) phonon exhibits a moderate slope. Intense transverse optical (TO) phonons are also present. At 180 K, the intensity of phonons is fairly enhanced, and we determined the accurate dispersions of LA and TA phonons by fitting the momentum-transfer (filled circle) or energy-transfer (filled square) averaged spectra. The solid lines represent the slopes of dispersion curves near the zone centers, which determine the group velocities: v_{LA} = 2841 m s^{-1} and v_{TA} = 1155 m s^{-1}.

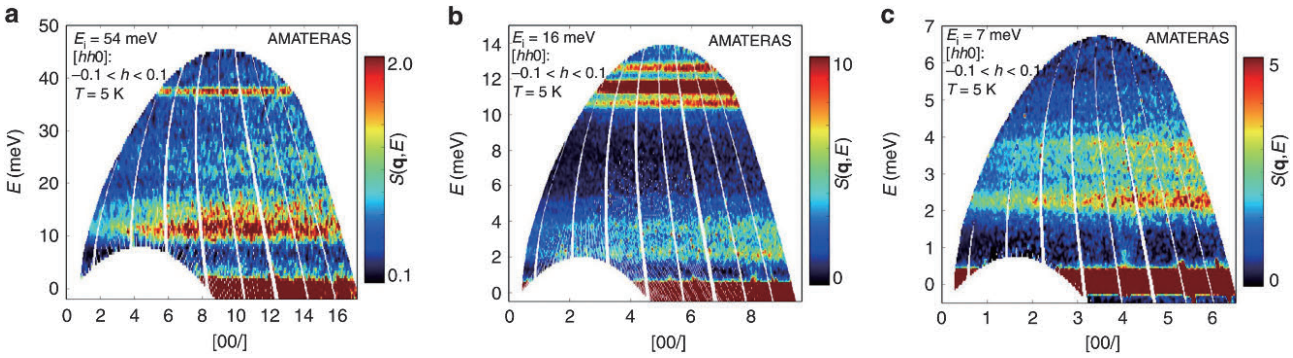

Figure 2. Longitudinal optical phonons at 5 K measured with different E_i, 54 meV (**a**), 16 meV (**b**) and 7 meV (**c**) (taken from Ref [9]).

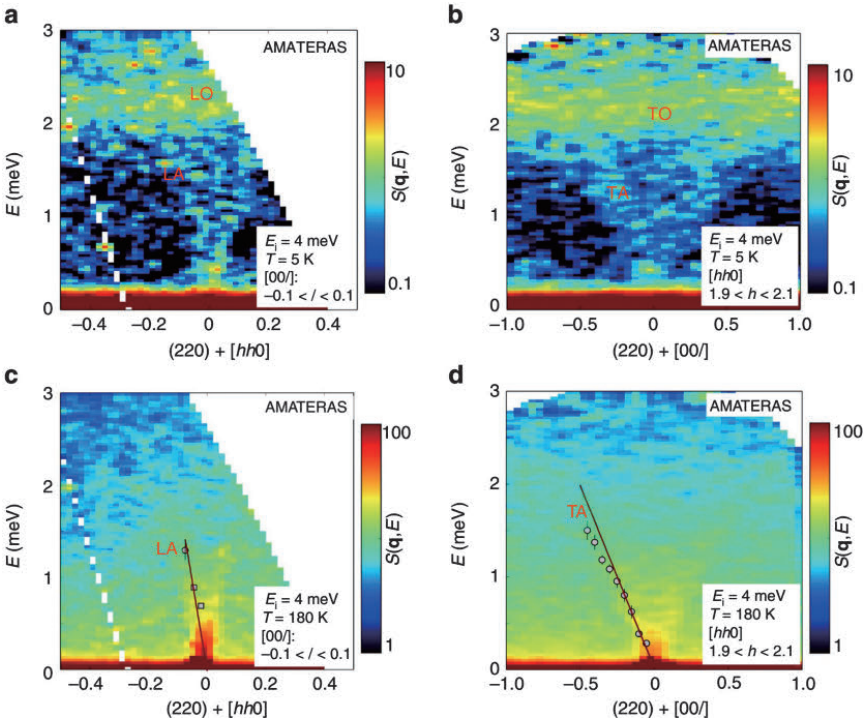

Figure 3. Phonon broadening at the orthorhombic-to-tetragonal phase transition (taken from Ref [9]).

- **Polar rotor scattering**

The most striking features of the temperature dependence of the atomic dynamics is that the LO and TO phonons completely *vanish,* whereas the acoustic phonons are robust, as the orthorhombic-tetragonal phase transition takes place. At 150 K, the lifetimes of TO phonons at 10.7 and 12.6 meV are 0.91(15) and 0.62(7) ps while those of LO phonons are 0.82(5) and 0.57(2) ps, respectively. At 180 K, just above the phase transition, both TO and LO phonons are too broadened to be distinguished. This means the actual lifetimes at 180 K are much shorter than those at 150 K. Such an intriguing behavior might originate from the selective scattering of the polar rotor $[CH_3NH_3]^+$ activated in the tetragonal phase. Just for this reason, the thermal transport is dominated by acoustic phonons rather than optical phonons due to their extremely short lifetimes. Similarly, the polar rotor scattering also plays an important role in the charge transport.

4. Conclusion and perspective

We determined precisely the jumping rotational dynamics of molecules and phonons in hybrid perovskite $CH_3NH_3PbI_3$ by conducting high-resolution QENS and INS measurements. The characteristic timescales of various dynamics were completely revealed. The dipole order of organic cations plays a decisive role in determining the physical properties, such as carrier mobility and thermal conduction, distinguishing it from the inorganic perovskites. Such observations could probably apply generally to all hybrid compounds with polar molecules. These fundamental insights are beneficial for the further study of the perovskite solar cells. Especially, the short-lived optical phonons may be important for the large polaron formation in this system.

References

[1] T. M. Brenner et al., *Nat. Rev. Mater.* **1**, 15007 (2016).
[2] M. Price et al., *Nat. Commun.* **6**, 8420 (2015).
[3] Y. Yang et al., *Nat. Photon.* **10**, 53 (2016).
[4] A. D. Wright et al., *Nat. Commun.* **7**, 11755 (2016).
[5] A. Filippetti et al., *Phys. Chem. Chem. Phys.* **18**, 15352 (2016).
[6] A. Pisoni et al., *J. Phys. Chem. Lett.* **5**, 248 (2014).
[7] J. Blakemore, *J. Appl. Phys.* **53**, R123 (1982).
[8] Y. Ren et al., *Cryst. Growth Des.* **16**, 2945 (2016).
[9] B. Li et al., *Nat. Commun.* **8**, 16086 (2017).
[10] A. M. A. Leguy et al., *Nat. Commun.* **6**, 7124 (2015).
[11] T. Chen et al., *Phys. Chem. Chem. Phys.* **17**, 31278 (2015).
[12] A. M. A. Leguy et al., *Phys. Chem. Chem. Phys.* **18**, 27051 (2016).
[13] K. Drużbicki et al., *J. Phys. Chem. Lett.* **7**, 4701 (2016).

Bing Li[1], Yukinobu Kawakita[1], Yucheng Liu[2], Masato Matsuura[3], Kaoru Shibata[1], Seiko Ohira-Kawamura[1], Takeshi Yamada[3], Kenji Nakajima[1], and Shengzhong (Frank) Liu[2,4]

[1]Neutron Science Section, Materials and Life Science Division, J-PARC Center; [2]School of Materials Science and Engineering, Shaanxi Normal University, China; [3]Neutron R&D Division CROSS-Tokai; [4]Dalian Institute of Chemical Physics, Chinese Academy of Sciences, China

Development of the Spin-Wave-Like Dispersive Excitations below the Pseudogap Temperature in the High-Temperature Superconductor $La_{2-x}Sr_xCuO_4$

1. Introduction

The origin of the pseudogap, a partial gap opening in the spin or charge channel, has been the focus of debate in the recent study of high-T_c superconducting cuprates [1]. Although inelastic neutron scattering (INS) studies have clarified the intimate correlations between the pseudogap and low-energy spin fluctuations, the nature of the magnetic spectrum in the pseudogap state remains to be understood, which requires the measurement of magnetic excitations in a wide energy range. For the magnetic excitations at base temperature (~5 K), systematic INS studies have clarified that carrier doping changes spin-wave excitations into the well-known hourglass-shaped dispersion in the superconducting state [2]. On the other hand, there has been no INS report using Fermi-chopper type spectrometer at high temperatures above room temperature for high-T_c cuprates. In order to elucidate the effect of the pseudogap on magnetic excitations, we performed systematic high-energy inelastic neutron scattering measurements using the chopper spectrometer 4SEASONS from the superconducting state (T = 5 K) to high temperatures (T = 500 K) well above the pseudogap temperature (~360 K) on underdoped high-T_c cuprate $La_{2-x}Sr_xCuO_4$ (LSCO) with x = 0.075 (T_c = 24 K) [3]. In addition, we measured the magnetic excitations in the parent compound La_2CuO_4 in the similar temperature range as a reference to understand the thermal effects on magnetic excitations at such high temperatures.

2. Experimental details

Single crystals were grown using the traveling solvent floating zone method. T_c for x = 0.075, defined as the midpoint of the transition, was determined to be 24 K from the shielding signal. We estimated the pseudogap temperature T^* for x = 0.075 to be 360 ± 20 K from the universal doping dependence of the pseudogap energy [4] and the scaling factor between the pseudogap energy and T^* [5]. Eight (with total mass of 75 g) and four (33 g) single-crystal rods were co-aligned for the underdoped LSCO (x = 0.075) and the parent compound, respectively. The INS data using the Fermi chopper spectrometer 4SEASONS were measured at T = 5, 300, 400, and 500 K for the underdoped LSCO (x = 0.075) and T = 5 and 400 K for the parent compound, as shown in the schematic phase diagram of LSCO (Fig. 1).

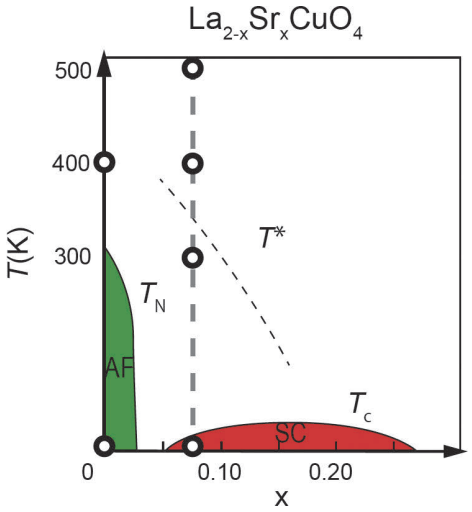

Figure 1. A schematic phase diagram of high-T_c cuprate LSCO. Measured temperatures and compositions are plotted as open circles in the diagram. AF and SC denote antiferromagnetic ordered phase and superconducting phase, respectively. T_c (T_N) are transition temperatures of the SC (AF) phase. The broken line shows the onset temperature of the pseudogap state (T^*). (from Ref. [3])

3. Results and discussion

Figures 2 (a) and (b) show contour maps of $\chi''(q,\omega)$ for the parent compound La_2CuO_4 measured at T = 5 K ($< T_N$) and 400 K ($> T_N$). At T = 5 K, we confirmed the well-known spin-wave signal. At T = 400 K, we still observed spin-wave signal due to the robust two-dimensional antiferromagnetic spin correlations. The thermal effect on spin-wave excitation is a slight softening: the estimated exchange constant J decreases from 136 ± 1 meV (T = 5 K) to 126 ± 1 meV (T = 400 K). In contrast, the overall spectrum is strongly affected by heating for the underdoped LSCO. First, the downward branch of the hourglass-shaped dispersion below 35 meV merges at 300 K. Then, the upward branch of the hourglass above 35 meV merges into a broad response above T = 400 K. Above the pseudogap temperature, magnetic signal is accumulated at the magnetic zone center in a whole measured energy range (< 200 meV). A similar broad ridge feature at the magnetic zone center has

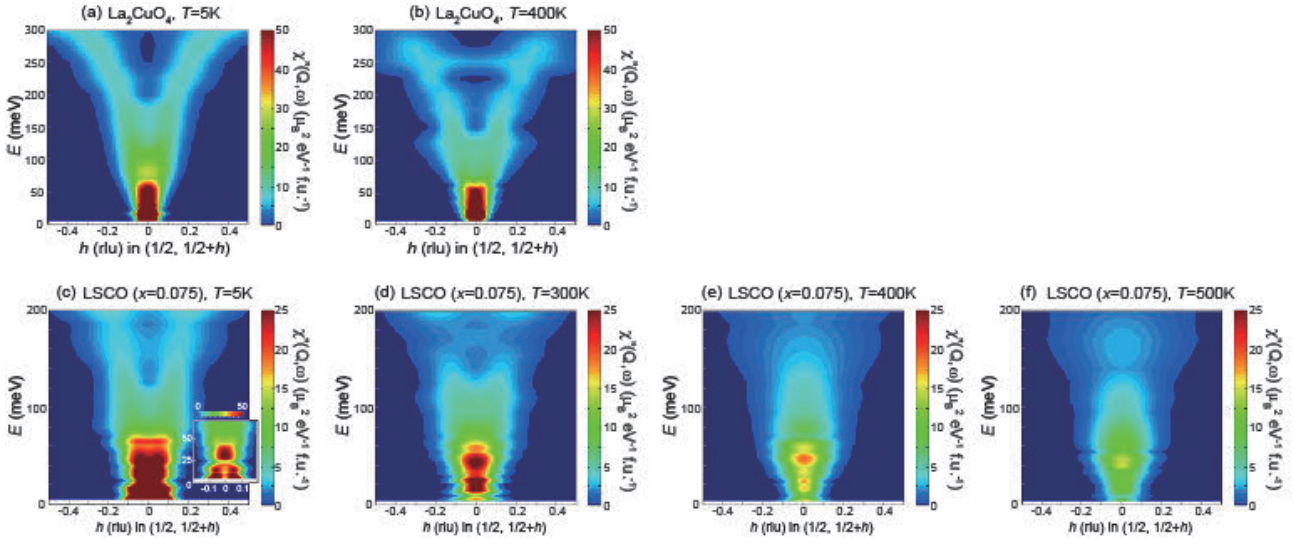

Figure 2. Contour maps of $\chi''(q,\omega)$ for (a), (b) La_2CuO_4 and (c)–(f) underdoped LSCO ($x = 0.075$), plotted in the energy momentum space. The inset in (c) shows the enlarged plot around the neck of the hourglass on a double intensity scale. (from Ref. [3])

been observed for itinerant antiferromagnets, such as Cr [6] and Vanadium Oxide [7], suggesting itinerant nature of spin excitations for $T > T^*$. In other words, the effect of pseudogap on the magnetic excitation is the recovery of the localized spin nature at the high-energy region. Thus, the current results support that the pseudogap is associated with the antiferromagnetic Mott insulator rather than a precursor of the Cooper pairs [8].

4. Summary

We have shown that the hourglass-shaped magnetic dispersion for the underdoped LSCO ($x = 0.075$) is significantly modulated into a broad ridge at temperatures well above T^*. This thermal variation of the upward branch in the hourglass-shaped dispersion contrasts with the almost unchanged spin-wave dispersion in the parent compound in the same temperature range.

References

[1] B. Keimer *et al*., Nature **518**, 179 (2015).
[2] M. Fujita *et al*., J. Phys. Soc. Jpn. **81**, 011007 (2012).
[3] M. Matsuura *et al*., Phys. Rev. B **95**, 024504 (2017).
[4] S. Hüfner *et al*., Rep. Prog. Phys. **71** 062501 (2008).
[5] T. Yoshida *et al*., Phys. Rev. Lett. **103**, 037004 (2009).
[6] T. Fukuda *et al*., J. Phys. Soc. Jpn. **65**, 1418 (1996).
[7] W. Bao *et al*., Phys. Rev. Lett. **78**, 507 (1997).
[8] S. Badoux *et al*., Nature **531**, 210 (2016).

M. Matsuura[1], S. Kawamura[2], M. Fujita[2], R. Kajimoto[3], and K. Yamada[4]
[1]*Neutron Science and Technology Center, CROSS;* [2]*Institute for Materials Research, Tohoku University;* [3]*Neutron Science Section, Materials and Life Science Division, J-PARC Center;* [4]*Institute of Materials Structure Science, KEK*

Spin-Orbital Correlated Dynamics in the Spinel-Type Vanadium Oxide MnV_2O_4

1. Introduction

In the condensed matter physics, the physical phenomena can be described by the creation, annihilation, and motion of quasi-particles such as phonons and magnons. Recently, the dynamical coupling of two or more degrees of freedom, such as an electromagnon [1, 2], has been extensively studied. In the present study, we focus on the dynamical coupling between spin and orbital degrees of freedom as an example of such a coupled quasi-particle. A magnon is a particle that quantizes the fluctuation from the magnetic ordered state, and transports the change in spin-angular momentum ΔS via magnetic exchange interaction. The orbiton is a dynamic modulation of the shape of electronic clouds in the analogy of a magnon [3]. The change in orbital angular momentum ΔL propagates via transfer integral term between neighboring transition metal ions. So far, the strong coupling between the orbital and lattice degrees of freedom hinders the observation of spin-orbital coupled waves. In addition, the momentum dependence of the orbital excitations has not been well investigated, since visible-light inelastic scattering was used in most of the previous reports.

We chose spinel-type vanadium oxide MnV_2O_4 for observing such spin-orbital coupled waves [Fig. 1(a)]. Mn^{2+} with a high-spin configuration ($S = 5/2$) on a tetrahedral site has no orbital degeneracy. The *d* orbitals of the V-site ion, coordinated by an oxygen octahedron, are split into lower-lying t_{2g} orbitals and higher-lying e_g orbitals. During cooling, a phase transition takes place into a collinear ferromagnetic order at $T_C = 58$ K. Below $T_{OO} = 53$ K, the magnetic structure changes into a non-coplanar ferrimagnetic order [Fig. 1(b)]. Simultaneously, a structural phase transition takes place from cubic to tetragonal, accompanied by the V^{3+}-site orbital order, in which $|yz\rangle$ and $|zx\rangle$ orbitals are alternately arranged along the *c*-axis [Fig. 1(c)]. In this study, we investigated the magnetic dynamics in MnV_2O_4 by inelastic neutron scattering (INS) for observing spin-orbital coupled waves.

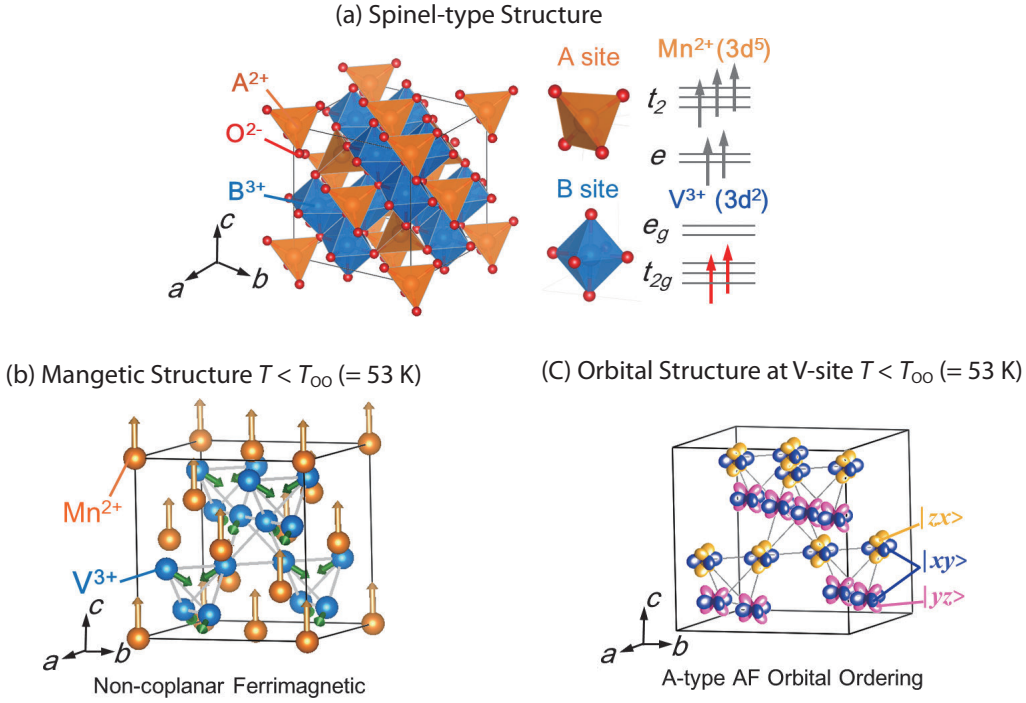

Figure 1. (a) Crystal structure of spinel-type oxide MnV_2O_4. Each A-site ion is surrounded by an oxygen tetrahedron. Each B-site ion is coordinated by an oxygen octahedron. The V^{3+} ion has orbital degeneracy in the t_{2g} orbital. (b) Magnetic structure in the tetragonal phase ($c<a$) below $T_{OO} = 53$ K. The spin moment of the Mn^{2+} ion is parallel to the c-axis and that of V^{3+} ion is in the opposite direction with a canted angle of 60° from the –c axis. (c) Proposed A-type antiferroic (AF) orbital structure at V-sites below $T_{OO} = 53$ K. (Taken from Ref. [4])

2. Experimental details

Single crystals were grown by the floating-zone method. They were characterized by powder x-ray diffraction and magnetization measurements. Four crystal bars, with a total mass of 10 g, were co-aligned using backscattering Laue photographs. The INS was carried out using the 4SEASONS spectrometer at MLF, J-PARC. The incident energies of neutrons were selected as 73, 34, 19, and 12 meV by a Fermi chopper. The temperature was maintained at 5.6 K.

3. INS results and spin-wave analysis

Figures 2 (a)-(c) show the experimental results of the INS at $E_i = 34$ meV and $T = 5.6$ K along three high-symmetry axes (a) $[hhh]_c$, (b) $[hh0]_c$, and (c) $[h00]_c$. The corresponding calculations are shown in Figs. 2 (d)-(f). Our experimental results are summarized as follows. First, we observed dispersive inelastic scattering intensity from 10 meV to 17 meV along $[hh0]_c$, which was not observed in the previous study [5]. Second, in Figs. 2(b) and (c), we can see a dispersive mode with large scattering intensity around 22 meV at both (2,2,0) and (4,0,0). The dispersive character of this scattering was clarified in the present study.

In order to identify spin-wave modes, we have performed spin-wave calculations based on the Heisenberg-type spin Hamiltonian with magnetic anisotropy. The magnetic scattering below 17 meV was sufficiently well reproduced by our spin-wave calculation. 22 meV-scattering, however, cannot be explained within our model. Therefore, 22 meV-scattering is not explained by simple spin-wave picture.

4. Possible origin of the 22 meV- scattering

This 22 meV-scattering was observed in Raman scattering [6], but it should not be attributed to two-magnon scattering. Here, we propose that the relativistic spin-orbit interaction $\xi \boldsymbol{l} \cdot \boldsymbol{s}$ (SOI) at the V-sites affects the energy levels of the magnetic excited state at Γ point within the first-order perturbation. For example, let us consider the SOI effect on the calculated spin-wave mode with the largest spin-fluctuation along c-axis ΔS_z. Then, this spin-wave mode should have a better chance to couple with the orbital excitation through the spin-orbit term $\xi l^z s^z$. In terms of orbital, l^z term leads to the transition between $|yz\rangle$ and $|zx\rangle$ orbitals. Interestingly, this spin-orbital correlated excitation might propagate as collective modes. Let us consider the excitation along the $[-101]_c$ direction [Fig. 2(l)-(n)]. In the ground state, the projection of spin

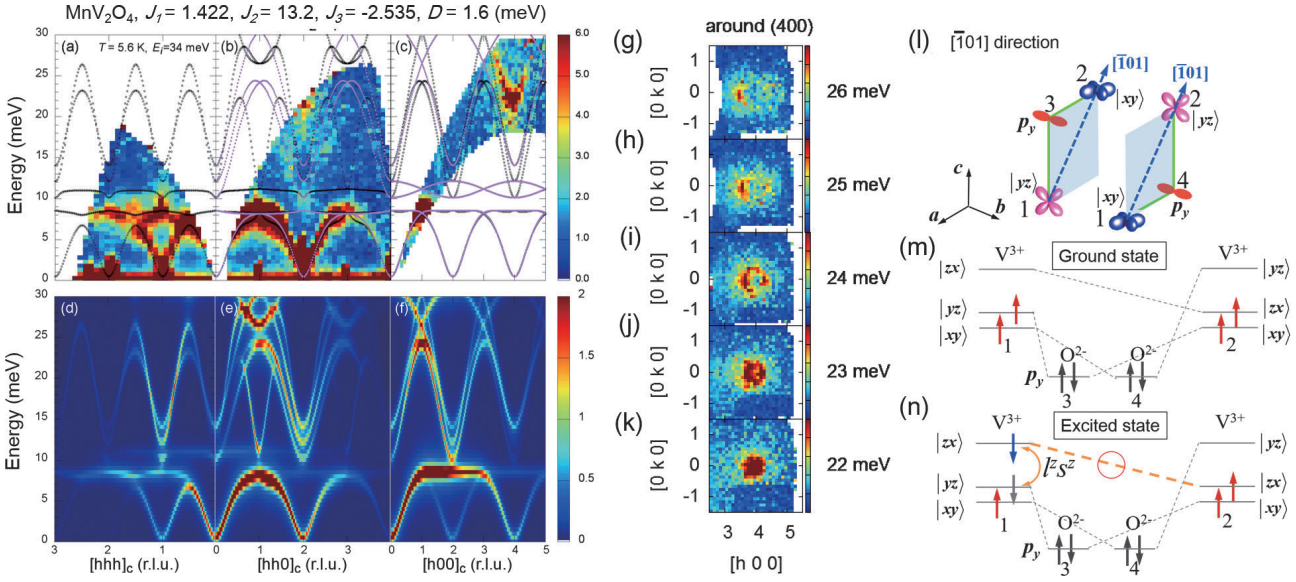

Figure 2. Experimental inelastic intensity contour and the corresponding calculated intensity contour along (a)(d) $[hhh]_c$, (b)(e) $[hh0]_c$ and (c)(f) $[h00]_c$ directions at $T = 5.6$ K. The purple filled and black open circles are the calculated spin wave dispersions along $[h0h]$ and $[hh0]$ directions in (b) and along $[00l]$ and $[h00]$ directions in (c), respectively. (g)-(k): Inelastic intensity contour in the $[h00]$-$[0k0]$ plane around [400]. (l) Schematic figures of superexchange paths via oxygen 2p orbital between neighboring V^{3+} ions for $[-101]_c$ direction. These figures are based on A-type antiferroic orbital ordering (See also Fig. 1(c)). The V^{3+} ions are at sites 1 and 2. The surrounding O^{2-} ions are at sites 3 and 4. (m) Electronic structure in the ground state for $[-101]_c$ direction. The spin moments are projected along the z direction. The dotted line indicates the overlapping between orbitals. (n) Excited state along $[-101]_c$ direction. (Taken from Ref. [4] and modified for the present report.)

moments at the V-sites in the *z* direction is ferromagnetic, as shown in Fig. 2 (m). A neutron flips the |*yz*, ↑> electron at site 1 to |*yz*, ↓> electron [Fig. 2 (n), gray arrow at site 1]. In this excited state, the SOI $\xi\, l^z s^z$ would excite the |*yz*, ↓> electron at site 1 to |*zx*, ↓> electron. This on-site excitation would recover the non-zero orbital angular momentum and gain energy of the SOI. In addition, the |*zx*, ↓> electron at site 1 can be exchanged with a |*zx*, ↑> electron at site 2 via direct exchange interaction [Fig. 2 (n)], propagating as the spin-orbital correlated collective mode.

5. Future Plans

In the present study, we clarified the magnetic dynamics in a spin-orbital coupled system MnV_2O_4 over wide momentum space with the use of INS. We found that magnetic scattering existed from 10 to 17 meV. Furthermore, we pointed out that the magnetic scattering around 22 meV was not simple spin-wave. In the future, we plan to perform INS on a single-domain sample for more exact analysis. The polarized inelastic neutron scattering should also provide us important information about the origin of the 22 meV-scattering.

Acknowledgement

The neutron experiments were performed at the Materials and Life Science Experimental Facility of the J-PARC under user program, Nos. 2012A0058, 2013A0141, 2014A0113, 2014B0152. We acknowledge T. Masuda, M. Soda, and S. Hayashida for their assistance in taking high-energy Laue photographs at the Institute for Solid State Physics, the University of Tokyo. The crystal structures were visualized using VESTA 3 [7].

References

[1] A. Pimenov *et al*., Nat. Phys. **2**, 97 (2006).
[2] N. Kida *et al*., J. Opt. Soc. Am. B **26**, A35 (2009).
[3] E. Saitoh *et al*., Nature **410**, 180 (2001).
[4] K. Matsuura *et al*., Phys. Rev. Lett. **119**, 017201 (2017) (and see also K. Matsuura *et al*., Physica B: Physics of Condensed Matter, in press).
[5] J. -H. Chung *et al*., Phys. Rev. B **77**, 054412 (2008) and Phys. Rev. B **87**, 139907 (E) (2013).
[6] K. Takubo *et al.,* Phys. Rev. B **84**, 094406 (2011) and S. L. Gleason *et al.,* Phys. Rev. B **89**, 134402 (2014).
[7] K. Momma and F. Izumi, J. Appl. Crystallogr. **44**, 1272 (2011).

K. Matsuura[1], H. Sagayama[2], A. Uehara[3], Y. Nii[4], R. Kajimoto[5], K. Kamazawa[6], K. Ikeuchi[6], S. Ji[6], N. Abe[1], and T. Arima[1]

[1]*Department of Advanced Materials Science, the University of Tokyo;* [2]*Institute of Materials Structure Science, High Energy Accelerator Research Organization;* [3]*Department of Applied Physics, the University of Tokyo;* [4]*Department of Basic Science, the University of Tokyo;* [5]*Neutron Science Section, Materials and Life Science Division, J-PARC Center;* [6]*Neutron Science and Technology Center, Comprehensive Research Organization for Science and Society (CROSS)*

Crystal Field Excitations on $NdFe_3(BO_3)_4$ Investigated by Inelastic Neutron Scattering

1. Introduction

Multiferroic materials, which exhibit both magnetic and dielectric orders, have been an intriguing topic since the discovery of a huge magnetoelectric (ME) effect in $TbMnO_3$ [1]. In the multiferroic materials, the rare-earth ferroborates $RFe_3(BO_3)_4$ (R = Y and rare-earth metal) are a series of new multiferroic compounds containing R^{3+} ($4f^n$) and Fe^{3+} ($3d^5$ $S = 5/2$) as magnetic ions. They show diverse ME effects as a function of the species of the R^{3+} ions (R = Y, Pr, Nd, Sm, Gd, and Tb), since there is a variety of the magnetic anisotropy of the R^{3+} moments coupled with the Fe^{3+} moments through the Fe^{3+} and R^{3+} moments (*f*-*d* coupling) [2]. Recent studies revealed that the mechanism of magnetoelectricity in these compounds is explained by the spin-dependent metal-ligand hybridization model [3, 4].

We focus on $NdFe_3(BO_3)_4$, in which the Nd^{3+} ions ($4f^3$) carry magnetic moment with $J = 9/2$. The crystal structure is trigonal with space group $R32$. The point symmetry of the NdO_6 octrahedra is D_3; a threefold rotational symmetry along the crystallographic *c*-axis and three twofold rotational axes in the *ab*-plane, as shown in Fig. 1. Studies on the specific heat, magnetic susceptibility [5], and ME effect [2] revealed that an easy-plane type antiferromagnetic (AF) order and a spontaneous electric polarization simultaneously occur at $T_N = 30$ K. The huge electric polarization is strongly enhanced by magnetic field. An optical spectroscopy study exhibited five Kramers doublets by the Nd^{3+} crystal field [6], and a recent inelastic neutron scattering (INS) study revealed that the magnetic anisotropy of the Nd^{3+} crystal field drove the multiferroicity in $NdFe_3(BO_3)_4$ [7].

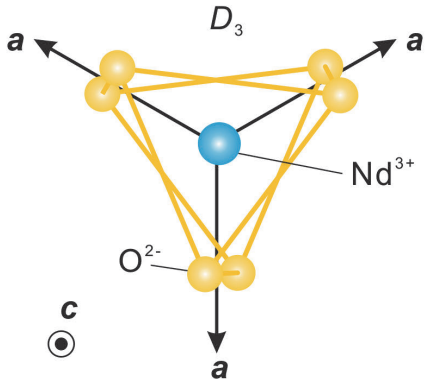

Figure 1. The *ab*-plane projection of the NdO_6 octahedra with D_3 symmetry [12].

In the present study, we explored the crystal field excitations of the Nd^{3+} ion in $NdFe_3(^{11}BO_3)_4$ using the INS technique. The investigation of the Nd^{3+} crystal field is important for further understanding of the ME effect in the rare-earth ferroborates.

2. Experimental details

Single crystals of $NdFe_3(^{11}BO_3)_4$ were grown by a flux method. 22 pieces of the single crystals were coaligned so that the $\boldsymbol{a}^*$-$\boldsymbol{c}^*$ plane was horizontal. We performed the INS experiment at the High-Resolution Chopper Spectrometer (HRC) installed in J-PARC/MLF. We used a GM-type closed-cycle cryostat to achieve 40 K and 15 K. The energy of the incident neutron beam was $E_i = 51.04$ meV yielding an energy resolution of $\Delta E = 2.5$ meV at the elastic position. We set the incident neutron beam with $\boldsymbol{k}_i // \boldsymbol{a}^*$.

3. Experimental results and discussions

An INS spectrum at 15 K is shown in Fig. 2(a). A well-defined flat excitation is observed at 17 meV and a weak flat one is observed at about 8 meV. The strong intensities at $\hbar\omega < 6$ meV in the wide Q range come from dispersive Fe-centered spin waves [7]. A weak flat intensity at about 20 meV comes from an instrumental artifact [7]. The dispersive spectra in the range of $Q > 2$ Å^{-1} come from the aluminum that is used for the sample can and sample holder.

One-dimensional energy cuts obtained by integrating the intensities in the range of 1.5 Å$^{-1} \leq Q \leq 1.9$ Å^{-1} are shown in Fig. 2(b). The red triangles and blue circles indicate the data measured at 40 K and 15 K, respectively. The data at 15 K are fitted by the sum of five Gaussian functions; the solid black curve is for an incoherent elastic scattering, the dashed curve is for the Fe-centered spin-wave excitation, the solid green curve is for a couple of intrinsic excitations, and the dotted curve is for the instrumental artifact. The peak energies of the green curve are estimated to be 8.5 meV and 17.4 meV, and they agree with the energy of the first and second excited states of the Nd^{3+} crystal field reported in the optical spectroscopy [6]. This suggests that these excitations are transitions from the ground state to the first and second excited states. A quite small temperature dependence is observed between the data at 40 K and that at 15 K.

We simulated the neutron intensities of the Nd^{3+}

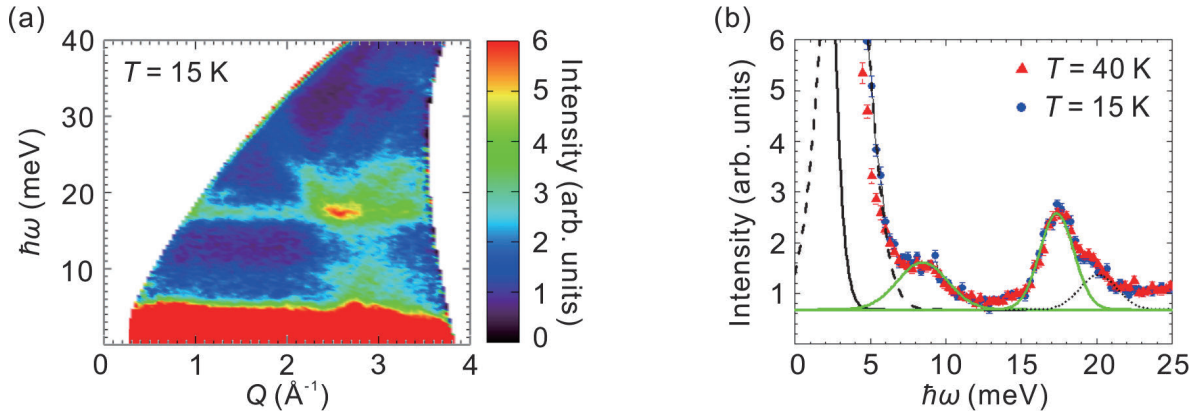

Figure 2. (a) An INS spectrum at 15 K. (b) $\hbar\omega$-dependence of the neutron intensities that are obtained by integration in the range of 1.5 Å^{-1} ≤ Q ≤ 1.9 Å^{-1}. The triangles and circles are data at 40 K and 15 K, respectively. Solid, dashed and dotted curves are Gaussian fits to the data at 15 K [12].

crystal field. At the Nd^{3+} site with the D_3 symmetry, the crystal filed Hamiltonian is defined as follows:

$$H_{CF}(D_3) = B_0^2C_0^2 + B_0^4C_0^4 + iB_3^4(C_3^4 + C_{-3}^4) + B_0^6C_0^6 + iB_3^6\,(C_3^6 + C_{-3}^6) + B_6^6(C_6^6 + C_{-6}^6)$$

The B_q^ps are the crystal field parameters and C_q^ps are the spherical tensor operators. We used the values of the parameters B_q^ps reported in Ref. [6].

We calculated the excitation energies and the neutron intensities of the transferred states from the ground state to the first and second excited stats using *McPhase* software suite [8]. The ratio of the calculated intensities $(I_{1st}/I_{2nd})_{cal}$ is 0.71, and that of the experimental intensities $(I_{1st}/I_{2nd})_{exp}$ is 0.49. The experimental results are semi-quantitatively consistent with the calculations. Furthermore, we obtained the temperature dependence of the intensity as $(I_{40K}/I_{15K})_{cal} = 0.93$ by assuming that the initial state was the ground state. The small temperature dependence is consistent with the data in Fig. 2(b). The observed excitations are, thus, interpreted as the first and second states of the Nd^{3+} crystal field.

It is noted that the peak at 8.5 meV is broader than the peak at 17.4 meV in Fig. 2(b). This broadening was also reported in the optical spectroscopy [6]. It is known that a spectrum of the crystal field excitation is broadened by coupling to a phonon [9] and dynamic Jahn-Teller effect [10, 11]. This broadening of the peak is ascribed to an interaction between the Nd^{3+} moment and lattice vibration since the magnetoelastic coupling was observed in $Nd_3(BO_3)_4$ [3].

4. Conclusion

The INS measurements were performed on the single crystals $NdFe_3(^{11}BO_3)_4$ to explore the Nd^{3+} crystal field excitations. In addition to the Fe-centered spin wave previously reported, dipersionless excitations were observed at 8.5 meV and 17.4 meV. Our analysis reveals that they are the transitions from the ground state to the first and second excited states of the Nd^{3+} ion in the crystal field.

References

[1] T. Kimura *et al*., Nature (London) **426**, 55 (2003).
[2] A. M. Kadomtseva *et al*., Low Temp. Phys. **36**, 511 (2010).
[3] A. I. Popov *et al*., Phys. Rev. B **87**, 024413 (2013).
[4] T. Kurumaji *et al*., Phys Rev. B **89**, 195126 (2014).
[5] N. Tristan *et al*., J. Magn. Magn. Mater. **316**, 621 (2007).
[6] M. N. Popova *et al*., Phys. Rev. B **75**, 224435 (2007).
[7] S. Hayashida *et al*., Phys. Rev. B **92**, 054402 (2015); MLF Annual report 2014, p22-23 (2015).
[8] M. Rotter, J. Magn. Magn. Mater. **272-276**, e481 (2004).
[9] E. T. Heyen *et al*., Phys. Rev. Lett. **67**, 144 (1991).
[10] S. Kern *et al*., Solid State Commun. **49**, 295 (1984).
[11] A. T. Boothroyd *et al*., Phys. Rev. Lett. **86**, 2082 (2001).
[12] S. Hayashida *et al*., J. Phys: Conf. Ser. **746**, 012059 (2016).

S. Hayashida[1], M. Soda[1], S. Itoh[2,3], T. Yokoo[2,3], K. Ohgushi[4], D. Kawana[1], and T. Mausuda[1]
[1]*The Institute for Solid State Physics, The University of Tokyo;* [2]*Neutron Science Section, Material and Life Science Division, J-PARC center;* [3]*Institute of Materials Structure Science, KEK;* [4]*Department of Physics, Tohoku University*

Damped Spin-Wave Excitations in the Itinerant Antiferromagnet γ–$Fe_{0.7}Mn_{0.3}$

1. Introduction

There has been renewed interest in magnetic excitations in itinerant antiferromagnets after the discovery of superconductivity in copper oxides and iron pnictides/chalcogenides. Metallic chromium, γ-FeMn, γ-Mn, and γ-Fe are prototypes of itinerant antiferromagnets. In the itinerant antiferromagnets, the maximum energy of the collective spin-wave excitations is relatively high compared to that of the Heisenberg magnets, and thus, the overall picture of the excitations has not yet been clarified. Unlike the case of the itinerant ferromagnets, there is still little experimental understanding of the spin-wave damping due to the continuum of the particle-hole excitations in itinerant antiferromagnets [1]. In the case of chromium, commensurate excitations, localized at the antiferromagnetic wave vector, extend up to more than 550 meV [2]. A recent theoretical study [3] predicted that the commensurate excitations merge with the continuum of the individual particle-hole excitations above 600 meV. However, spin excitations above 600 meV have yet to be elucidated experimentally.

To reveal the overall picture of the excitations in itinerant antiferromagnets, we focused on γ-FeMn, whose spin-wave velocity is much smaller than that of metallic chromium. The Fe_xMn_{1-x} alloy ($0.3 < x < 0.85$) is crystallized in a face-centered-cubic structure, the so-called γ phase. The Fe and Mn ions are located randomly at the origin and face-center positions. γ-FeMn shows the antiferromagnetic transition. Both Fe and Mn ions have magnetic moments. The transition temperature is $T_{AF} = 435$ K, and the average moment size is 1.97 μ_B for $Fe_{0.7}Mn_{0.3}$. We performed inelastic neutron-scattering measurements on $Fe_{0.7}Mn_{0.3}$ to elucidate magnetic excitations in an energy-momentum space wider than that in previously reported studies [4, 5].

2. Experimental Details

A $Fe_{0.7}Mn_{0.3}$ crystal was synthesized by a Bridgman-type induction furnace. The mass of the grown single crystal was about 40 g. Inelastic neutron-scattering experiments were performed on HRC [6]. The sample was mounted with a horizontal *hkk* scattering plane, sealed in an aluminum can under a ^{4}He gas atmosphere, and then set in a closed-cycle ^{4}He cryostat. Measurements were performed at $T = 14$ K.

3. Results

Figure 1 shows the obtained dispersion relation of the magnetic excitations. At the excitation energies $\hbar\omega = 48$ and 78 meV, there is no difference in the peak positions between all the three directions within the experimental error, which indicates that the dispersion is isotropic even at 78 meV. Then, we tried to fit the dispersion relation with a function. The energy gap was fixed to $\Delta = 10.2$ meV in the following fitting procedure, which was obtained with the $\hbar\omega$ dependence of the local spin susceptibility $\mathrm{Im}\chi(\hbar\omega)$, as described later. The black dashed curve in Fig. 1 shows the fit with the following equation

$$(\hbar\omega)^2 = c^2q^2 + \Delta^2, \quad (1)$$

which indicates that the function is unsuited. The dispersion could be fitted with Eq. (1) only below 40 meV. The black solid curve in Fig. 1 shows the fit below 40 meV. The spin-wave velocity is $c = 226(5)$ meVÅ. Below this energy, the dispersion is reasonably consistent with that in the previous reports for $Fe_{0.7}Mn_{0.3}$ at $T = 0$ K [$c = 195(30)$ meVÅ] [4] and $Fe_{0.47}Mn_{0.53}$ at room temperature (RT) (245–265 meVÅ) [5], shown by the green and blue dashed curves in Fig. 1. Above 40 meV, the gradient of the dispersion relation is considerably larger than that expected from Eq. (1). The linear fit with the function, $\hbar\omega = c'q + \Delta'$, above 40 meV yields the group velocity $c' = 470(40)$ meVÅ, shown by the black solid straight line.

The damping parameter γ was obtained under the assumption of a damped simple harmonic oscillator,

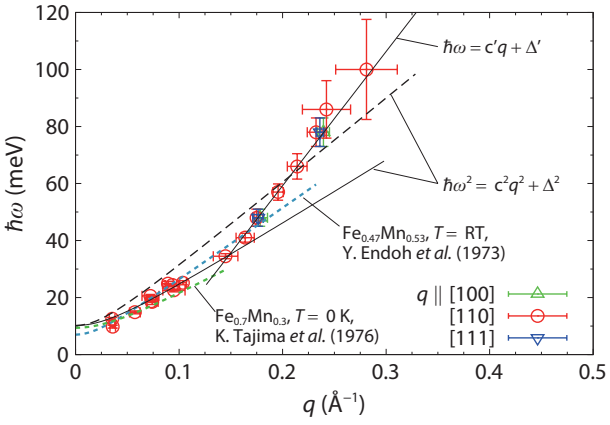

Figure 1. Dispersion relation of the magnetic excitations. The vertical error bars represent the energy resolution. The horizontal bars represent the fitting error.

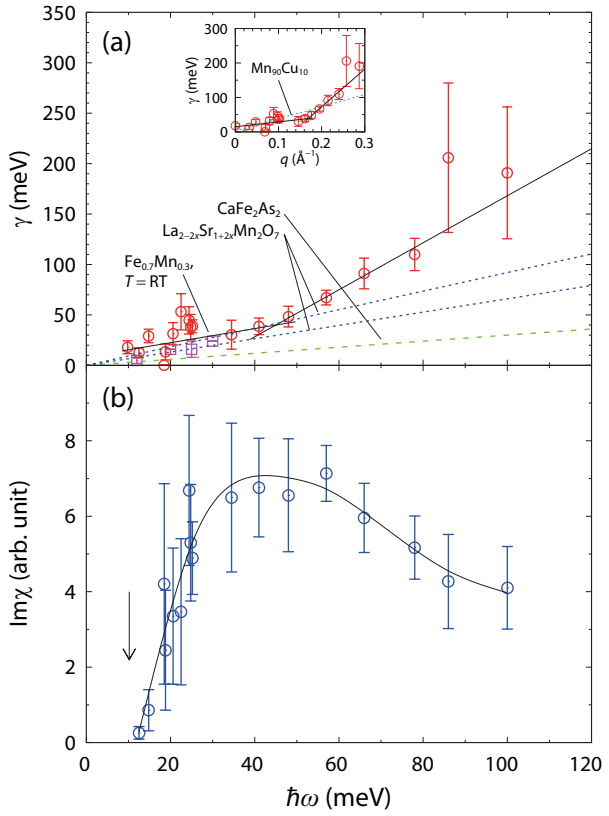

Figure 2. (a) $\hbar\omega$ dependence of the damping parameter γ. The black solid lines are guides to the eyes. The q dependence of γ is shown in the inset. (b) $\hbar\omega$ dependence of the local spin susceptibility $\mathrm{Im}\chi(\hbar\omega)$. The black solid line is a guide to the eyes. The arrow represents the gap energy.

which is shown in Fig. 2(a). γ below 30 meV is in agreement with the previous report at RT [4]. γ shows a steady increase above approximately 40 meV and reaches 110(16) meV at $\hbar\omega$ = 78 meV. γ above 40 meV is much larger than the metallic compounds, $La_{2-2x}Sr_{1+2x}Mn_2O_7$ [7] and $CaFe_2As_2$ [8]. The inset in Fig. 2(a) shows the q dependence of γ. γ increases steadily above q = 0.16 Å^{-1}. γ above 0.22 Å^{-1} is larger than that of $Mn_{90}Cu_{10}$, which is a dilute alloy of the itinerant antiferromagnet γ-Mn [9]. Figure 2(b) shows $\mathrm{Im}\chi(\hbar\omega)$. The energy gap was estimated to be Δ(14 K) = 10.2(7) meV by linear extrapolation of $\mathrm{Im}\chi$ below 15 meV. The result is consistent with the value previously reported [4], Δ(0 K) = 9.4 meV. $\mathrm{Im}\chi$ reaches the maximum value around 40 meV and clearly decreases above 60 meV.

4. Discussion

The deviation of the spin-wave dispersion from Eq. (1) above 40 meV indicates the existence of other excitations that interact with the spin-wave because the group velocity decreases with energy, if the spin wave does not interact. This result suggests that the spin wave merges with the continuum of the individual particle-hole excitations at 40 meV. When a spin-wave enters the continuum, an increase in the group velocity is expected for a ferromagnetic electron gas [10]. On the other hand, a magnon-electron interaction will not cause a sudden change. γ steadily increases above 40 meV, and $\mathrm{Im}\chi$ gradually decreases above 60 meV, which indicates that the spin wave gradually damps with increasing $\hbar\omega$ in the continuum. Of course, other scenarios for explaining the excitations cannot be ruled out. At least, it is unique that the spin-wave excitations show the linear q-dependent dispersion and broad energy width above 40 meV. A future theoretical study would be very interesting. This work has been published in [11].

References

[1] Y. Ishikawa, J. Appl. Phys. 49, 2125 (1978); Y. Endoh and P. Böni, J. Phys. Soc. Jpn. 75, 111002 (2006).
[2] For example, J. R. Lowden, P. W. Mitchell *et al.*, J. Magn. Magn. Mater. 140–144, 1971 (1995).
[3] K. Sugimoto, Z. Li, E. Kaneshita, K. Tsutsui, and T. Tohyama, Phys. Rev. B 87, 134418 (2013).
[4] K. Tajima, Y. Ishikawa, Y. Endoh, and Y. Noda, J. Phys. Soc. Jpn. 41, 1195 (1976).
[5] Y. Endoh, G. Shirane, Y. Ishikawa, and K. Tajima, Solid State Commun. 13, 1179 (1973).
[6] S. Itoh, T. Yokoo, S. Satoh *et al.*, Nucl. Instrum. Methods Phys. Res., Sect. A 631, 90 (2011).
[7] T. G. Perring, D. T. Adroja, G. Chaboussant, G. Aeppli *et al.*, Phys. Rev. Lett. 87, 217201 (2001).
[8] J. Zhao, D. T. Adroja, D.-X. Yao, R. Bewley, S. Li, X. F. Wang *et al.*, Nat. Phys. 5, 555 (2009).
[9] J. A. Fernandez-Baca, M. E. Hagen *et al.*, J. Magn. Magn. Mater. 104–107, 699 (1992).
[10] Y. Ishikawa, J. Appl. Phys. 49, 2125 (1978).
[11] S. Ibuka, S. Itoh, T. Yokoo, and Y. Endoh, Phys. Rev. B 95, 224406 (2017).

S. Ibuka[1,2], S. Itoh[1,2,3], T. Yokoo[1,2,3], and Y. Endoh[1,4,5]
[1]Institute of Materials Structure Science, KEK; [2]Neutron Science Section, Materials and Life Science Division, J-PARC Center; [3]Department of Materials Structure Science, School of High Energy Science, Graduate University for Advanced Science; [4]RIKEN Center for Emergent Matter Science; [5]Department of Physics, Tohoku University

Large Magnetovolume Effect Induced by Embedding Ferromagnetic Clusters into Antiferromagnetic Matrix of Cobaltite Perovskite

1. Introduction

Most of the solids expand on heating due to the anharmonic vibration of atoms. However, thermal expansion may cause problems in various fields, ranging from large structural components to precision instruments. On the other hand, some materials exhibit the opposite tendency, known as negative thermal expansion (NTE). The NTE materials have significant industrial merit because they can be used to compensate the unwanted thermal expansion and fabricate zero thermal expansion materials [1]. In some materials, NTE is coupled with spontaneous magnetization, which is called magnetovolume effect (MVE).

2. Results

Here we report a new class of NTE material; namely, a layered perovskite $PrBaCo_2O_{5.5+x}$ (see Fig. 1a), where x corresponds to the hole doping level [2, 3]. The value of volume expansion coefficient β [$\beta = dV/(V \times dT)$] for $x = 0.24$, as depicted in the inset in Fig. 1b, is -3.6×10^{-5} K^{-1}, making it one of the strongest NTE materials. The results (see Fig. 1c) of high-resolution neutron powder diffraction from SuperHRPD (BL08) under proposal No. 2014S05 demonstrate a striking MVE, i.e.,the square of magnetic moment M is linearly correlated with the volumetric order parameter ΔV for $x = 0.24$, where ΔV is extracted by subtracting the phonon contribution calculated on the basis of Debye-Grüneisen model (see Fig. 1b). After deriving the magnetic phase diagram (see Fig. 1d) from the neutron powder diffraction study, we found out that the MVE reaches its maximum near the boundary between the ferromagnetic (F) and antiferromagnetic (AF) phases in the phase diagram, indicating the essential role of the F-AF competition.

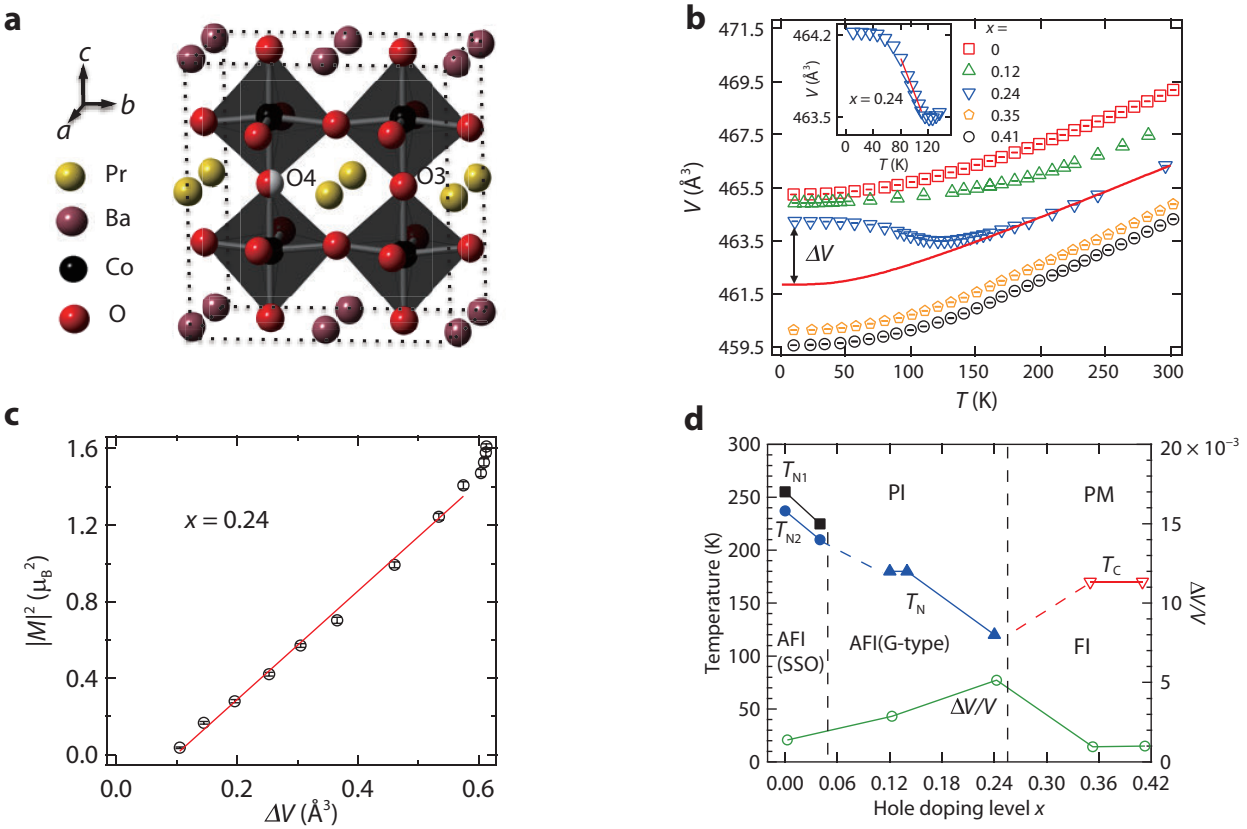

Figure 1. **a**, Schematic drawing for the general crystal structure of $PrBaCo_2O_{5.5+x}$. **b**, Volume of unit cell as a function of the temperature for various hole-doping fractions x determined through high resolution-neutron-powder diffraction (NPD). **c**, Square of magnetic moment $|M|^2$ as a function of the volumetric order parameter ΔV for $x = 0.24$. **d**, Phase diagram, characterizing the magnetic transition temperature and $\Delta V/V$ at 10 K as a function of x [3].

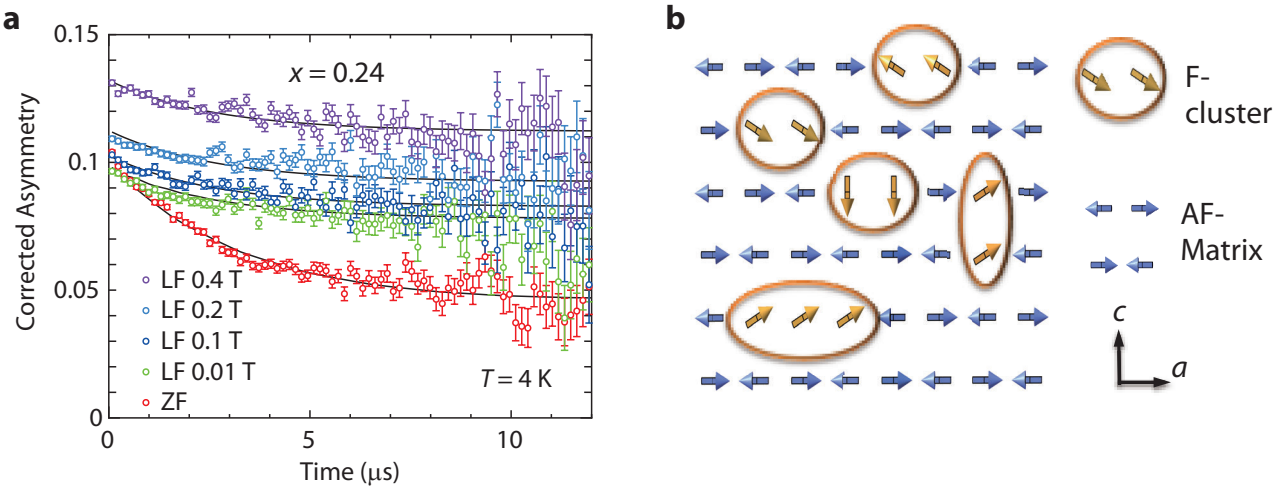

Figure 2. **a**, Muon spin relaxation (μSR) time spectra at 4 K under various longitudinal magnetic fields for $PrBaCo_2O_{5.5+x}$ (x = 0.24). **b**, Schematic drawing for the ferromagnetic clusters embedded in the antiferromagnetic matrix [3].

A further muon-spin-relaxation (μSR) experiment (see Fig. 2a) performed at MUSE under proposal No. 2017A0014, clearly exhibits the magnteoelectronic phase separation for x = 0.24 at ground state. Specifically, the damping of spectra under longitudinal field (LF) up to 0.4 T reveals the dynamic phase; an increase in the initial asymmetry by applying field indicates the static phase with internal field; the lift-up of spectrum under LF of 0.01 T suggests a static phase without internal field. These phases are the result of interaction between the F-clusters and the antiferromagnetic AF-matrix (see Fig. 2b). Such an inhomogeneous phase scenario is also evidenced by the neutron pair distribution function (PDF) analysis from NOVA (BL21) under proposal No. 2016A0023.

Through a comprehensive study with multiple probes (neutron, muon, electron and X-ray), we found the MVE originates from the competition between the F-clusters and the AF matrix.

References

[1] J. Chen, L. Hu, J. Deng, X. Xing, Chem. Soc. Rev. 44, 3522 (2015).

[2] P. Miao, X. Lin, S. Lee, Y. Ishikawa, S. Torii, T. Ueno, N. Inami, K. Ono, Y. Wang, T. Kamiyama, Phys. Rev. B 95, 125123 (2017).

[3] P. Miao, X. Lin, A. Koda, S. Lee, Y. Ishikawa, S. Torii1, M. Yonemura, T. Mochiku, H. Sagayama, S. Itoh, Y. Wang, R. Kadono and T. Kamiyama, Adv. Mater. 29, 1605991 (2017).

Ping Miao[1,2], X. Lin[3], A. Koda[1,2,4], S. Lee[1], Y. Ishikawa[1], S. Torii[1,4], M. Yonemura[1,2,4], T. Mochiku[5], H. Sagayama[1,2], S. Itoh[1,2,4], Y. Wang[3], R. Kadono[1,2,4], and T. Kamiyama[1,2,4]

[1]Institute of Materials Structure Science, KEK; [2]Department of Materials Structure Science, Sokendai; [3]College of Chemistry and Molecular Engineering, Peking University; [4]Neutron Science Section, Material and Life Science Division, J-PARC center; [5]National Institute for Materials Science

Neutron Tolerance Evaluation of Perpendicular-Anisotropy CoFeB-MgO Magnetic Tunnel Junctions using NOBORU at J-PARC

1. Introduction

Magnetic random access memory (MRAM) that employs magnetic tunnel junctions (MTJs) is a new non-volatile memory that is very promising due to its high operation speed. MRAM devices have already reached performance levels comparable to those of fast stand-alone memory such as static RAM (SRAM). Among MRAM technologies, MTJs that use spin-transfer-torque (STT) switching are attracting much attention for their potential to reduce both power consumption and interconnection delays [1]. MTJs with a perpendicular magnetic easy axis (p-MTJ) are expected to simultaneously realize a low STT switching current and high thermal stability factor, Δ. The highest Δ was recently obtained with an MgO/CoFeB/Ta/CoFeB/ MgO double-interface recording structure [2].

The physical dimensions of SRAM devices continue to be reduced along with the operation voltage and power consumption, so that SRAM has become more sensitive to fast neutron irradiation at ground level [3]. It has been claimed that MRAM is error-immune, based on the internal characteristics of the MTJ that stores the data. However, the neutron tolerance of p-MTJs with a CoFeB-MgO structure under fast neutron irradiation at ground level has not yet been specifically reported. For this reason, we have begun fast neutron irradiation experiments (Proposal Numbers: 2014A0102, 2014B0120, and 2015A0134) using the J-PARC BL10, NOBORU, beamline to evaluate the fast neutron tolerance of p-MTJ devices with a junction diameter (*D*) of approximately 50 nm and a double-interface recording structure.

2. Experimental methods

MTJ devices with the CoFeB-MgO structure were fabricated on a 40 × 40 mm^2 area (3-inch) SiO_2/Si wafer. 461 p-MTJ devices equipped with a CoFeB-MgO recording structure were used. Each p-MTJ has a stacked profile structure from the SiO_2/Si substrate side: Ta (5)/Ru (10)/Ta (5)/Pt (5)/[Co (0.34)/Pt (0.4)]$_6$/Co (0.34)/Ru (0.44)/[Co (0.34)/Pt (0.4)]$_2$/Co (0.34)/Ta (0.3)/ CoFeB/MgO/ CoFeB/Ta (1)/Ru (7), where the numbers in parentheses are the nominal thicknesses in nanometers, and the subscripts indicate the number of Co/Pt multilayers. The stack is processed into circular p-MTJs using electron beam lithography and Ar ion milling, followed by annealing at 300°C under vacuum with a perpendicular magnetic field of 0.4 T for 1 h. The junction diameter (*D*) of each p-MTJ was within the range of 46 to 64 nm. p-MTJ devices with tunnel magnetoresistance (TMR) ratios above 90% at room temperature were used.

The neutron irradiation experiment was conducted using the BL10, NOBORU, beamline at J-PARC. The neutron beam irradiation area was approximately 80 × 80 mm^2. Low-energy neutrons were separated from the neutron beam using 5 mm thick B_4C slits, while gamma radiation was blocked using a 25 mm thick Pb block. The total 1 MeV equivalent fluence of fast neutrons irradiated to the 461 p-MTJ devices was 3.79 × 10^{12} neutrons cm^{-2}, which corresponded to 1.90 × 10^{11} h (approximately 22 million years) irradiation in a fast neutron environment at ground level (20 cm^{-2} h^{-1}). The effect of fast neutron irradiation was evaluated by comparing the resistance-magnetic field (*R-H*) curves of the p-MTJs before and after neutron irradiation.

3. Results

Figure 1 shows *R-H* curves for a p-MTJ with *D* = 48 nm and a TMR ratio of 108% following neutron irradiation up to 3.79 × 10^{12} cm^{-2}. The dashed lines indicate the resistance values in the parallel and anti-parallel states prior to irradiation, R_P^{before} and R_{AP}^{before}, respectively. The resistance values and switching fields were observed to be unchanged from those prior to irradiation. Figure 2 shows a comparison of the TMR ratios of the 461 p-MTJs before and after irradiation of 3.79 × 10^{12} cm^{-2}. After irradiation, the variation induced in the TMR ratios and the standard deviation σ were approximately ±1% and 0.62%, respectively, and these values remained within the experimental error. Therefore, the properties of the CoFeB-MgO p-MTJ devices were not significantly affected by exposure to a fast neutron fluence of up to 3.79 × 10^{12} cm^{-2}. This study represents the first result of the effects of fast neutron irradiation on p-MTJs with a CoFeB-MgO structure and practical junction diameters [4].

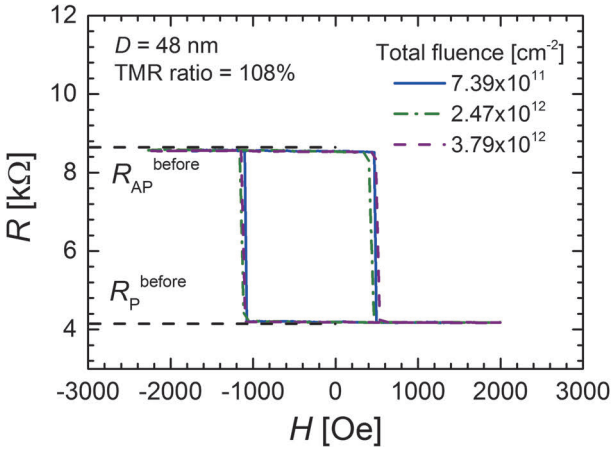

Figure 1. *R-H* curves for a p-MTJ with D = 48 nm and a TMR ratio of 108% following fast neutron irradiation up to 3.79 × 10^{12} cm^{-2}. R_P^{before} and R_{AP}^{before} indicate the resistance values in the parallel and anti-parallel states prior to irradiation, respectively.

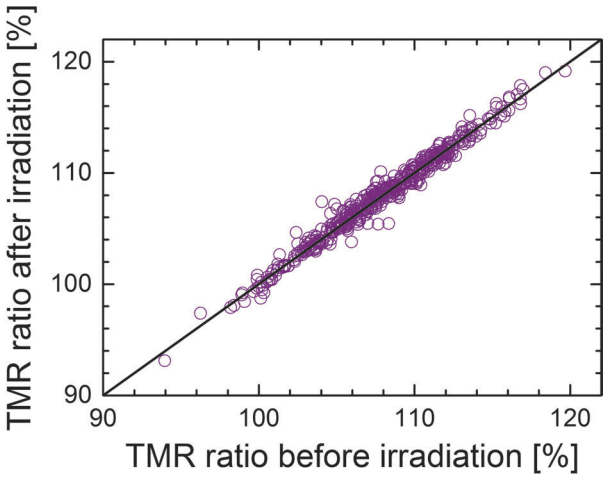

Figure 2. Comparison of TMR ratio before and after fast neutron irradiation of 3.79 × 10^{12} cm^{-2}.

4. Future Plans

SRAM has become more sensitive to fast neutron irradiation due to a reduction in the device size; therefore, it is important to ensure the fast neutron tolerance of p-MTJs with D below 50 nm. At present, we are evaluating the fast neutron tolerance of CoFeB-MgO p-MTJs with D < 20 nm.

We plan to attempt the measurement of *in situ* current-voltage (*I-V*) curves during fast neutron irradiation at NOBORU.

Acknowledgments

This work was supported by the Research and Development Project for ICT Key Technology of the Ministry of Education, Culture, Sports, Science and Technology. The authors wish to thank Dr. Motoki Ooi for technical support during the neutron irradiation work at J-PARC.

References

[1] S. Ikeda, J. Hayakawa, Y. M. Lee, F. Matsukura, Y. Ohno, T. Hanyu, and H. Ohno, IEEE Trans. Elec. Dev., **54** 991 (2007).

[2] H. Sato, E. C. I. Enobio, M. Yamanouchi, S. Ikeda, S. Fukami, S. Kanai, F. Matsukura, and H. Ohno, Appl. Phys. Lett., **101** 022414 (2012).

[3] E. Ibe, H. Taniguchi, Y. Yahagi, K. Shimbo, and T. Taba, IEEE Trans. Elec. Dev., **57** 1527 (2010).

[4] Y. Narita, Y. Takahashi, M. Harda, K. Oikawa, D. Kobayashi, K. Hirose, H. Sato, S. Ikeda, T. Endoh, and H. Ohno, Jpn. J. Appl. Phys., **56** 0802B3 (2017).

Y. Narita[1], Y. Takahashi[1], M. Harada[2], K. Oikawa[2], D. Kobayashi[3], K. Hirose[3], H. Sato[4,5,6,7], S. Ikeda[4,5,6], T. Endoh[4,5,6,8], and H. Ohno[4,5,6,7,9]

[1]Graduate School of Science and Engineering, Yamagata University; [2]Neutron Science Section, Materials and Life Science Division, J-PARC Center; [3]Institute of Space and Astronautical Science, Japan Aerospace Exploration Agency (ISAS/JAXA); [4]Center for Spintronics Research Network, Tohoku University; [5]Center for Innovative Integrated Electronic Systems, Tohoku University; [6]Center for Spintronics Integrated Systems, Tohoku University; [7]Laboratory for Nanoelectronics and Spintronics, Research Institute of Electrical Communication, Tohoku University; [8]Graduate School of Engineering, Tohoku University; [9]WPI Advanced Institute for Materials Research, Tohoku University

Two-Dimensional Microstructure Visualization in Engineering Materials using Bragg-Edge Imaging

1. Introduction

The neutron transmission of steel materials has characteristic energy dependency due to Bragg reflection (referred to as Bragg-edge spectrum). By obtaining and analyzing the Bragg-edge spectrum two-dimensionally, it is possible to visualize the microstructural properties of the sample, such as texture, crystalline phase, crystallite size, and lattice strain [1]. However, the results must be verified by comparing them with those obtained by conventional methods because the Bragg-edge transmission (BET) imaging is a new developing technique.

Bending is one of the most frequently used operations in sheet forming to produce functional parts. Bending deformation can introduce tension and compression stress states into materials simultaneously.

In order to examine the application of the BET imaging to nondestructive inspection of engineering products, we performed time-of-flight (TOF) 2D BET imaging experiments for plastically bent plates using high-intensity pulsed neutrons at J-PARC [2, 3]. The microstructure and residual elastic strain distributions of the samples were evaluated, and the analyzed Bragg-edge imaging results were validated using the well-developed neutron diffraction method and electron backscatter diffraction (EBSD) observations.

2. Experimental procedures

Two commercially available steels were used in the present investigation: a ferrite single-phase steel (FS) and a hot-rolled duplex stainless steel (DSS) consisting of face-centered cubic austenite and body-centered cubic ferrite. An example of a bent sample used in this study is shown in Fig. 1.

Pulsed neutron imaging experiments were performed at BL10 NOBURU of the MLF/J-PARC. A 100 × 100 mm area 2D detector with a 0.8 × 0.8 mm pixel resolution was used to measure the position-dependent transmission spectra. The RITS code [1] was used for Bragg-edge spectral analysis to obtain 2D maps of texture, crystallite size, and phase volume fraction. Neutron diffraction experiments were performed at BL19 TAKUMI of the MLF/J-PARC. Neutron diffraction data were collected with the gauge volume of 2 × 2 × 2 mm. The bent samples were scanned at 14 positions from the outer to the inner regions shown by a red box in Fig. 1 in intervals of 1 mm. The Z-Rietveld software [4] was used for diffraction pattern analysis to obtain texture, residual lattice strain, and phase volume fractions. EBSD measurements were conducted at a Hitachi 4300 SEM fitted with an EBSD system. The local crystallographic orientation, grain size, and phase discrimination of the samples were determined by means of EBSD analysis.

3. Results and discussion

Figure 2 shows an example of the measured and fitted transmission spectra of the FS sample, obtained at points A, B, and C as indicated in Fig. 1, the shape of the BET spectra changes due to the bending plastic deformation. Enlarged views of the ferrite 110 edges in both insets represent the single-edge profile fitting, which provide the lattice plane spacing, d_{110}.

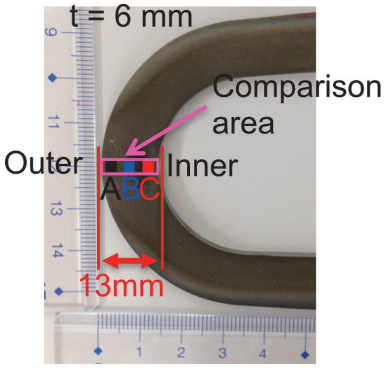

Figure 1. Photograph of a bent sample.

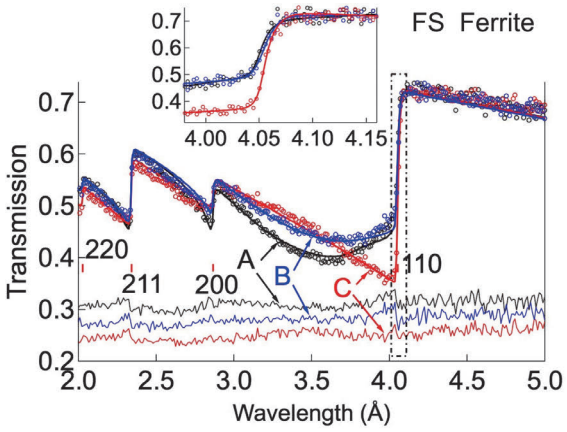

Figure 2. BET spectra of FS sample measured at the points indicated in Fig. 1.

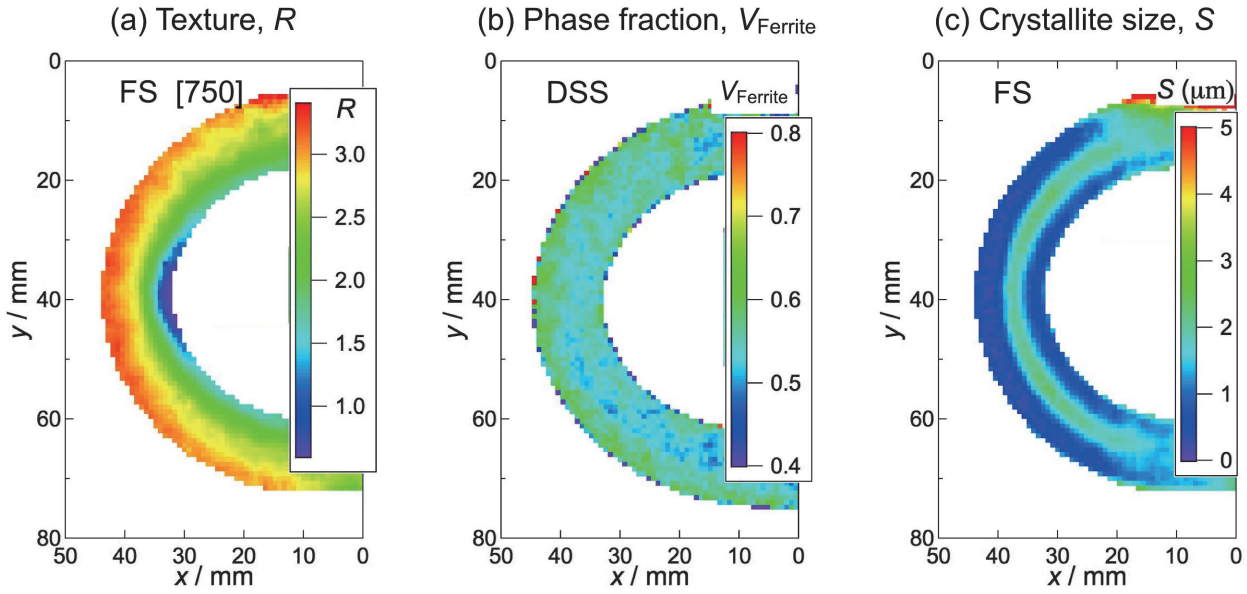

Figure 3. 2D maps determined by BET imaging: (a) texture variations, R, for the FS sample, (b) phase volume fraction, $V_{Ferrite}$, for the DSS sample and (c) crystallite size, *S*, for the FS sample.

Texture variations, crystallite size, and phase volume fraction in both samples were analyzed by the RITS code and are mapped in Fig. 3. A coefficient of the March–Dollase (MD) function, *R*, provides the degree of the preferred orientation, namely $R = 1$ for a random texture sample and $R < 1$ ([*hkl*] // incident beam) or $R > 1$ ([*hkl*] $\perp$ incident beam) for a textured sample, where [*hkl*] represents the preferred orientation vector. Figure 3(a) shows the map of the refined parameter *R* for the FS sample. The coefficient *R* decreases gradually from the outer to the inner zone in the bent sample. This map indicates that the [750] orientation is perpendicular to the beam direction in the outer zone, whereas it is parallel to the beam direction in the inner zone. Figure 3(b) shows the map of ferrite phase volume fraction, $V_{Ferrite}$, of the DSS sample, which was calculated with the obtained projection data of the atomic number density of ferrite and austenite of the sample. It indicates a mostly homogeneous distribution within the bulk of the sample with some slight variation along the outer edge. A value for $V_{Ferrite}$ of 0.6 is estimated as the average over the entire measured region of the sample. It confirmed that phase transformation does not occur by plastic deformation in the DSS sample. Figure 3(c) shows the map of the crystallite size of the FS sample, which was evaluated by the Sabine's primary extinction parameter, *S*. The crystallite size of the center zone is obviously larger than that of the inner and outer zones, which tells us that the average crystallite size is reduced due to the tensile or compressive deformation.

Then, quantitative microstructure characteristics for both samples obtained by the BET imaging method were compared with those gained by neutron diffraction and EBSD microscopic observations. Figure 4 shows the representative results. Firstly, Figure 4(a) shows texture variations for FS sample by comparisons *R* results obtained by BET imaging and those of neutron diffraction methods. The coefficient R of the ferrite [750] orientation for the ferrite steel sample obtained using both methods shows a similar texture evolution from the outer to inner zone, although the absolute values differ from each other. The coefficient R obtained from the BET imaging method is a little higher than that from the diffraction method, which might be caused by differences in the effective thickness of the samples. Secondly, ferrite phase volume fraction, $V_{Ferrite}$, of DSS sample (Fig. 4(b)) obtained by BET imaging, neutron diffraction and EBSD is compared together. Thirdly, the residual elastic strain distribution results (Fig. 4(c)) of ferrite 110, ε, in DSS sample are compared, which are obtained from the BET single-edge and diffraction single-peak fitting results. Furthermore, the crystallite size distribution results of BET imaging for both samples are also discussed by comparison with the EBSD sub-grain analysis results [2, 3]. All the above-mentioned BET-imaging results are in good agreement with those from the neutron diffraction and EBSD.

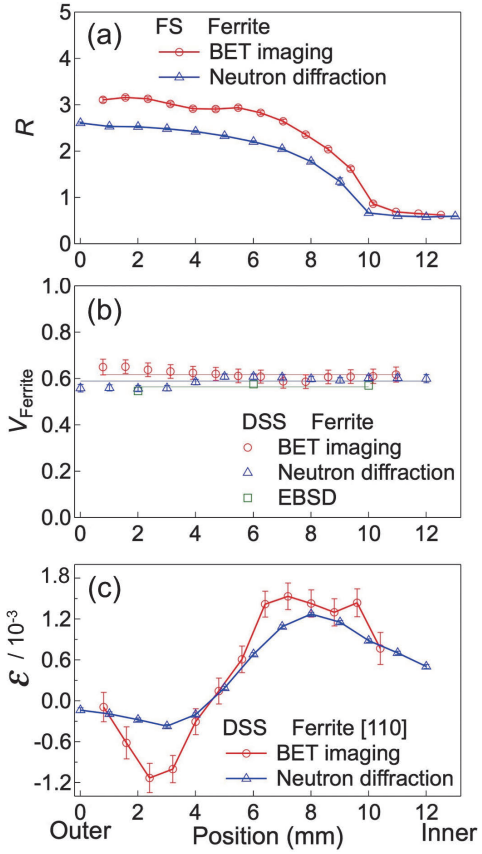

Figure 4. Comparisons of BET imaging results with those obtained by diffraction, and EBSD methods: (a) texture, R, for the FS sample, (b) phase volume fraction, $V_{Ferrite}$, for the DSS sample and (c) residual lattice strain, ε, for the DSS sample.

4. Conclusions

All of these results confirm that quantitative 2D TOF neutron BET imaging is a very effective and powerful tool for revealing the microstructure and elastic strain in engineering materials. These obtained 2D maps of the crystallographic texture, crystallite size, and volume fraction distribution of constituent phases are applicable for nondestructive inspection of complicated engineering products.

Acknowledgments

This work was supported by the Photon and Quantum Basic Research Coordinated Development Program from the Ministry of Education, Culture, Sports, Science and Technology, Japan. Neutron experiments were performed under proposal Nos. 2014B0026 and 2015P0700 at MLF/J-PARC.

References

[1] H. Sato, et. al., Phys. Procedia., 43 186-195 (2013).
[2] Y. H. Su, et. al., Mater. Sci. Eng. Mater. Sci. Eng. A 675 19-31 (2016).
[3] K. Oikawa, et. al., Phys. Procedia., 88 34-41 (2017).
[4] R. Oishi-Tomiyasu, et. al., J. Appl. Cryst. 45 299-308 (2012).

Y. H. Su[1], K. Oikawa[1], S. Harjo[1], T. Shinohara[1], T. Kai[1], M. Harada[1], K. Hiroi[1], S.Y. Zhang[2], J. D. Parker[2], H. Sato[3], Y. Shiota[4], Y. Kiyanagi[4], and Y. Tomota[5]

[1]Neutron Science Section, Materials and Life Science Division, J-PARC Center; [2]Neutron Science and Technology Center, CROSS; [3]Faculty of Engineering, Hokkaido University; [4]Graduate School of Engineering, Nagoya University; [5]Research Center for Strategic Materials, National Institute for Materials Science

Neutron Study on the Nanoscale Structures and Dynamics of Rubber Materials for Tires

1. Introduction

Tires play an essential role of the automobile operation: supporting a vehicle's weight in addition to driving, turning and stopping. At the same time, now there is a growing market demand for tires that feature not only excellent grip performance to ensure safety, but also superior fuel-efficiency performance to meet the needs of consumers with an increasing environmental awareness, as well as wear-resistance performance in response to the desire for longer lasting tires. To fulfill those diverse tire performance requirements, the need for the development of high-performance rubber materials for tires is growing.

As shown in Fig. 1, tire rubber is composed of a polymer framework to which solid nanoparticles such as silica and carbon black (i.e. filler) have been added to reinforce the rubber. It also includes other additives, such as oils or resins, as well as crosslinking agents that link the polymer chains together. Those materials are dispersed throughout the rubber in an extremely complex disposition.

The different ingredients form hierarchical structures within the rubber that extend from the nanoscale to the macroscale. Figure 2 depicts the temporal-spatial hierarchical structure of tire rubber. These temporal-spatial hierarchical structures within the rubber are intimately related to the overall tire performance. Therefore, to develop high-performance rubber materials, it is necessary to elucidate further the nature of these temporal-spatial hierarchical structures.

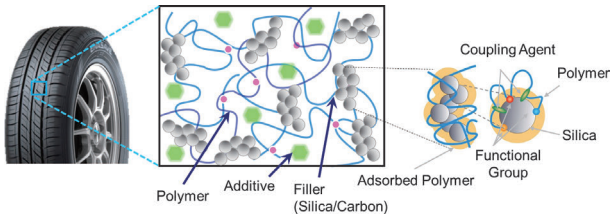

Figure 1. Internal structure of tire rubber.

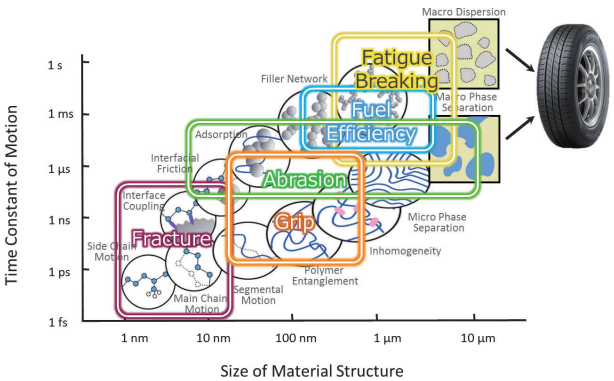

Figure 2. Relationship between tire performance and the temporal-spatial hierarchical structure of tire rubber.

Quantum beams, such as neutron beams and x-rays, are effective tools for analyzing the nanoscale structures and dynamics of rubber shown in Fig. 2.

At Sumitomo Rubber Industries, we have successfully developed a new materials development technology that utilizes the world-class, cutting-edge research and experimental facilities known as "J-PARC" and "SPring-8" to shed light on the nanoscale structures and dynamics within rubber, combined with the powerful supercomputer known as the "K computer", to perform advanced molecular dynamics simulations. This new technology, called "ADVANCED 4D NANO DESIGN," is used currently to develop new rubber materials with superior wear-resistance performance.

In this report, we introduce the results of our recent research, conducted using ADVANCED 4D NANO DESIGN, through which we elucidated successfully the structures and dynamics of the polymer adsorbed to the filler surface, which is an internal rubber structure, believed to have a powerful effect on the overall tire performance.

2. Overview of Experiments

The neutron reflectivity is used to analyze the adsorbed polymer of the silica surface. It is difficult to examine the adsorbed polymer of the filler surface within bulk rubber. Thus, we used a silicon substrate as a model sample to simulate the silica within rubber. In this experiment, we took advantage of the fact that neutron scattering produces a pronounced contrast between hydrogen (protium) and deuterium by preparing samples of partially deuterated styrene-butadiene copolymer rubber, in which only the styrene component was replaced with deuterated styrene and then placing these samples on a silicon substrate using spin coating. The samples were then measured using SOFIA (BL16) and Motofit software [1] was used to perform model analysis of the resulting reflectivity data.

Quasi-elastic neutron scattering (QENS) was used to examine the polymer dynamics. These experiments were conducted using DNA (BL02) and AMATERAS (BL14). As DNA and AMATERAS have different capabilities in terms of measurable temporal and spatial ranges (for example, DNA can measure slower motion than AMATERAS), these two spectrometers were utilized in a mutually complementary manner. Samples with varying filler contents or filler interface modifications were prepared to study the effects of filler content and interface state on the polymer mobility in polymers and polymer composite materials.

Utilizing the neutron reflectivity method, we were able to examine the adsorption structure of the polymer adsorbed to the surface of silica depth-wise with high precision by substituting a silicon substrate for the silica surface. However, within actual tire rubber the silica forms particles. Thus, we utilized small-angle neutron scattering (SANS) to examine the structure of the polymer adsorbed to the silica interface within bulk rubber. Previous research has shown that, when toluene (a good polymer solvent) is added to crosslinked rubber, the polymer in the vicinity of the filler interface shows greater resistance to solvent swelling [2]. Thus, we added toluene to crosslinked rubber and then utilized SANS to measure the contents of the solvent in both silica-interface polymer and matrix rubber. These experiments were conducted using J-PARC TAIKAN (BL15). Because neutron scattering produces a pronounced contrast between hydrogen (protium) and deuterium, we used deuterated toluene for the experiments.

3. Results and Analysis

Figure 3 shows the reflectivity curve obtained through the neutron reflectivity experiments. The solid line on the left, which matches closely the experimental results, is the reflectivity curve, as derived from the scattering length density distribution profiles shown on the right. We found out that the scattering length density of the styrene-butadiene rubber increases in the vicinity of the SiO_2 surface (i.e. the oxide layer of the silicon substrate). The styrene-butadiene samples used in these experiments were composed of deuterated styrene and nondeuterated butadiene. We discovered that the styrene component of the rubber had a higher scattering length density when compared with the butadiene component. Thus, we can surmise that the increase in scattering length density around SiO_2 indicates that the styrene component of this styrene-butadiene copolymer has a distribution bias toward the silica interface. These results indicated that the styrene component of styrene-butadiene copolymers has strong interactions with the silica interface.

Next, we examined the effects of various silica filler contents and silica surface modifications on the mobility of the polymer in the vicinity of the silica interface. For these experiments, we prepared rubber samples with varying silica filler contents, as well as samples with a fixed silica filler content and various silica surface modifications, before using QENS to examine the mobility of the polymer in the samples.

Figure 4 shows an example of the results of our QENS measurements of silica-compounded rubber using AMATERAS. Since hydrogen atoms possess a large incoherent scattering cross section, we can view these results as measuring motion derived from the hydrogen contained in the polymer component of the rubber samples. We then performed data fitting based on the sum of a single delta function (solid black line) and two Lorentzian functions (blue and pink solid

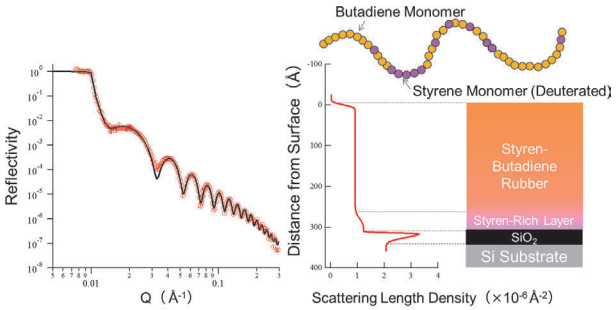

Figure 3. Neutron reflectivity curve of styrene-butadiene rubber on a silicon wafer. The solid curve indicates reflectivity, as derived from the model scattering length density distribution profiles shown on the right.

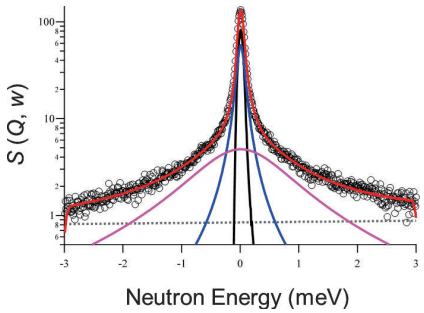

Figure 4. Quasi-elastic neutron spectra of silica-filled rubber.

lines). The result of this data-fitting calculation is the solid red line, which closely reflects our experimental results. Using this model, we were able to derive the relaxation rate. We also utilized the same type of model to analyze QENS measurement results from samples with varying silica filler contents or surface modifications.

Figure 5 shows the variation in relaxation times with varying silica filler rates within rubber, as measured in our QENS experiments. These results indicate that the polymer motion does not simply decelerate in proportion to filler content, but it rather accelerates upon reaching a certain filler content. In addition, when we examined the effects of various silica surface modifications on relaxation time, we found that the polymer mobility could be controlled by altering the silica surface modification. Further, when we analyzed the elastic scattering component of our QENS measurements to examine the amount of polymer bound to the silica surface, we found out that altering the modification also resulted in changes in the amount of the bound polymer. In other words, we have discovered that both interactions between styrene and silica and the mobility of proximate polymer can be controlled through silica surface modifications.

We then utilized SANS to investigate the thickness of the polymer adsorbed to the filler surface as one of the physical properties related to the amount of bound polymer. The results of these SANS experiments revealed that the thickness of the polymer adsorbed to the filler surface was extremely thin, at

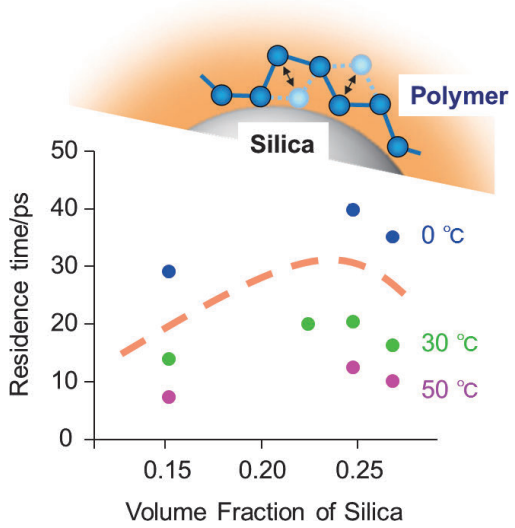

Figure 5. Dependence of the silica volume fraction on residence time in the silica-filled rubber.

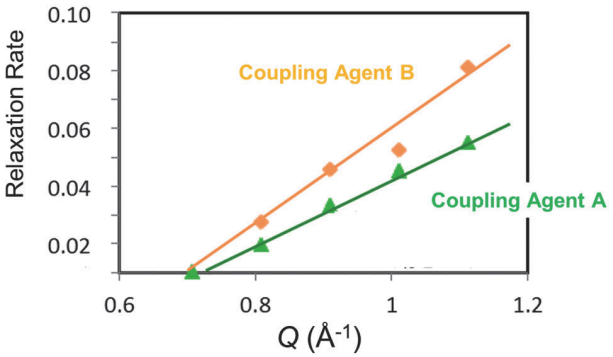

Figure 6. Relaxation times measured in the silica-filled rubber.

just a few nanometers, in polymer that is resistant to solvent swelling, indicating that it is important to analyze not only the structures, but also the mobility of the polymer.

Currently, research analyzing the structures and mobility of the polymer adsorbed to the filler surface using NSE [3] is beginning to shed light on the relationship between the structure of the polymer adsorbed to the silica interface (as understood through analysis of solvent swelling using SANS) and polymer mobility (as understood using QENS).

Then we utilized the K computer to perform large-scale molecular simulations based on the structure and mobility data obtained from the described experiments. Thanks to these simulations, we were able to elucidate the causes behind the various forms of stress and heat generation that occur within rubber during deformation. Further, from simulation studies of various new material designs developed to reduce rubber internal stress, we used SPring-8 BL20B2 to perform 4D-CT scanning with high spatial resolution to analyze the breaking resistance of rubber samples. These experiments allowed us to prove that the rubber samples with the best ability to reduce internal stress were the same as the ones that were able to suppress the formation of voids, which is one of the causes of tire wear.

We have already found practical applications for the results of the described research, incorporating our findings into the development of our ENASAVE NEXT II fuel-efficient tires, which have achieved a 51% improvement in wear-resistance performance, compared with the previous generation of tires, while maintaining the same high level of fuel-efficiency (environmental) performance and grip (safety) performance.

Acknowledgements

The authors would like to thank the following people and organizations for their immense and invaluable assistance in carrying out this research: Dr. K. Nakajima, Dr. K. Shibata, Dr. S. Kawamura, Dr. T. Kumada and Dr. D. Yamaguchi of the Japan Atomic Energy Agency's J-PARC Center; Dr. N. L. Yamada of the High Energy Accelerator Research Organization's Institute of Material Structures Science; Dr. T. Tominaga, Dr. T. Yamada, Dr. S. Takata, Dr. K. Ohishi and Dr. J. Suzuki of the Comprehensive Research Organization for Science and Society; Professor S. Koizumi and Dr. Y. Noda of Ibaraki University, Associate Professor T. Koga of the State University of New York; and Photon and Quantum Basic Research Coordinated Development Program "Fundamental Understanding of 'Wear' and 'Lubrication' through Coordination of Neutrons and Muons" Project.

References

[1] A. Nelson. Journal of Applied Crystallography (2006), 39, 273-276.

[2] M. Takenaka et al., Macromolecules (2009) 42 308-311.

[3] N. Jiang et al., Macro Letters (2015) 4 838-842.

T. Masui and H. Kishimoto

Chemical Analysis Center, Research & Development HQ. SUMITOMO RUBBER INDUSTRIES, LTD.

Hydrogen/Deuterium Dynamics in Kagome Hydroxyl Salts $Co_2(OH)_3Cl/Co_2(OD)_3Cl$

The hydroxyl salts $M_2(OH)_3X$, where M represents a d-electron magnetic ion and X represents a halogen ion have been known for a long time. These hydroxyl salts, specifically the ones that crystallize in deformed pyrochlore structures, have recently attracted attention because they were found to be geometrically frustrated magnets exhibiting intriguing magnetic properties due to the competing interactions on the geometric configurations. Furthermore, simultaneous changes in their unit cell lengths and dielectric constants occurred at their respective magnetic transition temperatures T_N, demonstrating universal magneic-lattice-dielectric couplings in these hydroxyl salts [1]. Of particular interest is the finding of apparent ferroelectric responses in the deuterated hydroxyl salts of high crystal symmetries, i.e., rhombohedral $Co_2(OD)_3Cl$ and $Co_2(OD)_3Br$, at temperatures (220-230 K) much higher than their T_N [1]. However, the mechanism for the ferroelectricity is still unclear, and there are very few experimental resources that are capable of detecting the hydrogen dynamics.

On this background, we performed a comparative muon-spin-relaxation (μSR) study on $Co_2(OH)_3Cl$ and $Co_2(OD)_3Cl$ to explore the idea that μSR could "see" the dynamics of deuterium or hydrogen atoms through probing the fluctuation of their nuclear fields. This is enabled by the fact that the majority of the positive muon should form a steady water-like combination with the hydroxyl OD^-.

Polycrystalline $Co_2(OD)_3Cl$ and $Co_2(OH)_3Cl$, as synthesized from hydrothermal reaction of NaOD/NaOH and $CoCl_2$, was used for the μSR experiments at the J-PARC as well as RIKEN-RAL Muon Facility of the Rutherford Appleton Laboratory, Didcot, UK. The powder samples of $Co_2(OD)_3Cl$ and $Co_2(OH)_3Cl$, respectively, were pressed into a pellet 3 cm in diameter and 1 mm thick, and then tightly covered with a 25-μm thick high-purity silver foil and mounted to a sample-holder. A double-pulsed positive surface muon beam was used with the temperature controlled by a standard He-4 gas flow cryostat.

Examples of μSR spectra at two typical temperatures for $Co_2(OD)_3Cl$ under zero-field (ZF) and longitudinal-field (LF), are given in Fig. 1. Although $Co_2(OD)_3Cl$ showed magnetic transition at T_C = 10.5 K, the μSR experiments revealed magnetic couplings at much higher temperatures. The ZF-μSR spectrum consists of Kubo-Toyabe relaxation or dynamic Kubo-Toyabe relaxation due to the nuclear fields of D and Cl nuclei, and exponential relaxations due to the magnetic spins of Co^{2+}. For example, for $Co_2(OD)_3Cl$ at 215 K, a longitudinal field of 100 G eliminated the Kubo-Toyabe relaxation due to the nuclear fields, thus only the exponential relaxations remained (Fig. 1a). Meanwhile, the dynamics of the nuclear field at 271 K are apparently different from those at 215 K (Fig. 1b). Therefore, by analyzing the ZF-μSR and LF-μSR spectra, the distribution of the nuclear fields and their dynamic change with temperature, i.e., the dynamics of the deuteriums on the lattice of $Co_2(OD)_3Cl$ at various temperatures, can be estimated.

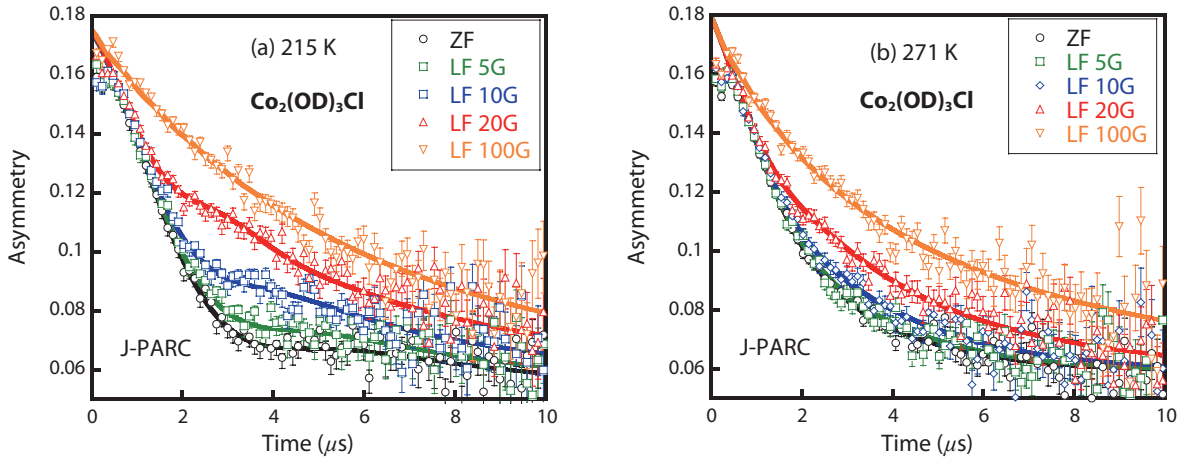

Figure 1. An example of the μSR spectra under zero-field and longitudinal fields for $Co_2(OD)_3Cl$ at 215 K and 271 K, respectively, showing the change in the dynamics of nuclei. The solid lines are fitted according to Eq. (1).

We found that the ZF-μSR spectra can be precisely fitted by a physical model assuming two muon stopping sites near the (OD)/(OH) and Cl, as illustrated in Fig. 1. In detail, the amplitude of muon spin polarization, $A(t)$, can be expressed by

$$A(t) = A_1 \exp(-\lambda_1 t) G_z^{\mathrm{DKT}}(t, \Delta_1, \nu) + A_2 \exp(-\lambda_2 t) G_z^{\mathrm{KT}}(t, \Delta_2) \quad (1)$$

Here, the first term is for the [OH/OD]-site muons given by a combination of an exponential relaxation due to the magnetic field of Co^{2+}, and a Dynamic Kubo-Toyabe function due to dynamically fluctuating dipolar moments, where Δ_1 represents the line width determined by the nuclear dipolar fields, and ν its fluctuation rate. The second term is for the Cl-site muons given by a combination of the exponential magnetic relaxation and a static Kubo-Toyabe function due to the quasistatic Cl nuclei.

The most interesting result was reflected in the temperature dependence of the fluctuation rate ν, as is seen in Fig. 2. In the paraelectric phase near room temperatre, the nuclei of D/H fluctuated quickly with a rate of several MHz. For $Co_2(OD)_3Cl$, ν rapidly decreased and showed a critical slowing down following with $T_c = T_\varepsilon =$ 230 K. Therefore, the deuterium atoms were violently fluctuating at the paraelectric state, then they drastically slowed down toward the ferroelectric transition. On the other hand, the hydrogen atoms in $Co_2(OH)_3Cl$ showed a similar critical slowing toward $T_c = 210$ K. One evidence adding credit for the fitting was that being revealed in the inset plot of Fig. 2, wherein the ratio of the fluctuation rates for the hydrogen and deuterium atoms in $Co_2(OH)_3Cl$ and $Co_2(OD)_3Cl$ is plotted versus the temperature. At temperatures above 280 K, the ratio was almost equivalent to a square root of their mass ratio,

$$\text{i.e.,} \quad \frac{\nu_H}{\nu_D} \approx \sqrt{\frac{m_D}{m_H}} = \sqrt{2}.$$

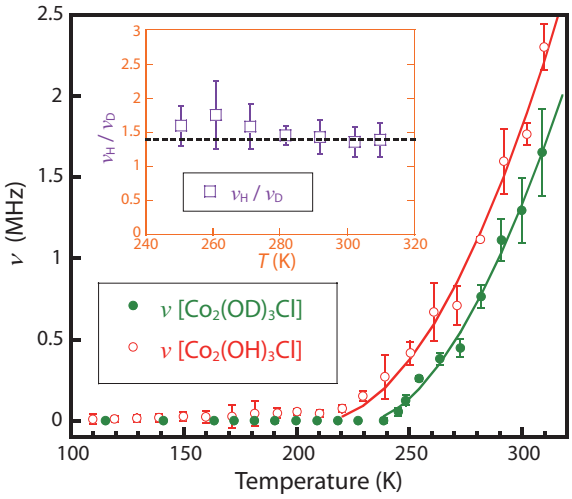

Figure 2. Temperature dependence of the fluctuation rates ν of the nuclear fields for $Co_2(OD)_3Cl/Co_2(OH)_3Cl$. The thin solid lines are fitted curves according to the formula $\nu = \nu_0 (\frac{T}{T_c} - 1)^{1.8}$ with $T_c = 230$ K and 210 K, respectively, for $Co_2(OD)_3Cl$ and $Co_2(OH)_3Cl$.

This strongly suggests the validity of the present analysis. Therefore, although some imperfectness remained with the fitting function in Eq. (1), it fairly well described the dynamics and the critical slowing of the hydrogen and deuterium atoms in the present system. The critical slowing of the quantum atoms, however, may involve more complicated processes, like those occurred in the proton-ferroelectric KH_2PO_4 (KDP) [2].

In summary, the present study has revealed that the newly-identified ferroelectric response in the geometrically frustrated magnet $Co_2(OD)_3Cl$ occurs with a drastic change in the dynamics of the deuterium atoms. The present research supplemented by experiments of NMR and Raman spectroscopic investigations has been published in a recent paper [3].

References

[1] X. G. Zheng *et al*., Phys. Rev. B **87** (2013) 174102 (1-8).
[2] S. Koval *et al*. Phys. Rev. Lett. **89** (2002) 187602; Phys. Rev. B **71** (2001) 184102.
[3] X. L. Xu *et al*., Phys. Rev. B **95** (2017) 024111 (1-10).

X. G. Zheng[1], X. L. Xu[1], I. Yamauchi[1], and I. Watanabe[2]
[1]*Department of Physics, Saga University;* [2]*Advanced Meson Science Laboratory, RIKEN Nishina Center for Accelerator-Based Science*

Behavior of Hydrogen as Simulated by μ^+ in Conductive and Functional Cement C12A7

Electric conductivity and optical transparency are often contradicting features in electric materials, as one can see that metals are shiny and optically nontransparent. Further, the low-work function (minimum energy for a photon to excite a photo-electron) and stability of the material in the air are often incompatible features, as it has been observed, most low work function materials, such as, alkaline metals or alkaline earth elements, are unstable due to high reactivity to air moisture.

Mayenite $Ca_{12}Al_{14}O_{33,}$ which has the same composition as 12 CaO (quick lime) and 7 Al_2O_3 (alumina), and is hence abbreviated as C12A7, is one of the rare examples of such incompatible features: it has low-work function (~2.4 eV being comparable to alkaline metals) as well as high stability in the air. These magical properties stem from the material's peculiar structure: C12A7 consists of a positively charged lattice framework (Fig. 1), which looks like a series of cages, and loosely bound oxide ions O^{2-} within the cage in the pristine insulator phase. The oxide ions are easily reduced by Titanium reducer to leave an electron in the cage. This material is, hence, a class of *electride,* in which single electron serves as an anion, a negatively charged species to balance the charge neutrality of the material, a role usually taken by negatively charged ions. Because of the light mass and quantum mechanical overlap of the extended wave function of electrons in the cage, this material becomes conductive after reduction. The low-work function occurs because of the loose binding energy of the *electride* electrons, and the stability is due to the strong cage structure of the lattice framework. The electrically contradicting features of this material are thus realized by the sharing of roles of the lattice structure and *electride* electrons [1].

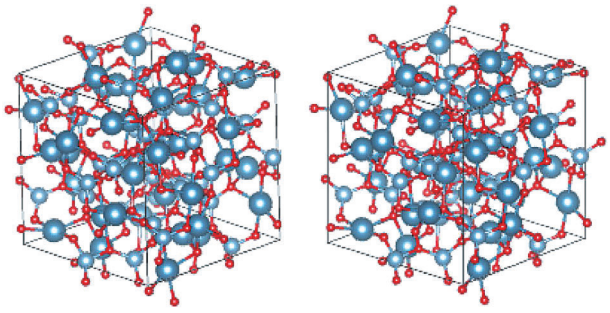

Figure 1. 3D representation of the crystal structure of C12A7 Mayenite in stereogram. Cages of Al-Ca-O are interconnected with each other. Ca, Al and O are represented as large dark gray, medium light gray, and small red spheres, respectively.

In 2012, Ruthenium loaded C12A7 was identified to have a catalytic activity for ammonia synthesis under much lower pressure and temperature than in the industrialized Haber-Bosch method [2]. Although the catalytic function occurs at the surface of Ruthenium, the C12A7 *electride* serves as an electron donor for the reaction mechanism and the cage structure for the temporal storage of hydride ions (H^-), which otherwise covers the Ruthenium surface to lose its catalytic function (hydrogen poisoning). In this context, to understand the functionality of C12A7, it is necessary to conduct a microscopic probe to clarify the behavior of the hydrogen, which may take positively charged H^+, neutral H^0 or negatively charged H^- states.

Beams of positive muons (μ^+) are employed to tackle this question; the muon is an elementary particle with sufficiently high intensity and spin polarization available at large accelerator facilities, such as, Materials and Life Science Experimental Facility (MLF) at J-PARC (Japan Proton Accelerator Research Complex), which makes it possible to use muon beams as a probe to investigate the materials' properties. Depending on the surrounding environment, a positive muon in a matter captures zero, one or two electrons to form the positively charged μ^+, neutral muonium Mu^0, or negatively charged Mu^- state, simulating the behavior of impurity hydrogen in the low-concentration limit. By spectroscopy, called muon spin relaxation (μSR), the three charged states are readily distinguished by observing the effective gyromagnetic ratio (the frequency vs. applied magnetic field ratio) to distinguish between Mu^0 and other charged states, and by high-field chemical shifts, between μ^+ and Mu^-.

Figure 2 shows the time evolution of the muon spin in C12A7, with nominally pure insulating composition [3]. The observed effective gyromagnetic ratio between the precession frequency and applied magnetic field is that for diamagnetic muons in charged states (μ^+ or Mu^-), rather than in the neutral state Mu^0. The sign of the chemical shift and doping dependence of the precession signals indicate that the muon takes a μ^+ state in the insulating C12A7, most likely the $[O–\mu]^-$ ($= O^{2-}–\mu^+$) complex with the oxide ion O^{2-} in the cage, whereas it transforms into the negatively charged state Mu^- as the electron doping proceeds by reduction (oxide ion removal) [3].

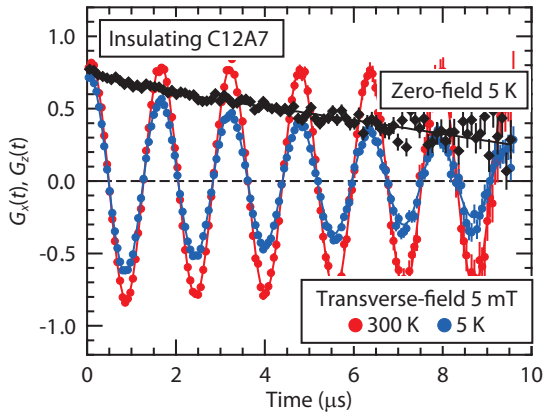

Figure 2. Time evolution of the muon spin in insulating C12A7 observed at a temperature of 300 and 5 K. The precession frequency for the applied transverse field (TF = 5 mT) exhibits the signature of charged muon states (μ^+ or Mu^-). For Mu^0 state, the frequency would have been 100 times faster [3].

To test the $[O–\mu]^-$ complex scenario in the insulating C12A7, the muon position was calculated within the framework of the density functional theory (DFT) for electrons. The calculation shows that the $[O–\mu]^-$ complex site is stable, and estimates the crystalline orientation dependence of the nuclear dipolar fields from Al (Fig. 3). A qualitatively identical orientation dependence was observed by the muon measurement, supporting the $[O–\mu]^-$ complex formation [3]. By combining calculation at the KEK supercomputer and muon measurement at MLF of J-PARC and other facilities (PSI in Switzerland and TRIUMF in Canada), the muon (= hydrogen) electronic and positional states in C12A7 functional material were clarified.

This work was supported by MEXT Elements Strategy Initiative to Form Core Research Center. The theoretical calculations were performed under the Large Scale Simulation Program No.14/15-13 (FY2014-2015).

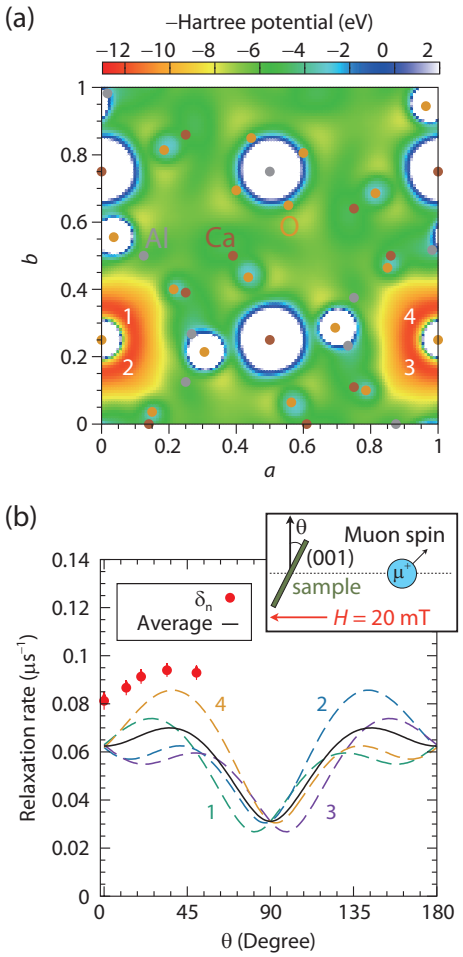

Figure 3. (a) Hartree potential calculation and stable muon positions (1-4) in insulating C12A7, and (b) comparison of the angle dependence for the muon spin relaxation rate between measurement (δ_n) and theory (lines).

References

[1] J. A. McLeod *et al.*, Phys. Rev. B85, 045204 (2008).
[2] M. Kitano *et al.*, *Nature Chem.* **4**, 934 (2012).
[3] M. Hiraishi *et al.*, Phys. Rev. B93, 121201(R) (2016).

M. Hiraishi[1], K. M. Kojima[1,2], M. Miyazaki[1], I. Yamauchi[1], H. Okabe[1], A. Koda[1,2], R. Kadono[1,2], S. Matsuishi[3], and H. Hosono[3,4]
[1]Muon Science Laboratory and Condensed Matter Research Center, Institute of Materials Structure Science, High Energy Accelerator Research Organization; [2]Department of Materials Structure Science, The Graduate University for Advanced Studies (Sokendai); [3]Materials and Structures Laboratory, Tokyo Institute of Technology; [4]Materials Research Center for Element Strategy, Tokyo Institute of Technology (MCES)

Chemical Environmental Effect on Negative Muon Capture by an Atom Targeted to Gaseous Simple Carbon Oxides: CO, CO_2

1. Introduction

Muonic atom is an atomic system, where a negative muon (muon) replaces an electron. When a muon is stopped in a substance, it can be captured by the Coulomb field of a nucleus and a muonic atom is formed. The captured muon's individual quantum state is like that of an orbital electron, and the muon is in a highly excited state right after the muonic atom formation. The captured muon immediately cascades down to muonic 1s state through characteristic X-ray (muonic X-ray) and Auger electron emissions (muon cascading process). The energies of the muonic X-rays are very high due to muon's heavy mass. The intensity of the muonic X-ray reflects the muon capture probability of the atom, and the X-ray structure reflects the initial quantum state (principal quantum number and angular momentum quantum number) of the captured muon. In this paper, such muonic atom formation is defined as direct capture.

In hydrogen containing system, very unique muonic atom formation is occurred. When a muon is stopped in hydrogen-containing substance, it is captured by a hydrogen atom, the only electron in the atom is replaced by the muon and a muonic hydrogen atom is formed. The muonic hydrogen atom can be regarded as a tiny electrically neutral particle due to the strong shielding effect of nuclear charge by the muon. In fact, the muonic hydrogen atom can diffuse in the substance easily like a neutron. The muonic hydrogen atom can penetrate an electron cloud without Coulomb repulsion and approach closely the nucleus of another atom. When the muonic hydrogen atom reaches the heavier nucleus ($Z > 2$), it transfers the muon to the deeper atomic levels of the nucleus (muonic Z atom is formed). This phenomenon is called muon transfer process. Since the energy potential of the Z atom (muon accepter) is more stable than that of the muonic hydrogen atom (muon donor), the muon transfer process progresses spontaneously.

It is known that the muon capture processes are strongly influenced by the structure of the muon capturing molecule. The muon capture probability of each atom (muon capture ratio) and the initial quantum state of the captured muon change drastically. For example, the muon capture ratio of boron atom to nitrogen atom for boron nitride with a cubic structure is 20% smaller than that of a hexagonal structure [1]. This is known as the chemical environmental effect on muon capture.

There are many studies related to muon capture phenomena, but the chemical environmental effects still have not been well investigated. Due to difficulties in the experimental method, most of the previous studies have targeted only high-density samples, such as solids, liquids and high-pressure gases. In such conditions, muon capture processes are quite complicated. Since the muon cascading process and the electron refilling process compete with each other in high-density materials, the muonic X-ray structure varies according to the sample density. In fact, a previous study reported that muonic X-ray structures are strongly influenced by sample's density (density effect) [2]. Unless the density effect is grasped precisely, the initial process of muon capture cannot be understood from the muonic X-ray structure.

To reveal the chemical environmental effect on muon capture, we focused on low-pressure (below 100 kPa) gases. In these conditions, we can simplify the muon cascading process. Our group previously performed muon irradiations of simple gaseous molecules containing nitrogen and oxygen atoms (NO, N_2O and NO_2) [3]. For this study, we chose molecules containing carbon and oxygen atoms (CO, CO_2) and their hydrogen mixture as muon irradiation samples.

2. Experimental

All muon irradiation experiments were performed at D1-Port, Muon Science Establishment (MUSE) in MLF. The experimental setup is shown in Fig. 1. Low-pressure sample gases (40 kPa CO, 20 kPa CO_2, 99 kPa H_2 + CO (1%), and 99 kPa H_2 + CO_2 (1%)) were put into a gas chamber and irradiated with low-momentum muon beam (18.8 MeV/c). Muonic X-rays were measured by germanium semi-conductor detectors. From a previous experiment [3], we determined the sample pressures that ignorable the density effect.

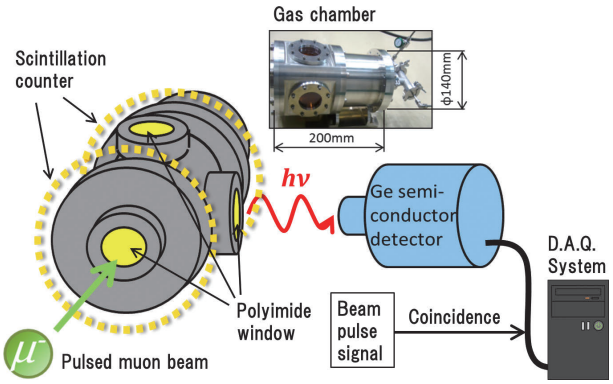

Figure 1. Schematic view of the setup for the muon irradiation experiment.

3. Results and discussions

Muonic X-ray spectra for CO and its hydrogen mixture (H_2 + CO) are shown in Fig. 2. A high-purity muon beam enabled us to obtain higher transition than K_γ X-rays.

The muonic X-ray structures (K_β/K_α, K_γ/K_α … X-ray intensity ratios to K_α) for muonic carbon, and muonic oxygen, are shown in Fig. 3. The initial energy level of the captured muon can be estimated from the muonic X-ray structures. In the case of direct muon captures for CO and CO_2, tremendous difference appears in the X-ray structure of the muonic carbon (Fig. 3 a). This result implies that the initial capture level of the muon is different between CO and CO_2. Whereas, in the case of the muon transfer from muonic hydrogen, muonic X-ray structures are almost the same between CO and CO_2 (Fig. 3 c, d). This result indicates that the molecular structure does not affect the initial quantum state of the muons captured by carbon and oxygen atoms via the muon transfer process.

The muon capture probabilities of carbon and oxygen atoms can be obtained from the total intensity of the muonic Lyman X-ray series of each atom, since the captured muon finally de-excites to muon 1s state. The experimental muon capture ratios per atom (*A(C/O)*) for CO, and CO_2 molecules are determined as shown in Table 1. In the case of direct muon capture, we found more than 30% difference in the muon capture ratios between CO and CO_2 [4]. Whereas, in hydrogen mixture samples, we found the muon capture ratio *A(C/O)* of CO to be similar to that of CO_2 [5].

From the result of muonic X-ray structure and muon capture ratio, we concluded the following: 1) The captured muon undergoes a different cascade process depending on whether it is acquired by direct capture or muon transfer, 2) In this experimental condition, the effect of the chemical environment on the muon transfer process is much smaller than on the direct muon capture process.

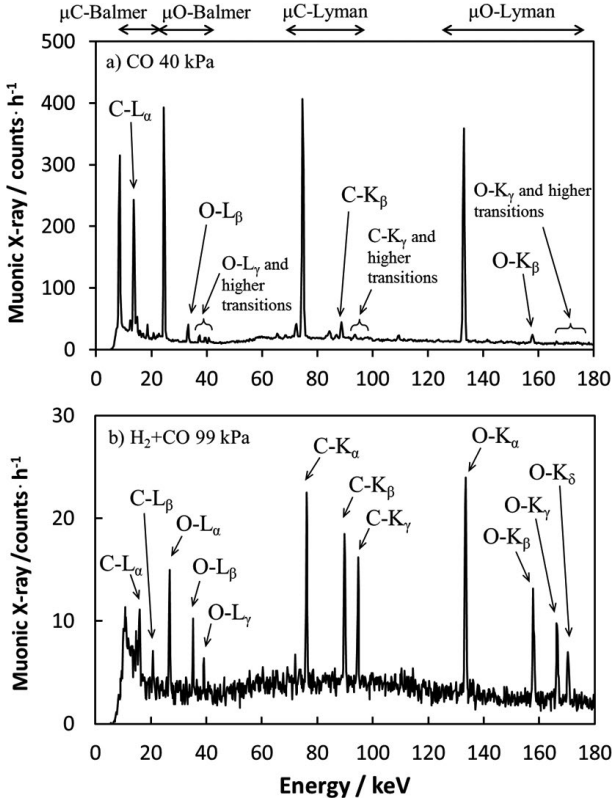

Figure 2. Muonic X-ray spectrum of a) CO 40 kPa, and b) H_2 + CO 99 kPa, obtained by germanium semiconductor detector measurement. Higher transition than K_γ X-rays are observed in both spectra. Spectrum (a) is reflected muon direct capture, spectrum (b) is reflected muon transfer.

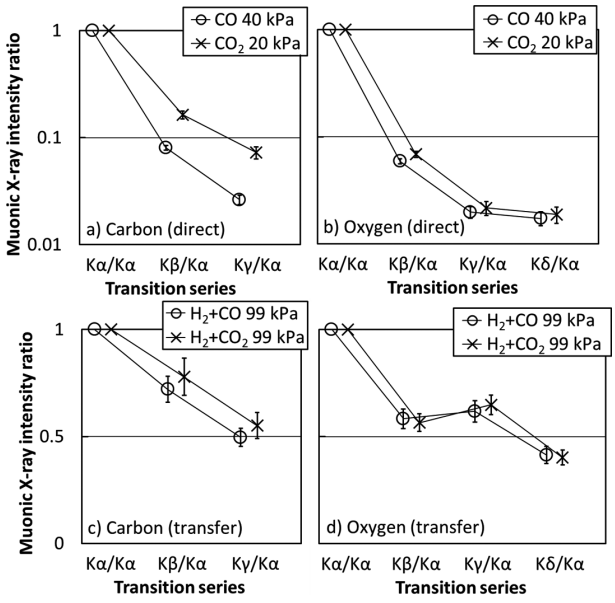

Figure 3. Muonic X-ray structure of CO and CO_2 sample. These graphs indicate the relative muonic X-ray intensity (per K_α) of each transition series. The tops of two spectra are reflected the direct capture and the vertical axis is log scale (a, b), the bottom two spectra reflect the muon transfer and the vertical axis is linear scale (c, d).

Table 1. Relative muon capture probability of carbon to oxygen atom (muon capture ratio). These values are corrected by the number of atoms in the molecule.

samples	A(C/O)
CO, 40 kPa	0.753 ± 0.021
CO, 20 kPa	0.549 ± 0.023
H_2 + CO (1%), 99 kPa	0.649 ± 0.032
H_2 + CO_2 (1%), 99 kPa	0.656 ± 0.036

4. Conclusion

We performed negative muon irradiation to low-pressure gaseous samples (40 kPa CO, 20 kPa CO_2, 99 kPa H_2 + CO (1%), and 99 kPa H_2 + CO_2 (1%)) at D1-port, MUSE, MLF, and determined the muon capture ratio of carbon atom to oxygen atom and the muonic X-ray structure of carbon and oxygen atoms. From the experimental result, we found that the captured muon undergoes a different cascade process depending on whether it is acquired by direct capture or muon transfer. Also, we realized that the effect of the chemical environment on the muon transfer process is much smaller than on the direct muon capture process.

5. Future Plans

The chemical environmental effect on muon capture has not been comprehended enough. We hope that our study will be an important milestone in revealing the chemical properties of the muonic atom, and will establish a whole new scientific field. Recently, we performed muon irradiation for COS and CS_2 gases, and their hydrogen mixture. We also found that the muon capture ratio per atom (A(S/C)) changed after the muons were captured by COS and CS_2 molecules via muon transfer. Such a trend has never been reported before, however, the results did not provide sufficient statistics to confirm it. We expect to obtain enough statistical data in the next experiment, and start the new discussion.

References

[1] H. Schneuwly, M. Boschung, K. Kaeser, G. Piller, A. Ruetschi, L. A. Schallcr and L. Schellenberg, Phys. Rev. A**27**, 950 (1983).

[2] K. Kirch, D. Abbott, B. Bach, P. Hauser, P. Indelicato, F. Kottmann, J. Missimer, P. Patte, R. T. Siegel, L. M. Simons and D. Viel, Phys. Rev. A**59**, 3375 (1999).

[3] K. Ninomiya, W. Higemoto, T. U. Ito, T. Nagatomo, P. Strasser, N. Kawamura, K. Shimomura, Y. Miyake, M. Kita, A. Shinohara, K. Kubo, and T. Miura, KEK-MSL Progress Report 2011 (2012) 31.

[4] G. Yoshida, K. Ninomiya, T. U. Ito, W. Higemoto, T. Nagatomo, P. Strasser, N. Kawamura, K. Shimomura, Y. Miyake, T. Miura, M. K. Kubo and A. Shinohara, J. Radioanal. Nucl. Chem. **303**, 1277 (2015).

[5] G. Yoshida, K. Ninomiya, M. Inagaki, W. Higemoto, N. Kawamura, K. Shimomura, Y. Miyake, T. Miura, M. K. Kubo, and A. Shinohara, Radioisotopes **65**, 113 (2016).

G. Yoshida[1,2], K. Ninomiya[2], M. Inagaki[2], T. U. Ito[3], W. Higemoto[3], P. Strasser[4], N. Kawamura[4], K. Shimomura[4], Y. Miyake[4], T. Miura[1], M. K. Kubo[5], and A. Shinohara[2]

[1]Radiation Science Center, KEK; [2]Graduate School of Science, Osaka University; [3]Advanced Science Research Center, Japan Atomic Energy Agency; [4]Muon science laboratory, Institute of Materials Structure Science, KEK; [5]College of Liberal Arts, International Christian University

Metastable Hydrogen Configurations in the $BaTiO_{3-x}H_x$ Oxyhydride Associated with Hydrogen Exchange and Transport

1. Introduction

Oxyhydrides of perovskite titanates $ATiO_{3-x}H_x$ (A = Ba, Sr, Ca) are a new class of hydrogen ion conductors, obtained from $ATiO_3$ by CaH_2 reduction [1-3]. O^{2-} ions in the perovskite lattice are randomly substituted by H^- ions without creating any detectable amount of vacancies. The substitutional hydridic hydrogen in $ATiO_{3-x}H_x$ is in sharp contrast with the established hydrogen configuration in $ATiO_3$, namely, interstitial protonic hydrogen H^+ bound to an O^{2-} ion. Macroscopic gas analysis revealed that the hydrogen in the solid phase is mobile and exchangeable in its gaseous environment at a relatively moderate temperature of 400°C. Furthermore, the CaH_2 reduction turns the parent band insulators into paramagnetic metals. These transport and hydrogen exchange characteristics make these materials potentially suitable for application in mixed electron/hydrogen ion conductors and hydrogen membranes.

Several theoretical models have been proposed on the stability of hydrogen ions in $ATiO_{3-x}H_x$ and their dynamics [4-8]. These studies consistently concluded that the most stable configuration is the substitutional H^- in an n-type carrier-rich environment. On hydrogen kinetics, two types of scenarios have been proposed. One is based on the idea of correlated migration of H^-, O^{2-}, and oxygen vacancy V_O in the network of the anion site (type-I hydrogen migration) [1,4], as illustrated in Fig. 1(a). The other model (type-II hydrogen migration) involves two metastable hydrogen configurations, as shown in Fig. 1(b). One is the interstitial H^+, which supports rapid proton diffusion [7]. The other is a hydrogen exchange center composed of two hydrogen atoms trapped in an oxygen vacancy, which forms as a result of the interaction between a substitutional H^- and an incoming interstitial H^+. Two charge configurations (hydridic $2H^-$ [6] and molecular H_2 [7]) were proposed on this center.

In contrast to the theoretical advancements, the experimental insights into the mechanisms of hydrogen transport and exchange in $ATiO_{3-x}H_x$ are still quite limited. Here we report microscopic insights from the μ^+ spin rotation and relaxation (μ^+SR) method on metastable hydrogen configurations related to the type-II hydrogen migration in a prototypical $BaTiO_{3-x}H_x$ compound.

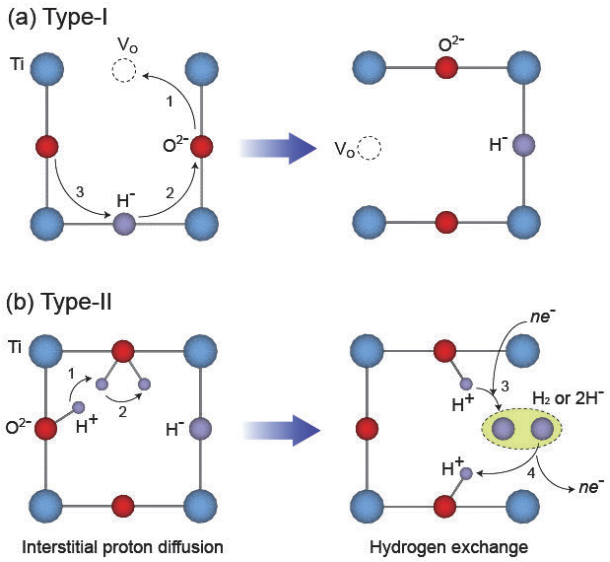

Figure 1. Schematic illustrations of (a) the type-I and (b) the type-II hydrogen migration models. The conversion between the interstitial H^+ and the hydridic $2H^-$ in (b) involves an electron capture and release (n = 2).

2. Experimental Insights into the Type-II Hydrogen Migration Mechanism from μ^+SR

μ^+SR measurements on powder samples of $BaTiO_{3-x}H_x$ (x = 0.1, 0.2, 0.3 and 0.5) were carried out in the D1 area of J-PARC MUSE, Japan, and in Port 2 of RIKEN-RAL, U.K., using a 4-MeV surface muon beam. Spin-polarized positive muons implanted into a solid lose their kinetic energy by electromagnetic interactions with the host atoms and are then trapped in local potential minima, not necessarily at the global minimum. The electronic structures of muonium (a hydrogenlike μ^+-e^- bound state: Mu) and its ionized species Mu^+ and Mu^- in matter are supposed to be very similar to those of hydrogen. The as-implanted mixture of Mu states is far from equilibrium and can involve metastable excited states. In $BaTiO_{3-x}H_x$, implanted muons are expected to behave as incoming excess hydrogen and mimic excited configurations involved in the type-II hydrogen migration model together with H^- in the host lattice.

Figure 2(a) shows the time evolution of muon spin polarization $P(t)$ at 15 K in zero applied field (ZF) for the x = 0.5 and x = 0.3 samples. The time scale of muon spin relaxation indicates that it is mainly caused by quasistatic magnetic interactions between muons in

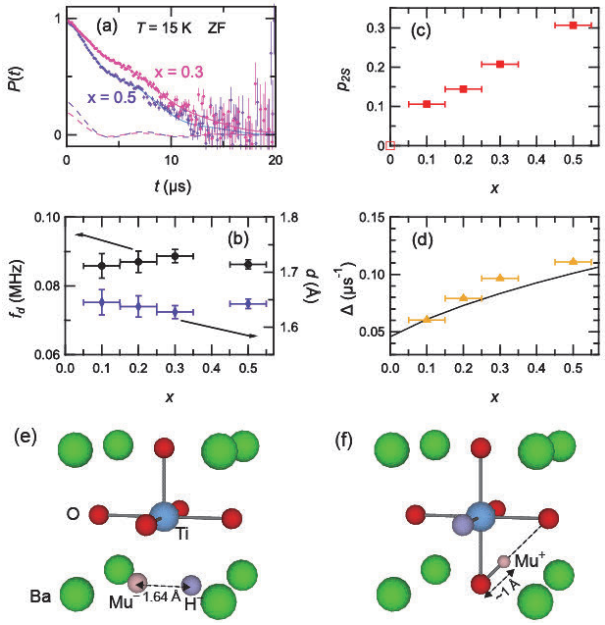

Figure 2. (a) ZF-μ⁺SR spectra of the $x = 0.5$ and 0.3 samples at 15 K. The solid curves show the best fits to the relaxation function in Ref. [9]. Partial contribution from the oscillating component is displayed by the dashed curves. (b, c, d) x dependences of f_d and d, p_{2S}, Δ at 15 K in ZF. (e, f) The most probable atomic configurations associated with the oscillating component and the Gaussian component. In the model (f), O^{2-} at the third nearest neighbor and further anion sites is randomly replaced by H^- with a probability of $x/3$.

diamagnetic environment (Mu^+ or Mu^-) and surrounding nuclei. The $P(t)$ curves have a damped cosine-like feature superposed on a Gaussian relaxation curve. The oscillating signal is a signature of the formation of an entangled two spin-1/2 system with a ^{1}H nuclear spin that is placed very close to the muon. On the other hand, the Gaussian relaxation curve is usually ascribed to muons that interact with a large number of surrounding nuclei without creating such a special magnetic coupling. The two components were tentatively assigned to the metastable configurations involved in the type-II model: the oscillating component for the hydrogen exchange center and the Gaussian component for interstitial Mu^+, as illustrated in Fig. 2(e) and (f), respectively. ZF spectra at 15 K were analyzed based on this picture [9] and the x dependence of fitting parameters were obtained, as shown in Fig. 2(b, c, d). f_d is a characteristic frequency of the oscillating component, which is a function of the distance d between a muon spin and a strongly coupled ^{1}H spin. Its average length of 1.64(1) Å agrees well with the theoretical H-H distances of 1.67 and 1.64 Å for hydridic $2H^-$ centers in $SrTiO_{3-\delta}$ [5], which have a slight difference in their local structure. This agreement suggests that a hydridic (Mu^-, H^-) configuration is more likely than a molecular MuH one with $d = 0.74$ Å. A linear increase in the fraction of the two-spin component p_{2S} with the oscillating feature consistently supports this picture. Δ is a Gaussian relaxation rate for the interstitial Mu^+ component. The x dependence of Δ is reproduced well with a numerical calculation of the root-mean-square width of the nuclear dipolar field at the interstitial Mu^+ site, as shown in Fig. 2(d) with a solid curve.

We also investigated temperature dependences of these parameters for the $x = 0.5$ sample up to 450 K and obtained evidence for interstitial Mu^+ diffusion and retrapping at a deep defect [9]. This retrapping process is not taken into account in the type-II hydrogen migration model and could be a rate-limiting step of macroscopic hydrogen transport in the $BaTiO_{3-x}H_x$ lattice.

3. Conclusion and Outlook

We investigated metastable hydrogen configurations associated with the type-II hydrogen migration mechanism in the $BaTiO_{3-x}H_x$ lattice by the μ⁺SR spectroscopy. Our experimental results are mostly in line with the theoretical proposal involving the hydridic $2H^-$ intermediate state, which would work as a hydrogen exchange center. On the other hand, our approach tells nothing about the type-I hydrogen migration in this compound. The μ⁻SR method, another branch of μSR using negatively charged muons, may give us an alternative way to challenge this issue because it enables to trace the diffusion of (muonic) oxygen ions closely connected to that of hydride ions.

References

[1] Y. Kobayashi *et. al.*, Nat. Mater. **11**, 507 (2012).
[2] T. Yajima *et al.*, J. Am. Chem. Soc. **134**, 8782 (2012).
[3] N. Masuda *et al.*, J. Am. Chem. Soc. **137,** 15315 (2015).
[4] X. Liu *et al.*, J. Mater. Chem. A **5**, 1050 (2017).
[5] Y. Iwazaki *et al.*, J. Appl. Phys. **108**, 083705 (2010).
[6] Y. Iwazaki *et al.*, APL Mater. **2**, 012103 (2014).
[7] J. Zhang *et al.*, J. Phys. Chem. C **118**, 17254 (2014).
[8] J. B. Varley *et al.*, Phys. Rev. B **89**, 075202 (2014).
[9] T. U. Ito *et al.*, Phys. Rev. B **95**, 020301(R) (2017).

T. U. Ito[1,2], A. Koda[2,3], K. Shimomura[2,3,4], W. Higemoto[1,2,5], T. Matsuzaki[6], Y. Kobayashi[7], and H. Kageyama[7]
[1]Advanced Science Research Center, JAEA; [2]Materials and Life Science Division, J-PARC Center; [3]Institute of Materials Structure Science, KEK; [4]RCNP, Osaka University; [5]Department of Physics, Tokyo Institute of Technology; [6]Advanced Meson Science Laboratory, RIKEN; [7]Graduate School of Engineering, Kyoto University

Application of Profile-Fitting Method to Neutron Time-of-Flight Protein Single Crystal Diffraction Data Collected at the iBIX

1. Introduction

The neutron time-of-fight (TOF) method uses pulsed neutrons with continuous wavelengths and is more efficient than the monochromatic method. The IBARAKI Biological Crystal Diffractometer (iBIX) at the Japan Proton Accelerator Research Complex (J-PARC), which is installed on BL 03 at the Materials and Life Science Experimental Facility (MLF) of J-PARC, is a neutron TOF single crystal diffractometer used mainly for elucidating the hydrogen, protonation, and hydration structures of biological macromolecules in various life processes [1, 2] (Fig. 1). The peak intensities of neutron diffraction from protein single crystals are relatively weak because neutron beam intensity is lower than X-ray synchrotron intensity, and proteins have lower crystallinity than organic or inorganic compound crystals. Thus, iBIX has installed a H_2 coupled moderator (CM). Some weak peaks are hidden under the error of strong background generated by strong incoherent scattering of hydrogen atoms in the protein crystals. Therefore, effective methods to determine accurate integrated intensities for weak peaks are essential for TOF neutron protein crystallography structural analysis. It has been demonstrated that the application of profile-fitting methods to monochromatic X-ray diffraction data can provide more accurate integrated intensities than summation-integration methods, especially for weak peaks. The profile-fitting method for the *x* and *y* detector positions has been implemented in monochromatic X-ray single crystal data processing software such as DENZO, MOSFLM, and XDS.

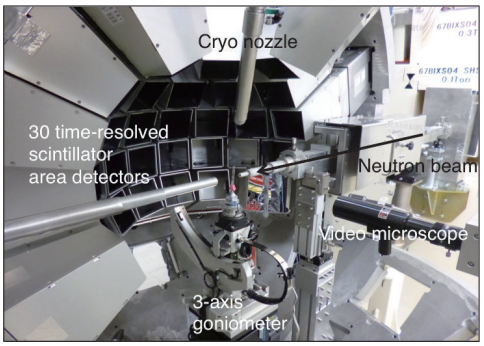

Figure 1. The inside view of iBIX. 30 two-dimensional detectors are installed. The active area of each detector is 133 × 133 mm and the distance from the sample to the detectors is 490 mm (Taken from Ref. [7]).

To the best of our knowledge, one example of applying profile-fitting methods in reciprocal space (*Q* space) to the TOF single crystal analysis involved TOPAZ, which is installed on BL 12 at the SNS with a poisoned decoupled moderator [3]. Because this case did not include protein single crystals measured using a diffractometer with a CM, the same fitting function could not be applied to the neutron diffraction data collected from the iBIX. Thus, we attempted to find an appropriate fitting function and develop a profile-fitting algorithm for the integration method applicable to the full set of TOF neutron protein diffraction data collected at the iBIX.

2. Evaluation of asymmetric fitting function

The TOF neutron diffraction data containing the spatial position and TOF for each neutron are converted to histogram data. The number of observed neutrons at *x*, *y*, and *t* corresponding to the horizontal and vertical detector positions (*x*, *y*) and a time-of-flight channel (*t*) are recorded. Because the number of observed neutrons at each pixel of the peak position of three-dimensional (3D) data was insufficient to fit the functions accurately, we used projections of the 3D peak in the direction of the TOF axis to improve the statistical precision. Because the pulsed neutron shape was asymmetric when using a CM, the projections of the 3D peaks in the direction of the TOF axis were also asymmetric. Thus, asymmetric functions had to be used in the profile-fitting method. In order to determine proper fitting functions for the TOF diffraction data, four asymmetric functions were evaluated using strong intensity peaks, with no overlapping, of TOF diffraction data from ribonuclease A collected at the iBIX. These were a Gaussian convolved with two back-to-back exponentials, a pseudo-Voigt function convolved with two back-to-back exponentials, a Gaussian convolved with the Ikeda–Carpenter function derived from TOF profile functions in the GSAS program suite [4], and a Gaussian convolved with the Landau function. It is important to predict the peak positions and estimate the background accurately to determine the integrated intensity, especially for weak peaks. All four asymmetric functions fit well with the strong intensity peaks and significant differences were not found (Fig. 2). In order to reduce

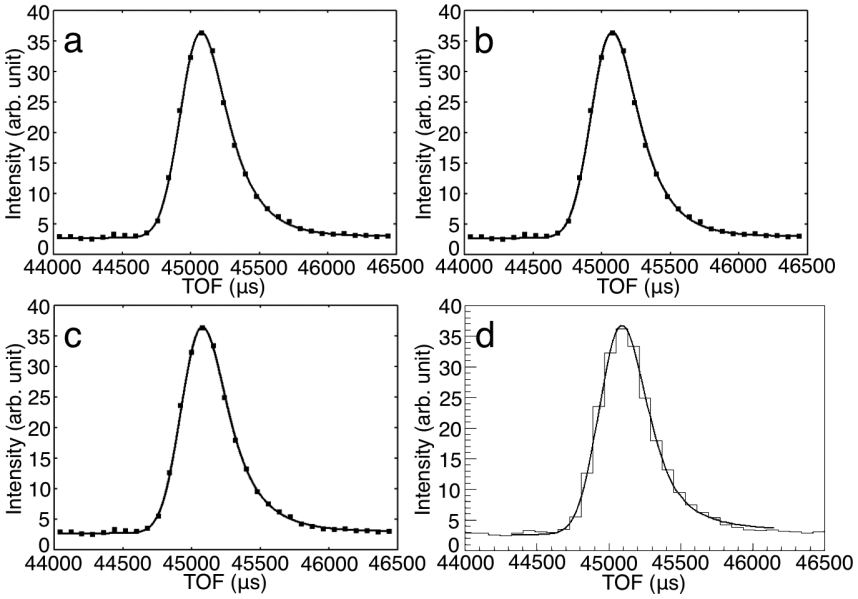

Figure 2. Profile-fitting to the *hkl* = –8 1 0 peak from ribonuclease A crystal using four asymmetric functions. (a) Gaussian convolved with two back-to-back exponentials fit. (b) Pseudo-Voigt function convolved with two back-to-back exponentials fit. (c) Gaussian convolved with Ikeda–Carpenter function fit. (d) Gaussian convolved with Landau function fit. In panels (a–c), SciPy was used to fit the functions and results were plotted by Gnuplot. In panel (d), because Gaussian convolved with Landau function contains convolution part in the equation, ROOT was used to fit the function and plot the results. Both four points of the outside regions of the integration region were used as the background region (Taken from Ref. [7]).

the processing time and the number of parameters, the Gaussian convolved with two back-to-back exponentials was selected as the most suitable fitting function and used in the profile-fitting method. This function is analytical and has five parameters: A, α, β, σ, and T_{ph}.

3. Implemented fitting function in profile fitting

Further details on the fitting function and its parameters are provided as follows.

$$H(\Delta T) = \int G(\Delta T - \tau) E(\tau) d\tau$$
$$= AN[e^{u}\, erfc(y) + e^{v}\, erfc(z)]$$

where

$$erfc(x) = \frac{2}{\sqrt{\pi}} \int_{x}^{\infty} e^{-t^2}\, dt.$$

$erfc(x)$ is an intrinsic function of the scipy.special package in SciPy.

Here,

$$E(\tau) = 2Ne^{\alpha\tau} \quad \text{for } \tau < 0 \quad \text{and} \quad E(\tau) = 2Ne^{-\beta\tau} \quad \text{for } \tau > 0,$$

where α and β are the rise and decay coefficients for the exponentials. A is an intensity scale parameter. The original function without A is normalized, and the integrated function area is 1. A refers to the integrated function area. The normalization factor, N, is

$$N = \frac{\alpha\beta}{2(\alpha + \beta)}$$

The Gaussian function is

$$G(\Delta T - \tau) = \frac{1}{\sqrt{2\pi\sigma^2}} \exp\left[-\frac{(\Delta T - \tau)}{\sqrt{2\sigma^2}} \right],$$

and the Gaussian variance is the coefficient σ^2.

The coefficients u, v, y, and z are

$$u = \frac{\alpha}{2}(\alpha\sigma^2 + 2\Delta T),\ v = \frac{\beta}{2}(\beta\sigma^2 - 2\Delta T),$$

$$y = \frac{\alpha\sigma^2 + \Delta T}{\sqrt{2\sigma^2}},\ \text{and}\ z = \frac{\beta\sigma^2 - \Delta T}{\sqrt{2\sigma^2}}.$$

ΔT is the difference in TOF between the peak position, T_{ph}, and the profile point, T.

$$\Delta T = T - T_{ph}$$

The parameters α, β, and σ are related to the function profile and are not independent of each other.

4. Correlation between fitting function parameters related to profile and TOF

Two conditions for which the profile-fitting method was accurate were proposed [5]. Firstly, peak positions can be accurately predicted. Recently, detector parameters (distance between each detector and sample, detector position angles, etc.) and 3-axis goniometer offset angles were accurately calibrated and accuracy of peak position prediction was clearly improved. So, the first condition was satisfied. Secondly, peaks located within a region of reciprocal space or detector space have the same profile. This is the key assumption when determining weak peak profiles. A projection profile in the

direction of the TOF axis mainly depends on the TOF, scattering direction, and crystal orientation with respect to the beam. The active area of each detector is 133 × 133 mm and the distance from the sample to the detectors is 490 mm. The maximum scattering angle difference among peaks within a detector is approximately 15°. iBIX contains 30 detectors and each of them measures different scattering angles. Because the maximum scattering angle difference among peaks within a detector is approximately 15°, we assumed that peak profiles at one crystal orientation and one detector change depending only on TOF. To prove this assumption, we investigated whether there is a correlation between fitting function parameters related to profile and TOF. The parameters α, β, and σ are related to the profile. In order to reduce the parameter error values, α was fixed to a proper value and the A, β, σ, and T_{ph} parameters were calculated by non-linear least square minimization. Peaks whose $I/\sigma(I)$ were over 5 and with lower parameter errors were selected and the β and σ parameter values were plotted against TOF at one crystal orientation and one detector. The result from the detector whose $2\theta_{center}$ is 51° at one crystal orientation is shown in Fig. 3 as an example. The overall tendency regardless of detectors and crystal orientations is that β and σ are almost linearly dependent on TOF. Adjacent TOF peaks have similar β and σ values. Because β and σ are parameters related to profile shape, these plots show that adjacent TOF peaks have the same profile. Additionally, the maximum scattering angle difference among peaks within a detector is approximately 15°, so adjacent TOF peaks are located within a region of reciprocal space or detector space. We could confirm that the conditions of the profile-fitting method are satisfied. The weaker peaks with adjacent TOF have larger parameter errors and the variances of β and σ in these peaks tend to be larger. To determine β and σ of weak peaks more accurately, adjacent TOF and accurate peaks were selected based on $I/\sigma(I)$, peak intensity, and parameter errors. Accurate peaks with larger TOF occasionally do not have similar β and σ values to Fig. 3a. Because there are few weak peaks adjacent to those peaks, we do not think this circumstance has a negative effect on determination of the weak peak profiles.

5. Application of profile-fitting method to a full set of protein neutron diffraction data

We developed a test program and applied it to a full set of ribonuclease A neutron diffraction data with non-overlapping peaks. The program could fit asymmetric functions to weak peaks as well as strong ones. Intensity statistics, with peaks $I/\sigma(I)$ larger than 0, were calculated using the iBIX data processing software STARGazer program [6], and joint refinements of neutron and X-ray data were carried out using the PHENIX program. In order to evaluate the algorithm utility, the intensity and refinement data statistics of the profile-fitting method were compared to those of the summation-integration method implemented in STARGazer by using the same integration regions, peaks and initial refinement model.

A summary of the intensity data and refinement results of ribonuclease A is provided in Tables 1. More observed reflections could be used in the profile-fitting method than in the summation-integration method. This implies that the accuracy of a part of the negative intensity peaks on the summation-integration method was improved by the profile-fitting method. The higher the resolution, the lower the data quality indices R_{merge}, R_{pim}, R_{work}, and R_{free} were on the profile-fitting method than on the summation-integration method. The greatest improvement in R_{merge}, R_{pim}, R_{work}, and R_{free} was observed in the highest resolution shell. The differences were 9.5%, 6.8%, 2.3%, and 1.7%, respectively. Because higher resolution shells contain a higher percentage of weak peaks, it was shown that the profile-fitting method is effective

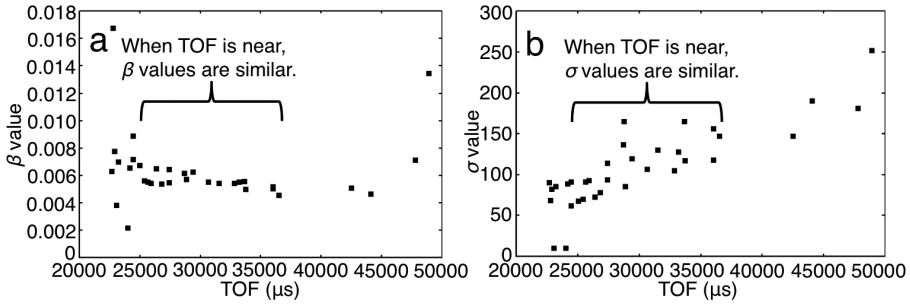

Figure 3. Plots of parameters related to the peak profile against TOF in ribonuclease A neutron diffraction data. The peaks whose $I/\sigma(I)$ is over 5 and obtained by one detector located at 51° in $2\theta_{center}$ and one crystal orientation were used. (a) Plot of parameter β against TOF. The peaks whose β errors are less than 1 were used. (b) Plot of parameter σ. The peaks whose σ errors are less than 10000 were used (Taken from Ref. [7]).

Table 1. Statistics of neutron intensity data and X-ray and neutron joint refinement of ribonuclease A (Taken from Ref. [7]).

Neutron data collection

Space group	$P2_1$							
Cell dimensions of a(Å), b(Å), c(Å), β(°)	30.29, 38.65, 53.36, 105.30							
	Observed reflections		Independent reflections		R_{merge}		R_{pim}	
Resolution (Å)	Profile fitting	Summation integration	Profile fitting	Summation integration	Profile fitting	Summation integration	Profile fitting	Summation integration
15.45 – 3.44	5,696	5,479	1,525	1,518	0.083	0.081	0.047	0.047
3.44 – 2.73	7,128	6,888	1,575	1,575	0.083	0.083	0.042	0.043
2.73 – 2.39	7,825	7,603	1,602	1,600	0.093	0.099	0.046	0.050
2.39 – 2.17	7,763	7,514	1,567	1,565	0.113	0.118	0.055	0.058
2.17 – 2.02	7,703	7,461	1,557	1,557	0.139	0.151	0.068	0.074
2.02 – 1.90	7,409	7,196	1,555	1,555	0.160	0.192	0.081	0.097
1.90 – 1.80	6,985	6,733	1,577	1,572	0.194	0.244	0.103	0.133
1.80 – 1.72	6,174	5,931	1,554	1,545	0.206	0.259	0.117	0.150
1.72 – 1.66	5,496	5,296	1,515	1,508	0.250	0.327	0.151	0.209
1.66 – 1.60	5,244	5,048	1,492	1,482	0.280	0.375	0.180	0.248
15.45 – 1.60	67,423	65,149	15,519	15,477	0.114	0.127	0.060	0.068

X-ray and neutron joint refinement

	No. of reflections (work / test)		R_{work}		R_{free}	
Resolution (Å)	Profile fitting	Summation integration	Profile fitting	Summation integration	Profile fitting	Summation integration
15.37 – 2.88	2,478 / 130	2,472 / 128	0.180	0.179	0.210	0.211
2.88 – 2.29	2,517 / 133	2,514 / 133	0.176	0.174	0.222	0.219
2.29 – 2.00	2,503 / 141	2,502 / 141	0.147	0.152	0.174	0.183
2.00 – 1.82	2,465 / 169	2,462 / 169	0.157	0.168	0.189	0.210
1.82 – 1.69	2,442 / 119	2,431 / 118	0.167	0.180	0.209	0.222
1.69 – 1.60	2,293 / 114	2,280 / 112	0.181	0.204	0.253	0.270
15.37 – 1.60	14,698 / 806	14,661 / 801	0.170	0.175	0.207	0.213

* Cell constants were calculated from X-ray diffraction data.

with weak peaks, as in previously reported results. R_{merge}, R_{pim}, R_{work}, and R_{free} in the overall resolution range were slightly improved over the summation-integration method. On the other hand, as peak intensities are stronger and background counts are relatively lower in the lower resolution shell, it seems that there is hardly any difference of R_{merge}, R_{pim}, R_{work}, and R_{free} between the profile-fitting method and summation-integration method.

In this study, we demonstrated for the first time that the profile-fitting technique is also applicable to comparatively weak peaks and high-background TOF neutron protein diffraction data using a CM, and that the technique could improve data statistics [7].

The integration component with the profile-fitting method has already been implemented in STARGazer and its user manual has been updated. The software and its manual are available for distribution to the iBIX users.

6. Future plans

In the future, the accelerator power of J-PARC will be increased to 1000 kW, and we will be able to collect single crystal neutron diffraction data for larger unit cell crystals, including membrane proteins. Because iBIX was designed to measure samples with unit cells up to approximately 135 Å, problems caused by overlapping of adjacent peaks are expected. To solve those problems, we are attempting to apply the profile-fitting technique to separate overlapped peaks in the TOF direction.

References

[1] Tanaka, I. et al., Acta Cryst. D66, 1194-1197 (2010).
[2] Kusaka, K., et al., J. Synchrotoron. Rad. 20, 994-998 (2013).
[3] Schultz, A. J. et al., J. Appl. Cryst. 47, 915-921 (2014).
[4] Larson, A. C. & Von Dreele, R. B., Los Alamos National Laboratory Report LAUR. 86-748 (2004).
[5] Pflugrath, J. W. Acta Cryst. D55, 1718-1725 (1999).
[6] Ohhara, T. et al., Nucl. Instr. Meth. Phys. Res. A600, 195-197 (2009).
[7] Yano, N. et al., Sci. Rep. 6, 36628 (2016).

N. Yano, T. Yamada, and K. Kusaka
Frontier Research center for Applied Atomic Sciences, Ibaraki University

Neutron Source

Progress of Neutron Source Section

In fiscal year 2016, the important task of the Neutron Source Section was to overcome two serious problems that occurred in the previous year. The first task was to restore the performance of the cryogenic hydrogen system for the moderators by taking proper measures against abnormal increase of the differential pressure at the heat exchangers and the adsorber of the helium refrigerator. The second was to fabricate a neutron production target vessel with robust structure capable to withstand the thermal stress due to the repetitive beam trip during the operating period.

As it is described later, the fabrication of the target vessel took more time to assure the feasibility of the new fabrication method and welding condition through various mock-up tests. This forced us to extend the use of the target vessel, which has been operated since February 2016. Considering that the current target vessel does not have the gas micro-bubbles injection system to suppress the pitting damage, the beam power was lowered from 200 kW to 150 kW after the summer shutdown period to ensure reliable neutron production while extending the operation for another year.

1. Efforts to restore the performance of the helium refrigerator of the cryogenic hydrogen system

The performance degradation of the helium refrigerator forced us to do the purification operation for 6 days after a 3-week operating period that started in February 2016. After each operating period, we sampled the helium gas from the heat exchanger and the adsober to measure the content of impurity elements in the gas with a quadrupole mass spectrometry. However, we could not find elements composing water such as H_2, O_2 and H_2O. After investigating the past events that resulted in performance degradation in the large helium refrigerator at other facilities, oil contamination in the heat exchanger was suggested as a possible cause.

Therefore, in the summer maintenance period, we removed the heat exchangers of the helium refrigerator from the cold box and transported them to a factory for cleaning with Freon. We also replaced the adsorber with a new one (see Fig. 1). As a result, about 90 g of oil was extracted from the heat exchanger and a felt in the adsorber. Furthermore, we replaced all filters of the oil separators of the helium compressor with new ones, where the 300 kg of active charcoal was also exchanged. After purifying the active charcoal for about 4 weeks, we restarted the operation of the helium refrigerator in the late October of 2016. Due to various efforts mentioned above, the differential pressure between the heat exchanger and the adsorber never increased during the operating period from November to March 2017, meaning that the reliable operation was restored.

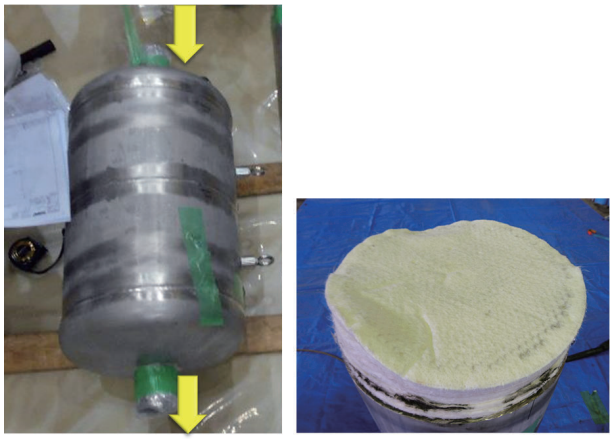

Figure 1. Photo of adsorber (left) and a felt (right) removed from inside of the adsorber. Top layer of the felt was yellowish because of incoming oil.

2. Improvement of the design of the mercury target

Based on the lessons learned from the failure on the water shroud of the target vessel that occurred during the 500 kW operation, we have been making efforts to improve the mercury target vessel under the following plan: 1) minimizing the weld part and the bolt joint between the water shroud and the mercury vessel, and 2) improving inspection technique to find cracks in the weld part on the multi-layer structure with a thickness of 3 mm for the shrouds and 8 mm for the mercury vessel.

We have made a step-wise design upgrade scenario, as shown in Fig. 2. In the first step, the front part of the target, where the heat load is high during the beam operation, was changed, so that the water shroud could be integrated with the mercury vessel. The benefit was that the welding line could be reduced by more than 30%. The change required us to employ a new fabrication procedure to cut out the integrated forepart structure with coolant channels from a steel block by means of a wire-electron-discharge-machining (wire-EDM) technique. The aim in the second step of the design was to make a constrain-free structure between the water shroud and the mercury vessel in the forepart by removing the ribs. And finally, the water-shroud was separated from the mercury vessel completely.

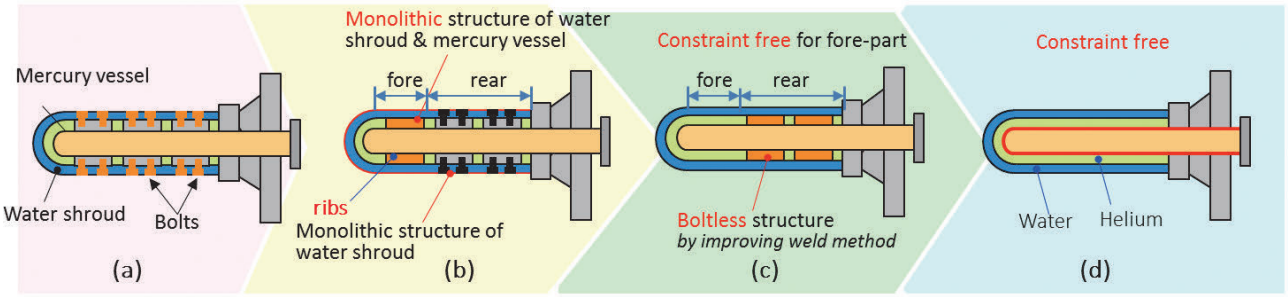

Figure 2. Schematic horizontal cross-sectional views of mercury target vessel's strategic step-wise design improvement. (a) previous design, (b) target vessel with monolithic structure under fabrication since 2015, (c) constraint-free structure for fore-part, (b) entirely constraint-free type.

To apply the wire-EDM technique, many mock-up tests were performed. It was time-consuming to cut the complicated big geometry with wire-EDM. We also took time to stabilize the welding condition to suppress the deformation in the allowable range. Furthermore, we increased the frequency for the radiographic and ultrasonic tests. As a result, in the end of March 2017, the fabrication of the target vessel was still on the way of welding rear part of the mercury vessel to the forepart with an integrated structure.

In fiscal year 2016, we have also started a structural design of a target vessel with a constrain-free structure in the forepart (second step design). For the fabrication of this target, we employed a new electron beam welding technique for reducing the thermal stress in welding. To investigate the EBW welding condition for the rib structure in the narrow gap of 3 mm between the outer and inner water shroud plates, some mock-up tests were performed. The bid of fabrication contract was awarded in January 2017.

3. Efforts to shorten the time of target vessel replacement

In J-PARC, it takes about 32 working days to replace the target vessel, during which period, the target replacement itself, with remote handling tools, requires 10 days. The off-gas processing is a major cause for the long time. It plays role in reducing the amount of radioactivity of gaseous radioactive materials of Xe-127 and tritium, generated in mercury via the spallation reaction, to an amount less than the value allowable for exhausting from the stack before removing the target vessel from the mercury circulation pipes. It also collects helium gas filled into the mercury target system for the leak check after installing a brand-new target vessel.

In 2016, we took measures to double the volume of the gas holders (see Fig. 3), aiming at shortening by 4 days in the helium gas process after the leak check. As the next step, further improvement will be made so that the processing and the gas release to the stack cloud be done at the same time.

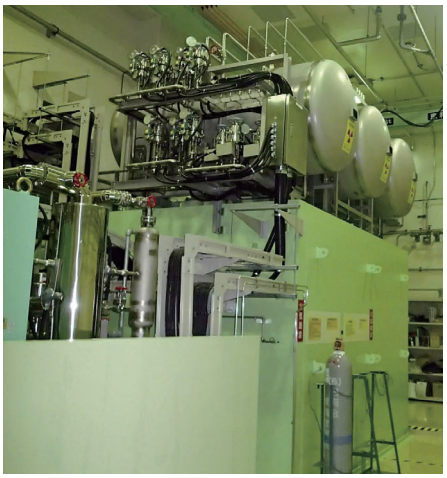

Figure 3. Photo of off-gas processing system with three newly installed gas holders.

H. Takada
Neutron Source Section, Materials and Life Science Division, J-PARC Center

Approaches to Improve the Robustness of the Mercury Target Vessel

1. Introduction

During the proton beam operation at ca. 500 kW in 2015, leakage of a small amount of coolant water from the water shroud was detected in the fifth and seventh mercury target vessels. It was determined that the cause of the leakage was an initial welding defect, which propagated because of repeated thermal stress. To prevent such problems in the future, the structure of the mercury target vessel was improved to reduce the number of the weld lines and the stress generated by proton beam injections in addition to testing of the fabrication process of the new mercury target vessel using mock-up models prior to fabrication. Furthermore, radiographic and ultrasonic tests are added to strengthen the welding inspection.

2. Structure improvement

A schematic of the mercury target vessel is shown in Fig. 1. The length, flange diameter, and total weight are approximately 2 m, 1.2 m and 1600 kg, respectively. The target vessel has a triple-walled structure consisting of the mercury vessel and the double-walled water shroud. The fore part of the mercury vessel with a length of ca. 1 m is covered with a water shroud. The intermediate space between the mercury vessel and the water shroud is filled with helium gas. The design pressure of the mercury is 0.5 MPaG and that of the coolant water and the helium gas is 0.2 MPaG.

The previous and the improved designs of the fore part are shown in Fig. 2. The front-part, where the high heat is loaded during the beam operation, is cut out from a large block using wire electric discharge machining (EDM) to achieve the monolithic structure tying with ribs in the improved design. Plate parts of the water shroud of the rear part are cut out from thick plates using the wire EDM. As a result, the total length of the welding line is reduced by half.

The stresses of the mercury target vessel during the beam operation at 1 MW were estimated using the numerical analysis. The position and width of the ribs between vessels were optimized to reduce the stress. Tresca stress distribution on the inner surface of the external vessel caused by combination of internal pressure and thermal loading is shown in Fig. 3. The peak value of the thermal stress in the front part satisfies the criteria of JIS B 8265 when elasto–plastic deformation mode is taken into consideration. Therefore, new target is available for the 1 MW beam operation.

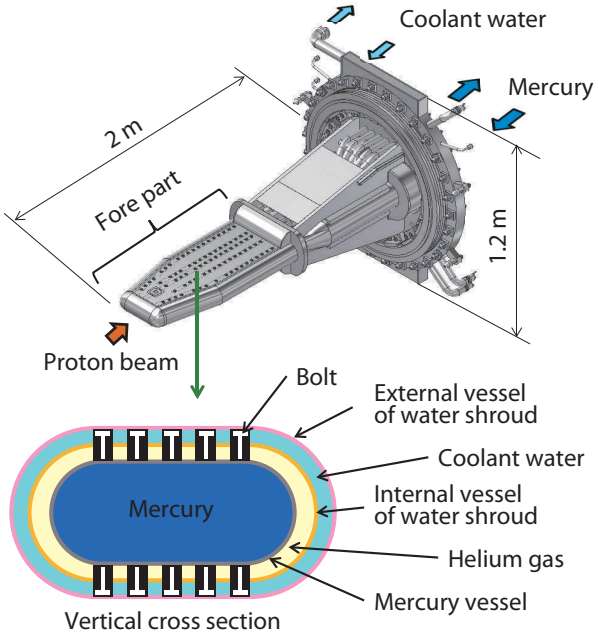

Figure 1. Schematic of the mercury target vessel.

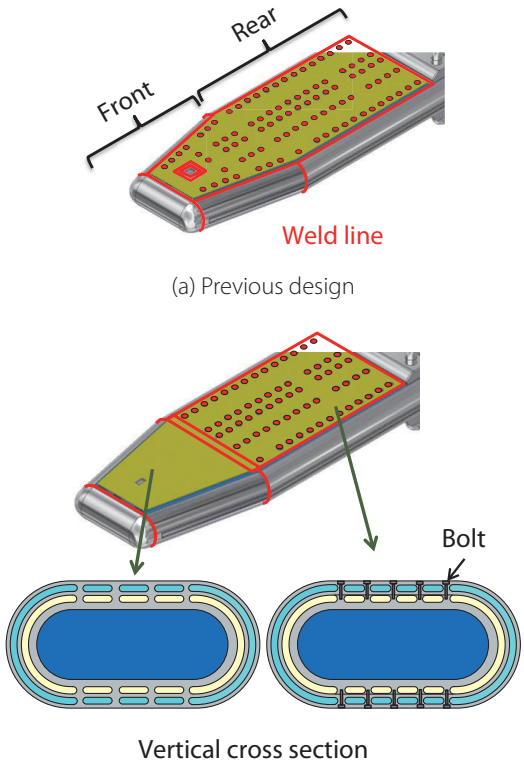

Figure 2. Schematic of the fore part.

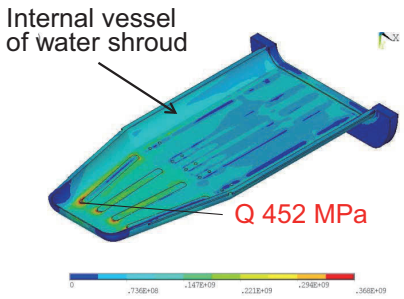

Figure 3. Tresca stress distribution in the inner surface of the external vessel due to the internal pressure and thermal loading. Conventional finite element method code; ANSYS R15.0 was used.

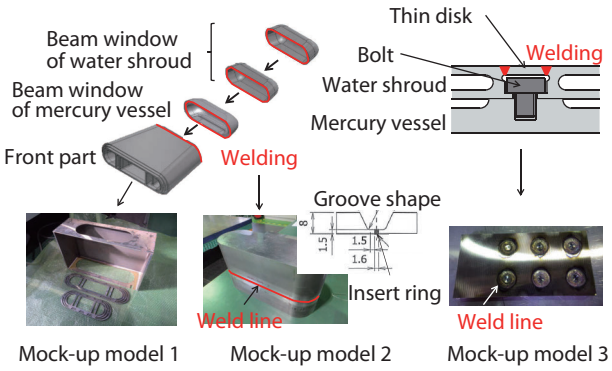

Figure 4. Mock-up models to confirm the fabrication process.

3. Confirmation of the fabrication process using mock-up model

The parts of the mercury vessel are joined by a gas tungsten arc welding. Mock-up tests were conducted to confirm the fabrication process shown in Fig. 4.

The many ribs connecting the vessels machined using the wire-EDM. The machining accuracy was confirmed using the mockup model 1 with dimensions of approximately 150 × 500 × 350 mm, because the thickness accuracy of the thin vessel affected the structural strength.

The gradual changes in the wall thickness of the vessels' side cause the concern that the side's welding line may have a weld defect, which could result in a large deformation. In order to achieve a reliable full penetration weld, the suitable groove shape with an insert ring and welding procedure were determined using the triple-walled mock-up model 2 with a size of 120 × 350 × 200 mm.

In the rear part, upper area of bolt are covered with thin disks with a size of ϕ22 × t1.5 mm by welding after tightening the mercury vessel and the water shroud. In order to decrease an amount of the weld and prevent weld defects, the suitable welding condition was determined using the mock-up model 3 with dimensions of 80 × 160 × 15 mm.

4. Strengthening of inspection

The penetrant test and the pressurized test have been conducted as welding inspection. The radiographic test and the ultrasonic test were also added to welding inspection to detect the small weld defect. Against the repeated thermal stress in 1 MW operation, the allowable size of the weld defect was estimated to be less than 0.4 mm.

The detectable defect size of the radiographic test is approximately 2% of thickness of the test subject. However, the result of the mock-up test showed that the detection size in the multi-walled structure decreases by scattering at the intermediate space between vessels. Therefore, the ultrasonic test should also be conducted.

Since the JIS prescribes the ultrasonic method for plates with thickness of more than 6 mm, this method can't be used in the inspection of the water shroud with 3-mm thin wall. The water-immersion ultrasonic test using scanning ultrasonic system (Insight k.k, Flex Scan) is used, which is suitable for thin plates. The frequency of the ultrasonic probe and the scan pitch are 50 MHz and 0.1 mm, respectively. The result with the mock-up test showed that the detectable defect size is approximately 0.2 mm for a 3-mm plate (Fig. 5).

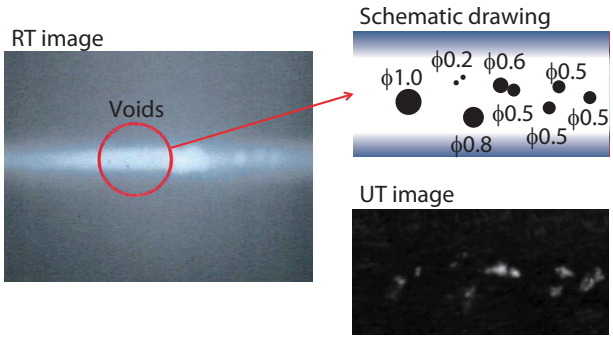

Figure 5. Typical result of radiographic test (RT) and ultrasonic test (UT) on the specimen with artificial weld defects.

T. Wakui, E. Wakai, H. Kogawa, T. Naoe, K. Haga, and H. Takada
Neutron Source Section, Materials and Life Science Division, J-PARC Center

The Status of the Cryogenic Hydrogen System

1. Introduction

At MLF, a cryogenic hydrogen system provides cryogenic hydrogen to the moderators at supercritical pressure of 1.5 MPa, with para-hydrogen concentration of more than 99% and temperature lower than 20 K, generating high-performance pulsed cold neutron beams. This system consists of a helium refrigerator system and a hydrogen circulation system, as shown in Fig. 1.

Since January 2015, the pressure differences at the heat exchangers (HX-1 and HX-2) and an adsorber (ADS) increased gradually [1]. Various investigations and measures were performed, but the problem was not solved. In the 2016 summer maintenance period, we decided to carry out cleaning of the inside heat exchangers, replacement of ADS, a check of the oil separators and an exchange of the filters on the assumption that oil accumulation may have caused the performance degradation [1].

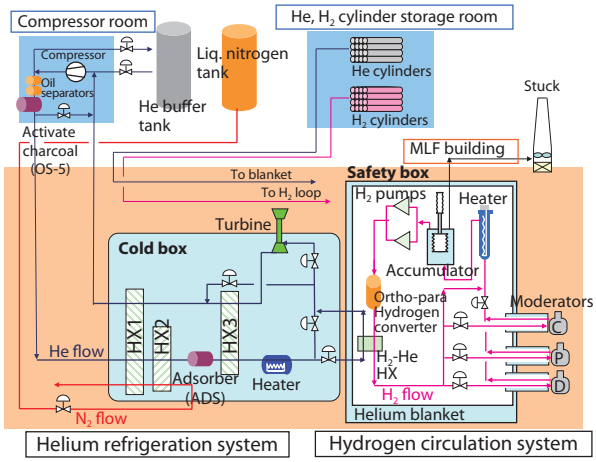

Figure 1. The cryogenic hydrogen system.

2. Operation until the summer outage

In order to keep the user beam schedule, which was already planned until the end of June, we changed the operation cycle of the cryogenic hydrogen system, to 3-week operation (up to the allowed maximum pressure difference) and a 1-week shutdown until the summer maintenance period. Because we found out that after every restarting operation, the pressure difference dropped to its initial level in the previous operations. We also reduced the helium flow by 25% to suppress the oil exhaust from compressor to downstream. This operation cycle worked well for the user schedule until the end of June.

3. Recovery measures during the summer outage

3.1 Cleaning of the inside heat exchangers

The heat exchangers (HX-1 and HX-2) with HX-3 were taken out from the cold box (Fig. 2). They were transported to a cleaning factory in Hyogo. The Freon, ASAHIKLIN AK-225G (c.a. 480 litters) was used to clean the inside heat exchangers.

The cleaning procedure was as follows: filling with Freon, circulating for 1 hour, circulating again with nitrogen gas bubbles for 1 hour, dipping overnight, circulating again, and then removing the Freon. The extracted Freon (c.a. 350 ml) was analyzed to measure the oil content by the NVR (Non-volatile residue) method. These procedures were repeated three times. We found that total amount of accumulated oil inside the heat exchangers was about 94 g. It seemed that the amount of measured oil was roughly equivalent to the projected one from the accumulation of oil contained in the helium gas (10 ppb), which was the design value.

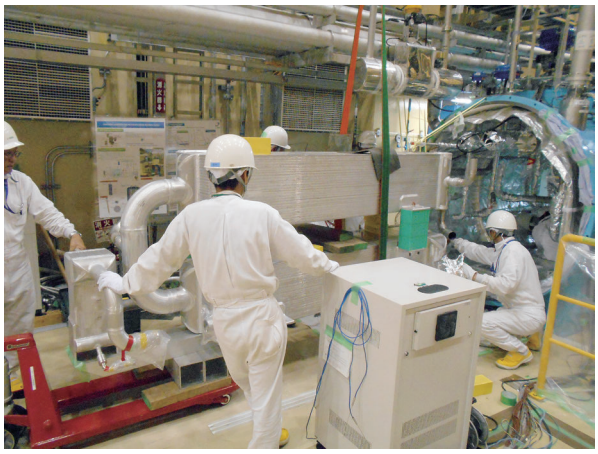

Figure 2. Taking out the heat exchangers from the cold-box.

3.2 ADS replacement and analysis

The ADS was replaced with a new one because most of the pressure difference was generated there. The ADS was removed from the cold box, and then a new one with the same design was installed in the same position. The activated charcoal in the new ADS was regenerated by nitrogen gas heated to 100°C in order to remove moisture.

We observed the inside of the inlet and outlet area of used-ADS by fiber scope and ultraviolet light. The surfaces of the inlet and outlet area were relatively clean. There was little glistening oil that was illuminated by ultraviolet light. The used-ADS was dismantled to its

components, such as felt and activated charcoal. We found that the just surface (3 mm in thickness) of the upper felt, where the helium gas entered first, was yellowed, visually it resembled oil color. We measured the amount of oil in the felt. The oil concentration in the felt and charcoal was analyzed by solvent extraction and infrared spectroscopy. The upper and lower felts have eight separate layers and the thickness of the felt is 4 cm. The analyzed results are shown in Fig. 3. The total amount of accumulated oil was 48.0 g in ADS, however, the total accumulated oil in ADS was also equivalent to the projected one from accumulation of oil contained in helium gas. Almost all oil (45.6 g) was trapped in the upper felt and even more surprisingly, 17.7 g of it was accumulated in the first layer of the upper felt. It seemed that the upper felt played the role of an oil filter. Generally, the felt was used not as an oil filter, but for holding the activated charcoal. We concluded that even if small amount of oil builds up, the accumulated oil forms a film on the surface of the felt that might cause pressure difference during the cooling down process.

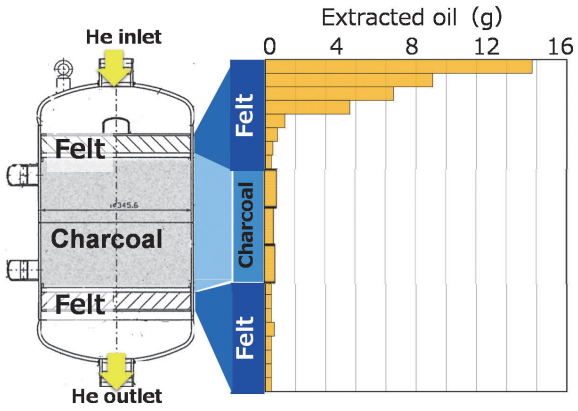

Figure 3. Result of the oil analysis of the used ADS.

3.3 Other maintenance

We have three oil separators (OS-2, 3, 4) and one oil adsorber (OS-5) unit in order to separate the oil from the helium gas after going through the screw compressor. During the summer outage, we confirmed that the OS-2, 3, 4, and 5 were in their normal condition, without any clogging or breakage of the filter. No problems were found during the check. Although the filters had not reached the end of their lifetime, they were exchanged new ones to maximize the oil separation capability.

The lowest piping that is an outdoor piping between the compressor and the cold box in this refrigerator was observed by a fiber scope and ultraviolet light. As a result, no oil reaction was registered, oil did not accumulate in the piping.

4. Recovery of the refrigerator performance

After the described measures taken during the summer outage in 2016, the refrigerator could be operated for the total of over fifty days (November 1 to December 20, 2016 and January 12 to March 8, 2017) without any problem. During the operation, the differential pressure at the heat exchangers (HX-1 and HX-2) and the ADS did not increase excessively, as shown in Fig. 4. The outlet temperature of the heat exchanger HX-2 also did not increase.

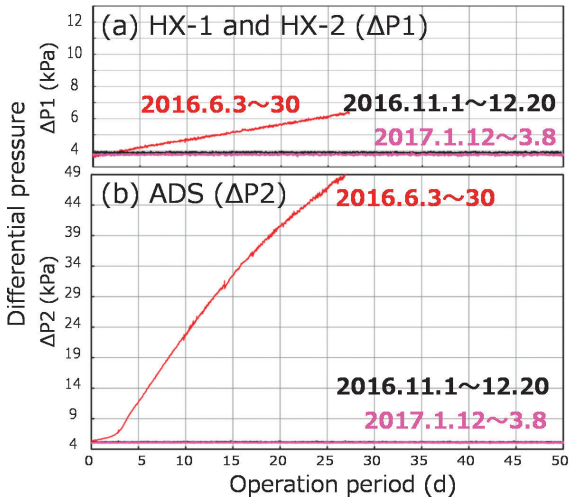

Figure 4. Trend of differential pressure at heat exchanger HX-1 and HX-2 (ΔP1) and ADS (ΔP2) before and after the summer maintenance.

5. Summary

The performance of helium refrigerator has been restored by maintenance measures to remove oil, such as cleaning the heat exchangers with Freon and replacing ADS. However, at this moment, we still have not identified the cause of the incident. We will carry out further investigations, including experiments and adding monitoring in order to reveal the phenomena.

Reference

[1] T. Aso et al., MLF Annual Report 2015, 57-58, (2016).

T. Aso, M. Teshigawara, S. Hasegawa, H. Muto, K. Aoyagi, and K. Nomura
Neutron Source Section, Materials and Life Science Division, J-PARC Center

Present Status of the Spare Decoupled Moderator Fabrication

1. Introduction

The structural material of the moderator and reflector, such as aluminum alloy, will reach its design value (20 DPA) around 2019 due to an accumulated-irradiation-damage. The fabrication of a spare moderator and reflector is moving ahead according to a 2013 plan to replace these components. This year, the fabrication of the decoupled moderator was just completed, following the completion of the coupled moderator and reflector. Finally, the poisoned decoupled moderator will be fabricated in 2018. We report the production status of the decoupled moderator.

2. Decoupled moderator fabrication

The Silver-Indium-Cadmium (Ag-In-Cd) decoupler was used for producing neutron beams with sharp pulse shape in the previous decoupled moderator and reflector. Gold (Au), instead of Ag, was selected to reduce dramatically the radioactivity of used components without sacrificing neutronic performance. However, the bonding between Au-In-Cd (AuIC) and aluminum alloy (A5083), which is a part of the structural material of the decoupler layer of the decoupled moderator, is required in terms of heat removal and thermal stress.

The issue is to develop decoupler layer with curved curvature of AuIC and A5083 alloys (A5083 (1 mm) - AuIC (3 mm) - A5083 (3 mm)) bonding material that has a curved curvature for the decoupled moderator as shown in Fig. 1. We applied a new casting technique to produce AuIC plate with curvature and a Hot Isostatic Pressing (HIP) technique to make bonding material between AuIC and A5083 alloys.

Since the Restriction of Hazardous Substances directive was enforced by the European Union in 2006, it has become impossible to make new materials that include Cd on an industrial scale in Japan. When a new alloy based on Cd is produced for research purposes, we can only obtain it by developing it ourselves, and even then it is only in laboratory amounts.

We could produce AuIC plates with curved curvature with thicknesses of 3 mm by casting an AuIC ingot (with diameter of 80 mm and thickness of 20 mm) in an alumina boat. The AuIC ingots were produced by an ohmic heating method [1]. These plates were cut to the desired shape using a wire electrical discharge machining (WEDM) method, and were spread along curved curvature of aluminum mold as shown in Fig. 2. The manufacturing tolerance was within ±0.3 mm, which satisfied the required design. This small manufacturing errors are very important to suppress the deformation caused by the HIP process.

As mentioned above, the HIP process was applied to obtain the bonding material between AuIC and A5083 alloys. The optimal bonding condition (100 MPa pressure, 535°C temperature and 1-hr holding time) was already found for AuIC coin shaped small test piece (3 cm in diameter × 2 mm in thickness) by adopting a HIP process [2]. We produced successfully a decoupler with curved curvature based on this HIP process condition. Figure 3 shows the result of the ultrasonic reflection test. All reflections between AuIC and A5083 were found in the ultrasonic reflection images, resulting in no separation between the AuIC and A5083 alloys.

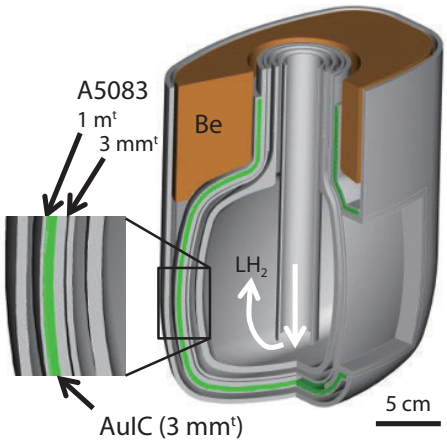

Figure 1. Cutway view of decoupled moderator.

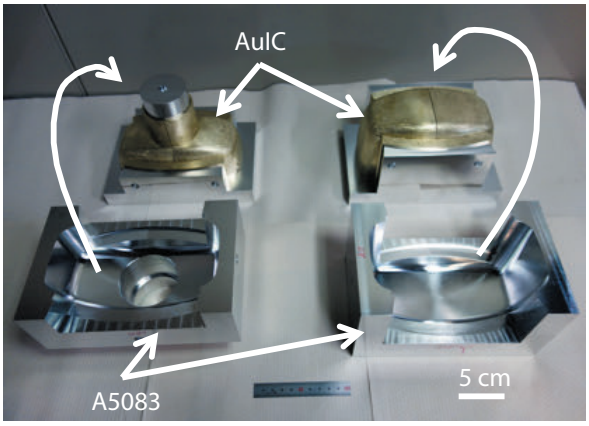

Figure 2. Preparation of HIP process parts with curved curvature (AuIC and A5083).

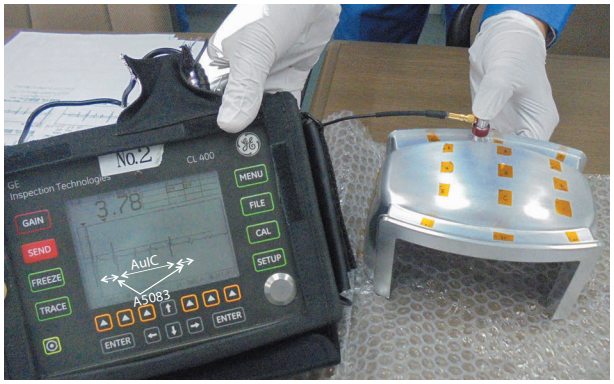

Figure 3. Ultrasonic reflection test after HIP and machining process.

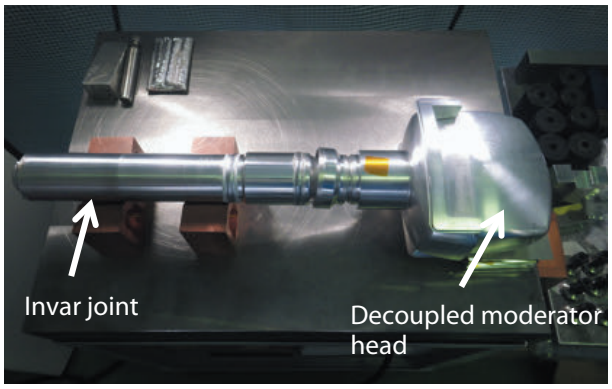

Figure 4. Photograph of decoupled moderator head during fabrication process.

In the spare moderator design, the invar joint with the lowest thermal expansion was also adopted to improve the special fabrication, such as an asymmetrical setting at an elbow-shaped bend in the cryogenic (hydrogen) pipe due to thermal shrinkage of aluminum and stainless steel (SS316L), which was employed for the previous moderator design. The invar joints, such as invar-A6061 and invar-SS316L joints were developed by the friction weld method [3] to utilize in the cryogenic pipe and implemented in the moderators, as shown in Fig. 4. The adoption of invar alloy ensured an easier fabrication due to the low thermal expansion in comparison with the previous one. Finally, many tests, such as appearance inspection, dimensional check, welding inspection, cooling test, etc. were performed before the decoupled moderator fabrication was completed.

M. Teshigawara, M. Harada, and M. Ooi
Materials and Life Science Division, J-PARC Center, JAEA

Acknowledgment

We are grateful for the cooperation of Metal Technology Co. Ltd. in the fabrication of the spare decoupled moderator. We also thank the Nippon Advanced Technology Co., Ltd. staff for their help in the Au-In-Cd material preparation.

References

[1] M. Ooi, et al., Journal of Nucl. Mat. Vol. 431 (2012) pp. 218-223.
[2] M. Ooi, et al., Journal of Nucl. Mat. Vol. 450 issue 1-3 (2014) pp. 117-122.
[3] M. Harada, et al., Journal of Nucl. Mat. Vol. 450 issue 1-3 (2014) pp. 104-109.

Progress of the Proton Beam Transport (3NBT)

1. Introduction

In Japanese Fiscal Year (JFY) 2016, a beam for neutron and muon production with power of 150 and 200 kW had been steadily delivered by 3NBT, which is beam transport from the 3-GeV synchrotron (called Rapid Cycling Synchrotron: RCS) to the target placed at the MLF. Since the mercury target was not equipped with a helium bubbler to mitigate the pitting erosion, the high-power beam operation was prohibited in JFY 2016. After the planned replacement of the mercury target during the summer outage in 2017, the beam operation with 300 kW will resume and the power will reach 1 MW in a few years. The introduction of higher proton beam power to the target will require attention to the beam operation to guarantee the necessary safety level. To ensure a reliable beam operation, a beam tuning tool and beam loss monitor will be required. Also, the increase of the radioisotope production in cooling magnet's water between the mercury target and the muon production target will require treatment of the water system.

2. Development of a beam tuning tool

Since the time for tuning of the beam was limited, an efficient tuning tool was required. To mitigate the pitting erosion at the mercury target, we developed nonlinear beam optics [1] using octupole magnets. With the nonlinear beam optics, a low current density of the beam at the mercury target can be achieved. However, the nonlinear optics complicates the beam tuning more than the conventional linear optics, in addition, the number of experts on beam commissioning at the MLF is limited, so an expert system of beam tuning was required. Therefore, an expert beam tuning system was developed, based on the Strategic Accelerator Design (SAD) [2] developed at the KEK accelerator.

Since SAD implemented the Experimental Physics and Industrial Control System (EPICS) [3], which was a standard control system used in J-PARC, the data monitor can easily transfer to the SAD. Based on the measurement of the beam position with the monitor, the beam orbit was immediately corrected by changing the steering magnet's current by the system. By the result of the beam width obtained by the Multi-Wire Profile Monitor (MWPM) [4], the emittance and the Twiss parameter of the beam can be obtained, as shown in Fig. 1. The present tool was also employed for diagnostics of the beam extracted by the RCS. By tuning the phase advance between the octupole magnet and the target, the nonlinear optics parameters were also obtainied to have a flat beam shape. By the result of beam study with nonlinear optics [4], a desirable phase advance was found, which maximizes the efficiently of the beam flatness and minimizes the beam loss due to deformation of the nonlinear optics.

Since a leakage field of the solenoid magnet for the muon U-line was found to affect about 4 mm vertical beam position at the mercury target, an application was developed to correct the orbit automatically with respect to the solenoid's current. Also, the leakage field of the bending magnet transporting to the Main Ring (MR) was automatically corrected by another application. The residual magnetic field of the pulse-bending magnet, which delivered the beam with low repetition rate (0.4 Hz) to the

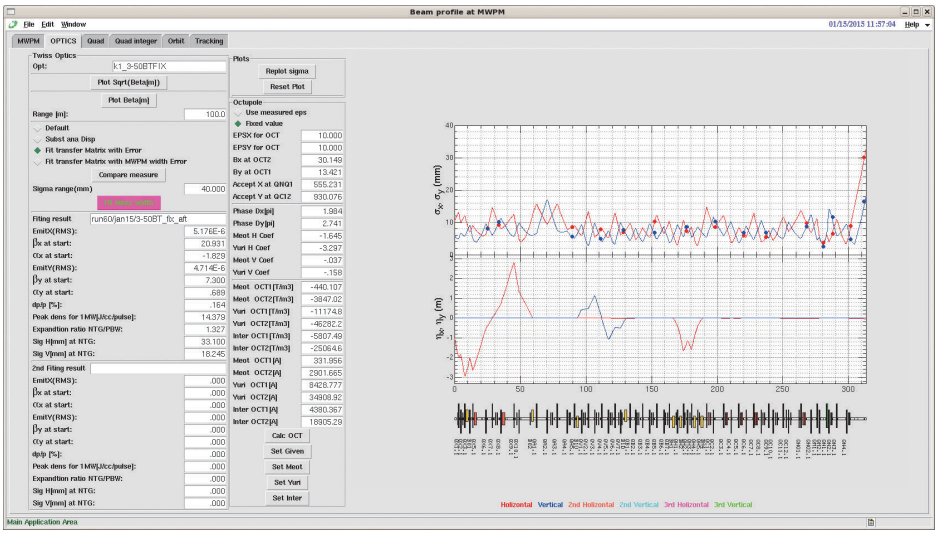

Figure 1. Screenshot of the expert system beam tuning of beam transport.

MR, was found to influence the horizontal beam orbit. A collection magnet with a current pattern supply was introduced to the pulse-bending magnet to compensate the residual field.

3. Beam loss

In the beam transport, the beam duct was activated slightly. To observe precisely the beam loss, we installed additional beam monitors of plastic scintillator to increase the sensitivity. Whenever the beam delivery started, the beam loss was carefully observed by the high-sensitivity monitor. With the new monitor, the beam loss due to the scattering at the muon production target can be controlled very well. Furthermore, we have developed a dosimeter system with nanoDot™ [5] to observe the residual radiation dose due to the beam loss. Thanks to the new beam loss monitors, the beam operation can be performed more confidently.

Although no loss was observed by the new beam loss system, slight activation continued at downstream in front of the muon target. Especially, the duct flange at the final bending magnet was activated, which was placed at the farthest downstream point in the beamline, at a distance of 120 m from the mercury target. Since the neutrons produced from the target may activate the duct, to confirm their intensity, a neutron detector was placed at the final bending magnet. The experiment revealed that the intensity of the neutrons at the duct flangewas about 10^3 times higher than at other places around the flange. To observe the spatial neutron distribution, a GafChromic™ film, which can detect neutron by recoil proton in the film, was placed. Figure 2 shows the result of the imagining. It was found that a clear image of the neutron was obtained with shape of the beam duct, the duct flange and detector holder. It can be concluded that the activation was caused by the interaction of neutrons from the target, which is inevitable in beam tuning. Even though the flight path is very long (120 m) from the target, the neutrons can be transported the beam duct, which playes a role simular to neutron collimator. To avoid activation at the exit of the beam duct, the duct's thin window for extraction of neutrons will be utilized in the future.

4. Improvement of the water cooling system

In the previous year, copper was found to adhere to the ceramic insulator placed in the water loop for the magnet. We assumed that the copper presence was due to erosion at the coil of the magnet. To minimize the magnet coil erosion due to the water flow, we installed a deoxidized system on the water system for the magnet, except for the water around the muon production target. After installing the deoxidizer at the loop, the dissolved oxygen concentration was drastically reduced to the order of sub-ppb, and the amount of the copper adherence decreased.

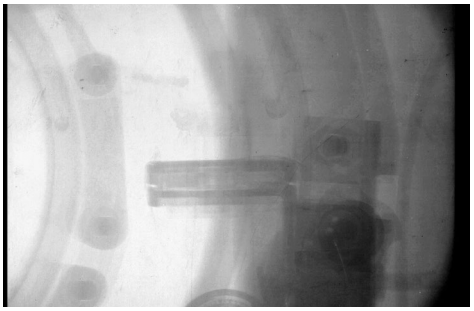

Figure 2. Image of GafChromic™ film placed at the final bending magnet. Shade of the flange and detector holder is shown.

Due to the radiation around the muon target caused by the interaction with the neutron target, the cooling water for the magnet between the muon and neutron target was activated and produced nuclides of ^{3}H and ^{7}Be. Management of the cooling water between both targets is one of the crucial issues in operating the MLF with high reliability. The problem has existed for a long time since the first beam in 2008 and the water impurity was caused by the coil. To sustain high purity, the water was replaced once in every two weeks.

The impurity caused by the coil contained a tiny amount of antimony. In JFY 2015, activated antimony (Sb-122) was detected in the disposal of the cooling water system. To control the activity, we have installed an additional purification system using ion-exchanger. After applying the additional ion-exchanger, the nuclide of ^{7}Be and ^{122}Sb was found to be almost entirely removed, which cannot be observed in the exit of the exchanger. To manage ^{3}H, we have added an extra tank in the water system.

References

[1] S. Meigo, et al., HB2016 WEPM2X01 (2016).
[2] http://acc-physics.kek.jp/SAD/.
[3] http://www.aps.anl.gov/epics/.
[4] S. Meigo, et al., IBIC2015 WEDLA03 (2016).
[5] https://www.landauer.com/product/nanodot.

S. Meigo[1], M. Ooi[1], S. Fukuta[1], T. Kawasaki[1], M. Nishikawa[1], and H. Fujimori[2]
[1]Neutron Source Section J-PARC Center, JAEA; [2]Muon Section J-PARC Center, KEK

Neutron Science

Neutron Science Section

1. User program

In 2016, the user program was negatively affected by two target incidents of cooling water leakage that happened in 2015. As a result, we decided to carry over all experiments approved in 2015A but not executed due to the problem. Because of that, the total available beamtime was reduced to 42 days for each of the 2016A and 2016B periods. After resuming the neutron beam operation on February 20, 2016, by operating an old-designed No.2 target with beam power of 200 kW, we had to reduce the beam power to 150 kW from November 2, to ensure a long stable operation of the target until the summer of 2017.

For the general-proposal submission period in 2016A, 85 neutron proposals were approved out of a total of 275 by the MLF Advisory Board after the Neutron Science Proposal Review Committee. The competition to be approved was so hard, 3.2 to 1. For 2016B, out of 234 submitted neutron proposals, 90 were approved so that the competition was 2.6 to 1.

2. Instruments

The layout of the neutron instruments at MLF, as of the end of JFY 2016, is shown in Fig. 1.

The construction of the polarized neutron spectrometer POLANO at BL23 was still in progress. To examine radiation safety, POLANO accepted the first neutron beam.

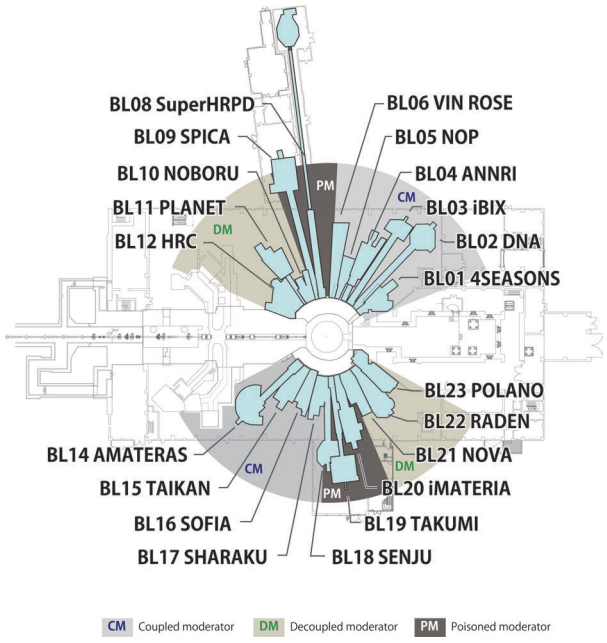

Figure 1. Layout of the neutron instruments at MLF as of JFY 2016. BL06 was in the commissioning phase. BL23 had its first neutron beam.

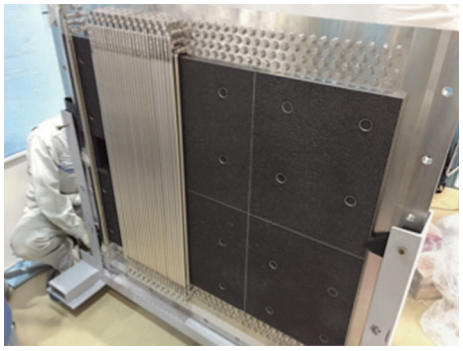

Figure 2. Double-layered low-angle detectors of HRC.

On-beam commissioning will be started in FY2017.

In the backscattering instrument DNA at BL02, Si-311 analyzer banks were installed to extend the energy-momentum space, and diffraction counters were re-installed with re-positioning.

Neutron Brillouin scattering (NBS), that is inelastic neutron scattering close to the forward direction, is effective for observing coherent excitations, such as ferromagnetic spin waves and acoustic phonons in the first Brillouin zone from non-single-crystal samples. This technique becomes feasible on the High Resolution Chopper Spectrometer (HRC) at BL12. Since then, HRC was improved to register the scattering intensities for NBS experiments: the low-angle detectors were aligned in a double layered configuration (Fig. 2), and the Fermi chopper and the collimator were improved.

3. International activities

From June 1 to 2, sixteen scientists and engineers from the European Spallation Source (ESS) visited J-PARC facilities and we held the first ESS - J-PARC Collaboration Workshop (Figs. 3 and 4). The ESS group has obtained the information of J-PARC in a broad range of fields, such as radiation safety issues, operation issues in accelerators, target handling, practical construction of neutron shielding and neutron instruments. At the end of the workshop, it was decided that the second workshop will be held at ESS in 2018.

The first Neutron and Muon School was held from November 22 to 26 (Figs. 5 and 6). That was the new reorganized school, previously known as MLF School, which was hosted by The Japanese Society for Neutron Science, Society of Muon and Meson Science of Japan, J-PARC, CROSS, Materials Sciences Research Center and the Nuclear Human Resource Development Center of JAEA, The Institute for Solid State Physics of

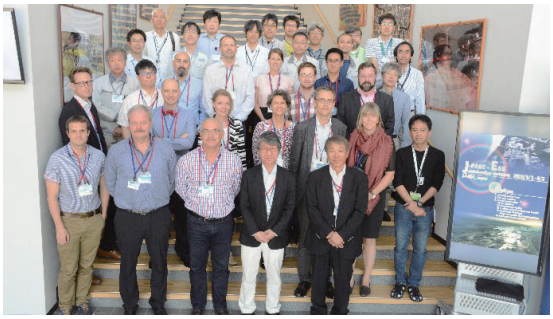

Figure 3. Participants of the first ESS - J-PARC Collaboration Workshop.

Figure 5. Group photo at the first Neutron and Muon School.

Figure 4. Prof. Yokoo explaining the inside structure of HRC to the ESS participants.

Figure 6. Prof. Kanaya, MLF Division Head, in discussion with students at a hands-on experiment at TAIKAN.

The University of Tokyo, Institute of Materials Structure Science of KEK and Ibaraki Prefecture with the support of The Graduate University for Advanced Studies and KEK. 29 young researchers and graduate students from Korea, Australia, Indonesia, India, Hong Kong, Taiwan, United Kingdom, as well as Japan participated in the school. From the neutron group, 8 neutron instruments contributed to hands-on experiments and 25 of 29 participants took part in neutron experiments. We, members of Neutron Science Section, leaded successful start of the newly organized school.

We held the J-PARC Workshop entilted "Neutron Biology for the Next Generation" on March 22. The purpose of the workshop was to promote investigations related to biology at MLF. At the workshop, we invited Dr. Ralf Biehl from Forschungszentrum Jülich GmbH and Dr. Frank Gabel from Institut de Biologie Structurale. The future prospects of research in the field of biology at MLF were discussed from both scientific and instrumental points of view.

4. Resultant outcomes

The research activities in neutron science at MLF resulted in more than 80 papers. The number includes articles in influential journals such as Science, Nature Communications and Scientific Reports.

The DNA beam line (BL02) group won the Technology Prize of the Japanese Society for Neutron Science for the development of the high-energy resolution near-back-scattering spectrometer (DNA).

The ANNRI beam line (BL04) group was awarded the Culture, Sports, Science and Technology Minister's Commendation of 2016 for the work of "Significant innovation and application of neutron resonance spectroscopy".

Development technology of high-performance tire technology by Sumitomo Rubber Industries, Ltd. (ADVANCED 4D NANO DESIGN) was awarded as the 28th Award of The Society of Rubber Science and Technology, Japan (June 6, 2016). The technology was confirmed that atomic scale structure and dynamics of tire by neutron and X-ray and computer simulations could be used to improve the inconsistent performances of car tires, namely, fuel consumption, gripping and wear resistance. Based on this technology, a new tire product was commercialized (November 1, 2016).

K. Nakajima[1], Y. Kawakita[1], S. Itoh[1,2], and T. Otomo[1,2]

[1]Neutron Science Section, Materials and Life Science Division, J-PARC Center; [2]Institute of Materials Structure Science, High Energy Accelerator Research Organization, KEK

BL01: 4D-Space Access Neutron Spectrometer 4SEASONS

1. Introduction and Statistics

4SEASONS is a thermal neutron Fermi-chopper spectrometer for inelastic scattering measurements, and one of the Public Beamlines in MLF [1]. The momentum-energy region for this spectrometer occupies the middle of the momentum-energy space covered by all the MLF spectrometers [2]. In 2016, the number of the approved proposals was limited, because the facility decided to decrease the beamtime for the 2016A and 2016B terms to accept the proposals postponed due to the facility troubles in 2014 and 2015. Only 8 General Use proposals, 1 Urgent Use proposal, 1 New User Promotion proposal, were approved for BL01 in JFY2016, in addition to 2 Element Strategy Initiative Use proposals and 1 Project Use proposal. Instead, 3 2014A General Use proposals and 7 2015A General Use proposals were performed in the 2016A term. In addition, we were able to give beamtimes to 3 reserved proposals. The number of international proposals started to increase since 2014, and currently it reaches about half of the total number of general proposals.

2. Detector Protection

^{3}He detector is vulnerable to vibration, especially while the electric power is supplied. As we reported last year, we have introduced an interlock system to prevent detector damage caused by earthquakes. This system is connected to seismometers placed in the experimental halls. It cuts the electric power supply to the detectors, once it detects an earthquake whose intensity is bigger than some specified value (currently bigger than 4 on the Japanese seismic scale). In addition, we replaced the power supplies for the detectors with new ones, which have a better compatibility with the interlock system. In 2016, this interlock system worked after being triggered by a real earthquake for the first time. Figure 1(a) shows the seismometer in Experimental Hall No. 1 of MLF, whose red warning lamp lit up after detecting an earthquake with seismic intensity of 4 on November 22, 2016. It successfully cut off the power supply to the detectors, as shown in Fig. 1(b) [3].

3. Improvement in the Oscillating Radial Collimator

To reduce the background scattering from the sample environment, 4SEASONS can be equipped with an oscillating radial collimator (ORC), which was developed by the Technology Development Section of MLF. It has a number of thin shielding blades made of cadmium-plated aluminum sheets, which surround the space for the sample environment device. The ORC is installed on the vacuum scattering chamber, and it is usually oscillated horizontally to avoid uneven intensity distribution on the detectors caused by shadows from the shielding blades [4]. However, this type of oscillation is not simple, because the unevenness in intensity depends on the oscillating speed and angle. Even after optimizing these parameters, we found that the shielding blades inevitably made shadows when they stopped at both ends of the oscillating angle to change the oscillating direction, even though the dead time was small (~20 ms). To solve this problem, we recently developed a new oscillating mode, called "shift-mode", which can shift the oscillating angle range gradually (Fig. 2). We confirmed that by changing the angle range by 0.1° per oscillation, we could obtain more even intensity distribution than in the normal oscillating mode [5].

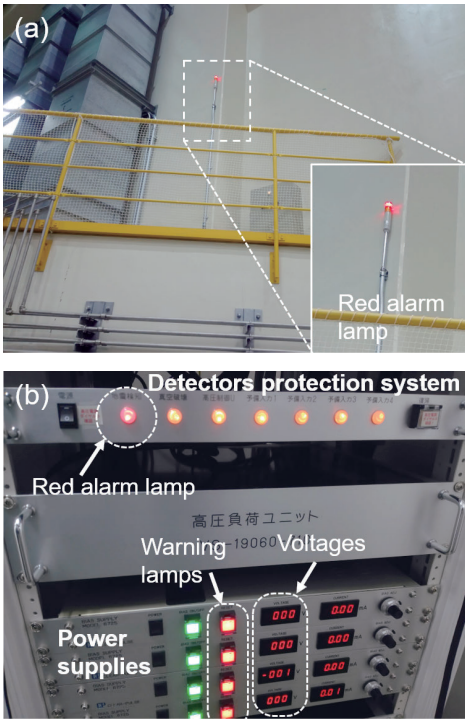

Figure 1. (a) Seismometer in MLF. (inset) The red alarm lamp is on by detecting an earthquake. (b) The detector protection system and the new high-voltage power supplies for detectors in the 4SEASONS cabin [3].

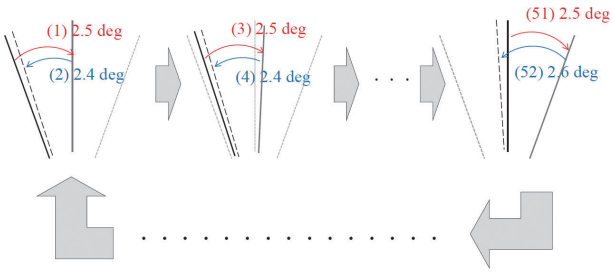

Figure 2. Schematic illustration representing the shift-mode operation. The angular separation between neighboring blades is assumed to be 2.5° in this figure [5].

4. 4D Mapping by Continuous Rotation of Single-Crystal Samples

One of the recent trends in the experiments on a single crystal using a chopper spectrometer is to grasp whole excitations in the 4D momentum-energy space by rotating the crystal over a wide angular range. Recently, the MLF Computing Environment Group developed a new measurement and analysis system, which enables the 4D mapping of the reciprocal and energy space by continuously rotating a single crystal [6]. We introduced this new measurement system on 4SEASONS this year. Figure 3 shows the phonon spectra of a single crystal of copper measured by continuously rotating the crystal using the new system [3]. By rotating the crystal at a reasonably fast speed (160°/h), we obtained the rough picture at an early measurement stage (Figs. 3(a) and 3(b)). The statistics improved with time by repeating the rotation (Fig. 3(c)). With this new system, we do not need to determine the rotation step size in advance and can visualize the data in real time, which gives us high flexibility in the 4D mapping measurements.

References

[1] R. Kajimoto, M. Nakamura, Y. Inamura, F. Mi-zuno, K. Nakajima, S. Ohira-Kawamura, T. Yokoo, T. Nakatani, R. Maruyama, K. Soyama, K. Shibata, K. Suzuya, S. Sato, K. Aizawa, M. Arai, S. Wakimoto, M. Ishikado, S. Shamoto, M. Fujita, H. Hiraka, K. Ohoyama, K. Yamada, and C. H. Lee, J. Phys. Soc. Jpn. **80**, SB025 (2011).

[2] H. Seto, S. Itoh, T. Yokoo, H. Endo, K. Nakajima, K. Shibata, R. Kajimoto, S. Ohira-Kawamura, M. Nakamura, Y. Kawakita, H. Nakagawa, and T. Yamada, Biochim. Biophys. Acta, Gen. Subj. **1861**, 3651 (2017).

[3] R. Kajimoto, M. Nakamura, Y. Inamura, K. Kamazawa, K. Ikeuchi, K. Iida, M. Ishikado, N. Murai, H. Kira, T. Nakatani, S. Ohira-Kawamura, R. Takahashi, N. Kubo, W. Kambara, K. Nakajima, and K. Aizawa, J. Phys.: Conf. Ser., to be published.

[4] M. Nakamura, Y. Kawakita, W. Kambara, K. Aoyama, R. Kajimoto, K. Nakajima, S. Ohira-Kawamura, K. Ikeuchi, T. Kikuchi, Y. Inamura, K. Iida, K. Kamazawa, and M. Ishikado, JPS Conf. Proc. **8**, 036011 (2015).

[5] M. Nakamura, W. Kambara, K. Iida, R. Kajimoto, K. Kamazawa, K. Ikeuchi, M. Ishikado, K. Aoyama, unpublished.

[6] Y. Inamura, T. Ito, and J. Suzuki, J. Phys.: Conf. Ser., to be published.

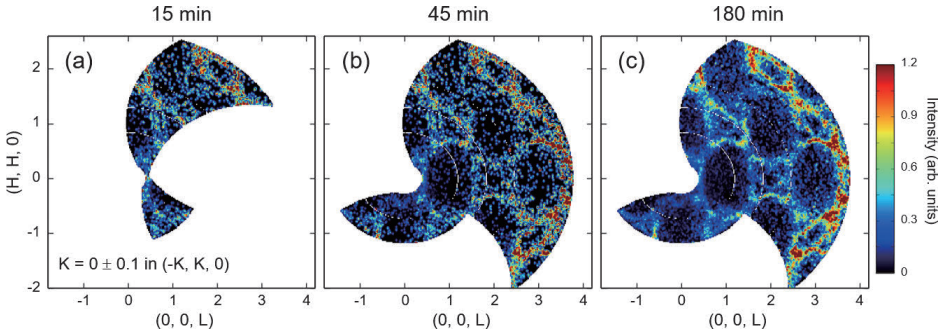

Figure 3. Phonon spectra of a single crystalline copper obtained by continuously rotating the crystal. The crystal was rotated horizontally at a rate of 160°/h. (a), (b), and (c) show the constant energy slices at 13 ± 1 meV, 15, 45, and 180 min after the start of the measurement, respectively [3].

R. Kajimoto[1], M. Nakamura[1], K. Kamazawa[2], Y. Inamura[1], K. Ikeuchi[2], K. Iida[2], M. Ishikado[2], N. Murai[1], T. Nakatani[1], K. Aoyama[1], and W. Kambara[1]

[1]*Neutron Science Section, Materials and Life Science Division, J-PARC Center;* [2]*Neutron R&D Division, Neutron Science and Technology Center, CROSS*

BL02: Current Status of the Broadband micro-eV Quasielastic and Inelastic Neutron Spectrometer DNA

1. Introduction

DNA, a time-of-flight (TOF) type near-backscattering spectrometer (n-BSS), is a unique instrument among the world's spallation pulsed neutron facilities because it is n-BSS equipped with a high-speed pulse-shaping disc-chopper [1]. The neutron beam from the coupled moderator, which provides the most intense yet broadest pulse among all three moderators in MLF, is handled flexibly in pulse width by this chopper while keeping its intensity and creating symmetrical pulse in a TOF spectrum. Si crystal analyzers, back-coated with a neutron absorber, reduce significantly the unfavorable background scattering of the instrument, reaching a signal-to-noise ratio of ~10^5. Those factors are highly beneficial for expanding the application fields into the dynamical behaviors of atoms and spins in biomolecules [2, 3], soft-materials and strongly-correlated electron systems in nanosecond timescale or in the micro-eV energy region.

Table 1. Instrumental specifications of DNA.

Items	Specification
Neutron source (NS)	Coupled Liquid H2 Moderator
L1 (source-sample)	42 [m]
L2 (sample-analyzer)	~ 2.3 [m]
L3 (analyzer-detector)	~2.0 [m]
Pulse sharpening chopper (PS-chopper)	
Max speed: 300 Hz at ~7.5 m from NS	
(Present max speed: 225 Hz by 4 slits on one disc)	
Crystal analyzer	
Crystal and reflection index	Si (111)
	Si (311) in test
Bragg angle of analyzers	~87.5 [deg.]
Energy resolution	
	~2.4 [μeV]: Si (111) with 10 mm Slit @225 Hz
	~3.5 [μeV]: Si (111) with 30 mm Slit @225 Hz
	~14 [μeV]: Si (111) without PS-chopper
	~12 [μeV]: Si (311) with 10 mm Slit @225 Hz
Momentum range	0.08 < Q < 1.86 [A^{-1}]: Si (111)
	1.0 < Q < 3.80 [A^{-1}]: Si (311) in plan
Scan energy range:	
Si (111):	−40 < E/μeV < 100: Single pulse scan around Ef
	−400 < E/μeV < 600: Multi pulse scan around Ef
	−500 < E/μeV <1500:
	Without PS-chopper in second frame
Si (311):	−150 < E/μeV <300: Single pulse scan around Ef
(Specifications obtained by the end of March 2017)	

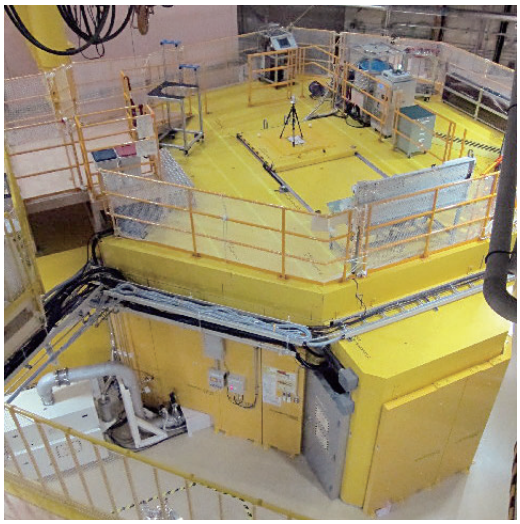

Figure 1. Photo of BL02 DNA (September 2016).

We made efforts to improve the instrumental activities, such as upgrading the data storage and data acquisition system, and rearranging the diffraction detector.

It should be also reported that our work on the construction and commissioning of DNA received an award from the Japanese Society for Neutron Science (JSNS), namely "The practical realization of the dynamics analysis spectrometer DNA by the construction group of the dynamics analysis spectrometer DNA".

Figure 2. Photo from the award ceremony at the JSNS meeting (December 2016).

2. Instrumental activities

In FY2016, the following instrumental activities were carried out:

(1) Commissioning and fabrication of a sample environments device.

The heat-conduction part of a BL-common top lording cryofurnace was improved. Also, a special sample stick for induced high voltage at the sample was fabricated.

(2) Upgrading the data storage and data acquisition system.
During the summer shutdown period, the data storage system was upgraded to the new Store Next System. Also, the data acquisition system was upgraded to new high-performance PC servers.

(3) Rearranging the diffraction detector.
Three 8-pack ^{3}He detector banks were moved to the position at the high scattering angle in the vacuum scattering chamber for long-d diffraction measurements.

3. User program in the 2016A and 2016B periods

Proposals in a wide variety of research fields were submitted for general use machine time on BL02 DNA. In 2016A, 15 proposals were submitted and 6 of them (28.0 days) were approved. In 2016B, 18 proposals were submitted and 7 of them (32.0 days) were approved. The 2 trial use proposals (4.0 days) and the 2 project proposals (10.0 days) were also carried out in 2016A and 2016B.

Other than that, the 10 proposals (2014B; 2 proposals (9.5 days) and 2015A; 8 proposals (27.0 days)) postponed due to some incidents that occurred in FY2014 and FY2015, were carried out in 2016A & 2016B. Finally, all carry-forward proposals approved in 2014B and 2015A, were carried out in the end of 2016B. Among the experiments, carried out in 2016A and 2016B, were the following three proposals: 2015A0141 [2], 2015A0143 [3], 2016A0048 [4], for which reports have been published.

On November 24th and 25th, 2016, a practice experiment was held as a part of lectures at the Neutron and Muon School 2016. Three students from Japan, Australia and Taiwan, respectively, took part and carried out measured and analyzed quasielastic neutron scattering (QENS) due to the proton conduction of Nafion membrane on the BL02 DNA.

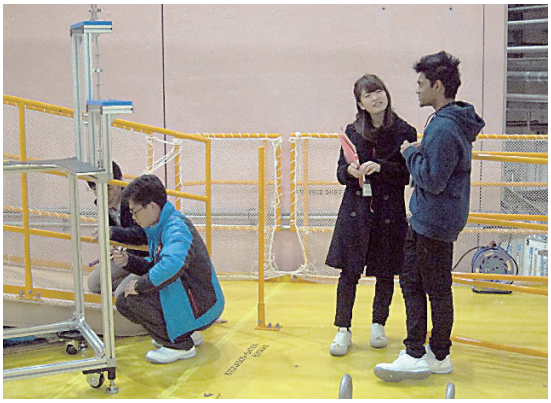

Figure 3. Photo of discussing students who were participated the Nafion QENS practice experiment on the BL02 DNA at the Neutron and Muon School 2016.

4. Future plans

The optimal combination of the major spectroscopic devices: pulse shaping chopper, Si crystal analyzer and so on, made it possible to measure the S (Q, E) with micro-eV high-energy resolution, high-beam intensity at the sample position and quite low instrumental background. Taking advantage of this feature, the scientific research field of using DNA will be expanded not only for quasi- elastic neutron scattering but also for inelastic neutron scattering with very precise energy resolution.

References

[1] Kaoru SHIBATA, et.al. JPS Conference Proceedings, 8, 036022 (2015).

[2] Tatsuhito Matsuo, Taiki Tominaga, Fumiaki Kono, Kaoru Shibata and Satoru Fujiwara, BBA - Proteins and Proteomics 1865 (2017) 1781–1789.

[3] Fujiwara Satoru, Chatake Toshiyuki, Matsuo Tatsuhito, Kono Fumiaki, Tominaga Taiki, Shibata Kaoru, Sato-Tomita Ayana, Shibayama Naoya, Journal of Physical Chemistry vol. 121 (2017), 8069-8077.

[4] Bing Li, Yukinobu Kawakita, Yucheng Liu, Mingchao Wang, Masato Matsuura, Kaoru Shibata, Seiko Ohira-Kawamura, Takeshi Yamada, Shangchao Liu, Kenji Nakajima and Shengzhong (Frank) Liu, Nature Communications., DOI: 10/1038/ncomms16086.

K. Shibata[1], Y. Kawakita[1], H. Nakagawa[1], W. Kambara[1], Y. Inamura[1], T. Nakatani[1], T. Yamada[2], M. Matuura[2], T. Tominaga[2], M. Kobayashi[2], and S. Kasai[2]

[1]Neutron Science Section, Materials and Life Science Division, J-PARC Center; [2]Neutron R&D Division CROSS-Tokai

BL03: IBARAKI Biological Crystal Diffractometer iBIX

1. Introduction

Single crystal neutron diffraction is one of the powerful methods to obtain the structure information, including that of the hydrogen atoms. The IBARAKI biological crystal diffractometer called iBIX is a high-performance time-of-flight single crystal neutron diffractometer to elucidate the hydrogen, protonation and hydration structures of organic compounds and biological macromolecules in various life processes [1].

In 2012, we upgraded the 14 existing detectors and installed 16 new detectors for the iBIX diffractometer (Fig. 1). The total solid angle of the detectors subtended by a sample and the average of detector efficiency became 2 and 3 times larger, respectively [2]. The total measurement efficiency of the present diffractometer become 10 times larger from the previous one coupled with the increasing of accelerator power. In the end of 2012, we were able to start the iBIX application in user experiments for biological macromolecules. The final specifications of the iBIX are shown in Table 1.

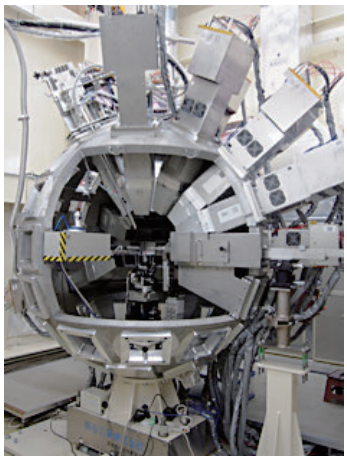

Figure 1. The iBIX diffractometer.

Table 1. Specifications of iBIX.

Moderator	Coupled
Wavelength of incident neutron	0.7 ~ 4.0 Å (1st frame) 4.0 ~ 8.0 Å (2nd frame)
Neutron intensity (@1 MW)	0.7×10^6 n/s/mm^2
L_1	40 m
L_2	500 mm
Solid angle of detectors	19.5% for 4π
Detector covered region	+15.5 ~ +168.5 deg.
Detector size	133 × 133 mm
Detectors pixel size	0.52 × 0.52 mm
No. of detectors	30

2. Current status

In 2016, the accelerator power of J-PARC become 150~200 kW. 6 organic compounds and 3 biological macromolecules were provided for the diffraction experiments using iBIX. Some interesting scientific results were obtained from these investigations by applying neutron structure analysis.

We have tried to collect the data-set of a protein crystal with the largest unit cell in the neutron diffraction experiment by using iBIX to estimate its own performance. The crystal selected for the purpose was Mn Catarase. The crystal volume was 2.0 mm^3. The cell parameters were a = 133.4 Å in a cubic form. The measurement conditions were as follows: accelerator beam power: 200 kW, range of wavelengths: 3.0~6.0 Å, number of measurement settings: 10, exposure time: 30 hours/setting, total amount of measurement time for full data-set: 12.5 days. Through data reduction and structure refinement, we obtained successfully 2.4 Å and reasonable structure with the information of hydrogen and deuterium atoms. These results show that iBIX could achieve the maximum cell dimension of design specifications without any peak de-convolution procedure.

The collection of a full data-set of biological macromolecules for neutron structure analysis by using iBIX proceeded as follows under the 1 MW operation. The maximum cell dimension was 135 × 135 × 135 Å^3. The average sample volume was about 2 mm^3. The average measurement time was about 2~4 days. We project that iBIX will become one of the world's best performing diffractometers under 1 MW operation.

3. Development

In order to improve the accuracy of the estimated position of Bragg reflections (= UB matrix) of TOF diffraction data for the integration procedure, we determined the detector parameters and the goniometer offset angle (distance between sample and detector surface, detector positions, tilted angles of the detector surface, Δchi and Δphi offset angle) with a laser tracker system. From the results, we found out that the center of the diffractometer was not positioned at the center of the beam line. We re-aligned the center of the diffractometer to the beam line and re-optimized the detector parameters and the goniometer offset angle based on the diffraction data-set from an inorganic compound. More precise detector parameters could be obtained,

and then the accuracy of the estimated position of the Bragg reflections could be improved for protein crystals with large unit cells.

A full data-set of a 2 mm^3 protein sample by iBIX can be obtained in about 2~4 days under 1 MW operation of accelerator power. However, the sample size is still too large, and the measurement time is still too long, which causes problems for the users. It is necessary to improve the measurement efficiency of the iBIX diffractometer. We started to develop a new scintillator unit with high sensitivity for the iBIX detector system. The development aim for the new scintillator unit is 1.4 times higher sensitivity than the previous scintillator. We hope to demonstrate this increased sensitivity by performing neutron experiments on a test piece.

4. Future prospects

In the future, the accelerator power of J-PARC will increase about 1 MW. iBIX should be available regularly for full data-set measurement of samples with the size of 1 mm^3. We will continue to develop the data reduction software and the beam line instruments to improve the accuracy of intensity data obtained from small samples. Furthermore, we should plan to install additional detectors looking toward an industrial use.

References

[1] I. Tanaka, K. Kusaka, T. Hosoya, N. Niimura, T. Ohhara, K. Kurihara, T. Yamada, Y. Ohnishi, K. Tomoyori andT. Yokoyama, Acta Cryst. D66 (2010) 1194-1197.

[2] K. Kusaka, T. Hosoya, T. Yamada, K. Tomoyori, T. Ohhara, M. Katagiri, K. Kurihara, I. Tanaka and N. Niimura J. Synchrotron Rad. 20 (2013) 994-998.

K. Kusaka[1], T. Yamada[1], N. Yano[1], T. Hosoya[1], I. Tanaka[1], T. Ohhara[2], and M. Katagiri[1]

[1]*Frontier Research Center for Applied Atomic Sciences, Ibaraki University, Tokai;* [2]*J-PARC Center, JAEA*

Measurement of the ^{133}Cs(n,γ) Cross-Section Using a New DAQ System at ANNRI

1. Introduction

Nuclear data on ^{135}Cs will be vital to develop a system for transmuting nuclear waste products into stable or shorter-lived nuclides, reducing the environmental impact of nuclear power. ^{133}Cs is an unavoidable contaminant in the presently available samples of the long-lived fission product ^{135}Cs. High-quality data for ^{133}Cs is necessary to analyze the experimental data of ^{135}Cs.

Recently, a new data acquisition system (DAQ system) has been installed for the high-purity germanium (HPGe) detector array at the Accurate Neutron-Nucleus Reaction Measurement Instrument (BL04-ANNRI) at the J-PARC MLF, notably featuring much lower dead-time in comparison to the previous DAQ system. Using this new DAQ system, a measurement of the ^{133}Cs(n,γ) cross-section has been conducted at the J-PARC MLF.

2. Experiment

Neutrons, produced at the Hg target in the MLF, travel a flight length of 21.5 m before interacting with a sample, then the resultant gamma-rays are measured by an array of HPGe detectors. The neutron energy is determined via the neutron time-of-flight (nTOF) method.

The HPGe array consists of two clusters of 7 HPGe detectors above and below the beamline, in addition to 8 co-axial detectors horizontally aligned with the beamline, for a total of 22 detectors. However, due to noise on the co-axial detectors, they were not used for this experiment. Detector signals from the HPGe detectors are fed into a pre-amp and then the pre-amp signal is digitized by CAEN v1724 14-bit 100-MHz ADC boards [1]. The ADC boards are then connected to a PC via optical-fiber cables for storing data for offline analysis, as well as online monitoring.

The ^{133}Cs sample was made by pressing 17.2 mg Cs_2CO_3 into a pellet of diameter 5.04 mm and thickness 0.329 mm, and then sealed in FEP film. Additionally, a sample of Au was prepared for calibrating the nTOF parameters and determining the relative neutron energy spectrum in the thermal energy range. A ^{10}B sample was prepared for determining the relative neutron energy spectrum in the epithermal to fast neutron energy range. A ^{208}Pb sample was measured to account for the effects of neutron scattering, and a blank sample of FEP film was used only to measure the background without sample influence.

The pulse-height and time-of-flight data from the ADC were recorded event-by-event. See Fig. 1 for the raw time-of-flight data from each sample.

A comparison of the time-of-flight spectrum surrounding the first and second resonances of ^{133}Cs(n,γ), using both the current and previous DAQs, can be seen in Fig. 2. Under the old DAQ system, large resonances suffer from severe dead-time effects, and dead-time correction accounts for nearly all of the information regarding the resonance height and shape. However, under the new DAQ system, the dead-time effects are mostly negligible. Due to the characteristics of the CAEN v1724 boards, the dead-time per event has been significantly reduced in comparison to the old DAQ system, from 175.2 μs to 3.18 μs, a reduction factor of approximately 55. Using the newly installed DAQ system, it is possible to measure larger capture yields, for either thicker targets or higher neutron fluxes, with higher energy resolution and in higher energy regions.

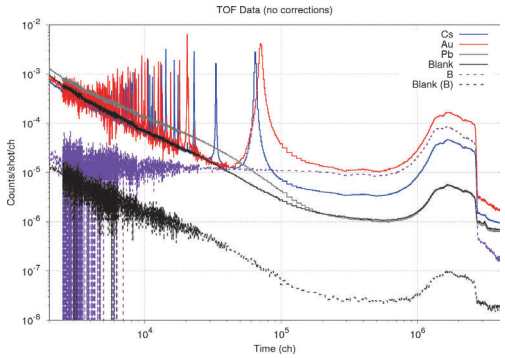

Figure 1. The measured time-of-flight spectrum for each sample. For the B sample, a pulse-height gate was placed to only count events from the 478 keV photopeak. Correspondingly, the analysis of the blank sample was repeated also using the same pulse-height gate.

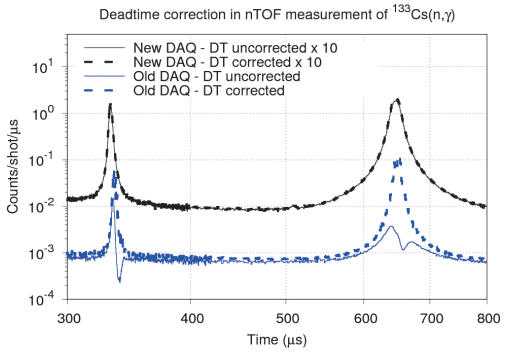

Figure 2. A comparison of the time-of-flight spectra for measurements of the ^{133}Cs(n,γ) reaction. Note that the beam power in the new DAQ measurement is also roughly twice as strong in comparison to the experiment for the old DAQ.

3. Analysis

The pulse-height weighting technique [2] is applied to convert the detector output pulse-height spectrum in a given time-of-flight bin to neutron capture yield. The pulse-height weighting function was calculated using the detector response, as simulated by GEANT4 [3]. The dead-time correction factor is calculated by tallying all detector events. Time-independent and time-dependent background effects (including frame-overlap effects) are deduced by using the time-of-flight data during the rest period when pulsed protons are sent to the 50 GeV synchrotron. The time-of-flight data are normalized to the total proton beam power of each measurement. Background counts without sample influence are subtracted by using the blank sample data. The effects of scattered neutrons from each measured sample are accounted for by subtracting the net ^{208}Pb data multiplied by the ratio of the total neutron scattering cross-section between ^{208}Pb and each measured sample. A self-shielding factor is calculated using PHITS [4] and applied.

The above analysis produces the capture yield, proportional to $\phi(E)\sigma(E)N$. In the energy region above 0.01 eV, the relative neutron energy spectrum, proportional to $\phi(E)$, is deduced from the number of 478 keV photopeak events from the ^{10}B sample and the evaluated cross-section of ^{10}B(n,$\alpha\gamma$) in JENDL-4.0 [5]. In the energy region below 0.01 eV, the relative neutron energy spectrum is deduced from the measured neutron capture yield from the Au sample and the evaluated cross-section of Au(n,γ) in JENDL-4.0. The reason for using Au in the thermal energy region is to avoid the large errors associated with self-shielding effects in the ^{10}B sample in the thermal energy region.

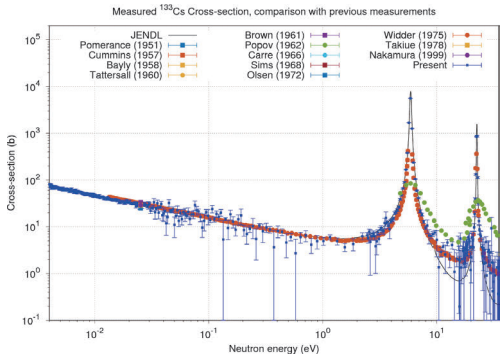

Figure 3. The measured cross-section of ^{133}Cs(n,γ) and comparison with previous measurements.

The relative cross-section of ^{133}Cs(n,γ) was then derived by dividing the measured neutron capture yield by the relative neutron energy spectrum. The measured relative cross-section data for ^{133}Cs(n,γ) has been normalized to its evaluated value at 0.0253 eV in JENDL-4.0 of 28.90 b [5]. The measured cross-section of ^{133}Cs(n,γ) in the energy range from 0.004 eV to 35 eV can be seen in Fig. 3, along with a comparison to previous measurements. The error analysis is ongoing.

4. Future plans

At the current stage of analysis, the measured cross-section of ^{133}Cs(n,γ) as a function of energy has been normalized to the evaluated value at 0.0253 eV in JENDL-4.0 of 28.90 b [4]. In the near future, we intend to deduce the absolute capture cross section of ^{133}Cs using the capture yield of the Au sample and the same pulse height weighting technique, which greatly reduces systematic error.

We are also working on measurements for the cross-sections of ^{135}Cs(n,γ) and ^{74,76,77,78,80,82}Se(n,γ) and publications of those results are expected shortly.

Acknowledgments

This work was funded by ImPACT Program of Council for Science, Technology and Innovation (Cabinet Office, Government of Japan).

References

[1] http://www.caen.it

[2] R. L. Macklin, J. H. Gibbons: Phys. Rev., 159 (1967), p. 1007.

[3] GEANT4: A Simulation toolkit - GEANT4 Collaboration (Agostinelli, S. et al.) Nucl.Instrum.Meth. A506 (2003) 250-303 SLAC-PUB-9350, FERMILAB-PUB-03-339.

[4] T. Sato, K. Niita, N. Matsuda, S. Hashimoto, Y. Iwamoto, S. Noda, T. Ogawa, H. Iwase, H. Nakashima, T. Fukahori, K. Okumura, T. Kai, S. Chiba, T. Furuta and L. Sihver, Particle and Heavy Ion Transport Code System PHITS, Version 2.52, J. Nucl. Sci. Technol. 50:9, 913-923 (2013).

[5] K. Shibata, O. Iwamoto, T. Nakagawa, N. Iwamoto, A. Ichihara, S. Kunieda, S. Chiba, K. Furutaka, N. Otuka, T. Ohsawa, T. Murata, H. Matsunobu, A. Zukeran, S. Kamada, and J. Katakura: "JENDL-4.0: A New Library for Nuclear Science and Engineering," J. Nucl. Sci. Technol.. 48(1), 1-30 (2011).

B. Hales, A. Kimura, S. Nakamura, and O. Iwamoto
Nuclear Data Center, JAEA

Status of Fundamental Physics Beamline BL05 (NOP) 2016

1. Introduction

"Neutron Optics and Physics (NOP/ BL05)" at MLF in J-PARC is a beamline for studies in the field of fundamental physics. The beamline is divided at the upstream into three branches, which are the so-called Polarized, Unpolarized, and Low-Divergence branches, used in different experiments in a parallel way [1-2].

A neutron lifetime measurement was performed at the Polarized beam branch with a spin flip chopper. Pulsed ultra-cold neutrons (UCNs) by a Doppler shifter are available at the Unpolarized beam branch. At the Low-Divergence beam branch, the search for an unknown intermediate force is performed by measuring neutron scattering with rare gases. The beamline is used also for R&D of optical elements and detectors [3].

2. Measurement of the Neutron Lifetime

A neutron decays into a proton, an electron, and an antineutrino. The decay lifetime is an important parameter for the unitarity of the CKM matrix and also for the primordial big bang nucleosynthesis. However, recently reported values for the neutron lifetime deviate significantly from the systematic uncertainties. An experiment to measure the neutron lifetime with a pulsed beam is ongoing at BL05 (NOP). The lifetime is measured as a ratio of the electron events of the neutron decay to the $^{3}He(n,p)^{3}H$ events caused by ^{3}He gas precisely doped in a time-projection chamber (TPC). Physics data have been collected for about 4 weeks by the TPC in 2016. The data were analyzed by using Monte Carlo simulation [4].

3. Time Focusing of Ultra-Cold Neutrons (Rebuncher)

Neutrons produced in a pulse source tend to spread with time. We use this characteristic to distinguish neutron velocities by time of flight method, but in other words, the neutron density is going to be diluted after production. We have been developing a time-focusing device, the so-called "rebuncher", that makes it possible to re-focus neutrons on a certain position at a certain time to reproduce the initial density of the pulse neutron source [5]. The rebuncer consists of a gradient dipole magnet and a frequency variable RF spin flipper. A neutron flipped in a magnetic field gains/loses its kinetic energy of 60 neV for 1 T. Then we can increase or decrease the neutron kinetic energies by changing the frequency of the RF flipper with the time of flight. We have demonstrated neutron time focusing using UCN from the Doppler shifter at the Unpolarized branch. The setup of the rebuncer is shown in Fig. 1 [6]. UCNs from the Doppler shifter, which were reduced to 0.5 Hz, transported to the rebuhcer were flipped in the RF coils in the gradient dipole magnet to control its velocity and focus it on a detector position at the 3.2 m position downstream. The maximum field of the gradient magnet was 1.0 T. RF frequency was varied from 6 to 30 MHz, which correspond to 0.2 to 1.0 T, by synchronizing with time of flight of UCN to focus on time. TOF spectra of UCN with and without RF are shown in Fig. 2. It can be observed that UCNs in 1,000–1,200 msec were swept out and focused at 1,250 msec [6].

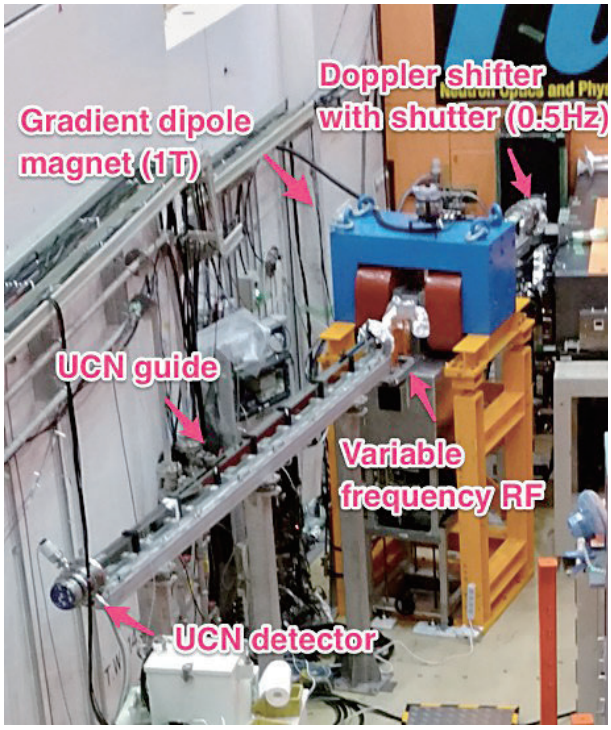

Figure 1. Experimental setup for the rebuncher for UCN [6]. UCNs from the Doppler shifter (0.5 Hz) through UCN guide (1.2 m) come to the rebuhcer, which is the RF coils in the gradient dipole magnet. Accelerated/decelerated UCN focuses on a UCN detector after the UCN guide (3.2 m).

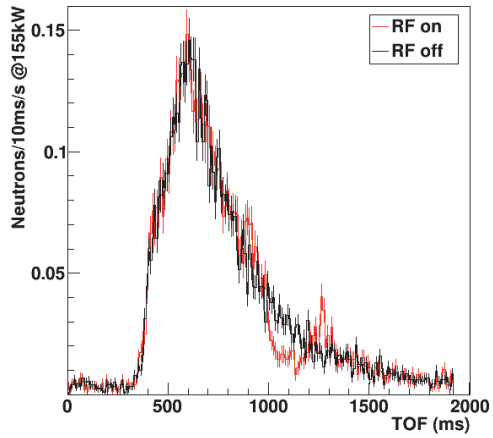

Figure 2. TOF spectra of UCN with and without RF are shown in here. It can be observed that UCNs in 1,000-1,200 msec were swept out and focused at 1,250 msec [6].

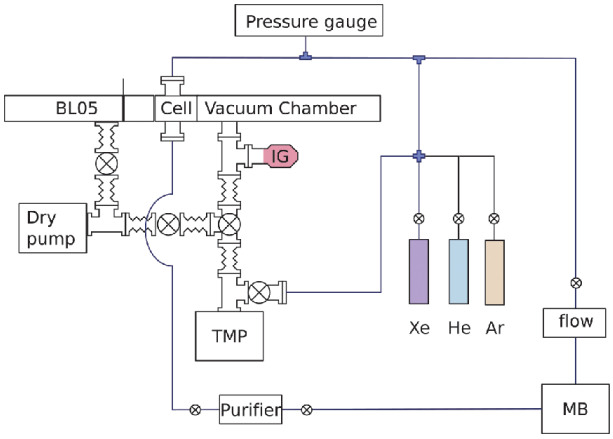

Figure 3. Gas handling system for the noble gas scattering experiment [7]. The circulation system with purifier prevents outgas contamination in the noble gas sample.

4. Search for Unknown Intermediate Force with Rare Gas Scattering

Since then, many experiments have been performed to measure the deviation from the inverse-square law of Newtonian gravity down to tens of micrometers. We are probing the short-range force in the nanometer scale by measuring the neutron scattering with noble gases.

In the simplest case with an unknown particle with a Compton wavelength of λ, the Yukawa force is expected to add to the Newtonian force so that the potential $V(r)$ between masses of m and M can be de- scribed as

$$V(r) = -G_N \frac{mM}{r}(1 + \alpha e^{-r/\lambda}) \quad (1)$$

where r is the distance between the masses, and G_N is the gravitational constant. Neutron scattering is a unique probe to measure the short-range forces because it has no charge and small polarizability. The extra forces described as eq. (1) increase forward angular distribution in neutron scattering.

Thanks to regulation change of the radiation control at MLF in 2016, gases, which can be activated, can be used as samples. For long-time measurement, we have implemented a gas circulation system, shown in Fig. 3 [7]. The 300 cm^3 of target gas with maximum pressure of 200 kPa was circulated with a gas purifier to prevent outgas contamination in the noble gas samples for long time measurements. We have measured 3 noble gases, He, Ar and Xe. The data are being analyzed.

References

[1] K. Mishima et al., "Design of neutron beamline for fundamental physics at J-PARC BL05," *Nucl. Instruments Methods Phys. Res. Sect. A*, vol. 600, no. 1, pp. 342–345, 2009.

[2] K. Mishima, "J-PARC Neutron fundamental physics beamline (BL05/NOP)," *Neutron Netw. news*, vol. 25, no. 2, pp. 156–160, 2015.

[3] K. Mishima et al., NOP2017, "Fundamental physics activities with pulsed neutron at J-PARC (BL05)", 2017. https://arxiv.org/abs/1712.06351

[4] N. Nagakura et al, "Precise neutron lifetime experiment using pulsed neutron beams at J-PARC", *Proc. Sci. 26th Int. Nucl. Phys. Conf.* 2016, to be published. arXiv:1702.03099.

[5] Y. Arimoto et al., "Demonstration of focusing by a neutron accelerator," *Phys. Rev. A - At. Mol. Opt. Phys.*, vol. 86, no. 2, pp. 4–7, 2012.

[6] S. Imajo et al., NOP2017 P46, "Time-focus Experiment of Ultracold Neutron by Improved UCN Rebuncher at J- PARC/MLF" 2017.

[7] N. Oi et al., NOP2017 P47, "A Search for Possible Deviations from Newtonian Gravity at the nm Length Scale Using Neutron-Noble Gas Scattering", 2017.

K. Mishima[1,2] on behalf of NOP collaboration

[1]*Neutron Science Section, Materials and Life Science Division, J-PARC Center;* [2]*Institute of Materials Structure Science, KEK*

BL06: Commissioning Status of VIllage of Neutron ResOnance Spin Echo Spectrometers (VIN ROSE)

1. Introduction

Neutron spin echo spectroscopy (NSE) uniquely enables us to explore the dynamics of various materials spatiotemporally. NSE has already achieved the highest energy resolution with neutrons as a probe [1], that is, the maximum Fourier-time has reached a submicrosecond.

Kyoto University and KEK have been installing two types of neutron spin echo (NSE) spectrometers with neutron resonance spin flippers (RSFs) at BL06 since FY2011, that is, a neutron resonance spin echo (NRSE) instrument and a modulated intensity by zero effort (MIEZE) instrument. NSE with RSFs is a rather new approach [2]. Furthermore, the combination of NSE and a pulsed neutron source makes it possible to scan a wide spatiotemporal space very efficiently. The beam line has been named "VIN ROSE" (VIllage of Neutron ResOnance Spin Echo spectrometers), which will spawn a new field of spectroscopic methods [3].

In FY2014, the first neutron beam was accepted, and the characteristics of the neutron guides were quantitatively investigated [4]. The first MIEZE signal was observed at the end of FY2014. Since then, various improvements and developments for the public use of BL06 have advanced.

In this report, the status of the MIEZE and NRSE spectrometers at BL06 in FY2016 is summarized. Figure 1 shows a recent photo of BL06.

2. Commissioning Status at BL06 in FY2016

Because the combination between time-of-flight neutron spectroscopy and MIEZE (TOF-MIEZE) is a novel approach, the quantitative verification is fundamentally important. In FY2015, the TOF-MIEZE signals were measured in various conditions, and compared with the theory [5]. The MIEZE signal with continuous neutron sources suffers from geometric restriction and this restriction can be relaxed by the TOF-MIEZE method, which was clearly shown experimentally with BL06. Following these investigations, a 400-kHz MIEZE was successfully generated [6]. In Fig. 2, the measured TOF-MIEZE signal and the corresponding power spectrum with 400 kHz is exhibited.

At the NRSE spectrometer, the two-dimensional ellipsoidal neutron-focusing supermirrors are now under development in close collaboration with the RIKEN center for advanced photonics. The ellipsoidal supermirrors are essential for NRSE with high-energy resolution, which will be installed before and after the sample position symmetrically to correct the path difference. The optical design is 1250 mm semi-major axis and 65.4 mm semi-minor axis with 900 mm length. Such a large ellipsoidal supermirror was unrealistic due to the difficulties in both the supermirror deposition and the substrate fabrication. Our strategy to develop such large ellipsoidal supermirrors is to assemble the segments deposited by the supermirror, shown in Fig. 3. We have established the necessary elemental technique [7], and achieved the reasonable characteristics evaluated by neutron reflectivity measurements.

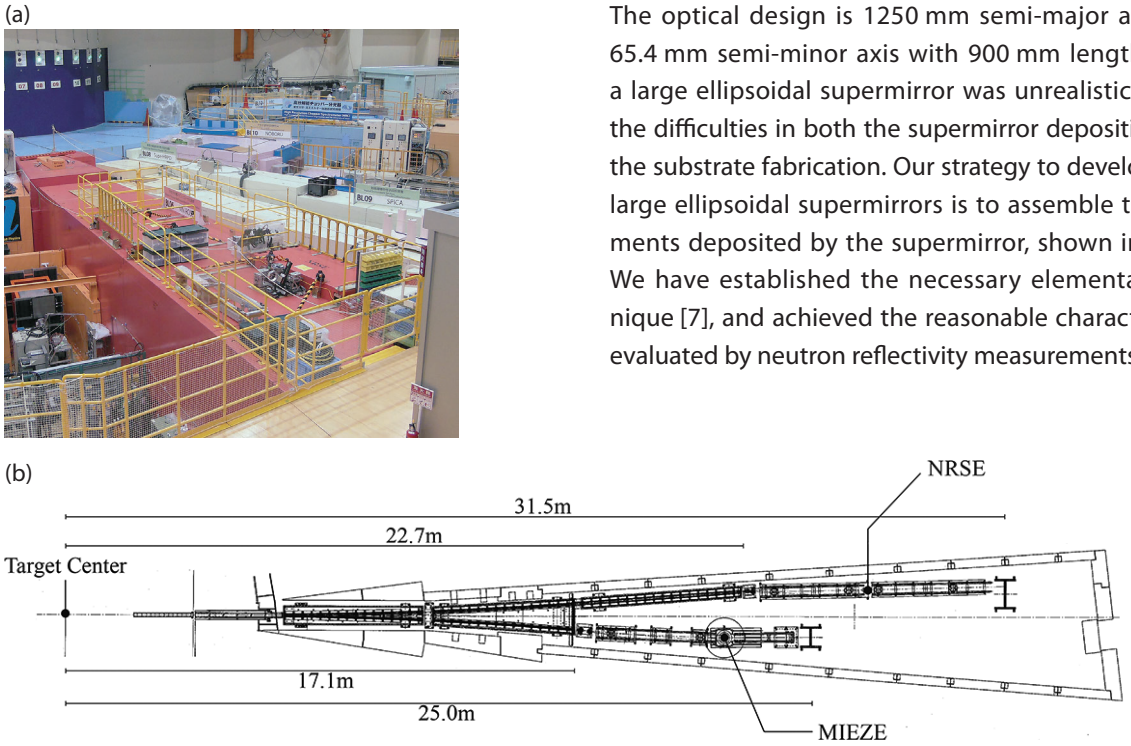

Figure 1. Current picture of BL06 (a), and a schematic top view of the MIEZE and NRSE beam line at BL06 (b).

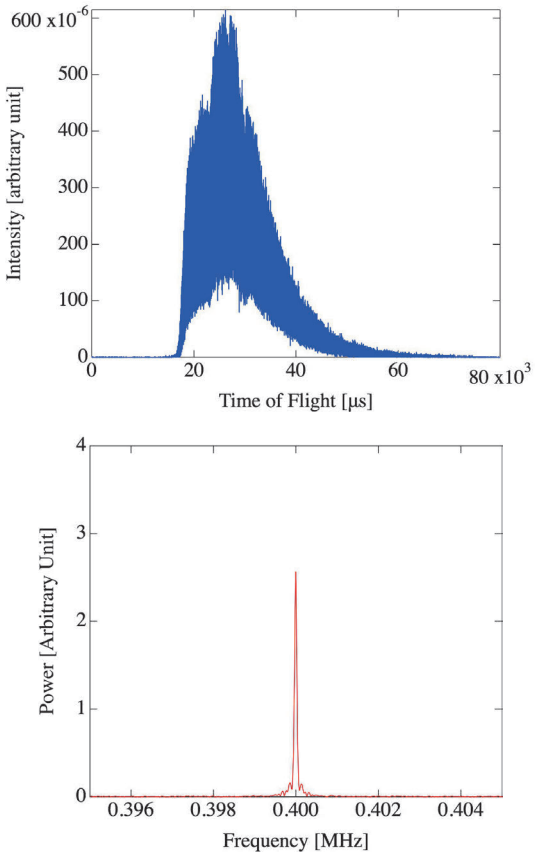

Figure 2. Top: Experimentally observed TOF-MIEZE signal with effective 400 kHz. Bottom: corresponding power spectrum by Fourier transformation.

3. Summary

This is a brief report about the current status of BL06 VIN ROSE. The main progress in FY2016 was the successful generation of a 400 kHz TOF-MIEZE signal. This result is very important for the public use, which is planned to start in FY2017. The other advancement at NRSE is the development of two-dimensional ellipsoidal neutron-focusing supermirrors, which has been

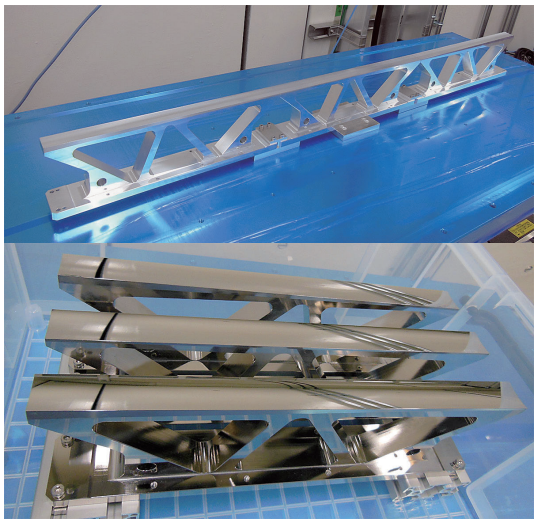

Figure 3. Top: 900 mm-length metallic substrate of elliptic mirror connected with three segments. Bottom: Segments with supermirror deposition.

a technical hurdle for the development of NRSE with high-energy resolution. Based on these successful achievements, we will work intensely on the commissioning of NRSE in FY2017.

References

[1] F. Mezei ed., Neutron Spin Echo, Lecture Notes in Physics, (Springer, Berlin) 128 (1982).
[2] R. Gähler and R. Golub, J. Phys. France, 49, (1988) 1195-1202.
[3] M. Hino, T. Oda, M. Kitaguch, N. L. Yamada, H. Sagehashi, Y. Kawabata, H. Seto, *Physics Procedia* **42**, (2013) 136.
[4] M. Hino et al., *J. Nucl. Sci. Tech.* accepted.
[5] T. Oda, Doctor Thesis, Kyoto University, (2016).
[6] T. Oda et al., *J. Phys. Soc. Jpn.* submitted.
[7] T. Hosobata et al., *J. Phys. Soc. Jpn*. submitted.

H. Endo[1], M. Hino[2], T. Oda[2], N. L. Yamada[1], H. Seto[1], and Y. Kawabata[2]
[1]Neutron Science Section, Materials and Life Science Division, J-PARC center, Institute of Materials Structure Science, KEK; [2]Kyoto University Research Reactor Institute

Status Report on Super High Resolution Powder Diffractometer, SuperHRPD

1. Introduction

In fiscal year 2016, seven general proposals and a part of the S-type project of 2014S05 were carried out at the BL08 beam line. The main activities included a high-temperature experiment using a vanadium furnace and a low-temperature experiment for magnetic structure analysis. In the S-type project, the commissioning of the 14-Tesla magnet delivered last fiscal year was conducted, and excitation test with neutron diffraction measurement could be carried out.

2. 14-Tesla Magnet commissioning

This 14-Tesla magnet is manufactured by Oxford Instruments PLC., and is designed specifically for high resolution measurement for SuperHRPD [1].

First, the 14-Tesla magnet was installed in the sample chamber of SuperHRPD, and the background was measured by empty sample. The proper adjustment of the incident beam slit made it possible to eliminate reflections from the copper tube of variable temperature inserts (VTI) in the immediate vicinity of the sample position. After that, Rietveld analysis was performed using standard powder sample (NIST Si SRM640d), and the reliability of the structural analysis was evaluated. Figure 1 shows the result of the Rietveld analysis of a standard sample. High-quality data with low background were obtained, and peak fitting allowed to obtain good results with Chi-square = 1.005734. Only the middle part of the backward detector bank divided into upper, middle and lower can be used from the window design of the magnet, the resolution $\Delta d/d \sim 0.06\%$ could be obtained (Fig. 2).

The magnet excitation test at the BL08 beam line was conducted in December 2016. Since it was the first excitation test after delivery, we spent considerable

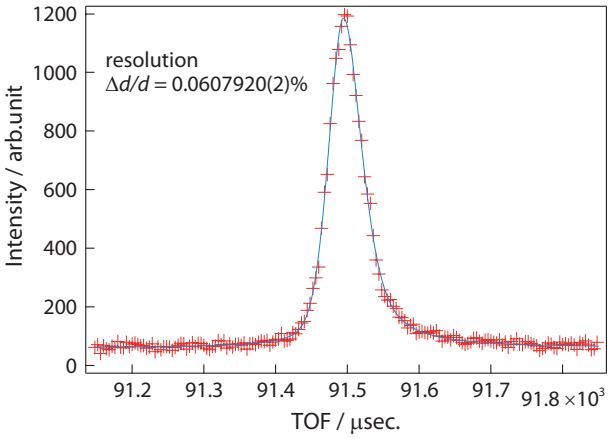

Figure 2. Resolution calculation of NIST Si data. A high resolution of $\Delta d/d \sim 0.06\%$ was obtained.

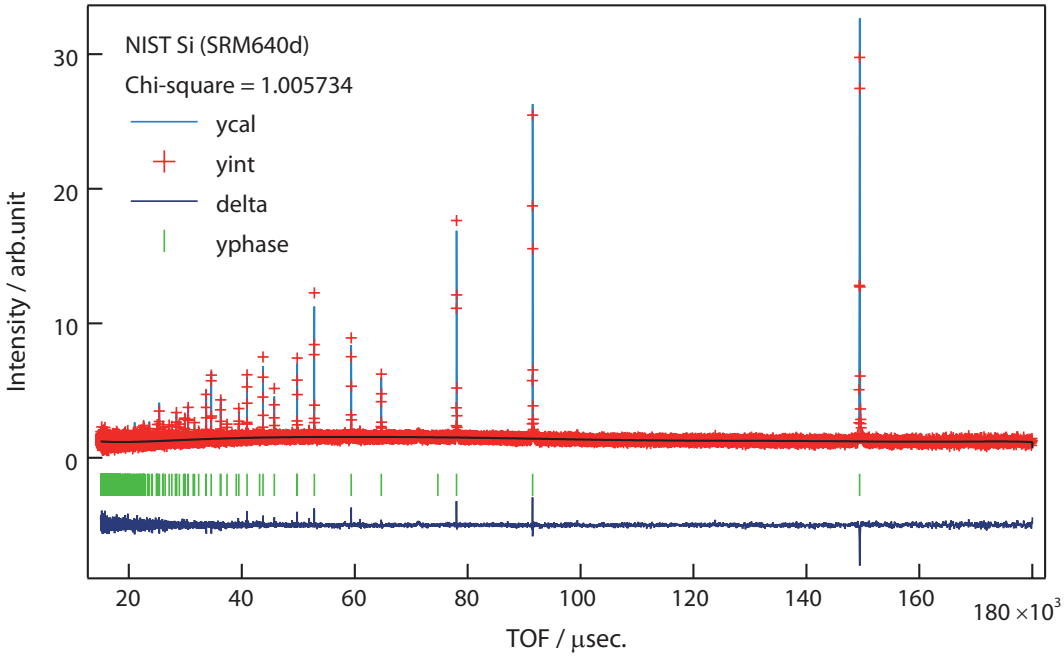

Figure 1. Result of the Rietveld analysis of a standard sample NIST Si. Despite installing the 14-Tesla magnet, very high-quality data with low background were obtained.

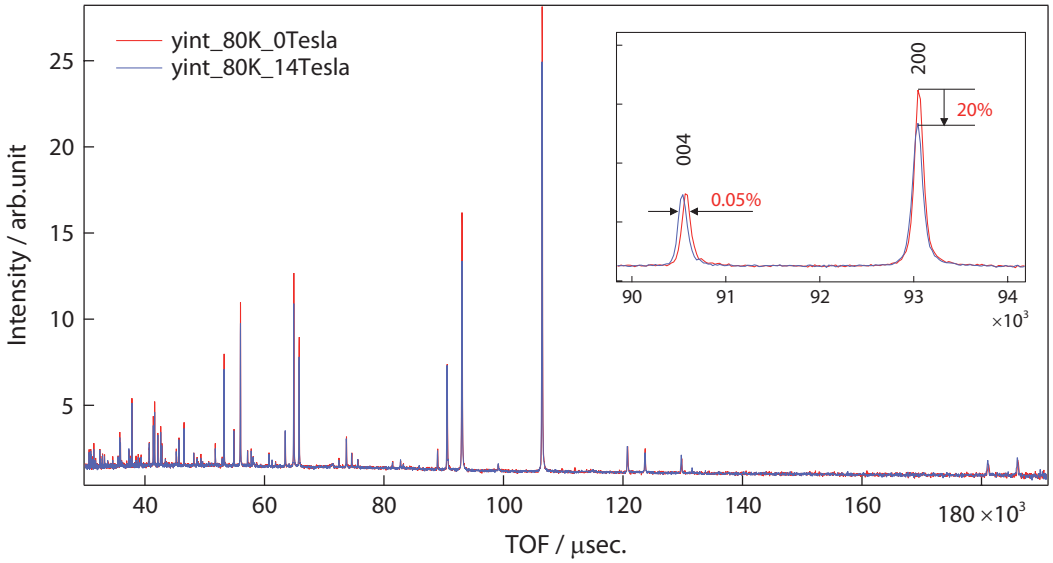

Figure 3. Diffraction pattern of Co oxide. High-quality data were obtained in low background. It can be seen at a glance that the 004-reflection shifted by 0.05% and the 200-reflection decreased by 20% with intensity dependent on the magnetic field.

time allocating various wires or piping and devices. The magnet has very large capacity, requiring one week for pre-cooling with liquid nitrogen and transferring liquid helium. An excitation experiment by on-beam was also performed, and even in the excited state, the background was low and it was possible to collect high-quality data (Fig. 3).

The volume of the magnet is so large, requiring a large amount of liquid nitrogen and helium for pre-cooling, and it need to exchange and transport the refrigerant vessel so many times. Therefore, to open this magnet for general users, it will take a little more time because it is necessary to establish an environment for efficient experiment preparation.

Reference

[1] S. Torii, P. Miao, S. Lee, Y. Ishikawa, M. Yonemura and T. Kamiyama, MLF Annual Report 2015, 79-80 (2015).

S. Torii[1,2], S. Lee[1,2], and T. Kamiyama[1,2]

[1]Neutron Science Section, Materials and Life Science Division, J-PARC center; [2]Institute of Materials Structure Science, KEK

BL09: Current Status of the Special Environment Powder Diffractometer, SPICA

1. Introduction

SPICA is a dedicated beam line for battery study using the *operando* technique [1]. Over the last few years, structure changes in electrode materials under operative conditions have been observed in various charge – discharge rates conditions, and they and their related investigations have already been reported [2-6]. In FY 2017, the neutron intensity will increase to 300 kW by a new structural mercury target. This higher neutron intensity will make it possible to collect *operando* data with shorter time reaction. Neutron monitor data is important to normalize TOF (Time-Of-Flight) diffraction data, especially related to short time-resolved data. To keep the reliability of the *operando* diffraction data, a high-efficiency and high-count rate neutron monitor detector is necessary. nGEM (Gas Electron Multiplier) detector [7] is one of the candidates for monitor detector, which was installed in SPICA. Some test data was collected. The monitor intensity of nGEM was 10^2 times higher than the one of the ^{3}He gas detector (efficiency: 10^{-3}) with no counting loss against the direct beam of BL09.

2. Commissioning of the nGEM detector

The commissioning of the nGEM detector was carried out on SPICA. For the commissioning, the nGEM detector was put on the sample position. As the initial step, the operating high voltage was determined by counting rate scanning with changing the negative high voltage. Figure 1 shows the counting rate response against the high voltage scanning. The plateau region was obtained from −2250 to −2400 V. From this result, the operating voltage was fixed at −2300 V.

The detection area was checked by observing a direct beam at the sample position. Figure 2 shows the two-dimensional imaging data and the one-dimensional beam profiles. A beam size was defined by Region-Of-Interest (ROI) which the region of over 3% intensity of the maximum value in the X projection (Y projection) distribution. In the condition of no beam shaping by slits, the beam size was 40.0 (W) × 77.6 (H) mm^2. The beam center was slightly shifted from the center of the detector, however, it didn't directly mean that the beam center was misaligned since this shifted value included the error of setting up the detector.

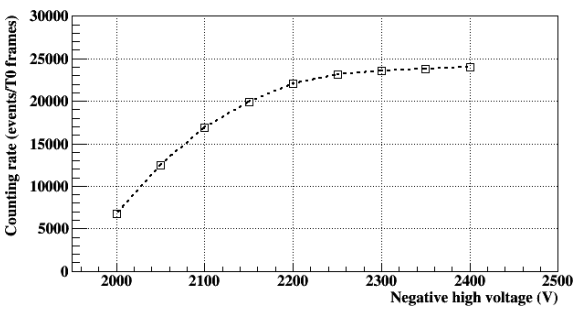

Figure 1. The high voltage dependence of count ratings. The counting rate was normalized with the number of T0 frames.

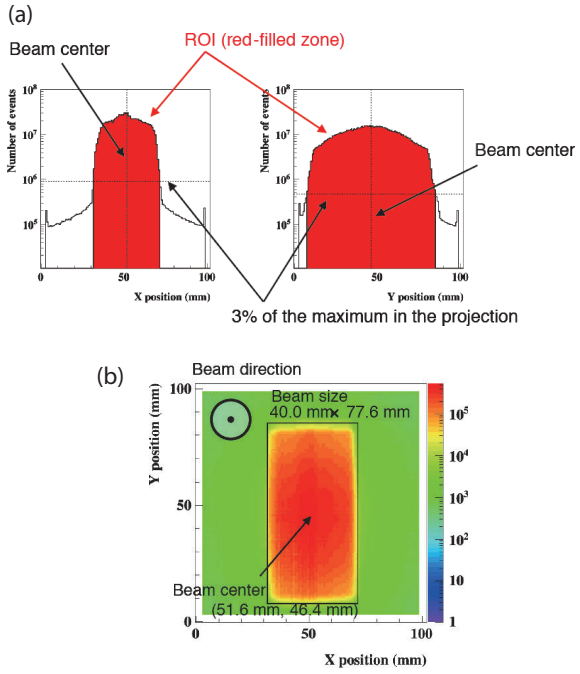

Figure 2. The beam profile at the sample position on SPICA. The all TOF data was merged at each position. (a) X, Y-projection beam profile. (b) Two-dimensional imaging map.

3. Installation of nGEM detector

SPICA had a ^{3}He gas detector (efficiency: 10^{-5}) as a beam monitor at the 48-m position from the decoupled poisoned moderator. Figure 3(a) shows the geometry of ^{3}He gas detector on the SPICA. This detector was located in a small cave at the last section of the downstream radiation shields. The size of the cave was 400 (W) × 603 (H) × 550(D) mm^3. And two quadrant slits were put on the upstream and downstream position from the ^{3}He gas detector. A 10-mm sintered B_4C radiation shield, which decrees background from the upstream and has a beam hall (100 (H) × 50 (W) mm^2), was installed just outside of the cave outlet.

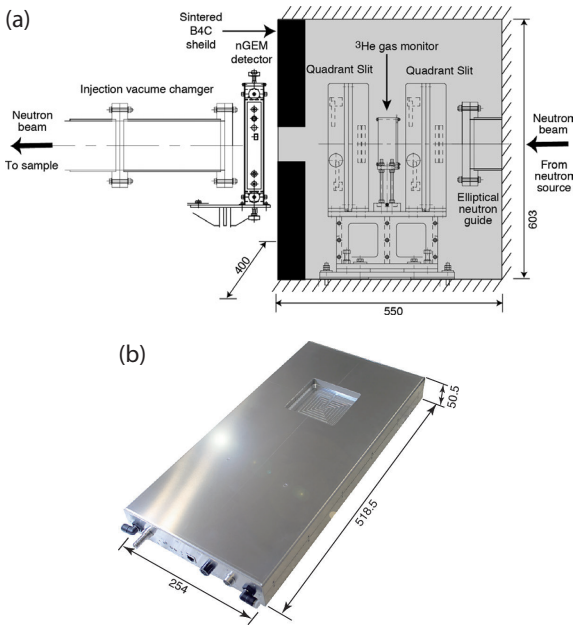

Figure 3. The picture of the installed nGEM monitor at 48.5 m position. (a) The geometry of each detectors location on the SPICA beamline. The dark-colored area is in radiation shields. (b) The external view of nGEM detector component made by BBT under license by KEK.

Figure 3(b) shows the nGEM detector component. This box contains the detector and an all-in-type electronic device to treat detection signals. The concave surface is the detector area. The size of the box is 50.5 (H) × 518.5 (W) × 254 (D) mm^3. This box size was too large to fit into the cave to substitute the ^{3}He gas detector for nGEM. Therefore, the nGEM (efficiency: 5 × 10^{-3}) detector was installed on the outside of the cave (shown in Fig. 3(a)). The position of nGEM detector was at 48.5 m from the moderator. As a result, the ^{3}He gas detector and the nGEM detector could be used as incident neutron monitor detectors at the same time on SPICA. This geometrical setting was helpful for an ability test of the nGEM detector.

4. Comparison between ^{3}He and nGEM as monitor detector

Figure 4 shows the incident direct beam profile against TOF for 5 minutes of collection time. The intensities from each detector were consistent with the efficiency of detectors respectively. The data of nGEM reached 10000 counts in the highest region and had a high amount of statics even within the 5 minutes. The

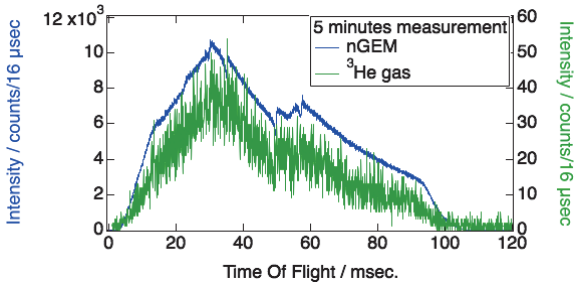

Figure 4. Time-Of-Flight dependence of an incident neutron beam on SPICA.

current goal of minimum time-resolved is 1 minute on SPICA. This high static provides reliability for normalization of the *operando* diffraction data in 1 minute. This new monitor detector will be expected to work effectively on SPICA. In addition, reviewing nGEM as a transmission detector on SPICA for a small angle scattering has been considered. In the near future, another nGEM detector will be installed at the downstream of the sample position.

Acknowledgement

This work was supported by the Research and Development Initiative for Scientific Innovation of New Generation Batteries (RISING2) project of the New Energy and Industrial Technology Development Organization (NEDO). The neutron scattering experiment was approved by the Neutron Scattering Program Advisory Committee of IMSS, KEK (Proposal No. 2014S10).

References

[1] M. Yonemura, et. al., J. Phys. Conf. Ser., 502(1) Article# 012053 (2014).
[2] S. Shiotani, et. al., J. Power Sources., 325, 404-409 (2016).
[3] S. Taminato, et. al., Scientific Reports., 6, Article# 28843 (2016).
[4] T. Matsunaga, et. al., Chem. Mater., 28(12), 4143-4150 (2016).
[5] K. Kino, et. al., Solid State Ionics., 288, 257-261 (2016).
[6] T. Matsunaga, et. al., J. Phys. Chem. Lett., 7, 2063-2067 (2016).
[7] H. Ohshita, et. al., JPS Conf. Proc., 8 Article# 36019 (2015).

M. Yonemura[1,2,3], H. Ohshita[1,2], Y. Ishikawa[1,2], S. Torii[1,2], and T. Kamiyama[1,2,3]
[1]Institute of Materials Structure Science, KEK; [2]Neutron Science Section, Materials and Life Science Division, J-PARC Center; [3]Sokendai (The Graduate University for Advanced Studies)

BL10: NOBORU

1. Introduction

In FY 2016, in addition to the postponed proposals from FY 2015, 13 general use and 1 proprietary use proposals were carried out at NOBORU. There was no interruption of the user program due to the instrument trouble.

This year, we added two filters for resonance absorption experiments to the present filter exchanger [1]; one is a 2-mm thick cadmium (Cd) plate and the other one is a 50-μm thick tantalum (Ta) and indium (In) foils sandwiched by a couple of 1-mm thick copper (Cu) plates. Figure 1 shows the installed filters on the exchanger at around 7.4 m position of the beamline.

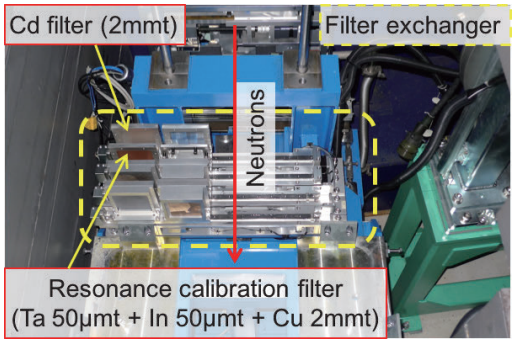

Figure 1. Two newly installed filters for resonance absorption experiments.

2. Epicadmium neutron spectrum measurement and imaging experiment using filters

Epicadmium neutrons, neutrons of kinetic energy higher than the effective cadmium cut-off energy of 0.5 eV, are useful not only for radiography of thick objects due to its high-penetration power but also for elementary analysis using resonance absorption of nucleus. Resonance absorption imaging, being used to visualize a spatial distribution of elements and/or temperature within a sample, is one of the important applications of an intense short-pulse neutron source. To perform resonance absorption imaging, however, the efficiency of the epicadmium neutrons for the existing counting type two-dimensional (2D) detector is insufficient. The 2012 model lithium-6 time-analyzer neutron detector (LiTA12) system [2], based on a lithium glass scintillator and multi-anode photomultiplier tube, has the highest neutron efficiency among the detectors for pulsed neutron imaging. The LiTA12 system provides high count rate of up to 10M cps, as seen in Fig. 2, which shows measured spectra of the resonance calibration filter with the Cd filter.

Neutron transmission images of the test targets made by gadolinium (Gd) and gold (Au) are shown on the left and right of Fig. 3, respectively. The image of the Gd was obtained by 10-minute irradiations with and without the target, then the former image was divided by the latter. The transmission image of the Au target was also obtained by irradiations lasting 17 hours with the target and 15 hours without it. The detailed experimental procedures have been covered in the literature [3]. Although the image of the Au target was not as clear as the Gd target due to lower statistics caused by the narrow energy range, the improvement of the spatial resolution was also significant in the resonance energy region. The original spatial resolution of 3 mm (by pixel) was drastically improved by the center-of-gravity calculation using event-recorded data of neutron detection. The estimated spatial resolution of the LiTA12 system with the center-of-gravity calculation was 0.7 mm for the energy at 4.9 eV.

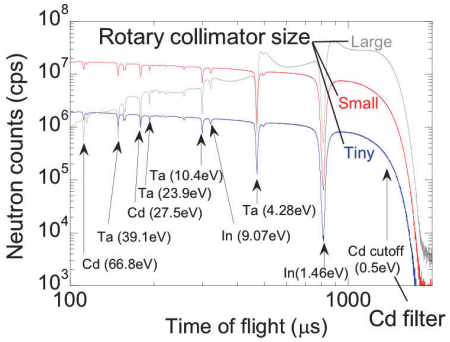

Figure 2. Measured resonance absorption spectra of Ta and In with Cd filter using the LiTA12 system.

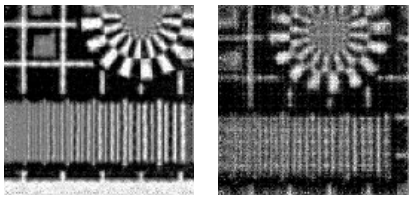

Figure 3. Neutron transmission images of Gd (left) and Au (right) targets. The neutron energy ranges were less than 0.1 eV for Gd and 4.79 – 5.01 eV for Au.

References

[1] M. Harada et. al., JPS Conf. Proc. **1**, 014015 (2014).
[2] S. Sato et. al., Physics Procedia **60** (2014) 363.
[3] T. Kai et. al., submitted to Physica B (Proceedings of ICNS2017).

K. Oikawa and T. Kai
Neutron Science Section, Materials and Life Science Division, J-PARC Center

BL11: *in-situ* Diffraction above 20 GPa with Diamond Anvil Cell

1. Introduction

Since the start of the beamline operation at 2013, developments to extend the accessible pressure and temperature range have been conducted and now we can routinely collect diffraction data up to 20 GPa. On the other hand, data collection above 20 GPa is still difficult. This year, we were determined to overcome this limit by using a diamond anvil cell (DAC) coupled with neutron optics, newly designed for it.

The diamond anvil cell is a high-pressure device, in which the sample is sandwiched and compressed by a pair of single crystal gem diamonds. Thanks to the hardness of the diamond and the effective concentration of the applied force to the sample, the device can generate pressures of more than 300 GPa despite its compactness (it is portable by one hand). Due to this advantage, the device is widely used in many synchrotron facilities. However, its use in neutron experiments is limited because the sample is so tiny (typically less than 0.01 mm^3) that a significant signal cannot be detected. To overcome this problem, we have developed the followings:

i) Increased the sample size by designing a new DAC equipped with large diamonds.
ii) Increased the incident beam flux by focusing the neutron beam with a supermirror guide.
iii) Increased the quality of the diffraction pattern by reducing the diamonds' Bragg spots contamination using radial collimators with gauge length of 1.5 mm.

The details of each development are described in the following sections.

2. Diamond anvil cell (DAC)

Figure 1 shows the diamond anvil cell, newly designed for time-of-flight (TOF) measurements. The sample is sandwiched between a pair of 0.35 carat diamonds (solid pink in the Fig. 1), which are conically supported from the backside by sintered diamonds (shaded pink). Both diamonds are kept coaxial during compression with a piston and a cylinder (blue). This assembly is encased in a load frame to apply force of maximum 100 kN (shaded). The pressure is generated by rotating the breech of the load frame. The piston-cylinder assembly is removable from the load frame, so that we can load gas in the sample chamber prior to the compression with a gas-loading system at the National Institute for Material Science.

Figure 2 shows the pressure generation curve when using diamonds with culet size of ϕ1.5 mm. In this case, the sample size is typically 0.7 mm in diameter and 0.14 mm in thickness. At present, we have succeeded in generating pressure of 30 GPa.

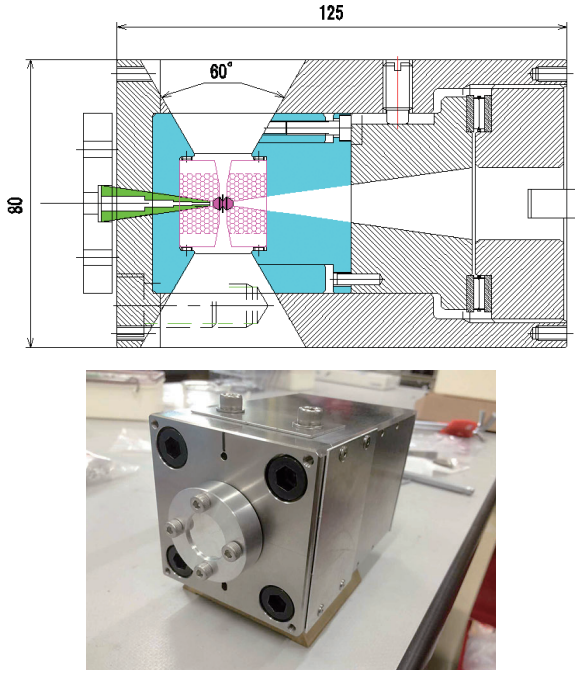

Figure 1. Cross section (top) and the photo (bottom) of DAC, newly designed for TOF neutron diffraction.

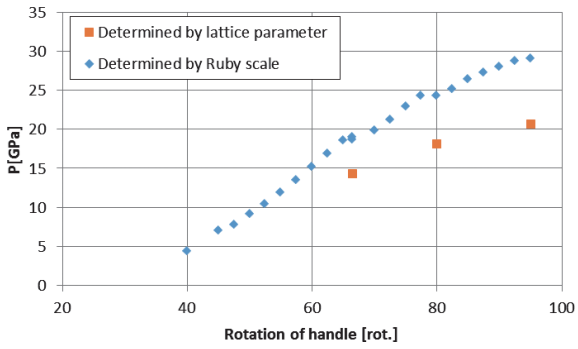

Figure 2. Pressure generation performance when using diamonds with culet size of ϕ1.5 mm.

3. Neutron optics

A focusing guide, newly designed for DAC, consists of Ni/Ti supermirrors with critical index of m = 4.0. To avoid unwanted degradation of the resolution of the diffraction pattern taken with horizontal scattering geometry, only the top and bottom glasses were coated

with Ni/Ti. The total length was 1.2 m and the focal point was at 60 mm distance from the exit of the mirror. Figure 3 shows the performance of the mirror. The effects on the intensity and resolution were evaluated by collecting the diffraction pattern of a tiny nano-polycrystalline diamond (NPD) and Si power (NIST SRM 640d), respectively. When the newly designed focusing mirror was used (see FD2 in the Fig. 3), the intensity increased by a factor of four at about $d = 2$ Å (corresponding to c.a. 20000 μs), compared to normal slits, while the resolution decreased by a factor of 1.5.

A set of radial collimator with gauge length of 1.5 mm was also manufactured to reduce the intensity of diamonds' Bragg spots, which contaminates the diffraction pattern. By coupling with the incident collimator with a hole of ϕ0.7 mm, the volume contributing to diffraction can be defined into the dimension of 0.7 mm in diameter and 1.5 mm in thickness. Even by using these optics, the contamination of the diamond peak could not be avoided (Fig. 4), but the contamination degree was decreased.

Figure 5 shows the diffraction pattern of ice VII obtained by masking these spots. We have managed to obtain diffraction patterns of ice VII up to about 20 GPa. Significant shift of the Bragg peaks was found at high pressures. Unfortunately, the peaks turned out to be very broad, probably due to the inhomogeneous pressure distribution in the sample chamber. Besides, it is known that the Bragg reflection of diamond anvils causes significant loss of the incident beam at certain energies (the so-called diamond dip) [1], which makes the quantitative analysis of diffraction patterns difficult. Now we are trying to fix this problem by collaborating with an author in Ref. 1.

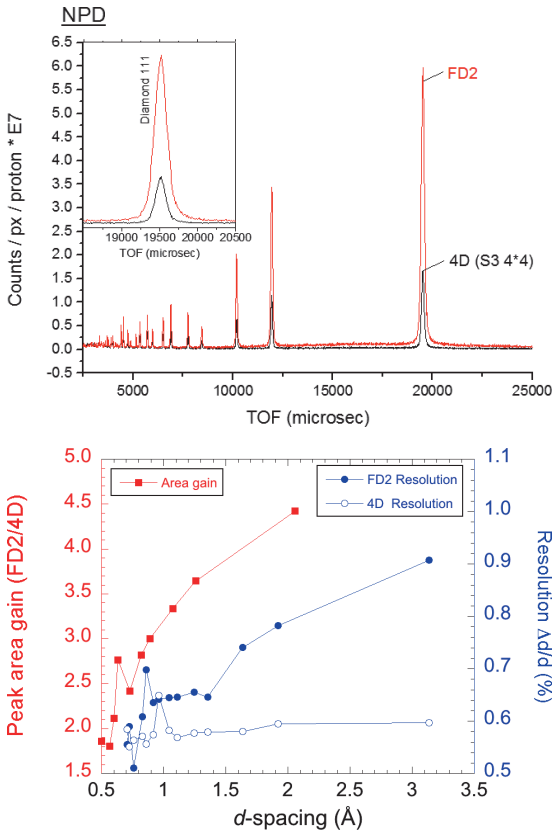

Figure 3. (Top) Diffraction patterns of NPD taken with different incident optics (4D: normal slit, FD2: newly designed focusing device). (Bottom) Intensity gain and resolution.

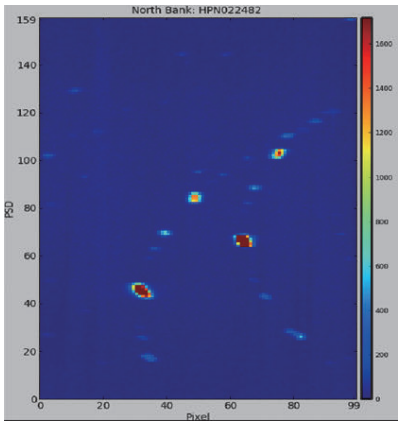

Figure 4. A two-dimensional pattern obtained with DAC.

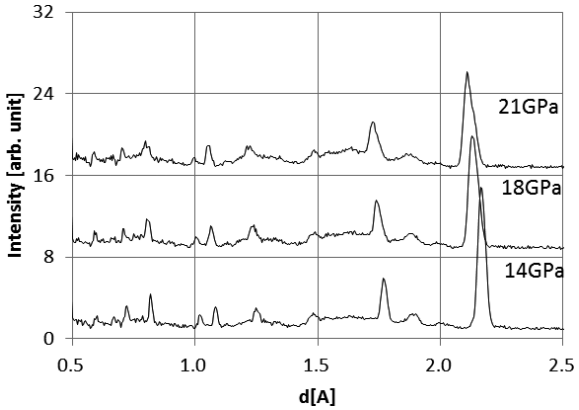

Figure 5. Diffraction patterns of ice VII obtained with DAC after masking diamonds' Bragg spots.

Reference

[1] M. Guthrie, *et al.*, J. Appl. Cryst., 50, 76 (2017).

T. Hattori[1], A. Sano-Furukawa[1], K. Funakoshi[2], J. Abe[2], and S. Machida[2]
[1]*Neutron Science Section, Materials and Life Science Division, J-PARC Center;* [2]*Neutron Science and Technology Center, CROSS*

HRC and Neutron Brillouin Scattering

1. Introduction

Neutron Brillouin scattering (NBS) is inelastic neutron scattering close to the forward direction, and is effective for observing coherent excitations in non-single-crystal samples, such as ferromagnetic spin waves in powder samples and acoustic phonons in liquids and polycrystalline samples. In order to detect such excitations, access to the energy-momentum space near to (000) is required. Access to such energy-momentum space can be achieved by using low-angle detectors, high-energy neutrons and high resolution. For example, the scattering intensity from ferromagnetic spin waves remains close to (000) only and rapidly decays with increasing the momentum Q by the powder average. Since the first success of NBS on HRC [1], HRC has been improved [2, 3]. Here, we describe recent improvement works for NBS on HRC [4].

2. Recent improvements for NBS on HRC

Since the solid angle of detecting area for NBS experiments is limited to very low scattering angles, improvements to gain scattering intensities are essential. We made some efforts to gain the neutron flux in various ways.

The configuration of the detectors for NBS was improved. In the low-angle detector bank, detectors are aligned in a double-layered configuration to increase the counting rate: the detectors in the front layer face the sample and the detectors in the rear layer are placed just at the lower stream of the front layer. The counting rate for the double-layer configuration is increased by a factor of 1.4 to that for the single layer configuration for the incident neutron energy of E_i = 100 meV as shown in Fig. 1(a). The detectors are mounted in the scattering angle range of 0.6 – 5.1°.

The Fermi chopper is composed of a slit package, which is a layered assembly of components of shielding plates and spacers sandwiched between curved walls. The slit package of a vertical slit, a cross section with dimensions 75 mm (width) × 64 mm (height) and length of 100 mm, is inserted to the side of a cylindrical rotor, with diameter 125 mm, which rotates around the vertical axis. The rotor and the slit package are distorted by the rotation stress at the frequency up to f = 600 Hz. In the Fermi chopper in the previous setup, the slit package, where the sum of the widths of the components equaled 75 mm, was inserted. In this assembly, a large distortion of the slit package is caused

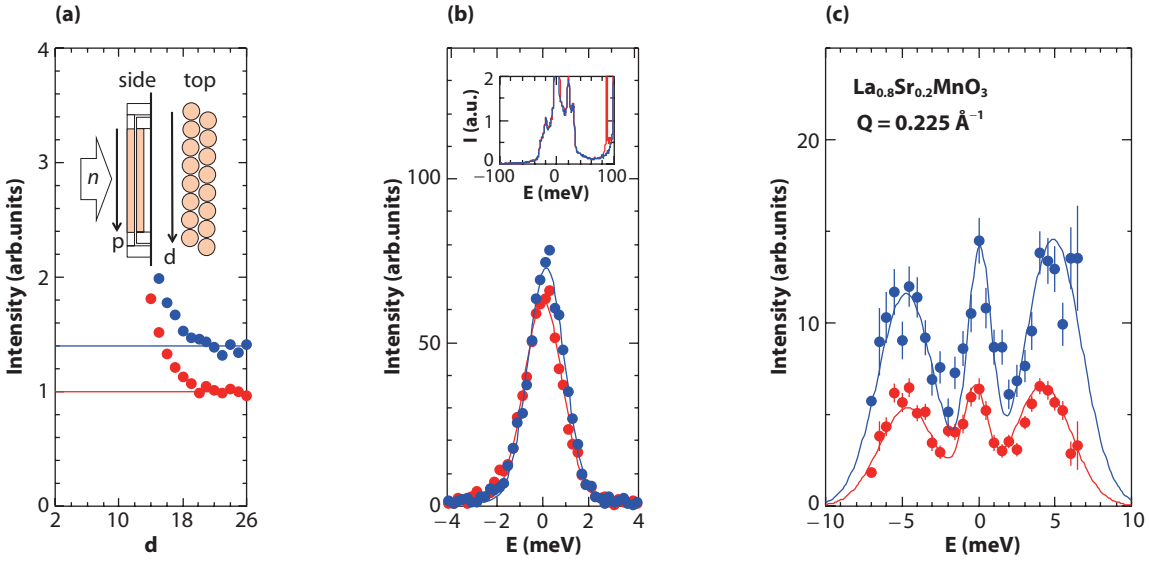

Figure 1. Improvement for the NBS experiments on HRC. Blue and red marks indicate the present and previous setups, respectively. (a) Detector configuration. Observed scattering intensities from a vanadium sample, which are integrated over the positions p along each detector, are plotted as a function of the detector number d, where d = 2 and 26 correspond to the scattering angles of 0.6 and 2.8°, respectively. Due to an incomplete mask for the sample, scattered neutrons spread from low angles. The intensities at high angles (large d) show the actual intensity gain. (b) Improvement of Fermi chopper. Elastic profiles of the vanadium are plotted with curves fitted with Gaussian functions. The inset shows inelastic spectra from the vanadium observed at 4 m from the sample using the 1.5° collimator. (c) Total intensity gain. Ferromagnetic spin waves in $La_{0.8}Sr_{0.2}MnO_3$ were observed with the present and previous setups. The solid lines are curves fitted with the scattering function for resolution-limited spin waves.

by the rotation stress. At present, the slit package's width (the sum of the widths of the components) was increased to 78.8 mm by increasing the number of the components, then pressed to the width of 75 mm and inserted into the rotor. It was visually confirmed that the distortion after rotation up to 600 Hz was greatly reduced. Figure 1(b) shows the inelastic spectra of the elastic scattering from a vanadium sample observed for the present and previous setups with E_i = 100 meV, f = 600 Hz with the detectors located at 5.2 m from the sample, and with 0.3° collimator. This change improved the energy resolution from ΔE = 2.0 meV to 1.9 meV, and the integrated intensity was increased by a factor of 1.1. In addition, the transmitted intensity at the half rotation of the Fermi chopper, which was observed at the energy transfer around E = 90 meV for the previous setup, disappeared in the present setup due to improved slit structure, and therefore, the observable energy-transfer range was also expanded.

The background noise was reduced at the scattering angles down to 0.6° for NBS experiments by using a collimator with collimation of 0.3°. This collimator composes a vertical slit of cadmium sheets with thickness of 0.1 mm. The collimation of w/L = 0.3° was realized with sheet spacing of w = 0.8 mm and collimator length L = 150 mm. The transmission of the 0.3° collimator was only 20% of the designed value, because it was very hard to maintain the flat sheets of thin cadmium. If the distortion of the cadmium sheet is constant, the transmission should be increased for longer L with the collimation w/L unchanged. A long collimator was introduced, where w = 1.55 mm, L = 295 mm. At present, we can select one of the four: the new long 0.3° collimator, the previous short one, the 1.5° one, and the blank. The 1.5° collimator is used for conventional experiments using detectors located at 4 m from the sample and at the scattering angles down to 3°.

3. Measurement of improved performance

In order to evaluate the performance of the system improved by the present works, an NBS experiment for a polycrystalline sample was performed. The sample is a nearly-cubic perovskite ferromagnet $La_{0.8}Sr_{0.2}MnO_3$ with ferromagnetic transition temperature T_C = 319 K [1]. The measurement was performed at 245 K (< T_C) with E_i = 100 meV at f = 600 Hz, by using the double-layered detector system, the improved Fermi chopper, and the long 0.3° collimator. Figure 1(c) shows an observed spectrum, where the background measured with an empty can was subtracted. The spectrum is well fitted to the scattering function for resolution-limited spin waves [1]. Also, the observed spectrum in the same condition but by using the single-layered detector system, the previous Fermi chopper, and the short collimator [1] is plotted in Fig. 1(c). This spectrum is also fitted to the scattering function for resolution-limited spin waves. From the intensity factors obtained by the fits, a factor of 2.4 was obtained as an intensity gain. Since the gain for the double-layered detector system to the single one is 1.4 and the gain for the improvement of the Fermi chopper is 1.1, the gain for the long collimator to the short one can be estimated to be 1.6.

4. Summary

By the success of NBS experiments on the HRC, some scientific results have been obtained from studies on spin waves and phononic excitations, mainly under the initially realized conditions for NBS [1-3]. By using the improved conditions, further results are expected. The NBS option differentiates the HRC from other chopper spectrometers, and opens opportunities for contributing to the current science by measuring coherent excitations from non-single-crystal samples.

References

[1] S. Itoh et al., J. Phys. Soc. Jpn. 82 043001 (2013).
[2] S. Itoh et al., J. Phys. Soc. Jpn. 82 SA034 (2013).
[3] S. Itoh et al., AIP Conf. Proc. in press.
[4] S. Itoh et al., J. Phys.: Conf. Series, in press.

S. Itoh[1,2], T. Yokoo[1,2], T. Masuda[3], H. Yoshizawa[3], M. Soda[3], M. Yoshida[3], T. Hawai[1,2], D. Kawana[3], R. Sugiura[3], T. Asami[3], and Y. Ihata[4]
[1]Institute of Materials Structure Science, KEK; [2]Neutron Science Section, Materials and Life Science Division, J-PARC Center; [3]Tne Institute for Solid State Physics, The University of Tokyo; [4]Technology Development Section, Materials and Life Science Division, J-PARC Center

YUI and HANA: Control and Visualization Programs for HRC

1. Introduction

We have constructed a computing system and software environment to control accessories and to handle neutron signals from position sensitive detectors (PSD) for High Resolution Chopper spectrometer (HRC), installed at BL12 in 2010 [1, 2]. In the software environment, the comprehensive-control program "YUI" and the visualization program "HANA" play central roles [3]. In this report we describe their basic constructs and characteristic functions at present, and briefly explain the future plans.

2. YUI

The comprehensive control program YUI (*Yasashii* or *Yoku-dekita* User Interface) has three fundamental functions: measurement by sequential operation of DAQ middleware (DAQ-MW) [4], control of the devices, and logging of their status. The main window of YUI is shown in Fig. 1. All the related accessories are controlled by YUI, although the communication protocols for the accessories are different. As a key solution, we installed a "device server," a virtual machine which intervenes between YUI and the corresponding accessory. The installed device servers work for DAQ-MW, MLF-server, Fermi chopper, Soller collimator, oscillating radial collimator, goniometer and temperature controller. Here, the MLF server is regarded as the accessory that gets the proton number for the normalization of incident neutron numbers. The device servers of the last two are prepared for each sample-environment apparatus, such as the GM-type refrigerator and ^{3}He circulation-type refrigerator [5]. The device servers of the T0 chopper and the vacuum chamber controller are only for data logging.

Users can control the devices in either of two ways. One is the manual control. For example, when setting frequency and incident energy of the Fermi chopper, users directly enter a command using the specialized control graphical user interface (GUI) as shown in Fig. 2. In this GUI, all the necessary functions on user-experiments are integrated and implemented. Such a GUI has been prepared together with the installation of a new accessory.

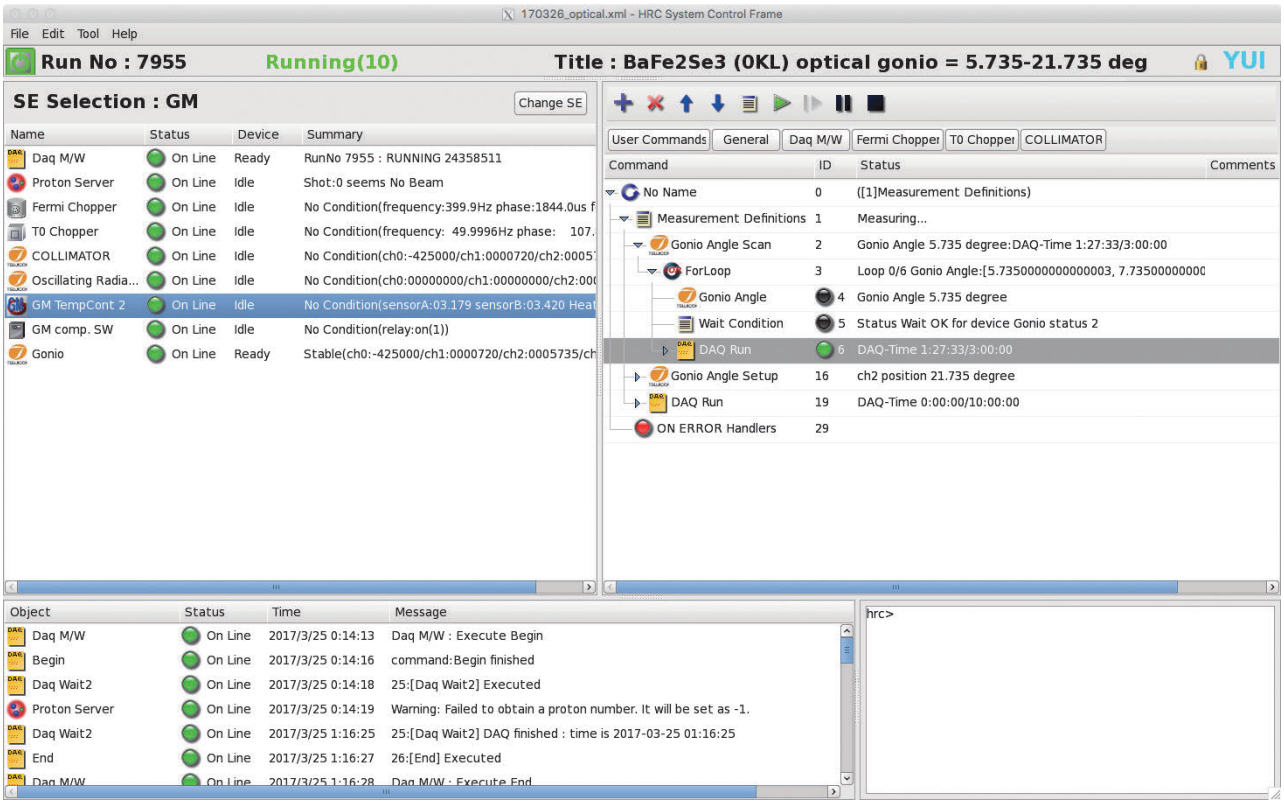

Figure 1. Main window of YUI. It consists of three display areas: list of the activated device servers (top-left), sequence edited by users and its progress states (top-right), and messages communicated with devices, called system log (bottom).

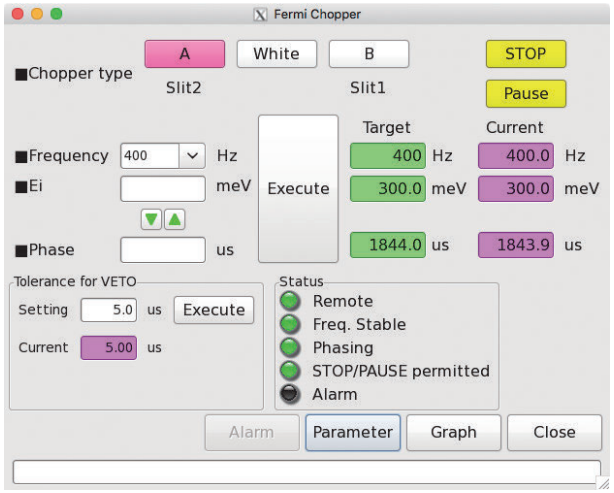

Figure 2. GUI to control Fermi chopper.

The other way is the automatic control by executing a macro of sequential commands. We prepared built-in macros called "user-commands" for users to edit their macro. Users can perform their experiment by just arranging these user-commands in an xml file. One user-command consists of a set of basic commands which are prepared for each device. For example, "DAQ Run" is one of the typical user-commands. While users execute DAQ Run, the basic commands of DAQ-MW: configure, begin, DAQ wait, end, unconfigure, and increment run number are executed in sequence. Furthermore, as an application of user commands, "Gonio-angle-scan" is a convenient user-command that consists of DAQ Run and a series of basic commands related to goniometer control.

Set and current values of the devices are continuously monitored and recorded to the log files every 5 seconds. The obtained log data can be graphically displayed on a browser page named "Log-visualizer". This helps users to check the time variation of the current values of the devices, such as stability of the phase of the Fermi chopper.

After a measurement, a report file is created. Not only the times of beginning and completion of the measurement, i.e. begin and end times of DAQ-MW, but also the set and monitored values of all activated devices are recorded to the report file.

In addition, the effective measurement time and the proton number, which is obtained from the server in MLF intranet [6], are also recorded. The proton number is used for normalization of the measured intensity.

3. HANA

HANA (HRC ANAlyzer) is a data-reduction program for the initial data handling and the data visualization. The basic flow is creation of intensity-histogram data from the event data, sequent reduction of the histogram data, and visualization of the dynamical structure factor in four-dimensional space.

On HANA, one detected neutron is treated as a data set labeled with three parameters of (d, p, t), where d, p, and t denote the PSD number, position on the PSD, and time of flight (ToF) of the neutron, respectively. Here, p is given from the ratio of the electrical pulse heights at the upper and lower ends [4]. The histogram data of the form (d, p, ω), where ω represents the energy transfer, is calculated by (d, p, t) and the incident energy E_i. Users can determine the observed value of E_i by a fitting procedure on HANA.

Two types of the reductions of the histogram data are available. One is for a single-crystal. The three dimensional momentum transfer $\boldsymbol{Q}$ is represented by the reciprocal-lattice coordinates of (Q_a, Q_b, Q_c). Their directions are defined from the given lattice parameters. Users can visualize a two-dimensional intensity map, on which two of the four parameters Q_a, Q_b, Q_c, and ω are selected as vertical and horizontal directions. The other case is for a powder sample. The momentum transfer is simply regarded as $|\boldsymbol{Q}| = Q$. Users can visualize an intensity map on the Q-ω plane.

The histogram data can be transformed to a data format of the visualization program DAVE MSlice [7] for convenience of the users. Furthermore, several histogram data with different measurement times can be combined by normalization using proton number recorded by YUI.

The alignment support function is indispensable in the beginning of single crystalline experiments. From a Laue profile measured by a white beam, users can obtain the information of the relation between the coordinate of the crystal and that of the spectrometer with an easy procedure.

As shown in Fig. 3, we have also developed the distribution version of HANA, for Mac and Windows, which is distributed to users who want it. They are able to perform the data reduction process using event data on their campus.

4. Future Plans

We have developed and improved YUI and HANA day-by-day for convenience of users and instrument staff members. Now we plan the installation of some new devices for sample environment, as well as their control from YUI in future. In HANA, we are planning to implement an analysis function for four-dimensional

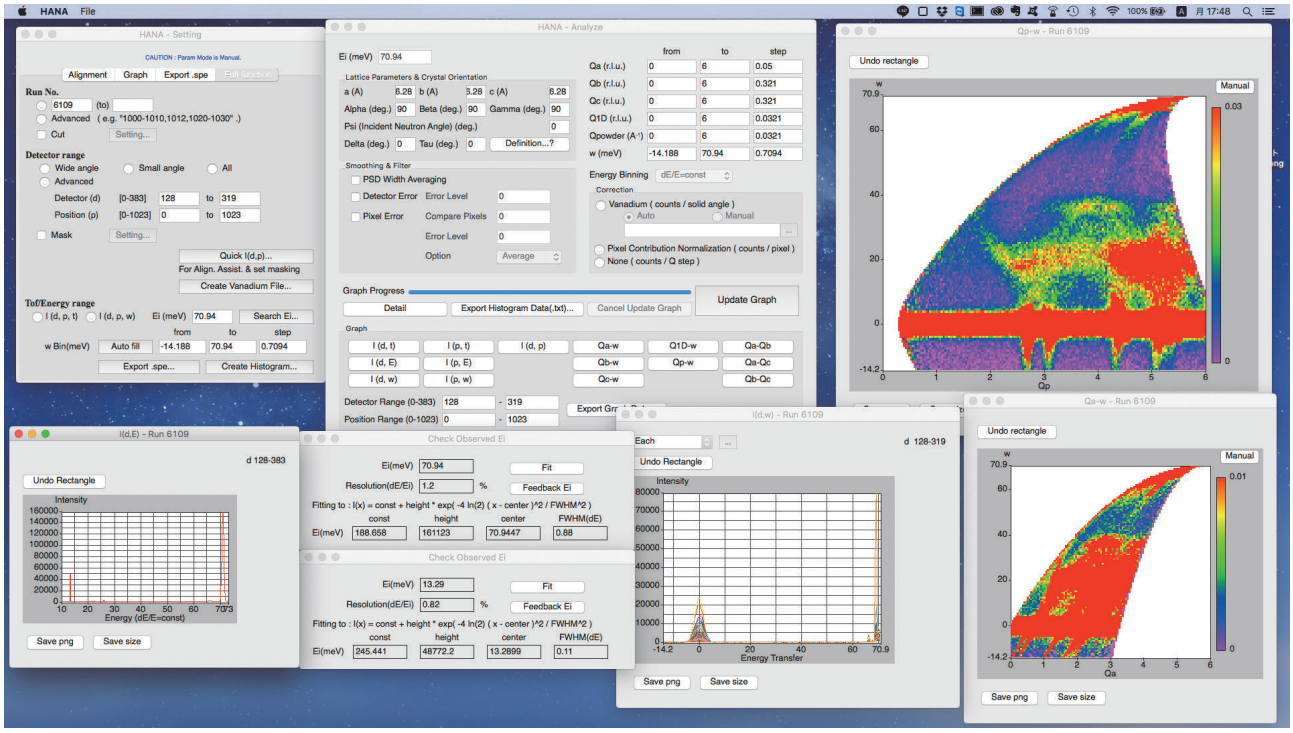

Figure 3. Distribution version of HANA.

data obtained from the continuously rotation scan of a single crystal. Recently, the programs have also been installed to the computing system in POLANO (BL23). For example, the function of arithmetic calculations for two intensity maps has been developed in HANA, in consideration of the polarization analysis on POLANO.

Acknowledgement

The previous and present HRC staff members M. Soda, S. Ibuka, M. Yoshida, T. Hawai, and S. Asai supported the operation checks of YUI and HANA, and T. Asami and R. Sugiura supported their installations. We would like to appreciate Bee Beans Technologies Co., Ltd. (Tsukuba, JAPAN) for gratefully supporting our works as partnership.

References

[1] S. Itoh et al., Nucl. Instr. and Math. Phys. Res. A **631** 90 (2011).
[2] S. Itoh et al., J. Phys. Soc. Jpn. **82** SA033 (2013).
[3] D. Kawana et al., submitted to Proc. on ICANS XXII (2017); see also arXiv:1710.00487 for details.
[4] S. Satoh et al., Nucl. Instr. and Meth. Phys. Res. A **600** 103 (2009).
[5] S. Itoh et al., proc. of ICANS-XXI (JAEA-Conf 2015-002/KEK Proc. 2015-7) 298 (2016).
[6] http://www-cont.j-parc.jp/MLF/, accessed on Oct. 11, 2017.
[7] R. T. Azuah et al., J. Res. Natl. Inst. Stand. Technol. **114** 341 (2009).

D. Kawana[1], T. Masuda[1], H. Yoshizawa[1], S. Itoh[2,3], T. Yokoo[2,3], and Y. Ikeda[4]
[1]Neutron Science Laboratory, Institute for Solid State Physics, the University of Tokyo; [2]Neutron Science Section, Materials and Life Science Division, J-PARC Center; [3]Institute of Materials Structures Science, KEK; [4]Institute for Materials Research, Tohoku University

BL14 AMATERAS

1. Introduction

FY2016 was the eighth year of operation of AMATERAS [1, 2], a cold-neutron disk-chopper spectrometer. We continued the user program. As it happened in the previous year, in this fiscal year, we encountered again some mechanical problems with the equipment of AMATERAS. There were changes in the staff of AMATERAS. A new research fellow, Dr. Maiko Kofu joined AMATERAS in October. On the other hand, Dr. Yukinobu Kawakita, who was engaged in both AMATERAS and DNA, moved from AMATERAS to concentrate on DNA.

2. User program, international activities & out-comes

In FY2016, MLF was smoothly operated without any seriously breakdowns. On AMATERAS, 20 general proposals, four JAEA project proposals and one elemental strategy proposal were carried out. The number of general proposals included 2014B and 2015A proposals, which were carried-over due to the interruption of the user program in FY2015. Also, the portion of the beam time of project proposals and elemental strategy proposals, which were not used in FY2015, were spent in FY2016. The number of general proposals submitted for the 2016A and 2016B periods was 28 (accepted: 4, reserved: 24) and 22 (accepted: 6, reserved: 16), respectively. As we will mention later, AMATERAS had several serious problems with auxiliary devices, which, unfortunately, affected some of users' experiments.

AMATERAS joined the first Neutron and Muon School held in November. Three students took part in a quasi-elastic neutron scattering (QENS) experiment for ionic liquids, which are attracting increasing attention in many fields (Fig. 1). We gave a lecture on an overview of AMATERAS and a TOF technique at the chopper spectrometer. They prepared the liquid samples, set them to a cryostat, and conducted a measurement. Through the hands-on experiment, they learned how to analyze the QENS data and how diffusive dynamics is examined by QENS. We hope that neutron scattering will become one of the experimental tools to be used in their future research activities.

As it happened the last fiscal year, AMATERAS had a guest from Korea, Dr. Sungil Park (Korea Atomic Energy Research Institute), in the framework of the Korea-Japan collaboration program in neutron science. He carried out a trial inelastic experiment on single crystals of 2D organic-inorganic hybrid magnets.

Figure 1. (Top) Three students who participated in the first Neutron and Muon School and staff members of AMATERAS. From the left, Dr. T. Kikuchi (J-PARC), Mr. Y. Ishii (Tohoku U.), M. Nakase (JAEA), Ms. N. I. P. Ayu (KEK), Dr. M. Kofu (J-PARC). (Bottom) They discuss data analysis and results.

In 2016, four refereed papers reporting results from AMATERAS were published. Two master theses including results from AMATERAS were written. Dr. Minoru Soda (RIKEN) won the 14th Japanese Society of Neutron Science Young Research Fellow Prize, which was a recognition of his research work involving the use of AMATERAS.

3. Instrumental activities

Since one of the compressors that operate the cryopump system was broken last year, we replaced several components, such as a displacer of the cold-head and an adsorber in the compressor this year. However, the repaired systems still had a problem, an abnormal sound, when they were re-installed at the instrument just before the beam operation was resumed. Then we took it back to the company again. Since we had to operate cryostats in low vacuum due to the lack of a cryopump, we substituted our standard cryostat for

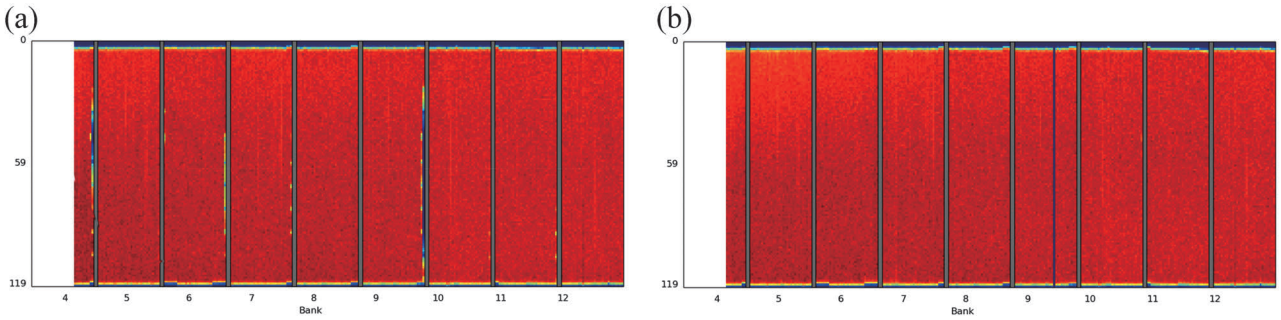

Figure 2. Detector map images taken (a) before and (b) after the refurbishment of vanes between detector banks. Some of detector pixels between the detector banks were hidden due to badly installed vanes before the refurbishment, which work correctly after the treatment.

other ones that can be commonly used at instruments. The cryopump system came back in January, but one of the three coldheads still has some failures. We decided to stop its operation until the next summer.

Last year, a newly designed vane was partly installed as a trial at the vacuum scattering chamber. Because it was quite effective, we replaced all the conventional vanes, which caused useless pixels in the data, with new ones. The data quality was improved after this refurbishment (Fig. 2).

In FY2016, we also made other improvements. Minor modification on utilities around the experiment area was done by in-house staff. More than half channels of high-voltage power supply have failed one after another since the last year, and we replaced some of them.

References

[1] K. Nakajima, S. Ohira-Kawamura, T. Kikuchi, M. Nakamura, R. Kajimoto, Y. Inamura, N. Takahashi, K. Aizawa, K. Suzuya, K. Shibata, T. Nakatani, K. Soyama, R. Maruyama, H. Tanaka, W. Kambara, T. Iwahashi, Y. Itoh, T. Osakabe, S. Wakimoto, K. Kakurai, F. Maekawa, M. Harada, K. Oikawa, R. E. Lechner, F. Mezei, and M. Arai, J. Phys. Soc. Jpn. **80**, SB028 (2011).

[2] K. Nakajima, RADIOISOTOPES **66**, 101 (2017).

K. Nakajima[1], S. Ohira-Kawamura[1], M. Kofu[1], T. Kikuchi[1,2], and Y. Kawakita[1]

[1]Neutron Science Section, Materials and Life Science Division, J-PARC center; [2]Chemical Analysis Center, Research & Development HQ, Sumitomo Rubber Industries, Ltd.

Upgrading TAIKAN

1. Introduction

The small and wide angle neutron scattering instrument TAIKAN (BL15) has been developed and upgraded to analyze precisely and efficiently microstructures or hierarchical structures of substances in various scientific fields with a 1 MW spallation neutron source in J-PARC [1]. In FY2016, it was upgraded further to perform measurements with a rheometer and middle-*q* measurement.

2. Upgrading for measurements with a rheometer

A rheometer MCR-302 (Anton-Paar Co., Ltd.) with a double cylindrical cell was introduced for the Rheo-SANS measurement of surfactant solutions, ionic liquid, etc. (Fig. 1). The cell is composed of an outer cylinder with 50 mm in inside diameter and an inner cylinder with 48 mm in outside diameter. The gap between the cylinders is 1 mm. The sample volume is about 22 ml. The rheometer has been used to measure viscoelasticity of a sample in torque of 1 nMm – 200 mNm at temperatures of –50°C – 150°C

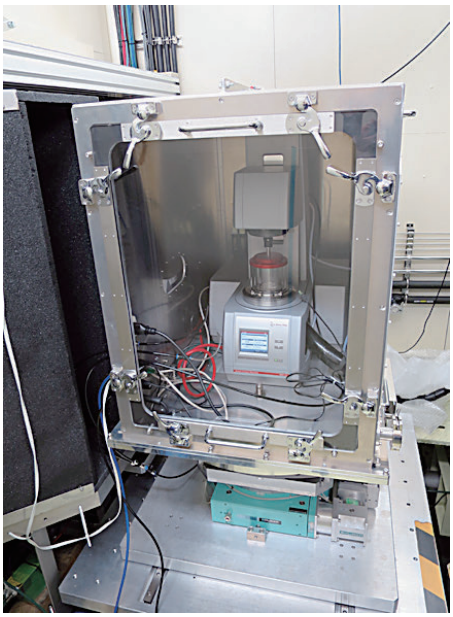

Figure 1. A rheometer on a sample stage of TAIKAN.

3. Upgrading for middle-*q* measurement

The detector system of TAIKAN is composed of 5 detector banks: the small-, middle-, high-, ultra-small-angle, and backward detector banks. On the middle-angle detector bank in the vacuum chamber, 288 ^{3}He PSD tubes were additionally installed. The measurement efficiency of the middle-angle detector bank increased twofold. The number of ^{3}He tubes then increased to 768, 592, 104, and 48 for small-, middle-, high-angle, and backward detector banks, respectively. Figure 2 shows a photo of the small- and middle-angle detector banks after installing the ^{3}He tubes.

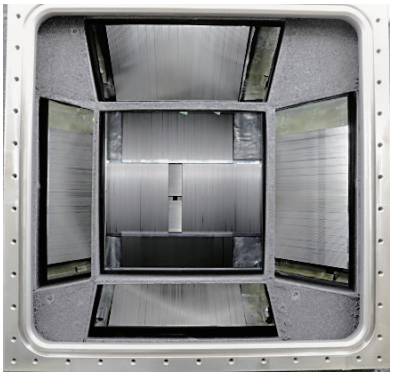

Figure 2. Small- and middle-angle detector banks.

4. Future prospects

The improvement of measurement efficiency by the installation of the detectors and the increase of the beam intensity makes time-resolved measurement easier. In the future, TAIKAN is expected to contribute to research not only of static phenomena but also of transient phenomena related to microstructures or the hierarchical structures.

Reference

[1] S. Takata, J. Suzuki, T. Shinohara, T. Oku, T. Tominaga, K. Ohishi, H. Iwase, T. Nakatani, Y. Inamura, T. Ito, K. Suzuya, K. Aizawa, M. Arai, T. Otomo and M. Sugiyama, JPS Conf. Proc. 8, 036020 (2015).

J. Suzuki[1], S. Takata[2], K. Ohishi[1], H. Iwase[1], T. Morikawa[1], Y. Kawamura[1], and M. Sahara[1]

[1]R&D Division, Neutron Science and Technology Center, CROSS; [2]Neutron Science Section, Materials and Life Science Division, J-PARC Center

Detector Development for the SOFIA Reflectometer

SOFIA is a horizontal-type neutron reflectometer constructed at Beamline 16 (BL16) of the Materials and Life Science Experimental Facility (MLF) of the Japan Proton Accelerator Research Complex (J-PARC) [1, 2]. Owing to the high-flux beam of J-PARC, less than one hour is needed for taking full *Q*-range data and only a few seconds for limited *Q*-range data in the case of a sample with 3 inches (76 mm) in diameter; even though the beam power is still one-third of the planned value, 1 MW. However, several hours are still needed for small samples such as 10 mm × 10 mm, which is the typical size of a sample for X-ray reflectometry. For this purpose, we are developing a focusing mirror to use a high flux beam with a large beam divergence.

On the other hand, the diverged beam makes angular resolution worse because the distribution of an incident angle to the sample increases. To avoid this problem, a position-sensitive detector is strongly required because the incident angle of neutrons can be distinguished by the reflection position under a specular condition. The angular resolution in this case is, however, limited by the spatial resolution of the detector. So far, we are employing a scintillation detector consisting of a ^{6}LiF/ZnS sheet and position-sensitive photomultiplier tube. Although the spatial resolution of the detector (about 1 mm) is acceptable for the purpose, there is much room for improvement in the counting efficiency (about 20% for thermal neutrons) and the counting rate (about 3000 count/s).

To upgrade the detector, we are developing a detector based on a solid converter made of boron in combination with a GEM (Gas Electron Multipliers) made of glass that we have already developed.

Upon absorption of a thermal neutron, ^{10}B undergoes the following reactions:

$$^{10}B + {}^{1}n \rightarrow {}^{7}Li + {}^{4}He + 2.3\ \text{MeV}\ [93\%]$$

$$^{10}B + {}^{1}n \rightarrow {}^{7}Li + {}^{4}He + 2.8\ \text{MeV}\ [7\%]$$

In either case, these particles deposit some of their energy in the surrounding gas, where a gaseous ionizing-radiation detector can be used to determine the time and position of the interaction. However, the thickness of the converter is limited (2 μm in an optimum condition) because the fission particles cannot leave the converter due to the self-absorption. As only 5% of thermal neutrons can be captured in the path of 2 μm even for enriched ^{10}B, some solutions using alternate stacking of converter layers and detection layers are proposed. The systems, however, become more complex and expensive, and unwanted scattered neutrons in the front layers may contaminate data in backward layers. To avoid these problems, we adopted a simple way: increasing the effective thickness by illuminating a converter with grazing-incidence geometry.

Figure 1 presents a schematic illustration of the new detector we are developing. Even though the converter is thin, the path length neutrons' travel in the converter becomes longer by the grazing-incidence geometry. Hence, the better the counting efficiency is, the smaller the incident angle is. Besides, the spatial resolution becomes better whereas the total detection area decreases effectively, since the incident angle is smaller. Therefore, the tilt of the detector should be controlled depending on the measurement condition.

To evaluate the effect of the grazing-incidence geometry on the counting efficiency, we made a prototype detector with a converter made of natural boron (Fig. 2). The natural boron with the thickness of 2 μm was sputtered on a Si substrate, and 2 nm copper layer was sputtered on the boron layer for coating and against a charge-up. The converter was mounted in a gas chamber with a GEM and readout board under a

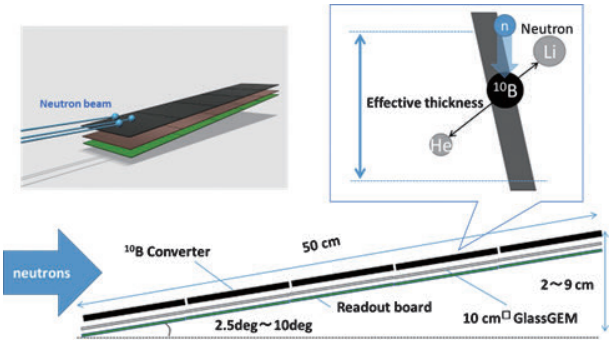

Figure 1. Schematic illustration of the new detector design.

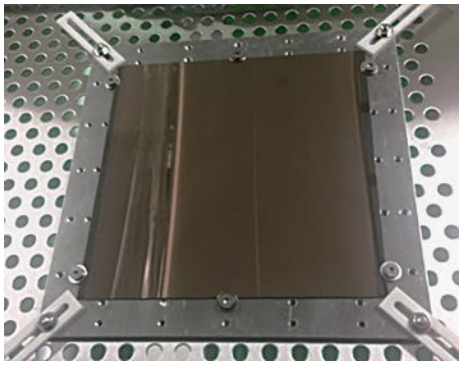

Figure 2. Photograph of a prototype converter made of natural boron with a valid area of 10 cm × 10 cm.

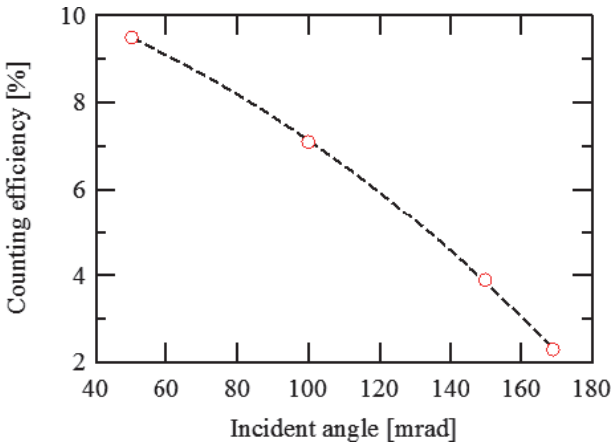

Figure 3. Counting efficiency of thermal neutrons with a prototype detector as a function of an incident angle of neutrons.

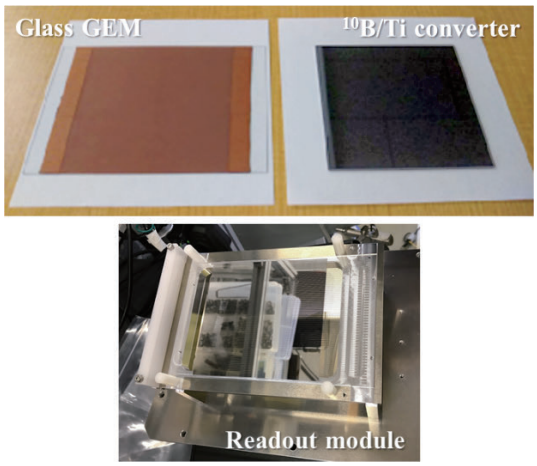

Figure 4. Photograph of an actual GEM made of glass, ^{10}B enriched converter, and readout module with the valid area of 10 cm × 10 cm.

gentle flow of 1 bar Ar/CH_4 (90:10). Figure 3 shows the counting efficiency of thermal neutrons with wavelength of 0.18 nm, as a function of the incident angle of neutrons. As the incident angle decreases, the counting efficiency increases as expected. Since the amount of ^{10}B in natural boron is 20%, this result indicates that the efficiency can reach approximately 50% with an incident angle of 50 mrad. Then, the effective detection area is 25 mm × 100 mm, and the spatial resolution is 0.05 mm, if a readout pat with 1 mm pixels is employed.

Next, we made a second prototype detector with actual components. Figure 4 presents photographs of the converter, GEM and readout module. The converter with the area of 10 cm × 10 cm is made of ^{10}B and covered by 2 nm titanium film for protection. The valid area of the GEM is the same as the converter, whose rims on two sides are cut for placing GEMs with small gaps of 0.5 mm. The readout module has a line and space pattern with 96 channels per 100 mm. The neutron signals are collected by the module and amplified by three charge amplifiers for 32 channels independently. The amplified signals are counted by time analyzers, LiTA [3], based on a field-programmable gate array.

Figure 5 shows the beam intensity profile taken by the second prototype, in which the beam width on the detector was 0.70 mm. The profile shape is consistent with the intensity distribution of neutrons although

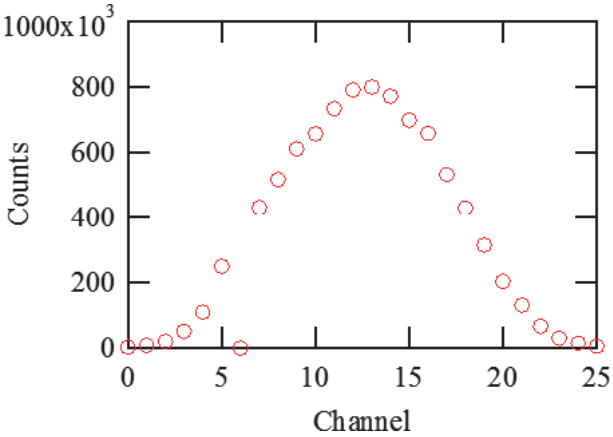

Figure 5. Beam intensity profile taken by the second prototype detector.

one channel is dead. As the pitch of the channels is 100/96 mm, the full width of the signal is 27 mm, and the incident angle is estimated to be 26 mrad. After careful evaluation of the prototype, we plan to make the final version of the detector with an area of 10 cm × 50 cm by arraying five units, and replace the scintillation detector in use at the SOFIA.

References

[1] N. L. Yamada *et al.*, *Euro. Phys. J. Plus* **126**, 108 (2011).
[2] K. Mitamura *et al.*, *Polymer J.* **45**, 100–108 (2013).
[3] S. Satoh, *Physics Procedia* **60**, 363-368 (2014).

N. L. Yamada[1,2], T. Fujiwara[3], M. Hino[4], and S. Sato[1,2]
[1]Institute of Materials Structure Science, KEK; [2]Neutron Science Section, Materials and Life Science Division, J-PARC center; [3]Research Institute for Measurement and Analytical Instrumentation, Advanced Industrial Science and Technology (AIST); [4]Kyoto University Research Reactor Institute, Kyoto University

BL17: Current Status of the Polarized Neutron Reflectometer, SHARAKU

1. Introduction

Neutron reflectometry (NR) is a powerful technique to investigate the nanometric structure of surfaces and interfaces in the depth direction of thin films. A neutron reflectometer at BL17 of MLF in J-PARC, SHARAKU, was constructed to conduct the structural analysis using polarized neutrons. An NR with a polarized neutron beam can probe not only a nuclear scattering length density (SLD) but also a magnetic SLD; therefore, SHARAKU can be used to study the magnetic structure in magnetic thin film samples. In SHARAKU, a two-dimensional neutron detector, multi-wired proportional chamber (MWPC), is installed for the measurement of off-specular reflectivity and grazing angle incidence small angle neutron scattering (GI-SANS), which are used to investigate the in-plane structure of the surfaces and interfaces of thin films. SHARAKU equips several kinds of sample environments such as electromagnets and refrigerators to enable the NR measurement in various environment conditions. While we continued the user experiments in 2016, we developed the measurement system using MPWC and some sample environments. In this report, we describe the current status of the MWPC and the sample environments.

2. Current status of MWPC

Figure 1 shows a photograph of the MWPC installed in SHARAKU. It has a neutron sensitive area of 128 × 128 mm^2 with 256 × 256 pixels, each of which has a size of 0.5 × 0.5 mm^2. The spatial resolution is 1.8 mm. The data acquisition system in MLF stores all information of each detected neutron: the time-of-flight (corresponding to wavelength) and the position, including the status of the sample environments. In the case of the NR data obtained by a two-dimensional detector, various kinds of data reduction should be performed from the experimental data: a two-dimensional q_x-q_z map for an off-specular reflectivity, a q_x-q_z map for GI-SANS, and so on. We implemented a data-reduction system for the event data of the MWPC in UTSUSEMI, which is the data analysis environment developed in MLF. Users can perform the data reduction in several formats with a user-friendly graphical interface.

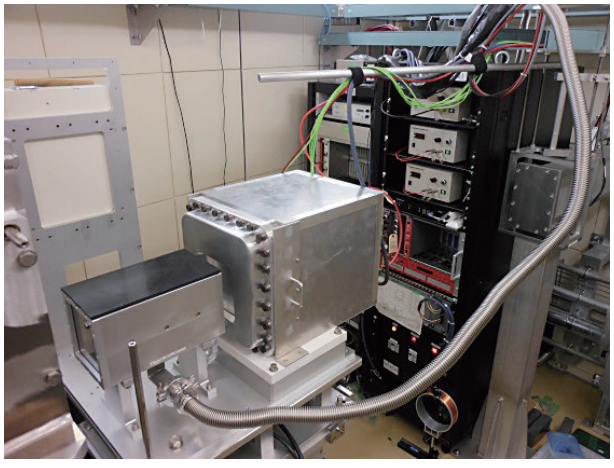

Figure 1. MWPC installed in SHARAKU.

Figure 2 (a) indicates the q_x-q_z map of an off-specular NR data for a Ni/Ti multi-layer thin film. The

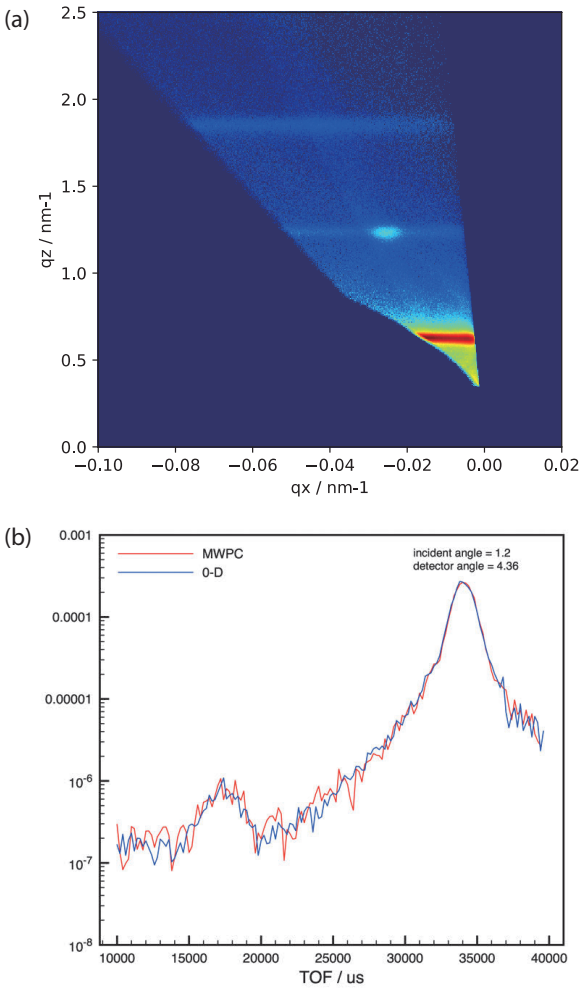

Figure 2. Off-specular NR measurement by MWPC. (a) q_x-q_z map for an off-specular NR data obtained by MWPC. (b) Comparison of the off-specular reflection spectra obtained by MWPC (red) and a ^{3}He tube detector (blue).

two-dimensional detection of the reflected neutron enabled the efficient measurement of a wide q_x-q_z range in an acquisition time of 8 h. At q_z = 1.25 nm^{-1} of the second Bragg reflection, a peak at q_x = –0.025 nm^{-1} is clearly observed, which corresponds to the correlation of the lateral roughness of the Ni/Ti interface. Figure 2 (b) compares the off-specular NR spectrum obtained by the MWPC and that by a 0-D detector, which has been employed for off-specular measurements in SHARAKU. They are in good agreement with each other, indicating that the MWPC installed in SHARAKU can be used for quantitative NR measurements.

3. Sample environments

SHRAKU is a powerful neutron reflectometer to analyze the magnetic structure in thin film samples; therefore, various sample environments for magnetic samples are installed: an electromagnet up to a magnetic flux density of 1 T, a super-conducting electromagnet up to 7 T, and a refrigerator down to a temperature of 4 K. In 2016, we carried out the commissioning of another electromagnet with a magnetic flux density of 4 T, which is equipped with a refrigerator at 1.2 K. Figure 3 (a) shows a photograph of the 4-T magnet. With this magnet, the magnetic field is applied along the beam axis. This magnet can be used for the NR measurement by highly polarized neutrons with a polarization ratio of > 0.9 at a wavelength range of 0.2 – 0.8 nm. This magnet will be used for a contract variation NR experiment by a dynamic nuclear polarization technique.

SHARAKU accepts user experiments not only for magnetic thin film sample but also for soft matters such as polymers and liquid crystals. A liquid immersion sample cell can be used for the NR measurement of a thin film sample immersed in a solvent. It has been used in the studies on the swelling behavior of polymer thin films and the solvation structure of ionic liquids at a substrate surface, etc.

(a) (b)

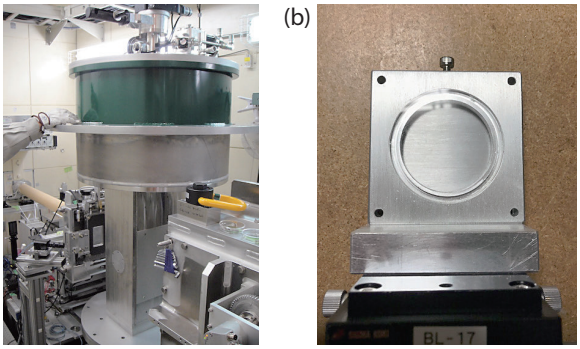

Figure 3. Sample environments installed in SHARAKU, a 4T-electoromagnet with refrigerator (a) and a liquid immersion cell (b).

4. Summary

A two-dimensional neutron detector MWPC has been installed for an off-specular NR and GI-SANS experiments. The data-reduction functions for the event data from the MWPC have been prepared in the UTSUSEMI data analysis software system for the ease of use in the user experiments. A 4-T electromagnet with refrigerator and a liquid environment cell has been prepared for the needs of user experiments in various research fields.

K. Soyama[1], H. Aoki[1], D. Yamazaki[1], N. Miyata[2], K. Akutsu[2], T. Hanashima[2], S Kasai[2], and J. Suzuki[2]
[1]Materials and Life Science Division, J-PARC Center, Japan Atomic Energy Agency; [2]Neutron Science and Technology Center, CROSS

Status of SENJU 2016

1. Introduction

SENJU is a TOF single-crystal neutron diffractometer designed for precise crystal and magnetic structure analyses under multiple extreme environments such as low-temperature, high-pressure and high-magnetic field, as well as for taking diffraction intensities of small single crystals with a volume of less than 1.0 mm^3 down to 0.1 mm^3 [1]. Ever since SENJU was launched in 2012, continuous commissioning and upgrading operations have been carried out.

In 2016, we developed an oscillating radial collimator to reduce the background in measurements with some extreme sample environment devices at SENJU. We also upgraded the software for data processing, STARGazer for SENJU.

2. Development of an oscillating radial collimator

One of the most important features of SENJU that makes the diffraction measurement of a small single crystal possible is the low background achieved by a properly designed vacuum sample chamber. However, when an MLF common extreme sample environment device, such as 2 K cryostat or niobium furnace, was installed in the vacuum chamber, the incident neutrons were scattered by a chamber or radiation shields of the installed device and consequently the background severely increased.

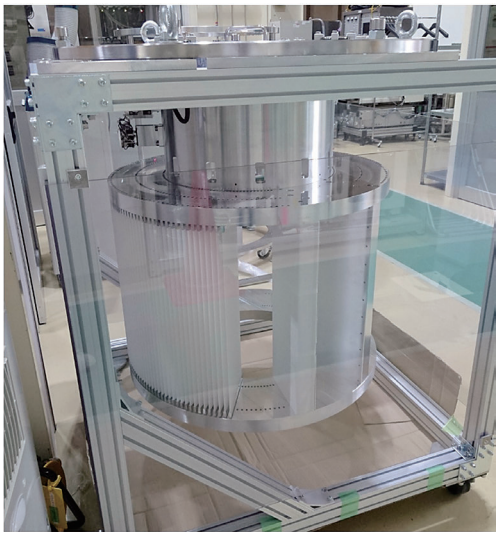

Figure 1. The oscillating radial collimator designed for SENJU.

To overcome this problem, we developed an oscillating radial collimator for SENJU. The collimator was designed for installation in the vacuum sample chamber of SENJU and has a ϕ400 mm MLF standard flange (Fig. 1). Slits were made by Gd_2O_3 coated mica and arranged with 2.0° repeating angle. The standard oscillating speed was 13 sec/deg and oscillating width was 2.0° with 1.0° offset.

In the first half of FY2016, we fabricated the collimator with 78 Gd_2O_3-mica slits. In this setting, the detectors

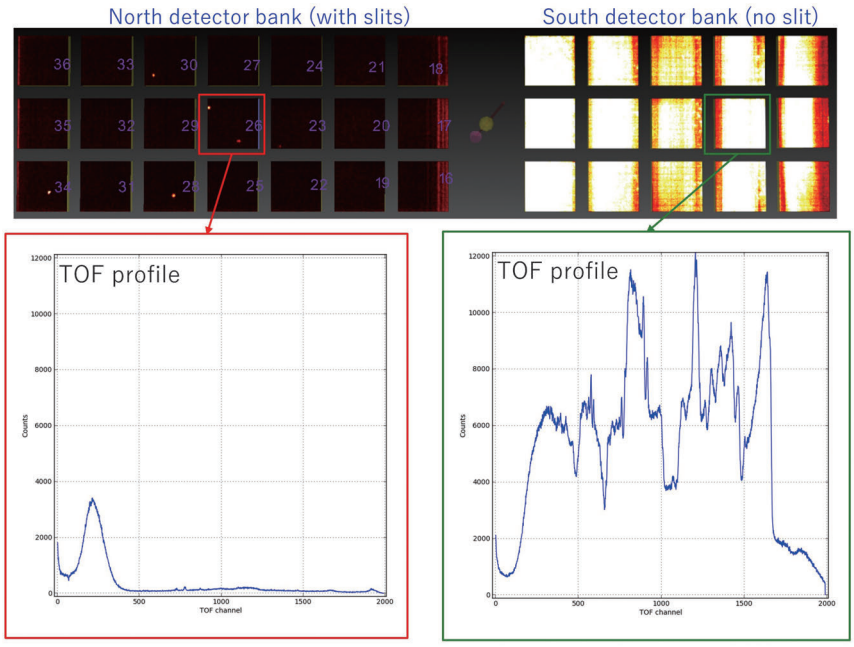

Figure 2. Diffraction image of a 0.1 mm^3 single crystal and a 1-mm thick and ϕ161 mm aluminum cylinder with the oscillating radial collimator.

at the north side of the direct beam (north detector bank) of SENJU was covered by the slits and the south detector bank was not. To assess the collimator's performance, we installed it in the vacuum chamber of SENJU, put a 0.1 mm^3 single crystal of an organic compound with a 1-mm thick and ϕ161 mm aluminum cylinder in the sample position and took a diffraction image. Figure 2 shows the obtained diffraction image. The background on the north detector bank (with slits) was drastically reduced and Bragg peaks from the sample were clearly observed, while huge background due to scattered neutrons from the aluminum cylinder was observed on the south bank burying the Bragg peaks.

In the second half of FY2016, after the preliminary measurement described above, we added 57 Gd_2O_3-mica slits to the collimator to cover the south detector bank. The collimator performs low-background measurements with the MLF common extreme sample environment devices at SENJU and will help us design new sample environment devices for SENJU.

3. Upgrading of the data processing software: STARGazer for SENJU

Software for data processing, i.e., making a reflection file (called "HKLF file") from raw data and data visualization, is one of the essential components for a single-crystal diffractometer. For SENJU, a program called "STARGazer for SENJU" is used for data processing and visualization.

In FY2016, an update of STARGazer for SENJU including development of

1. data scaling by using the GateNET system
2. integration of Bragg peaks at the edge of detectors,

was carried out.

The first one was developed to improve the reliability of the intensity-scaling process of several sets of diffraction data. In the previous version of STARGazer, the intensity-scaling was based on the number of T0 signals and consequently the influence of the accelerator power fluctuation was ignored in the scaling. Recently, we added "GateNET" modules, which produce a file that includes the accelerator operation status and the monitor-event number of the DAQ system of SENJU. Thus, we added a function to the STARGazer to read the GateNET output file and scale the intensities of several sets of diffraction data by using the information about the accelerator operation and the monitor-event, including the accelerator power fluctuation.

The second one was developed to improve the efficiency of the diffraction measurement. In the previous version of the STARGazer, partially recorded Bragg peaks at the detector edge region, usually 6 pixels from the edge, were ignored and consequently 1/3 of the measured Bragg peaks were not processed. Thus, we added a new function to the STARGazer to estimate the intensity of partially recorded Bragg peaks at the detector edge region by a profile-fitting technique using Gaussian function. The evaluation of the effectiveness of this new function is in progress and we expect to recover more than half of the wasted Bragg peaks with this technique.

Reference

[1] T. Ohhara et al., J. Appl. Cryst., 49 120 (2016).

T. Ohhara[1], R. Kiyanagi[1], A. Nakao[2], K. Munakata[2], T. Moyoshi[2], K. Moriyama[2], and T. Kuroda[2]

[1]Neutron Science Section, Materials and Life Science Division, J-PARC Center; [2]R&D Division, Neutron Science and Technology Center, CROSS

BL19: 2D Detectors Installed to the Back-Scattering Bank of TAKUMI

In JFY 2016, a back-scattering detector bank, equipped with two-dimensional scintillator detectors with wavelength-shifting fiber readout, was installed at the Engineering Material Diffractometer TAKUMI at BL19. Thanks to the higher scattering angle of this bank, the diffraction peak resolution exceeded the existing ±90° banks. Further, these detectors can evaluate the evolution of the texture in materials during mechanical deformation.

The back-scattering detector bank of TAKUMI consists of three detector modules, as shown in Fig. 1. The scattering angle of the center and the secondary neutron flight path length of the detector bank are $2\theta = 155°$ and $L_2 = 1.75$ m, respectively. Each detector module has 64 × 64 pixels with the size of 5 mm × 5 mm namely the size of the sensitive area of one detector is 320 mm × 320 mm. The details of the detector itself can be found in reference [1].

Simple data reduction software based on the software of Utsusemi [2] and Manyo-Lib [3] was developed. The two-dimensional intensity distribution of 221 reflection from $La^{11}B_6$ powder (in a vanadium can with a diameter of 6 mm) on the detectors is shown in Fig. 2. A part of the Debye-Scherrer ring from $La^{11}B_6$ powder was clearly observed and the S/N ratio of the diffraction pattern was high enough for the engineering study at TAKUMI. The time-focused diffraction pattern, in which the d-spacing data for a particular scattering angle is gathered, of the whole TOF range of the $La^{11}B_6$ powder is shown in Fig. 3. The diffraction peak resolution was evaluated as $\Delta T/T = 0.15\%$ from the positions and the FWHMs of the peaks that were obtained through the Gaussian fitting. This value is approximately half of the value of the ±90° banks for the same incident beam condition. Hopefully, strain analysis with a resolution of less than 0.01% can be achieved by this bank.

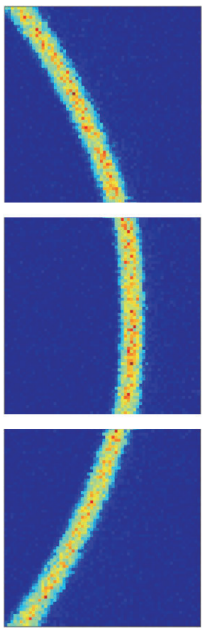

Figure 2. Part of the Debye-Scherrer ring of 221 reflection from $La^{11}B_6$ powder.

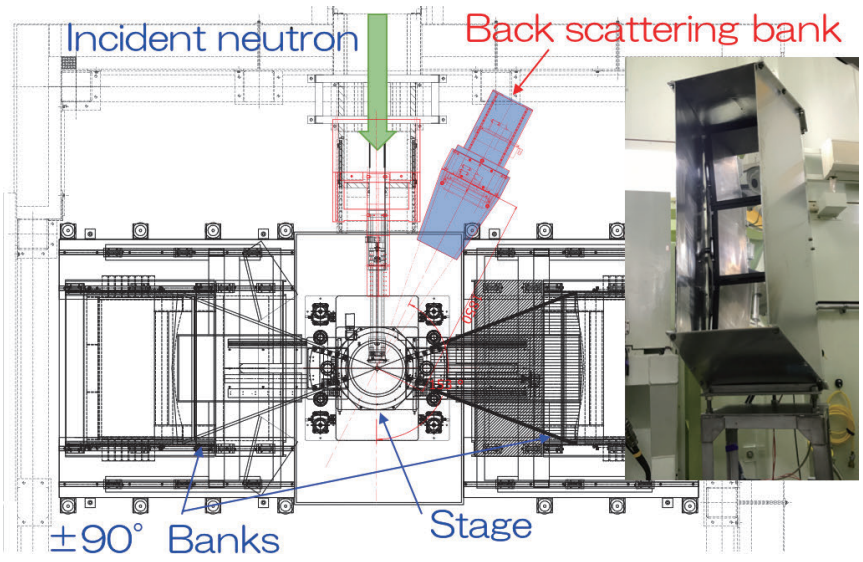

Figure 1. Plane view of TAKUMI and a photograph of the back-scattering bank.

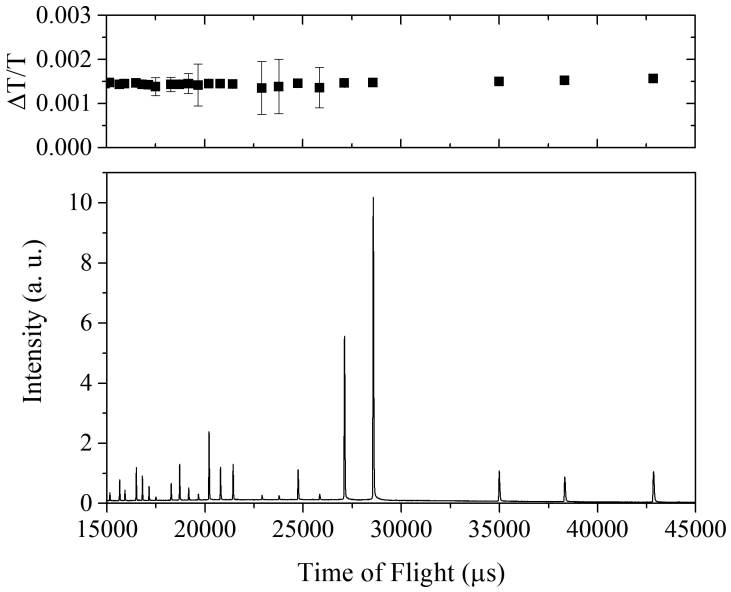

Figure 3. Time-focused diffraction pattern of $La^{11}B_6$ powder and the ΔT/T of each peak in the pattern.

The detector bank is already available for use, and will become a powerful tool for the engineering studies at MLF.

This work was partly supported by JSPS KAKENHI grant No. 15H05767.

References

[1] T. Nakamura et al., Nucl. Instrum. Methods, A 686 (2012) 64.
[2] Y. Inamura et al., J. Phys. Soc. Jpn., 82 (2013) SA031-1.
[3] J. Suzuki et al., Nucl. Instrum. Methods, A 600 (2009) 123.

T, Kawasaki[1], S. Harjo[1], T. Nakamura[2], K. Aizawa[1,3], and N. Tsuji[4]
[1]Neutron Science Section, Materials and Life Science Division, J-PARC center; [2]Neutron Device Section, Materials and Life Science Division, J-PARC Center; [3]Technology Development Section, Materials and Life Science Division, J-PARC center; [4]Department of Materials Science and Engineering, Kyoto University

The Current Status of the Versatile Neutron Diffractometer, iMATERIA

1. Introduction

Ibaraki prefecture, local government of Japan's area where the J-PARC sites are located, has decided to build a versatile neutron diffractometer (IBARAKI Materials Design Diffractometer, iMATERIA [1]) to promote industrial applications for the neutron beam in J-PARC. iMATERIA is planned to be a high-throughput diffractometer that could be used by materials engineers and scientists in their materials development work like the chemical analytical instruments.

The applications of neutron diffraction in materials science are (1) to do structural analyses of newly developed materials, (2) to clarify the correlation between structures and properties (functions), and (3) to clarify the relation between structural changes and improvements of functions, especially for practical materials. To achieve those purposes, a diffractometer with super high resolution is not required. The matching among intermediate resolution around $\Delta d/d = 0.15\%$, high intensity and wide *d* coverage is more important.

This diffractometer is designed to look at a decoupled-poisoned liquid hydrogen moderator (36 mm, off-centered) (BL20), and to have the incident flight path (L1) of 26.5 m, with three wavelength selection disk-choppers and straight neutron guides with a total length of 14.0 m. The instrumental parameters are listed in Table 1. There are four detector banks, including a low-angle and small-angle scattering detector bank. The angular coverage of each detector bank is also shown in Table 1. The rotation speeds for the disk-choppers are the same with a pulse repetition rate of 25 Hz for the most applications (SF mode). In this case, the diffractometer covers $0.18 < d\ (Å) < 2.5$ with $\Delta d/d = 0.16\%$ and covers $2.5 < d\ (Å) < 800$ at three detector banks of 90 degree, low angle and small angle with gradually changing resolution. When the speed of the wavelength selection disk-choppers is reduced to 12.5 Hz (DF mode), we can access a wider *d*-range, $0.18 < d\ (Å) < 5$ with $\Delta d/d = 0.16\%$, and $5 < d\ (Å) < 800$ with gradually changing resolution with doubled measurement time from the SF mode.

Table 1. Instrumental parameters of iMATERIA. L2 is the scattered flight path. The *d*-range (*q*-range) for each bank is the maximum value for 2-measurement mode.

L1	26.5 m	
Guide length		Total 14 m (3section)
Position of Disk choppers		7.5 m (double) 11.25 m (single) 18.75 m (single)
High	2θ	$150° \le 2\theta \le 175$
Resolution	L2	2.0 - 2.3 m
Bank	*d*-range	$0.09 \le d(A°) \le 5.0°$
Special	2θ	$80° \le 2\theta \le 100°$
Environment	L2	1.5 m
Bank	*d*-range	$0.127 \le d(A°) \le 7.2$
Low	2θ	$10° \le 2\theta \le 40°$
Angle	L2	1.2 - 4.5 m
Bank	*d*-range	$0.37 \le d(A°) \le 58$
Small	2θ	$0.7° \le 2\theta \le 5°$
Angle	L2	4.5 m
Bank	*q*-range	$0.007 \le q(A°^{-1}) \le 0.6$

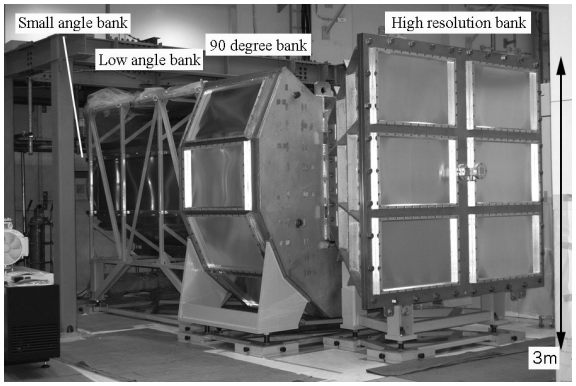

Figure 1. IBARAKI Materials Design Diffractometer, iMATERIA without detector for each bank and instrument shielding. The high-resolution bank, special environment bank (90° bank), and low-angle bank, can be seen from right to left. The small-angle detector bank, which is not shown in the picture, is situated in the low-angle vacuum chamber (left hand side of the picture).

2. Current status

All of the four banks, high-resolution bank (BS bank), special environment bank (90 degree bank), low-angle bank and small-angle bank, are operational. It takes about 5 minutes (DF mode) to obtain a 'Rietveld-quality' data in the high-resolution bank at 500 kW beam power for about 1 g of standard oxide samples.

Figure 2 shows a typical Rietveld refinement pattern for $LiCoO_2$ sample, cathode material for lithium ion battery (LIB), at the high-resolution (BS) bank by the multi-bank analysis function of Z-Rietveld [2]. It takes 20 min at the DF mode to collect the available Rietveld data, due to the high neutron absorption cross section for natural Li ($\sigma_s^{Nat} = 70$ barn).

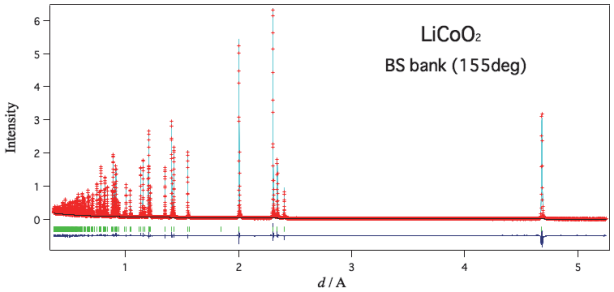

Figure 2. Rietveld refinement pattern for $LiCoO_2$ at the high-resolution bank of iMATERIA.

3. Sample Environments

The automatic sample changer is the most important sample environment for high-throughput experiments. Our automatic sample changer [3] consists of sample storage, elevating system of two lines, two sets of pre-vacuum chambers and a sample sorting system. We can handle more than 600 samples continuously at room temperature without breaking the vacuum of the sample chamber.

The V-furnace (~900°C), the gas flow furnace (~1000°C), the cryo-furnace (4K) and the 1K cryo are ready for experiments. Recently, the in-operando experiment system for LIB with a sample changer also became available in cylindrical and coin types of batteries.

References

[1] T. Ishigaki et al., Nucl. Instr. Meth. Phys. Res. A 600 (2009) 189-191.
[2] R. Oishi et al., Nucl. Instr. Meth. Phys. Res. A 600 (2009) 94-96.
[3] A. Hoshikawa et al., J. Phys.: Conf. Ser. 251 (2010) 012083.

T. Ishigaki, A. Hoshikawa, Y. Yoshida, T. Matsukawa, and Y. Onuki
Frontier Research Center for Applied Nuclear Sciences, Ibaraki University

Status of the High Intensity Total Diffractometer (BL21, NOVA)

1. Introduction

Total scattering is a technique to analyze non-crystalline structure in materials with atomic Pair Distribution Function (PDF). NOVA was designed to perform total scattering and is the most intense powder diffractometer with reasonable resolution ($\Delta d/d \sim 0.5\%$) in J-PARC. It is easy to adapt NOVA to a very wide variety of fields: liquids, glass, local disordered crystalline materials, magnetic structure of long lattice constant and so on. The observation of the hydrogen position in materials is one of the most important scientific themes of NOVA.

2. Magnetic diffraction measurements

Since NOVA can cover longer d-range with long neutron wavelength, 8.3 Å, and its high neutron flux, NOVA is suitable for magnetic diffraction measurements. Table 1 shows *Q*-ranges (*d*-ranges) of each detector bank and resolutions. The 90-deg bank of 0.6% resolution covers up to 6.3 Å. The minimum magnetic moments observed by NOVA is about 0.3 μ_B for $LaFeAsO_{0.55}H_{0.45}$ (Fig. 1), which was obtained during the research of Ref [1].

3. Sample environments

Table 2 shows the sample environments of NOVA. To reduce the backgrounds, a radial collimator will be installed in FY2017.

Table 1. *Q*-ranges (*d*-ranges) of NOVA.

Detector bank	Scattering angle (2θ) / degree	*Q*-resolution / %	*Q*-range (*d*-range) / Å
Small-angle	0.7~9	7 (4~50)	0.03 ~ 8 (0.8 ~ 209)
20-deg	12.6~28	2. 5 (1.7~3.9)	0.2 ~ 26 (0.2 ~ 31)
45-deg	33~57	1. 2 (0.9~1.5)	0.4 ~ 50 (0.1 ~ 16)
90-deg	72~108	0. 6 (0.5~0.7)	1 ~ 82 (0.08 ~ 6.3)
High-angle	135~170	0. 3 (0.3~0.35)	1.4 ~ 100 (0.06 ~ 4.5)

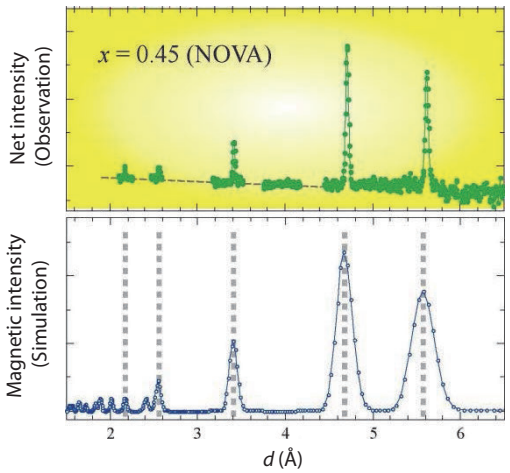

Figure 1. Magnetic diffraction of $LaFeAsO_{0.55}H_{0.45}$ (0.3 μ_B) measured with NOVA.

Table 2. Sample Environments of NOVA.

Apparatus	Specification
Sample Changer	sample: 10
Temperature controlled Sample Changer	sample: 18 temp: 20～500 (750) K
Top Load Cryostat	temp: 5～700 K
Vanadium Furnace	temp: ～1373 K
PCT	temp: 50～473 K press: ～10 MPa H_2/D_2
2K Cryostat (MLF SE)	temp: 1.7～300 K
Impedance **(under commissioning)**	temp: ～550 K freq.: 4 Hz～1 MHz

Acknowledgement

Operation and development of NOVA were performed under the S1-type program (2014S06) approved by the Neutron Scattering Program Advisory Committee of IMSS, KEK.

Reference

[1] M. Hiraishi et al., Nature Physics, **10**, 300-303 (2014).

T. Otomo[1,2], K. Ikeda[1,2], T. Honda[1,2], H. Ohshita[1,2], N. Kaneko[1,2], T. Seya[1,2], and K. Suzuya[2]

[1]Institute of Materials Structure Science, KEK; [2]Neutron Science Section, Materials and Life Science Division, J-PARC Center

Energy-Resolved Neutron Imaging System, BL22: RADEN

1. Introduction

A pulsed-neutron imaging instrument, named Energy-Resolved Neutron Imaging System "RADEN", has been constructed at beam line BL22 in the Materials and Life Science Experimental Facility (MLF) of J-PARC to conduct pulsed neutron imaging experiments, such as Bragg-edge, neutron resonance and polarized neutron imaging [1]. Together with the commissioning studies, RADEN started to accept user programs from FY 2015 and, in FY 2016, we have carried out 19 general-use programs and consequently about half of the total beam time was utilized by the users. In this report, we will cover the current status of RADEN's activity, including technical developments and application studies.

2. Improvement of Neutron Imaging Detector Systems

Together with the user programs, the instrument member of RADEN has performed development studies to improve imaging techniques. At first, the spatial resolution of the CCD camera-based detector was improved, and it became possible to access less than 50 μm resolution by means of combining a thin scintillator screen and a brighter optical lens system. Second, by means of an EMCCD camera system, a short stroboscopic imaging synchronized with the accelerator repetition of 25 Hz has been carried out. The shortest exposure time was about 20 msec. With this technique, dynamic imaging of liquid flows in narrow channels of an evaporator of an automotive air conditioning system was successfully achieved.

In addition, a counting-type neutron imaging detector system using micro-pattern plane named μNID, which is used mainly for the energy-resolved neutron imaging experiment, was improved to obtain higher count rate performance. The count rate was limited due to the slow data transfer speed of data acquisition electronics and drift velocities of secondary particles generated after the neutron absorption by the ^{3}He atom. Hence, we developed encoder modules with Gigabit Ethernet to achieve fast data transfer. Also, we changed the stopping gas into CF_4 and optimized the gas mixture to speed up the drift velocity. Owing to these upgrades, the count rate capacity was increased from 0.6 to 8 Mcps and the effective maximum count rate was also increased to 1 Mcps [2].

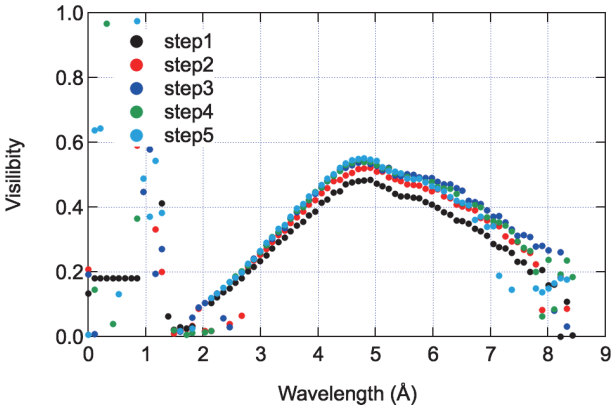

Figure 1. Wavelength dependent visibility of pulsed neutron phase imaging experiment. Each visibility was obtained by horizontally scanning the last grating in five points.

3. Development of a New Pulsed Neutron Imaging Technique

The RADEN instrument is dedicated to energy-resolved neutron imaging experiments using pulsed neutrons, and recently we began the development of the pulsed neutron phase imaging technique based on the Talbot-Lau interferometry under ERATO Momose Quantum Beam Phase Imaging Project [3, 4]. The neutron phase imaging technique has been developed at steady neutron sources with a course wavelength resolution of several tens percent, but the interference phenomenon intrinsically depends on the neutron wavelength and hence the phase imaging result also depends on the neutron wavelength. Then, we conducted wavelength-dependent neutron phase imaging measurements in combination with Time-of-flight method using μNID detector.

In the Talbot-Lau interferometer, the self-image after the phase grating G1 is resolved as a moiré pattern using an additional absorption grating G2. The visibility of this moiré fringe depends on the quality of the gratings and the wavelength resolution, and typical numbers for the visibility obtained in previous works were around 20%. On the other hand, the obtained visibility of moiré fringe in the current work indicated a continuous change against the neutron wavelength with a peak higher than 50% around 5 Å, which corresponded to the designed number of our interferometer (Fig. 1). Figure 2 shows the differential phase imaging of three kinds of metallic rods, Ni, Al and Ti. In this figure, the difference of signs of optical potentials between Al and Ti is clearly observed. This becomes even more evident by looking at the line profile along the X direction with a fine wavelength resolution (Fig. 3). The calculated differential phases of Al and Ti rods based on their optical values, indicated by solid

lines in Fig. 3, reproduced correctly the experimental results. This suggests that it is possible to evaluate the optical potential of a sample by using this technique.

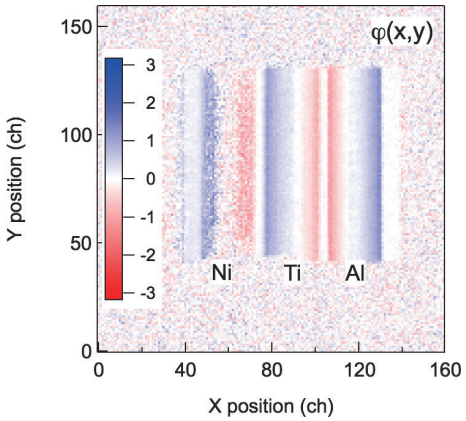

Figure 2. Result of a differential phase imaging experiment.

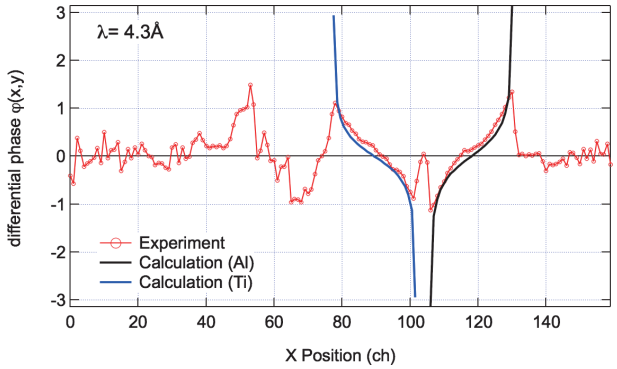

Figure 3. Line profile of differential phase along X axis. The solid lines are calculation results for Al and Ti metal rods using their optical potential values.

4. Summary and Future Plans

Together with the user programs, improvements of the imaging detector systems and development of pulsed neutron imaging techniques have been conducted at the RADEN instrument. The increased count rate of the counting type imaging detector μNID is very important for the effective energy-resolved neutron imaging experiment, so a further upgrade is needed. The pulsed neutron phase imaging has been demonstrated for the first time. We plan to develop a precise phase measurement technique by using the wavelength resolved method and to apply polarized neutrons to phase imaging to observe magnetic potential distribution.

Acknowledgement

This work was partially supported by JST ERATO Momose Quantum Beam Phase Imaging Project and by Photon and Quantum Basic Research Coordinated Development Program from the Ministry of Education, Culture, Sports, Science and Technology, Japan.

References

[1] T. Shinohara et al., J. Phys: Conf. Series 746 012007 (2016).
[2] J.D. Parker et al., 2016 IEEE Nucl. Sci. Symp. Conf. Rec. (2016).
[3] http://www.jst.go.jp/erato/momose/
[4] Y. Seki et al., J. Phys. Soc. Jpn. 86 044001 (2017).

T. Shinohara[1], T. Kai[1], K. Oikawa[1], M. Segawa[1], T. Nakatani[1], K. Hiroi[1], Y. Su[1], H. Hayashida[2], J. D. Parker[2], Y. Matsumoto[2], Y. Seki[1], W. Ueno[1], and Y. Kiyanagi[3]

[1]Neutron Science Section, Materials and Life Science Division, J-PARC Center; [2]R&D Division, Neutron Science and Technology Center, CROSS; [3]Graduate School of Engineering, Nagoya University

Recent Progress on the Polarized Neutron Spectrometer POLANO

1. Introduction

Since 2012, the POLANO team has persisted in its efforts to design and construct the POLANO spectrometer and its neutron devices. POLANO represents the younger generation of spectrometers operating in MLF [1-3]. Three direct geometry chopper spectrometers are now part of the user program. They cover a rather wide energy and momentum space for investigation of the dynamical structures in internal degrees of freedom in materials. The POLANO was designed as the same type of chopper spectrometer as the other three instruments, however, it has polarization analysis capability. In the light of the recent discoveries in material science, many of the observed complex phenomena are largely due to the entangled physical degrees of freedom (spins, charges, orbitals, and even lattice vibration). A unique, effective, and direct way to observe these physical quantities separately is via the polarization analysis.

2. POLANO Specifications and Progress

Since the POLANO is located at the 23rd beam line (BL23) in MLF, viewing the decoupled hydrogen moderator, reasonable resolution and neutron intensity are achieved for the above purpose. With the specific geometrical length parameters of the POLANO spectrometer, an energy resolution of $\Delta E/Ei = 3$ to 5% (Ei: incoming neutron energy) and momentum resolution of $\Delta Q/ki = 1$ to 2% (ki: neutron's initial wave number) are expected [3].

In 2016, many components of the spectrometer were manufactured, installed, and adjusted. Most of those major items are now ready for the start of the neutron beam operation. A set of position sensitive detectors (PSD) is one of essential components. In Fig. 1, the installed PSD array in the large vacuum chamber and electronic modules out on the back of the chamber are shown. For the range that interests us, we adopted PSD with 60 cm effective length, 3/4" diameter, 10 atm of ^{3}He gas pressure, and SKYN2 feedthrough developed in MLF. 32 PSDs were positioned in a detector bank, covering a scattering angle of about 20°. In the vertical direction, there were three layers of PSD arrays. In the horizontal (central) layer, all the scheduled PSDs were installed (from −20° to 120°).

Other devices were also installed. A remarkable achievement was the setup of magnetic devices [4] and super mirror analyzer. The magnetic devices are composed of several assembled permanent magnets, which retain magnetic field along the neutron path called guide field, with the purpose to prevent depolarization of the neutron spins. These guide fields are on the order of several tens of Gauss. Considering terrestrial magnetism and the interference with other fields, we optimized the combination of different types of magnets. Particularly, the magnet after the sample should have a wide acceptance for the scattered neutron beam. The arc-shaped magnets were designed as minimizing the

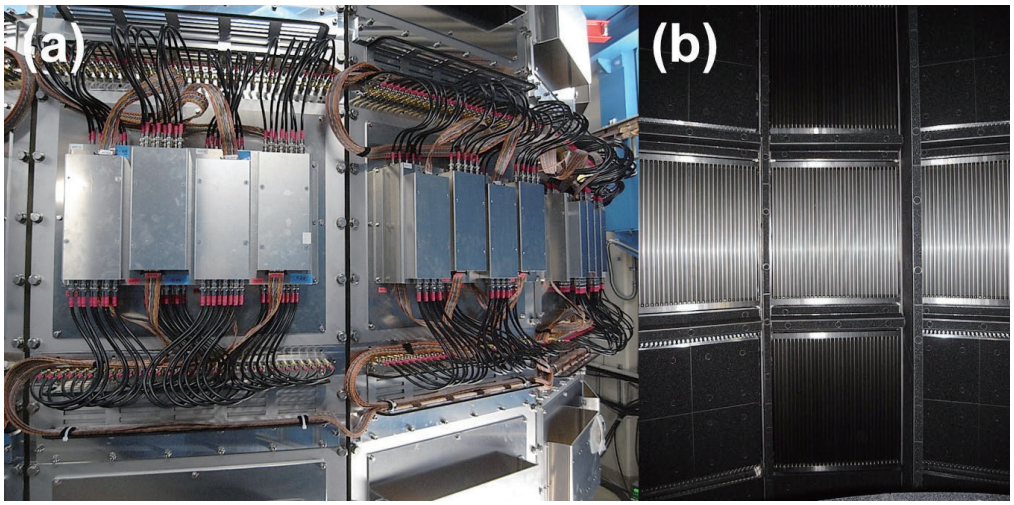

Figure 1. Detector systems of POLANO. (a) Electronic modules and cables set up in the back of the detector bank. (b) Installed position sensitive detector tubes.

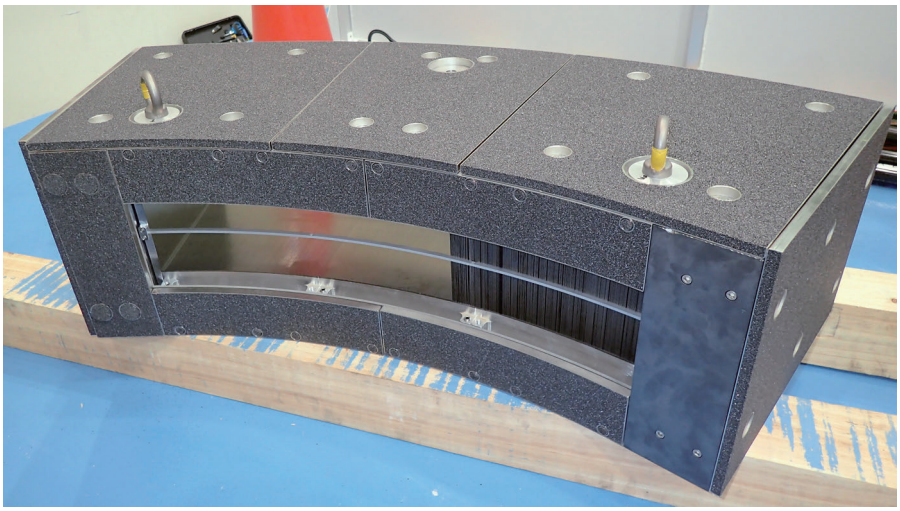

Figure 2. Bending super mirror analyzer system.

shadow of magnet structure's "dark-angle" and placed along the scattering angle. The super mirror analyzer is also one of the key devices. It can "analyze" the spin polarization of scattered neutrons via the reflection from the supper mirror. It is placed just after the arc-shaped magnet in the vacuum chamber. As shown in Fig. 2, this is the array of super mirror thin blades, currently covering 20° of the scattering angle. Since it is necessary to cover completely the designed scattering angle (from −20° to 120°), we designed a scanning mechanism for the analyzer in the tank. It is rather heavy (about 80 kg), magnetic (about 400 Gauss) and super expensive, so we need careful designing, manufacturing and setup. Also, it was very hard to build the scanning system with mechanical motors in the vacuum.

The data acquisition and device control system (YUI) and the data visualization and analyzing system (HANA) have been continuously developed for day-one of the POLANO experiment [5]. The current versions of YUI and HANA were set up in POLANO's computing system, and their operation and network connection were checked. The remote device control via the connection will be a crucial technique for performing the polarization experiment in near future. We have to keep updating those controlling and analyzing systems for further devices and new techniques of analyzing the polarization data sets.

3. Future Plans

We have so far focused on the designing and construction of devices and instruments. In the next year, we will start commissioning using a real neutron beam. Still, we must develop a few new devices, such as spin flippers, controlling system of the correlation chopper, high-performance polarization devices [6] and so on. Therefore, our efforts target both developing and tuning instruments. Also, we are going to give more attention to the relationship with our community to ensure future collaborations and scientific projects to be investigated at POLANO.

References

[1] T. Yokoo et al., J. Phys. Soc. Jpn., 82 SA035 (2013).
[2] T. Yokoo et al., J. Phys.: Conf. Ser., 502 012046 (2014).
[3] T. Yokoo et al., EPJ Web Conf. 83 03018 (2015).
[4] K. Ohoyama et al., J. Phys. Conf. Series 711 012010 (2016).
[5] Y. Ikeda et al., this annual report.
[6] T. Ino et al., J. Phys. Conf. Series 711 012011 (2016).

T. Yokoo[1,2], S. Itoh[1,2], M. Fujita[3], Y. Ikeda[3], N. Kaneko[1,2], M. Ohkawara[3], T. Ino[1,2], K. Ohoyama[4], S. Sugai[1,2], and M. Sakaguchi[1,2]
[1]Neutron Science Section, Materials and Life Science Division, J-PARC center; [2]Institute of Materials Structure Science, KEK; [3]Institute for Materials Research, Tohoku University; [4]Graduate School of Science and Engineering, Ibaraki University

Development of an *in-situ* Polarized ^{3}He Neutron Spin Filter for POLANO

1. Introduction

A ^{3}He neutron spin filter (NSF) is one of the essential devices in POLANO for polarization of the incident neutron beam. It is operated *in-situ* to provide a stable neutron polarization, and the spin-exchange optical pumping method is employed to polarize the ^{3}He gas. A compact *in-situ* ^{3}He NSF system, suitable for the limited space in POLANO, has been developed.

2. NSF for POLANO

The *in-situ* polarized ^{3}He NSF system for POLANO is shown in Fig. 1. All essential components are enclosed for laser safety in an aluminum box, 60 cm long, 60 cm wide, and 25 cm high.

The *in-situ* ^{3}He NSF can reverse the ^{3}He spins instantaneously by adiabatic fast passage (AFP) NMR [1]. By sweeping the frequency of the oscillating magnetic field generated by a cosine theta coil inside an aluminum oven (Fig. 2), the ^{3}He spin reversal and its NMR measurement are simultaneously performed in 100 ms. The ^{3}He polarization loss during the ^{3}He spin reversal has been confirmed to be less than 1×10^{-4} per flip.

The absolute ^{3}He polarimetry for the *in-situ* ^{3}He NSF has been performed by measuring the Rb EPR frequency shift during the optical pumping [2], and a ^{3}He polarization of more than 80% was attained in a laboratory test.

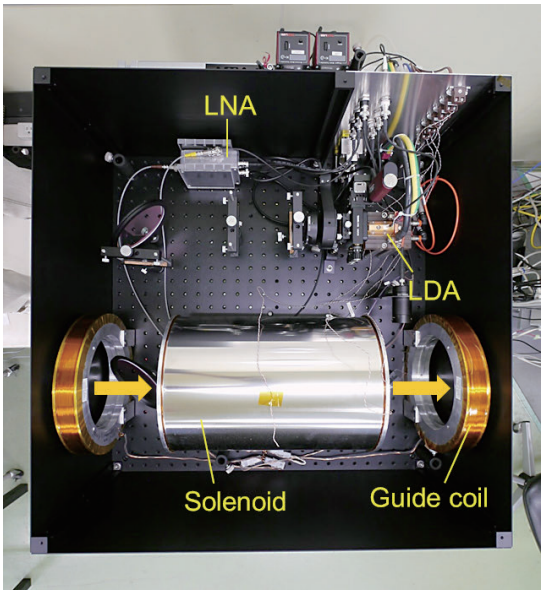

Figure 1. A magnetically-shielded solenoid, a guide coil for polarized neutrons, a laser diode array (LDA) with optical components for the optical pumping of Rb, and a low noise amplifier (LNA) for NMR are all in an aluminum enclosure. An aluminum oven with a ^{3}He cell is at the center of the solenoid (not seen). The neutron beam is shown as arrows.

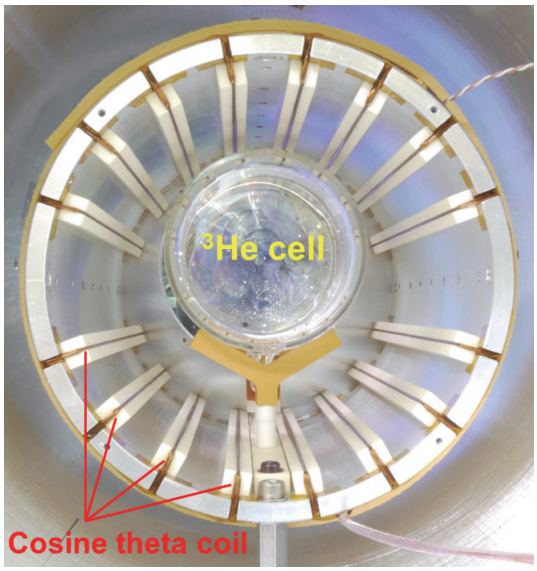

Figure 2. A cylindrical ^{3}He cell inside the AFP oven. The ^{3}He cell diameter is 60 mm, and the length is 60 – 100 mm. The ^{3}He pressure varies from 2 to up to 3.5 atm.

3. Installation

The *in-situ* ^{3}He NSF is almost ready to go and currently is being tested in a laboratory to check its performance and durability. It will be installed in POLANO soon.

References

[1] A. Abragam, The Principles of Nuclear Magnetism, Oxford University Press (1961).

[2] M. V. Romalis and G. D. Cates, Phys. Rev. A 58, 3004 (1998).

T. Ino[1,2], M. Ohkawara[3], T. Yokoo[1,2], Y. Ikeda[3], M. Fujita[3], K. Ohoyama[4], and S. Itoh[1,2]

[1]Institute of Materials Structure Science, KEK; [2]Neutron Science Section, Materials and Life Science Division, J-PARC Center; [3]Institute for Materials Research, Tohoku University; [4]Graduate School of Science and Engineering, Ibaraki University

The Current Status of the Computing Environment on POLANO

1. Introduction

As a new-generation pulsed-neutron instrument, the polarized neutron spectrometer, POLANO, has been designed with the ability to perform polarization analysis capable of handling a wide dynamic range of energy and momentum transfer (*E*-***Q***) [1]. The construction of the major equipment for POLANO has been already completed and now the commissioning is steadily under way. In this report, we present the current status of the computing environment on POLANO.

2. Configuration of the computing environment

POLANO is a sister instrument of the High Resolution Chopper spectrometer, HRC, installed at beam line 12 in MLF [2, 3]. Specifically, part of the constituent devices and data processing systems are almost the same as those of HRC [4], and the data acquisition (DAQ) middleware [5] is also driven on Scientific Linux machines. The schematic configuration of the computing environment on POLANO is illustrated in Fig. 1. When neutrons are detected at position sensitive detectors (PSD x352: x768 for full installation), the electronic signals are promptly converted into the event data via the DAQ electronics (NeuNET x48, and Gateway x1). The colossal amount of event data are processed by three DAQ servers (DAQ1-3; 2 TB x3) and stored into the network-attached storage (NAS) server of 30 TB with redundant arrays of inexpensive disks (RAID60). At present, one NAS server (NAS1) is used for a main storage, while the other NAS server (NAS2) is utilized as a backup machine of NAS1.

All installed devices (e.g. Fermi chopper, analyzer mirror, and band-definition disk choppers, etc.) are controlled via the DAQ operation (DAQ-OP) server. Note that users can easily control all devices via a terminal machine (terminal1; Macmini) with YUI program. A general-purpose server (server1; 6 TB, RAID5) is utilized as a logging machine to monitor a current/previous condition of all running devices, e.g. the stability of the chopper frequency, the time dependence of the temperature of a cryogenic system, etc. "FL net" is used to connect the computing system and the programable logic controller (PLC) of the vacuum chamber. This server is used to monitor the degree of vacuum in the scattering chamber and confirm the condition of valves and pressure switches.

For data analysis, POLANO has one more server (server2; SSD 240 GB + HDD 3 TB) and a terminal machine (terminal2; Macmini) in the control room. The users can visualize experimental data with the terminal machine via the HANA program.

3. Intelligent control program YUI and data visualization program HANA

The YUI and HANA programs [4] are adopted as a user interface programs on POLANO as well as HRC.

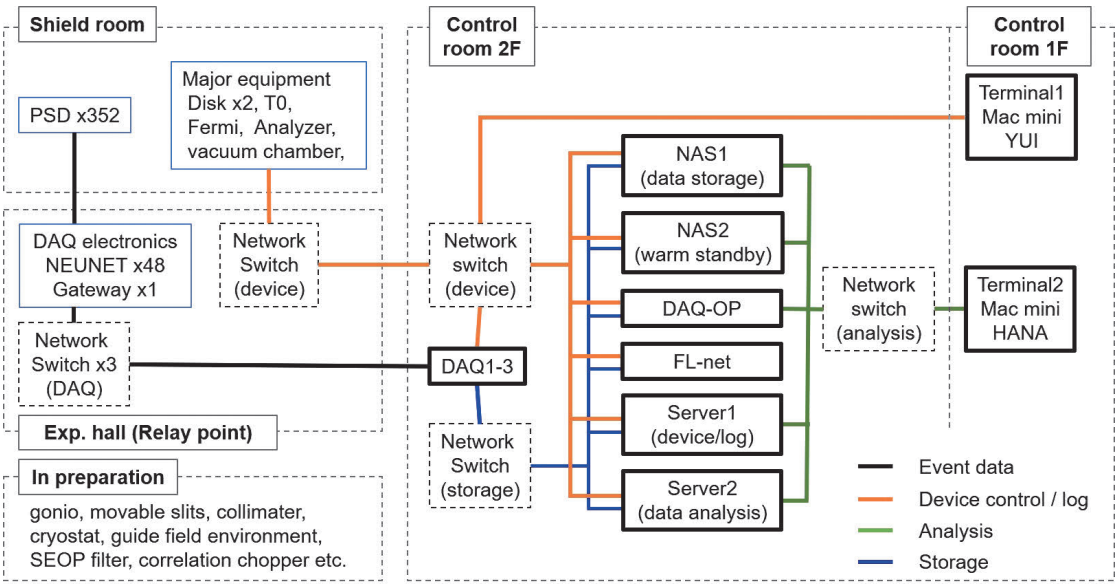

Figure 1. Schematic configuration of the computing environment on POLANO. Bold lines denote data flow, as shown in the bottom-right legend.

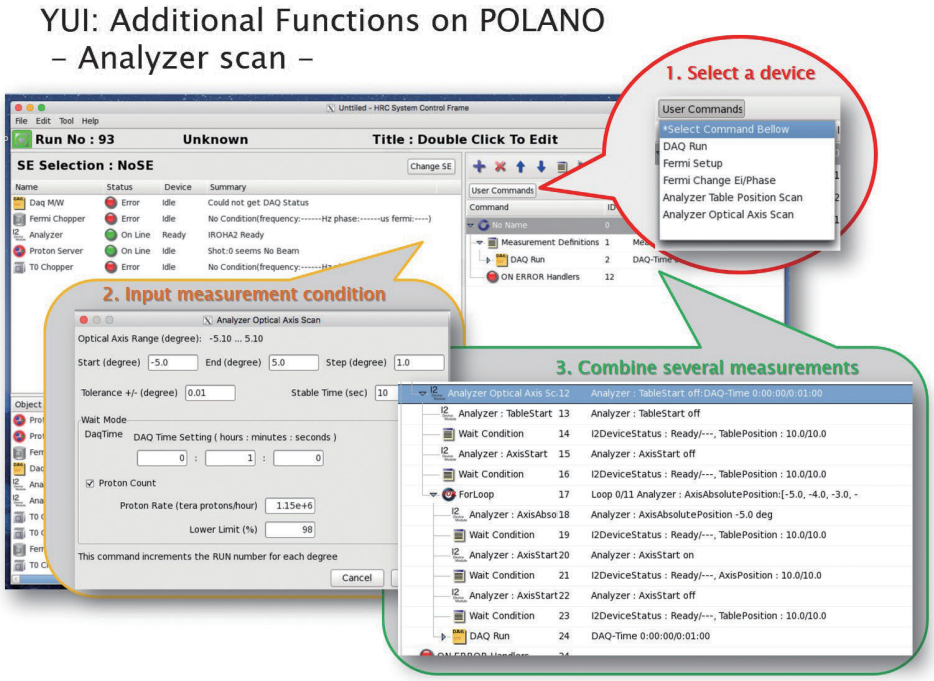

Figure 2. Additional functions of YUI on POLANO. Analyzer scan commands are available for polarization analysis.

Although the YUI and HANA programs on POLANO have almost the same functions as the ones installed on HRC, some additional functions are appended for polarization analysis. For example, POLANO's YUI has analyzer scan commands, as shown in Fig. 2. By using this function, the users can effectively acquire data moving the super-mirror analyzer. Furthermore, POLANO's HANA supports a basic arithmetic operation between two different histogram data for polarization analysis experiments.

4. Future plans

In the first commissioning with neutron beam, we verified that there were no harmful defects, at least in the major hardware of the computing environment, and successfully acquired and visualized the event data. As a next step, we will continue to work on refining specific devices and programs (YUI and HANA) on POLANO. In addition to the hardware preparation, further development of the control programs for SEOP devices, guide field environment, and cryogenic systems is indispensable for the polarization analysis experiment.

Acknowledgement

We acknowledge the support of D. Kawana (ISSP), KENS-DAQ group, and Bee Beans Technologies Co., Ltd. (Tsukuba, Japan).

References

[1] T. Yokoo, K. Ohyama, S. Itoh, J. Suzuki, K. Iwasa, T. J. Sato, H. Kira, Y. Sakaguchi, T. Ino, T. Oku, K. Tomiyasu, M. Matsuura, H. Hiraka, M. Fujita, H. Kimura, T. Sato, J. Suzuki, M. Takeda, K. Kaneko, M. Hino, and S. Muto, J. Phys. Soc. Jpn. **82**, SA035 (2013).

[2] S. Itoh, T. Yokoo, S. Satoh, S. Yano, D. Kawana, J. Suzuki, and T. J. Sato., Nucl. Instr. and Math. Phys. Res. A **631** 90 (2011).

[3] S. Itoh, T. Yokoo, D. Kawana, H. Yoshizawa, T. Masuda, M. Soda, T. J. Sato, S. Satoh, M. Sakaguchi, and S. Muto, J. Phys. Soc. Jpn. **82** SA033 (2013).

[4] D. Kawana, M. Soda, M. Yoshida, Y. Ikeda, T. Asami, R. Sugiura, H. Yoshizawa, T. Masuda, T. Hawai, S. Ibuka, T. Yokoo, and S. Itoh, submitted to Proceedings on ICANS XXII (2017); see also arXiv:1710.00487 for further information.

[5] S. Satoh, S. Muto, N. Kaneko, T. Uchida, M. Tanaka, Y. Yasu, K. Nakayoshi, E. Inoue, H. Sendai, T. Nakatani, and T. Otomo, Nucl., Instr. and Meth. Phys. Res. A **600**, 103 (2009).

Y. Ikeda[1], M. Sakaguchi[2,3], T. Yokoo[2,3], S. Itoh[2,3], M. Fujita[1], N. Kaneko[2,3], and M. Ohkawara[1]

[1]Institute for Materials Research, Tohoku University; [2]Neutron Science Section, Materials and Life Science Division, J-PARC center, [3]Institute of Materials Structure Science, KEK

Development of Proton Filter for POLANO

1. Introduction

We will start the commissioning of POLANO with relatively low-energy neutrons by using polarized ^{3}He gas for a spin filter. After the commissioning, we have a plan to polarize relatively high-energy neutrons, whose energies are several hundred meV.

To obtain a certain statistical variance in a short measurement time, it is necessary to prepare a spin filter with large P^2T. Here P is the polarization of the neutron beam transmitted through the spin filter and T is the neutron transmissivity of the spin filter. The neutron energy dependence of P^2T for spin filters using polarized ^{3}He or proton shows that proton filters are comparable for neutrons with kinetic energy of several hundred meV and superior for neutrons with energy larger than about 1 eV [1]. Therefore, we are considering preparing a proton filter.

2. Test System

As a first step to develop a proton filter for POLANO, we prepared a test system at KEK by using a cryostat with a 5 T superconducting dipole magnet and a 1 K ^{4}He evaporator. The diagram of this cryostat, used at the University of Michigan, is shown in reference [2]. In addition to the cryostat, we prepared a 213 MHz NMR system to measure the proton polarization and a microwave generator with output power of 20 W and center frequency of 140 GHz, to enhance the proton polarization by flipping the spin of the radicals that are doped in the proton filter.

As the magnetic moment of a radical is much larger than that of a proton, the thermal polarization of radicals, which is nearly equal to unity under the external magnetic field of 5 T and at the temperature of 1 K, is much larger than that of protons. Moreover, in flipping the radical spins, we can choose the microwave frequency so that we can flip at the same time only the proton spins that point to certain direction. In this situation, the polarization of the protons approaches that of the radicals due to the much shorter spin relaxation time of the radicals than that of the protons.

To test the system, we prepared a polyethylene film, which contains many protons, doped with TEMPO, which contains radicals. We put the film into the cryostat, applied static magnetic field of 5 T and cooled it down to 1 K. Without irradiating the microwave to the film, we observed the small NMR signal of the protons in the film, which corresponds to thermal proton polarization of 0.5%. The signal was increased by irradiating the microwave to the film and reached saturation in about an hour. As the signal is proportional to the proton polarization, we estimated it reached about 40% [1]. This result clearly shows that we have successfully prepared the test system.

References

[1] K. Taketani, S. Itoh, T. Otomo, T. Yokoo, N. Kaneko, S. Suzuki and S. Ishimoto, (2017). Proton filter for sub-eV neutron spectroscopy on POLANO, presented at the 22nd meeting of the International Collaboration on Advanced Neutron Sources, Oxford, UK.

[2] D. G. Crabb, C. B. Higley, A. D. Krisch, R. S. Raymond, T. Roser and J. A. Stewart, (1990) Observation of a 96% Proton Polarization in Irradiated Ammonia, Phys. Rev. Lett. 64, 2627.

K. Taketani[1,2], S. Itoh[1,2], T. Otomo[1,2], T. Yokoo[1,2], N. Kaneko[1,2], S. Suzuki[3], and S. Ishimoto[3]

[1]Neutron Science Section, Materials and Life Science Division, J-PARC center; [2]Institute of Materials Structure Science, KEK; [3]Institute of Particle and Nuclear Studies, KEK

Sample Environment at MLF

1. Introduction

The sample environment (SE) team is in charge of the preparation, maintenance and development of the beamline (BL)-common SE equipment, and aids the users in operating the equipment. The team has 14 members: 7 from JAEA, 5 from CROSS and 2 from an outsourcing company, and is divided into sub-teams of cryogenics and magnets, high temperature, high pressure, soft-matter, pulsed magnet and ^{3}He spin filter, etc. Light irradiation and hydrogen equipment are under development.

The status and activities of the SE team in JFY 2016 are summarized in this report.

2. Cryogenics and magnets

We had operated a superconducting magnet for users' experiments as equipment that has been commonly used at instruments until the last fiscal year. In JFY2016, we introduced three new cryostats, which are a top-loading ^{4}He cryostat, a dilution refrigerator insert and a bottom-loading ^{3}He cryostat, after finishing their commissioning. We supported nine experiment programs with these cryostats and this magnet in JFY2016.

We have upgraded the operation system for the superconducting magnet to enable users to control it with the IROHA2, which is the common software framework for instrument control. In MLF, there is a rule that at least one person has to monitor the magnet status on-site when applying the magnetic field for superconducting magnets without a warning light, to find a magnet quench as soon as possible. The new system on IROHA2 has a function to receive a quench signal from the power supply and turn on the warning light. Thus, the unmanned operation of this magnet has been allowed. It is expected that the introduction of this system will reduce the users' workload during experiments with a superconducting magnet.

3. High temperature equipment

The high-temperature sub-team has developed two furnaces as BL-common SE equipment.

3.1 Niobium furnace

The Niobium furnace was prepared for quasielastic neutron scattering and inelastic neutron scattering measurements, in which niobium foils are used as a heating element and radiation shields. It can be used with oscillating radial collimators to reduce the background of the elastic scattering from the niobium foils and the aluminum outer vacuum chamber. In 2016, we supported four users' experiments at BL14 and BL18 using the furnace. We are also installing an automatic safety operation system for the furnace. In 2016, the automatic operation of the sample stick rotation and the remote monitor of the temperatures in the operation room were realized.

3.2 Furnace for small-angle neutron scattering and neutron reflectivity measurement

In 2016, the aluminum windows were improved to reduce the unwanted background in the small-angle region, and the upgraded furnace (Fig. 1) was used for general proposal experiments.

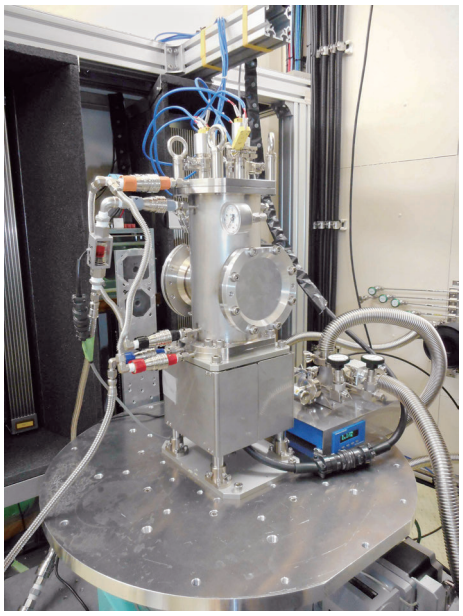

Figure 1. Furnace for small-angle scattering and neutron reflectivity measurement.

4. A pulsed magnet system

The work of the SE pulsed magnet group started in 2014. We have developed a prototype of a general-use pulsed magnet system, which consists of a solenoid coil, a sample stick and a pulsed power supply. The specifications are as follows: the maximum charging voltage and output current are 2 kV and 8 kA, respectively; the charging time of the power supply is approximately 30 seconds; the pulse width of the generated current is 2.65 msec at 50% of peak; the maximum magnetic field is 30 Tesla; the maximum scattering angle is 30.6°. The coil is immersed in liquid nitrogen and cooled at 77 K not only to decrease the resistance of the coil, but also to

remove the Joule heat generated by the pulsed current. The repetition rate of this system is one pulse per several minutes. The first neutron scattering experiments using this system were carried out at HRC (BL12). However, a problem occurred in the insert, and the temperature around the sample did not decrease below 4.2 K during the beam experiment. Currently, the insert is being improved and also a new one is being designed.

5. High pressure

To realize low temperature and high pressure (4 K, 10 GPa) experimental environment as a common SE equipment at MLF, we have developed a special cryosystem coupled with a Paris–Edinburgh (PE) cell (MG63 Co. Ltd., VX-5), as shown in Fig. 2. The PE cell is attached to the second stage of the closed cycle Gifford–McMahon (GM) type cryocooler (Sumitomo Heavy Industry Co. Ltd., RDK-415D). This is placed in a chamber for precooling with liquid nitrogen, which is surrounded by a radiation shield and an outer vacuumed chamber. While in use, the press is initially precooled with liquid nitrogen and then cooled only by GM and the chamber is filled with He exchange gas. This cryostat is mounted on the goniometer for sample rotation. The designed size of this system allows its installation in other beamlines with a vacuum chamber whose inlet is nominal diameter 400A in JIS standard.

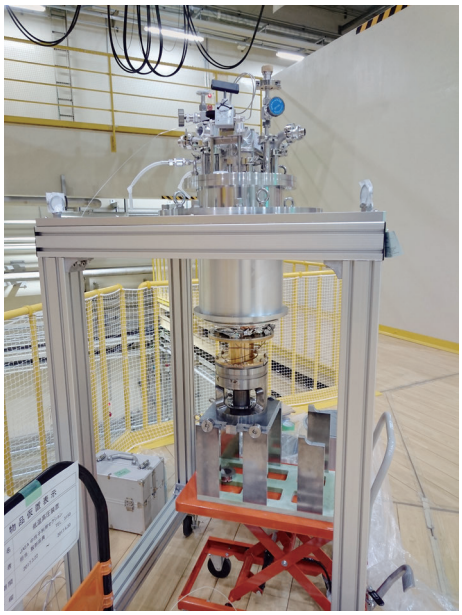

Figure 2. Newly constructed cryosystem for low-temperature and high-pressure experiments.

We have commissioned the system and found that it took 6.5 hours to cool the sample to 6.5 K. In contrast, it took more than 24 hours to raise the temperature to room temperature, due to the large heat capacity of the PE cell. Thus, we are now planning to attach additional heaters to the body of the cell to accelerate heating. This system has been already installed in several beamlines and is used for inelastic and quasielastic scattering experiments.

6. ^{3}He neutron spin filter

We have been developing a spin-exchange optical-pumping (SEOP) based polarized ^{3}He neutron spin filter (^{3}He-NSF) for efficient utilization of pulsed neutrons at J-PARC. We are in the process of preparation of the ^{3}He gas filling station for hybrid cell fabrication in the J-PARC research building in 2016. For maintenance and preparation of ^{3}He-NSF, a laser lab was prepared in the beam hall of MLF, and its operation started in May 2016.

As demonstrative experiments using ^{3}He-NSF, we performed the following measurements for the first time in 2016: 1) A polarized neutron single-crystal diffraction measurement at BL18 (SENJU). The sample was a single-crystal iron, and the polarity-dependent Bragg peaks from it were observed. The data analysis is in progress. 2) A polarized neutron Imaging experiment at BL22 (RADEN) with 2 on-beam SEOP setups at the same time, where one was for the polarizer, and the other one for the analyzer. The sample was an oriented soft steel piece with a thickness of 0.35 mm, winded with a magnetic field coil to apply a magnetic field on it. It was observed that the polarization degree of the neutrons transmitted through the sample depended on the neutron wavelength and the incident beam position on the sample, reflecting the magnetic domain state within the sample.

T. Oku[1], M. Watanabe[1], R. Takahashi[1], S. Ohira-Kawamura[1,2], M. Ishikado[4], K. Ohuchi[4], Y. Yamauchi[5], M. Nakamura[5], S. Isomae[5], K. Munakata[4], T. Hattori[2], S. Takata[1,2], Y. Sakaguchi[4], H. Kira[4], K. Sakai[1,3], T. Aso[1,3], and K. Aizawa[1]

[1]Technology Development Section, Materials and Life Science Division, J-PARC Center; [2]Neutron Science Section, Materials and Life Science Division, J-PARC Center; [3]Neutron Source Section, Materials and Life Science Division, J-PARC Center; [4]R&D Division, Neutron Science and Technology Center, CROSS; [5]Nippon Advanced Technology co.

Present Status of IROHA2

1. Introduction

Since 2015, the upgraded instrument control software framework "IROHA2" [1, 2] has been introduced and used in several neutron instruments at MLF, J-PARC. IROHA2 consists of four servers, which are the device control, the instrument management, the sequence management and the integrate control. One of the main features of IROHA2 is that users cooperate to use these servers with a web browser to carry out their experiments [3]. In this year, we have implemented two new functions to IROHA2. One is the support for the MLF common sample environment devices, which are the 7T magnet, the Nb furnace and the Signal Light by the IROHA2 device control server. The other is the remote experimental status monitoring system on the IROHA2 integrate control server. An experimental status is a web service for monitoring from the Internet the progression status of experiments conducted at MLF. Since the facility staff and users cannot monitor the experiment at the instrument all the time, this service is needed to reduce their workload in an experiment. We have developed the system for providing the experimental status in stages as a part of promoting environmental improvement of the remote access at MLF.

2. New device modules for common sample environment devices

We have developed the device modules of the IROHA2 device control server for the 7T magnet, the Nb furnace and the Signal Light, which are the common sample environment devices at MLF. The 7T magnet is the sample environment device that creates the magnitude of a strong magnetic field to be applied on the sample with the superconducting magnet. The 7T magnet is a complex device composed of a power supply producing a current to be applied on the superconducting magnet, refrigerators for the sample and the superconducting magnet, helium liquid level gauge and rotation controller for the sample. The Nb furnace is a device, which heats up a sample to a high temperature by electric heat. The Nb furnace is monitored through reading out the status from the programmable logic controller (PLC) and the recorder. The Signal Light is a device monitoring an apparatus generating high temperature, high pressure, strong magnetic field, and so on. The Signal Light consists of a PLC and red, yellow, green and blue lights. When something is wrong with the apparatus, the Signal Light indicates it by red and yellow lights according to the incident level. The green and blue lights indicate remote control and unattended operations.

The device module for the 7T magnet operates independently the power supply (Mercury iPS-M), the refrigerators (LakeShore 218 and 340), the helium liquid level gauge (Scientific Magnetics Helium Level Meter) and the rotation controller (Mclennan Single Axis Stepper System); it also operates sequentially the power supply and the refrigerator when the magnetic field changes. The users can carry out their automatic measurements composed by IROHA2 from the instrument data acquisition system and the 7T magnet.

The device module for the Nb furnace monitors various parameters like the present and set temperatures, the heater power (current and voltage), the vacuum pressure and so on from the PLC (KEYENCE KV-5000) and the recorder (CHINO KR2160MN2A). During their experiments, the users can monitor the status and record the parameters by using IROHA2.

The device module for the Signal Light monitors the alarm status of the apparatus connected to the Signal Light from PLC (DEC PFXLM4301TADDK). The module can also switch the remote control ON/OFF. Currently, the Signal Light is used for monitoring the baking system of the ^{3}He spin filter chamber in the J-PARC research building.

3. Experiment status monitoring system

Figure 1 shows screenshots of the experimental status. It is possible to browse the experimental list and the experimental status of each neutron instrument.

The system consists of servers for status collection from neutron instruments and web service of the experimental status. The status collection server creates HTML files, which include only static contents considering the security risk caused by the dynamic contents, based on the status information collected from each neutron instrument. By accessing the web server, the facility staff and users can browse the status information of their experiments transferred from the status collection server.

At the early stage of the system, it was possible to monitor only the states of the DAQ system, such as the state of each DAQ component, event counts and run number, and browse the experimental status within only J-PARC intranet. In this system, anyone could browse the experimental status without authentication.

(a)

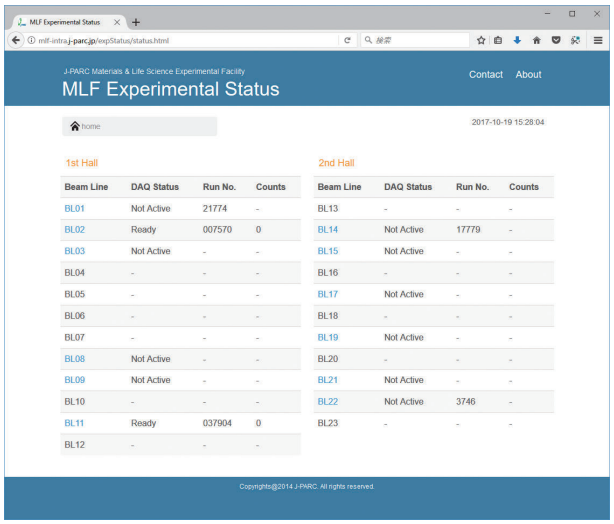

(b)

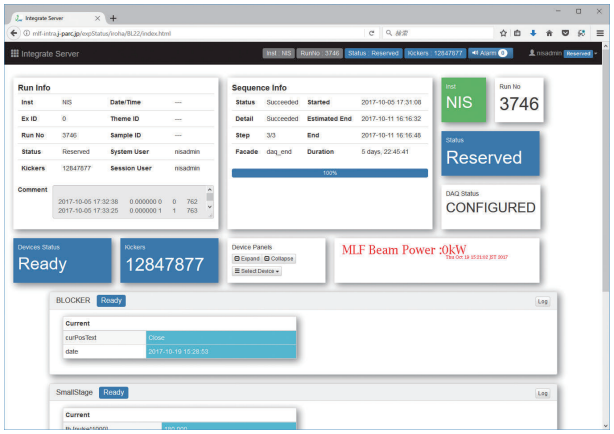

Figure 1. The screenshots of the list of experiments (a) and the experimental status (b).

After that, the system has been improved to cooperate with IROHA2, making it possible to monitor an integrated experimental status, including the status of the beam control apparatus and sample environment devices in addition to DAQ, which are made by IROHA2 integrate control server. Furthermore, the system can be accessed from the Internet by cooperation with an integrated authentication system based on an LDAP at MLF. However, this access was limited only to the facility staff. This is because the system was not able to ensure access control for each experimental group. Since the status information includes details about the experiment, such access control is essential to provide Internet access with facility users while retaining the uniqueness of the experiment.

Recently, we have updated the experimental status and IROHA2, enabling the access control for each experimental group by means of a one-time password (OTP). The IROHA2 integrate control server creates OTP and access control file as well as the status information file in HTML form. The status collection server creates list of experiments and OTP based on the set of files collected from each neutron instrument. Finally, these lists and each static HTML file are transferred to the web server to be able to access from Internet. When an experimental group accesses its experimental status, the access controls are performed based on the OTP.

4. Conclusion and future plans

By these developments, users of the instruments, where IROHA2 has been introduced, can carry out their experiments with devices easily integrated in the common sample environment and the data acquisition system, while monitoring the experimental status from the Internet. In FY2017, we will start using the devices for users' experiments with IROHA2 and offering an Internet access to the facility users of several neutron instruments such as BL18 and BL21 and plan to expand the access to the instruments in stages.

References

[1] T. Nakatani, Y. Inamura, T. Ito and T. Otomo, Proceedings of the ICANS-XXI, 493 (2014).
[2] T. Nakatani, Y. Inamura, T. Ito and K. Moriyama, Proceedings of NOBUGS2016, 76 (2016).
[3] T. Nakatani, Y. Inamura, T. Ito and T. Otomo, JPS Conference Proceedings, 8, 036013 (2015).

T. Nakatani[1] and K. Moriyama[2]
[1]Technology Development Section, Materials and Life Science Division, J-PARC Center; [2]Neutron Science and Technology Center, CROSS

A Large Area, Position-Sensitive Scintillation Neutron Detector

1. Introduction

The recent world-wide shortage of ^{3}He gas encouraged us to develop an alternative detector technology to replace the conventional ^{3}He gas-based detectors. To ameliorate this situation, we have developed a large area, position-sensitive scintillation neutron detectors for pulsed neutron scattering instruments [1, 2]. To make it usable for practical applications, the detector should be equipped with modularity and a large area, as well as superior detector performance comparable to those of the ^{3}He PSDs. It should be noted that the detector manufacturing costs should also be economically efficient because the detectors will cover more than a few m^2 required for typical neutron scattering instruments.

2. The large area, two-dimensional detector

A neutron-sensitive scintillator / wavelength-shifting fiber technology has been used to develop the large area detector. This technology has several advantages over the conventional clear-fiber one. They are its simple structure and flexibility of the pixel size. The detector comprises wavelength-shifting (WLS) fibers arrays in *x* and *y* directions and flat scintillator screens. The WLS fibers are placed at a regular pitch with an air gap between each other. By adjusting the length and a pitch of each WLS fiber, the area and the pixel size of the detector can be designed depending on the requirements. In order to make a large area detector, for example with a size over 50 × 50 cm several detector technologies have been developed and incorporated into the design. One of the important techniques is reading a scintillation light from both ends of the fiber. By introducing this, the light collection yield increases by 1.8 hold compared to the conventional one-side read out. This method positively compensates for the loss of collected light suffered while propagating through WLS fibers, ensuring a stable detector operation, as well as improved detection efficiency and count uniformity.

Figure 1 shows prototype detectors that have neutron-sensitive areas of 32 × 32 and 64 × 64 cm (denoted as Det 32 and Det 64 in the figure). The pixel size is designed to be 2 × 2 cm for both detectors: and can be reduced to 5 mm. The Det 64 detector is one of the largest two-dimensional detector modules of this type ever built in the MLF. Figure 2 shows a spatial count distribution measured with the Det 64 under a flood illumination from a ^{252}Cf source. The count uniformity over the detector area is evaluated to be 10% (= σ/mean) (Count dip appeared in cross is due to juncture part of the four scintillator screens). The detector exhibits detection efficiency of 40–50% for thermal neutrons with a ^{60}Co gamma-ray sensitivity of ~10^{-6}.

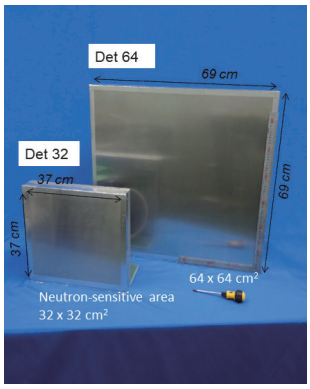

Figure 1. Prototype detectors with neutron-sensitive areas of 32 × 32 and 64 × 64 cm (Det 32 and Det 64) [2].

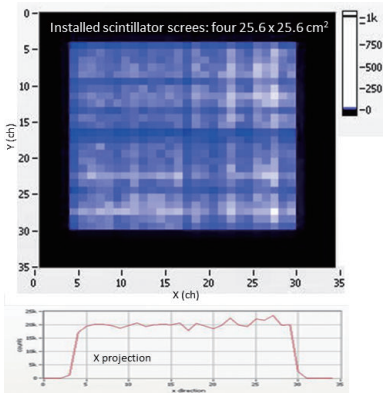

Figure 2. Spatial count distribution measured with the Det 64 under a food neutron illumination (1 ch. = 2 cm). Four 25.6 × 25.6 cm screens are implemented tentatively [2].

References

[1] T. Nakamura, J. of Phys. Conf. Ser. 528 (2014) 012042.
[2] T. Nakamura, et. al., in the proceedings of 2015 IEEE NSS conference record (2015).

T. Nakamura, K. Toh, N. Tsutsui, and K. Sakasai
Neutron Instrumentation Section, Materials and Life Science Division, J-PARC Center

A Scintillator / Wavelength-Shifting Fiber Coil Detector

1. Introduction

A detector technology, alternative to the ^{3}He-gas based detectors, should produce similar or even better detector performances than the conventional ones in terms of a neutron-sensitive area, detection efficiency, gamma-ray sensitivity, count rate capability, etc. Recently, we have proposed a scintillator / wavelength fiber coil (SFC) detector as one of the promissing solutions [1-3]. This new detector technology would pave the way to install high-performance scintillation neutron detectors into a high vacuum vessel to replace the conventional tubular ^{3}He PSDs in future.

2. The SFC detector

Figure 1 shows a photograph and a schematic view of the SFC element. The idea of the SFC structure is to create a detector element with a rolled WLS fibre coil sandwiched between cylindrical scintillator screens. With this unique element structure, the total thickness of the ^{6}Li:ZnS scintillatior screen can be effectively increased without loss in the collected light yield from the opaque scintillator. An incident neutron experiences four layers of scintillation screens, where the neutron absorption probabilty corresponds to that of a 6-bar 1-inch diameter ^{3}He PSD. Hence, the detector enhances its potential to exhibit a high-detection efficiecy.

A linear position-sensitive neturon detector can be built by alignining many elements in a row. Figure 2 shows a photograph and a schematic view (inside) of the small prototype detector. 14 SFC elements are implemented in the cylindrical aluminum tube. The tubular detector can be installed easily in a high vacuum vessel ($<10^{-3}$ Pa) mechanically. It is also possbile to tile many detectors side by side with a negligible gap similarly to the array of tubuler ^{3}He PSDs. Each neutron-sensitive element has two fiber outputs for light read out. These fibers are penetrating through the tube towards the end to connect with photomultiplier tubes. By coicidence measurement of the two fibers, the detector can identifly the lit element (position sensitivity). This readout method makes the detector pixelated in principle, hence assuring a high global count rate capability, which would exceed that of a conventional tubular ^{3}He PSD. Figure 3 shows beam profile meaurement with a 28-element detector by using a ^{252}Cf source.

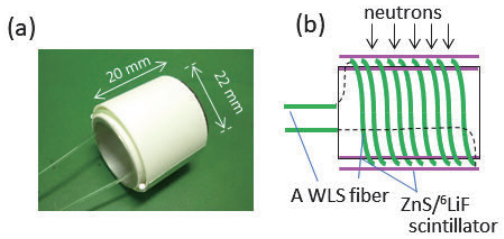

Figure 1. (a) Photograph of an SFC element and (b) a schematic view of the SFC element [2].

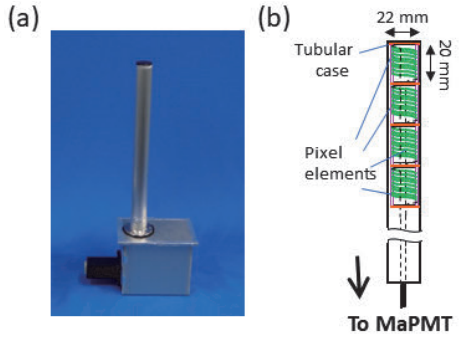

Figure 2. A 14-element prototype detector. (a) Photograph and (b) a schematic view of the detector.

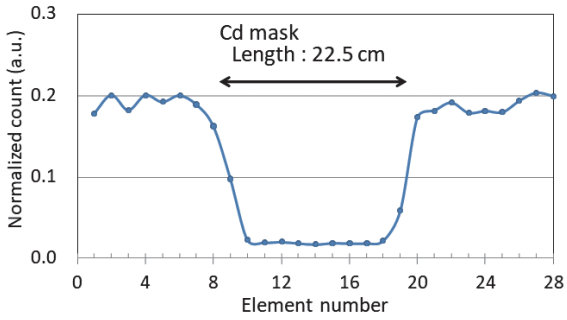

Figure 3. Cd-masked beam profile measured with a 28-element detector. One element has a width of 2 cm.

The detector measured the Cd-shielded neutron profile clearly with a spatial resoluiton of 2 cm. This result demonstrates the position senstivity of the proposed detector.

References

[1] T. Nakamura, et. al., US patent No.9268045, 2016.
[2] T. Nakamura, et. al., Nucl. Instr. and Meth. A 741 (2014) 42.
[3] T. Nakamura, et. al., in the proceedings of the 2016 IEEE NSS conference record.

T. Nakamura, K. Toh, N. Tsutsui, and K. Sakasai
Neutron Instrumentation Section, Materials and Life Science Division, J-PARC Center

Muon Science

Status of J-PARC MUSE: Overview

Because of the problems with the water leakage from the neutron target, we had to adopt the No.2 neutron target, which is not equipped with Helium bubbling function, so it cannot accept beams with intensity higher than 300 kW.

Finally, we managed to restart the MLF operation in the end of February 2016 with the restricted proton intensity of 200 kW. Since the beginning of October 2016, the proton intensity was restricted to less than 150 kW. Although the proton beam intensity was less than 200 kW, we ensured a rather stable operation at the MLF MUSE.

1. D-Line

The D-line, a superconducting decay/surface channel with a modest-acceptance (about 40 mSr) pion injector, was originally constructed with the re-used superconducting magnet, which had been used at KEK-MSL for more than 30 years, having cold bore (inner bore radius of ϕ 12), therefore it has beam windows at the inlet and outlet. In the summer shutdown period of 2015, we replaced the re-used superconducting magnet with a new one with a warm bore (inner bore radius of ϕ 20), therefore it has no beam window, with the purpose to extract lower momentum intense negative muons, which otherwise are stopped at the beam windows. We have been having beam commissioning to extract muons with lower momentum of decay. The beamline commissioning was further accelerated by installing an automatic tuning program, the so-called ForTune, providing the beamline parameters to deliver at the sample position a muon beam, which is well-focused and has a narrower momentum byte. Consequently, we managed to extract a negative muon beam with a momentum as low as 3.7 MeV/c (65 keV). The details of the beam commissioning results will be introduced in another document.

2. S-line

At the S-line, we extracted successfully not only surface muons, but also negative cloud muons with a momentum between 24 and 32 MeV/c, and then by installing Kalliope μSR detectors assembled in the spectrometer, we started actual users' runs even at the S1-area in fiscal year 2016, although, officially the use was expected to start in the begging of April 2017.

3. U-LINE

At the U-line, we observed successfully ultra-slow muons on February 21, 2016. As many as 35 ultra-slow muons per second by laser resonant ionization of muoniums evolved from hot tungsten (2000 K) were experimentally detected by a MCP, which is higher than that developed by KEK and RAL (20 μ^+/s) at the RIKEN/RAL. We have been making efforts to enhance the yield of ultra-slow muons, by replacing 3N W to 4N W, installing axial focusing superconducting magnets in the U-line, and by developing an YGAG AMP crystal for the solid-state laser system.

4. H-LINE

At the H-line, we installed successfully the front-end components near the muon production target, H-line beamline elements up to the H1 area and the iron shielding, including that for the H1 area experiments. The safety inspection of the MLF was successfully conducted, and the certificate was issued on November 7, 2016, from the Radiation Management Institute, Inc. The inspection items included the shielding construction prepared for a new muon beam line and the radiation dose measurements around it in MLF, particularly, for the muon beam line up to the H1 area.

Y. Miyake[1,2]

[1]*Muon Science Laboratory, Institute of Materials Structure Science, High Energy Accelerator Research Organization (KEK);* [2]*Muon Science Section, Materials and Life Science Division, J-PARC center*

Recent Developments of Monitoring Systems and Remote Handling Devices for Muon Production Target at J-PARC MLF MUSE

At J-PARC MLF, a muon rotating target made of an isotropic graphite is located at 30-m upstream of a neutron mercury target. In the summer maintenance period of 2014, the spent fixed target was replaced with a rotating target [1].

1) Diagnosis of the rotating system and temperatures

The muon rotating target is consumable with a finite lifetime. Rotary supports, bearings and shafts of the muon rotating target are exposed to very intense radiation and high heat by the pulsed 3-GeV proton beam irradiation. The radiation damage of the graphite is dispersed by rotation. We are developing a monitoring system for multiplexing of the interlock system, life prediction and abnormality portent of the muon rotating target.

It is predicted that the life time of the muon rotating target is determined by the failure of the rotary support. We are monitoring the torque of the rotary motor in order to diagnose the condition of the rotation system. The number of rotations from the first introduction into the proton beamline up to the present time (March 2017) is around 5 million rounds (5400 hours). Service life time of the bearing using a solid lubricant made of a tungsten disulfide is around 100 million rounds. The torque of the motor has not changed since the initial introduction. Recently, a motor-acoustic diagnosis by a microphone has been initiated. Currently, we have a directional microphone installed near the rotating motor, and the motor sound is the subject of analysis. The frequency analysis of the recorded sound indicated in Fig. 1 shows that the acoustic components include the electric noise, driving sound due to cooling water and the air conditioner and the sound of the rotary motor and transmissions. It is possible to measure selectively the sound of the rotation. Currently, we ordinarily monitor the amplitude and peak frequency of the sound during rotation.

It is not possible to measure the temperatures of the muon rotating target by direct contact because a thermometer cannot be attached to the rotating body. Thermocouples are attached to the cooling jacket to measure the temperature rise due to thermal radiation from the muon target. However, the proton beam cannot be stopped rapidly in this monitoring system, in case of excessive temperature rise. We are developing a real-time two-dimensional radiation thermometer to monitor the temperature. The major problem in introducing the infrared camera is that the camera breaks down due to radiation. We measured the radiation dose with glass dosimeters at the M1 tunnel where the camera will be installed. The measured dose at 312 hours of 0.15-MW beam operation was 20 mSv. This value corresponds to 1 Sv when operated for 1 year (2000 hours) with 1 MW operation. Since the infrared camera (ULVVIPS-04171SL made by Vision-Sensing Co., Ltd.) to be introduced withstands up to 5 Sv by irradiation with gamma rays, it is estimated to be usable for more than 5 years. The radiation hardness against neutrons and fast charged particles is unknown, and we plan to conduct a radiation tolerance test by installing a test machine in the future.

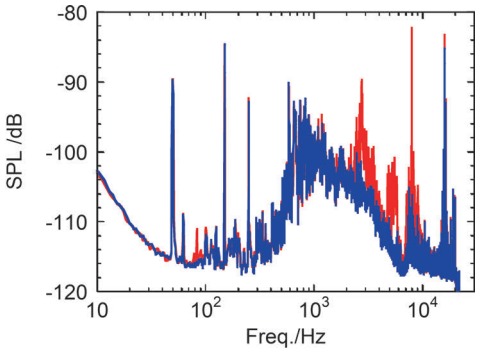

Figure 1. Sound pressure level as a function of frequency of the sound during rotation (red) and stop (blue).

2) Remote-controlled commissioning for volume reduction

The muon target will be so highly activated that hands-on maintenance cannot be conducted. The muon fixed or rotating target is rigidly fabricated into a Target rod. The Target rod is integrated into a stainless-steel plug shield through four screws. The assembled component is called target assembly. The used target rod on the target assembly is replaced with a new target rod and the plug shield is reused. In the Hot cell, the replacement is performed by remote handling devices, such as a plug stand, an exchange device, a cutting device, a power manipulator, several master slave manipulators, and an in-cell crane. The exchange device gives up-down motion, left-right motion, forward-backward motion and rotation to dismount the Target

rod from the plug shield. The cutting device has two holding mechanisms and a cutter. The whole two holding mechanisms can be rotated with 90° toward the HL-LT storage vessel. The two holding mechanisms can be moved with up-down motion independently. Only the upper holding mechanism can be moved with left-right motion and forward-backward motion. The target assembly with the replacement of the Target rod is transported to the beam line and installed again.

The upper and lower holders of the Target rod are held by the upper and lower supports of the exchange device, respectively. The fixing screws are loosened remotely by a power-manipulator. Finally, the Target rod is dismounted from the plug shield by the upward motion and the backward motion of the exchange device. The dismounted Target rod is stored in a storage facility outside of the MLF facility. However, the volume of the highly radioactive part from the Target rod must be reduced to save space for storage.

The Target rod is remotely cut into three pieces by the cutting device. The most radioactive part (1–2 Sv/h at surface) is stored in a vessel with functions of support and enclosure, because they are not self-standing and radioactive. Because that vessel is transported to another facility for long-term storage, it is called high-level (HL) long-term (LT) storage vessel. The moderately-radioactive part (20–40 mSv/h at the surface) and the low-radioactive part (100–200 μSv/h at the surface) is stored in another vessel with functions of support and brief enclosure. The vessel is called middle-level (ML) long-term (LT) storage vessel. Both storage vessels can be transported remotely by the in-cell crane. Figure 2 shows pictures of the HL-LT storage vessel.

For volume reduction, the HL-LT storage vessel without a hat-shaped lid is set on a base table of the cutting device. The dismounted Target rod is given to the cutting device from the exchange device. The holding mechanism grasps the Target rod and is rotated with 90° toward the HL-LT storage vessel. The holding mechanism is lowered and inserted into cutting position of the storage vessel. After cutting by the cutter, the high-level part of the Target rod is stored in the HL-LT storage vessel. Figure 3 shows a picture of the mock-up Target rod held by the cutting device from the exchange device on the left and a picture of the mock-up Target rod in the HL-LT storage vessel just after cutting by the cutting device. Then the holding mechanism is removed from the upside of the storage vessel. The hat-shaped lid is set on the storage vessel and the fixing screws are tightened by the power-manipulator. Finally, the integrated HL-LT storage vessel is transported to a temporary storage position. As of the ML-LT storage vessel, the holding position of the Target rod is changed with the assistance of the in-cell crane. Then the moderately radioactive part is stored in the ML-LT storage vessel with procedures similar to those of the HL-LT storage vessel. The lowly radioactive part can also be stored in the ML-LT storage vessel by the in-cell crane. Using mock-ups of the Target rod, the commissioning tests of volume reduction in the Hot cell was successfully completed in 2014 and 2016.

Figure 2. A picture of the HL-LT storage vessel.

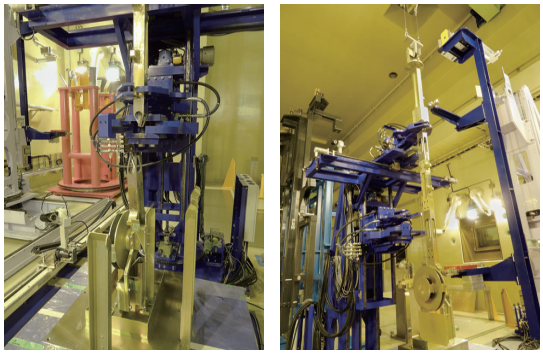

Figure 3. A picture of the mock-up Target rod held by the cutting device from the exchange device on the left and a picture of the mock-up Target rod in the HL-LT storage vessel on the right.

Reference

[1] S. Makimura *et al.,* Development of Muon Rotating Target at J-PARC/MUSE, Journal of Radioanalytical and Nuclear Chemistry **305** (2015) 811-815.

S. Matoba[1,2], S. Makimura[1,2], N. Kawamura[1,2], Y. Matsuzawa[3], H. Aoyagi[3], H. Kondo[3], S. Sakata[3], M. Meguro[3], and M. Tabe[1,2]

[1]Muon Science Laboratory, Institute of Materials Structure Science, High Energy Accelerator Research Organization (KEK); [2]Muon Science Section, Materials and Life Science Division, J-PARC center; [3]Nippon Advanced Technology Co., LTD (NAT)

Present Status of D-line

In FY2015, during the summer shutdown period, the new solenoid was installed into an existing beamline. This solenoid is a warm-bore type, and requires no foils for protection from thermal radiation. The inner radius of the coils was increased from 12 to 20 cm. Thus, a drastic improvement of the low energy muon (~100 keV) intensity is expected. To determine this low-energy decay muon, two new experimental tools were prepared.

Firstly, we used a new type of beam profile monitor, which was made using a plastic scintillator surrounded by optical fiber, as shown in Fig. 1. The muon beam passes through the plastic scintillator, and the beam profile is obtained by a CCD camera downstream; in addition, the photons collected by the optical fiber, which are converted to electrical signals by a photo diode, provide information about the incoming time and total intensity of a beam.

Next, an automatic optimization program for beam line components, such as magnetic bends and quadrupoles (named FORTUNE), was developed, based on the TRIUMF beam tuning program. In this tuning, the time gated signal of muons, which is obtained by an optical fiber of the beam profile monitor, was adopted as inputs into the D2 area.

After commissioning these apparatuses, we spent several days performing beam tuning; finally, the muon intensity that was obtained was more than 100 times larger than that at 5 MeV/c at momentum (~120 keV in energy). Therefore, the expected intensity of the negative muon is ~3×10^3 muon/s @1 MW.

We also performed a slit and beam profile at the focusing point optimization using the same apparatus and at this stage, its parameters were, horizontally 10 mm, vertically 30 mm with a narrow momentum width (Fig. 3). Further improvement is expected prior to next year's commissioning.

In the D1 area, we also performed dedicated tuning in an almost identical way, and got a beam profile smaller than the previous one, as shown in Fig. 4. In addition, to reduce the noise component, a flypast chamber was installed The flypast chamber is a long vacuum pipe, and a sample is mounted in the flypast chamber as shown in Fig. 5. Using the flypast chamber, 16% (Maximum) of the asymmetry can be obtained with a 5×5 mm^2 sample.

Several kinds of refrigerators are available at D1. The lowest temperature is obtained by using a top-loading dilution refrigerator (DR). In a common dilution refrigerator, the dilution unit should be warmed up to room temperature in order to change the sample. Therefore, it takes a few days to change and cool down a sample. Meanwhile, in our top-loading DR, the sample can be changed by unloading or loading only the sample holder. This feature is quite useful for μSR experiments.

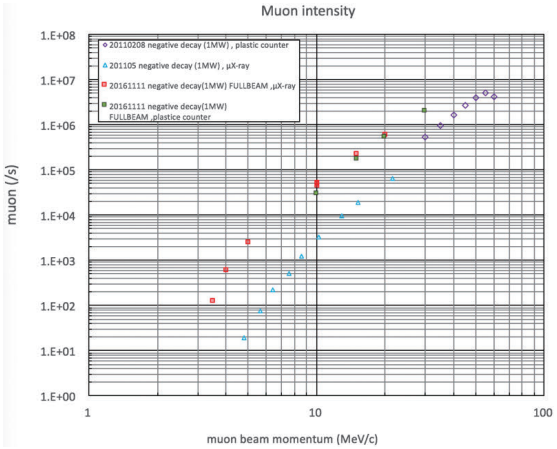

Figure 2. Comparison of the muon intensity with the old (cyan and purple) and new (red and green) solenoid.

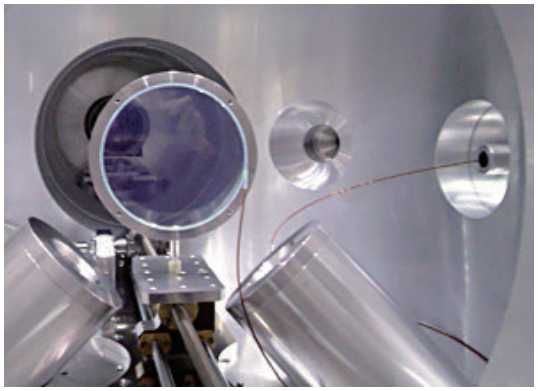

Figure 1. Beam profile monitor at the D2 area.

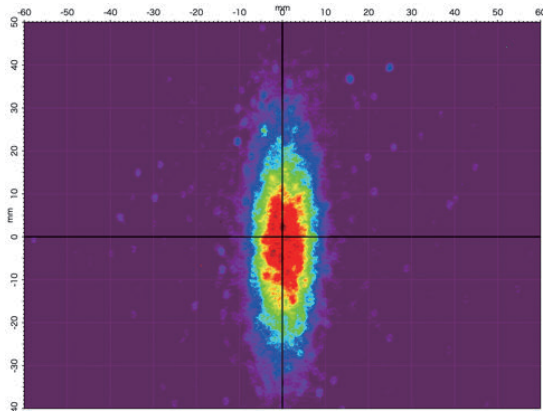

Figure 3. Beam profile of decay muon at the D2 area focusing point.

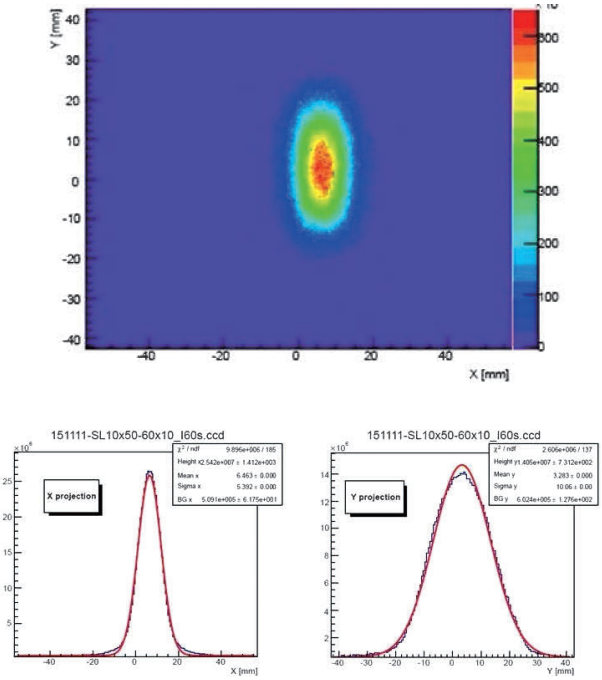

Figure 4. Example of the beam profile of surface muon at D1.

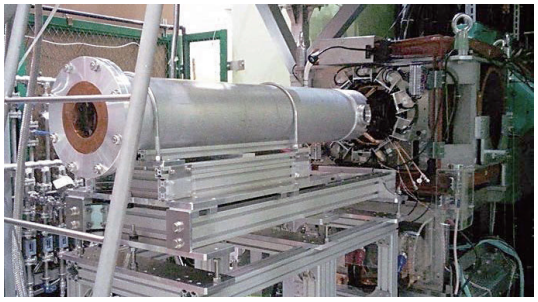

Figure 5. Flypast chamber installed at D1.

Furthermore, the cooling system of the DR is based on the pulse-tube type refrigerator, and liquid Helium is not required to cool down the system. Currently, the DR can be used only at the D1 area. The cooling down of the system, including the pre-cooling process, can be performed automatically by using an integrated operation program. After evacuation of the vacuum can to high vacuum, it takes roughly 1.5 days to reach the lowest temperature from room temperature. The changing of a sample requires 0.5 day. The dimensions of the sample area are 40 × 40 mm^2. A specimen is mounted on the pure silver plate using Apiezon N grease or GE varnish, and is covered by thin Ag (10 μm) foil.

Helium 4 cryostats are also available at D1. The most popular one is "Minicryo" which can be used down to 4 K within a few hours. In minicryo, the sample is placed in vacuum and a silver sample holder is used.

A high-temperature infrared furnace is also available at D1. In the furnace, a sample can be warmed up from room temperature to 1000 K.

The muon kicker system is used to separate a double pulse muon beam into two single pulses and to feed them to two experimental areas (D1, D2) simultaneously. The beam operation with the kicker system started successfully in the winter of 2011. It was found, however, that the kicker noise to the particle detector system appeared to be associated with the ignition of the kicker power supply. The amplitude of the noises ranged from a few tens to several hundreds of millivolts, and the frequency was between 6 and 10 MHz. The noises were radiated into the air, and/or dispersed through the AC lines, the detector signal lines and the ground lines. The kicker noise level was drastically improved by RF-shielding with copper sheets of the transmission lines and by reinforcing both the ground lines of the kicker system and the detectors. Measures with bypass capacitors at the New D1-μSR spectrometer were also successful.

Further improvements were required for the negative muon experiments at the D2 area, and for the ultra-slow muon at the U1A area. Therefore, we tried to insulate electrically the kicker chamber from the beam ducts and its base, and reduce the ground impedance. However, despite that, the radiation noises increased. A method to utilize a saturable inductor (SI) was also tested to suppress the surge current at the ignition. However, it was not successful because of the non-linear response of SI: the magnitude of the surge current was too high to suppress. This time, a Low-Pass-Filter (LPF) using only linear elements is tested instead of the SI.

The pi-type LC filter was tested as a low-pass filter to eliminate the kicker noise to the particle detector used in the negative muon experiments at the D2 experimental area. The filter filtered successfully the surge current produced at the kicker ignition. However, the noises to the detector were not mitigated. The noise frequency ranged between 1 and 3 MHz, which coincided with the dominant frequency component of the kicker pulse whose width was 1 μs.

H. Fujimori[1,2], Y. Irie[1,2], K. Kojima[1,2], Y. Ikedo[1,2], T. Adachi[1,2], M. Tampo[1,2], K. Hamada[1,2], S. Doiuchi[1,2], W. Higemoto[3], S. Sakata[4], M. Meguro[4], N. Kawamura[1,2], A. Koda[1,2], N. Kurosawa[5], P. Strasser[1,2], K. Shimomura[1,2], and Y. Miyake[1,2]

[1]Muon Science Laboratory, Institute of Materials Structure Science, High Energy Accelerator Research Organization (KEK); [2]Muon Science Section, Materials and Life Science Division, J-PARC center; [3]Advanced Science Research Center, Japan Atomic Energy Agency (JAEA); [4]Nippon Advanced Technology Co., Ltd. (NAT); [5]Cryogenics Science Center, High Energy Accelerator Research Organization (KEK)

The Status of the U-line

Ultra-Slow Muon beamline

Compared to the conventional "surface" and "decay" muon beams, the Ultra-Slow Muon beams have specific features, such as low kinetic energy, small beam-size, and short time distribution. Thus, there is a need for a new magnetic probe to investigate the material properties of subsurfaces, interfaces and small-size samples.

Initially, the generation of Ultra-Slow Muon involves the emission of muonium (Mu) with thermal energy from tungsten foil (2000 K) into vacuum. Then, Mu is excited and is ionized by 122-nm light (Lyman-α of Mu) and 355-nm light.

In February 2016, we observed Ultra Slow muons for the first time in J-PARC. Since then, we continued to perform the beam commissioning to increase the beam intensity and to optimize the beam properties. The generation rate of Ultra-Slow Muon was gradually increased to 55 μ^+/s by increasing the intensity, and optimized for the alignment and position of laser lights (Fig. 1). Considering the detection efficiency of the microchannel plates, the rate was estimated to be more than 100 μ^+/s.

Another development in the U-line was the increase of the intensity of the surface muon beam incident on the Mu production target using an Axial Focusing Solenoid No. 3 and No. 4. An axial Focusing Solenoid is a pair of superconducting coils in a cryostat with a warm bore. Six sets of Axial Focusing Solenoids are designed to transport and focus surface muon beams on the Mu production target. However, Axial Focusing Solenoid No. 3 and No. 4 were not used because of the instability of the high voltage power supply for positron separators, which is a Wien Filter type supply that is used to eliminate positrons from muon beams, was enhanced by applying the magnetic field of an Axial Focusing Solenoid. In November 2016, we restarted the aging of the separator in condition by exciting Axial Focusing Solenoid No. 3 and No. 4. Then, we found the condition of applying a high voltage at the separator with the solenoid field. Figure 2 shows the time structure of an Ultra-Slow Muon with and without a solenoid field at the separator. It is clearly seen that the Ultra-Slow Muon rate was increased by ~30% compared with the case when not using Axial Focusing Solenoid No. 3 and No. 4. We continue to conduct beam commissioning to realize a more intense Ultra-Slow Muon and to optimize further the beam properties. In addition to increasing the laser intensity, Ultra-Slow Muon spin rotation experiments will be performed in the near future.

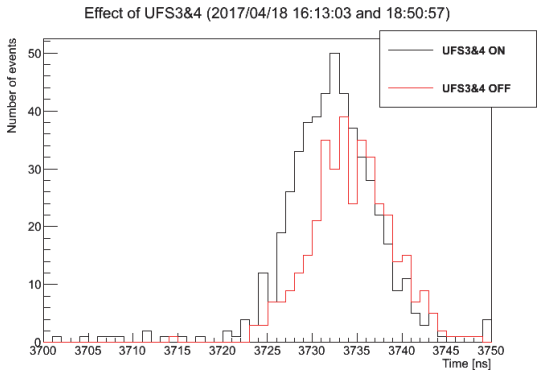

Figure 1. Ultra-Slow Muon generation rate to vary the timing of 355-nm light with respect to the Lyman-α of muonium.

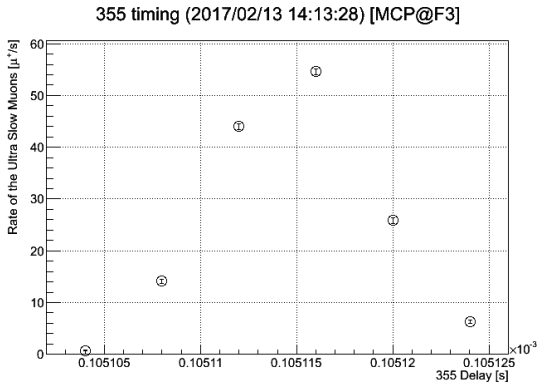

Figure 2. Ultra-Slow Muon generation rate to vary the timing of 355-nm light with respect to the Lyman-α of muonium.

Laser system for Ultra-Slow Muon generation

Ultra-Slow muons can be generated in resonant optical ionization by the simultaneous irradiation of 122.09-nm-wavelength light, which is the muonium Lyman-α resonance wavelength and corresponds to the 1S-2P transition of muonium, and 355-nm light. Therefore, the high-energy coherent Lyman-α light source is a very important element for the efficient generation of high-power Ultra-Slow muons.

In order to generate intense Lyman-α light, we chose the two-photon resonance four-wave-mixing scheme in krypton. A 212.556-nm pulse for two-photon excitation and a tunable near-infrared pulse are required for this method. The tunable near-infrared source can tune the wavelength around 820.649 nm and 845.015 nm to generate a resonant Lyman-α for a muonium and a hydrogen atom, respectively.

The output pulses at 212.556 nm and near-infrared from all-solid-state laser and subsequent wavelength

conversions were independently loosely focused and coaxially superposed in the middle of a 1-m long krypton-argon mixture gas cell to achieve a long interaction length and suitable mode-matching. The Kr and Ar gas mixing ratio was adjusted to satisfy phase matching in four-waves because Kr gas has a negative dispersion in the Lyman-α wavelength region. The Lyman-α laser system is described in Ref. 1.

In our last report, we showed that by installing a gas mixer into a system, the ratio of the experimentally suitable Ar/Kr mixed gases was in agreement with the theory [2]. However, the Lyman-α intensity gradually decreased after it was filled with the gas mixture. Moreover, the gas-exchange procedure influenced the degree to which the intensity of the Lyman-α fell. It was recognized that the intensity of the Lyman-α fell to around 20–30% just after the introduction of the gas mixture over about 18 h. The depredate intensity of Lyman-α is shown in Fig. 3. The reason for such a degradation is being investigated using a time- history analysis of gas contaminations. In any case, we improved a gas mixer and vacuum control device to enable it to exchange the gas mixture automatically. In this way, we performed gas exchange every few hours, which corresponded to the muon-beamline separator shut down, and we were able to maximize the beam-commissioning time.

Another major improvement in the laser system was the shape of the spectrum. To realize efficient ultraslow muon generation by laser ionization, the synchronization between the spectrum shapes of the laser with the Doppler broadening of the thermal muonium (~230 GHz) is very important when significant laser power is provided. The spectrum shape of Lyman-α is determined by the spectrum shape of the seed laser, which is based on the wavelength-tunable Ti:sapphire laser. The spectrum shape of the seed laser had comb- like discrete spectrum due to the output coupler of the Ti:sapphire laser cavity. To improve the spectrum shape, the output coupler was replaced by a new one. The spectrum shape was successfully smoothed, as shown in Fig. 4. The obtained broad spectrum has a ~90-GHz bandwidth full width at half maximum (FWHM) that corresponds to one third of the band width of thermal muonium Doppler broadening. The complete band width matching will be

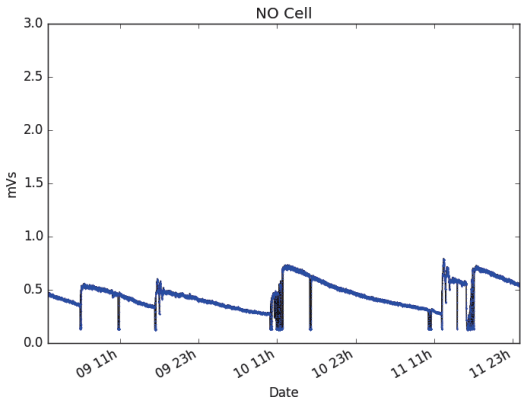

Figure 3. Long term evolution of Lyman-α intensity measured by NO gas ionization signal.

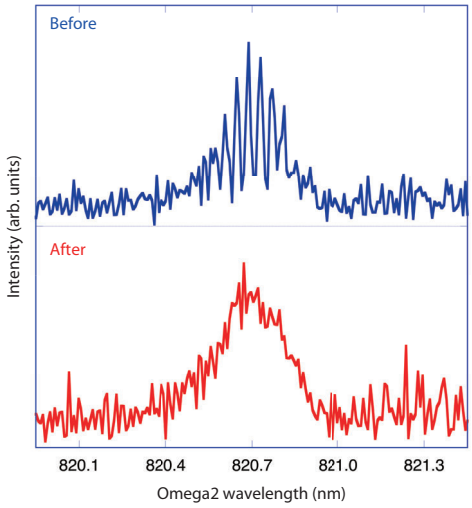

Figure 4. The spectrum shape of the seed laser before the output coupler (blue line) was replaced and after (red line).

achieved using a spectrum filter in the Ti:sapphire cavity.

In conclusion, we have successfully installed an automatic gas exchanger to improve the stability of the Lyman-α intensity. Then, we successfully operated the laser system to generate ultraslow muons and subsequent beamline tuning for a long time. In addition, the laser spectrum was improved for efficient Ultra-Slow muon generation.

References

[1] N. Saito *et. al.*. *Opt. Exp.* 24 (2016) 7566-7574.
[2] O.A. Louchev *et. al.*. *Phys. Rev. A* 84 (2011) 033842(1-9).

T. Adachi[1,2], Y. Oishi[1,2], A. D. Pant[1,2], Y. Ikedo[1,2], H. Fujimori[1,2], J. G. Nakamura[1,2], T. Iwashita[3], P. Strasser[1,2], T. U. Ito[2,4], W. Higemoto[2,4], K. Shimomura[1,2], R. Kadono[1,2], Y. Miyake[1,2], E. Torikai[4,5], M. Iwasaki[5], N. Saito[5], and S. Wada[5]

[1]Muon Science Laboratory, Institute of Materials Structure Science, High Energy Accelerator Research Organization (KEK); [2]Muon Science Section, Materials and Life Science Division, J-PARC center; [3]Nippon Advanced Technology Co., Ltd. (NAT); [4]Advanced Science Research Center, Japan Atomic Energy Agency (JAEA); [5]Integrated Graduate School of Medicine, Engineering, and Agricultural Sciences, University of Yamanashi

Experimental Area S1: from Beam Commissioning to Sample Environment and Autorun of ARTEMIS Spectrometer

A new surface muon beamline (S-line) is being constructed in the Materials and Life Science Facility (MLF) building at J-PARC. This beamline is designed to provide high-intensity low-energy muon beams, typically surface muons with a momentum of 28 MeV/c, that will be used mainly for materials and life science (μSR) experiments. The S-line will eventually comprise four beam legs and four experimental areas (namely S1–S4) that will share the double-pulsed muon beam. However, so far, the secured funding was sufficient to construct and operate the beamline toward only one of the four planned experimental areas, i.e., area S1.

Since the first beam delivery on October 29, 2015 [1], the beamline commissioning has been extensively performed by using the μSR spectrometer ARTEMIS [2], fabricated by the Element Strategy Initiative project for Electronic Materials. An automatic beam tuning program, named "ForTune" and developed specifically at MUSE, was used to obtain a well-focused muon beam at the sample position by observing μ–e decay events counted by Kalliope detectors assembled in the μSR spectrometer. The beamline parameters were optimized to achieve an optimum muon flux with a good S/N ratio within a small sample size (~20 mm). The tuning of the beamline slits led also to the suppression of positron contamination in the muon beam and a narrower beam spot size at the target position. A beam collimator with a diameter of 40 mm was placed at the end of the beamline just in front of the sample position to reduce the beamline related background. Smaller collimator sizes were also available to further reduce the beam size. The typical surface muon flux for a beam size of φ20 mm after significant tailoring (including narrowing slits) was 8.5×10^4 μ^+/s at the sample position obtained at 150-kW proton beam power operation.

A muon beam profile monitor developed to diagnose pulsed muon beams at MUSE [3] was used to monitor the muon beam shape and size at area S1. Muons stopped in a scintillation screen produce light that is captured by a large aperture lens and sent to a gated image intensifier connected to a cooled CCD camera. Figure 1 shows muon beam profiles observed at S1 with (a) beamline slits wide open, and (b) after significant tailoring by narrowing down the width of the slits (φ40-mm beam collimator was used in both cases). The optimized beam spot (Fig. 1b) has a Gaussian shape with a FWHM of 22 mm horizontally and 25 mm vertically. For comparison, the beam spot with slits open (Fig. 1a) has a FWHM of 34 mm horizontally and 26 mm vertically, respectively.

The commissioning of the new electric kicker system SK12 [4] that delivers a single-pulsed muon beam to areas S1 and S2 was also performed. The results show that all four kicker modes can send the muon beam to S1 without any significant changes in the beam spot size or shape (same FWHM). Figure 1c shows the observed beam profile at S1 with the electric kicker SK12 (1313-mode) that should be compared to Fig. 1b when the switchyard magnet SSY12 is used. The only difference is that the muon yield is 4–5% smaller when using the kicker.

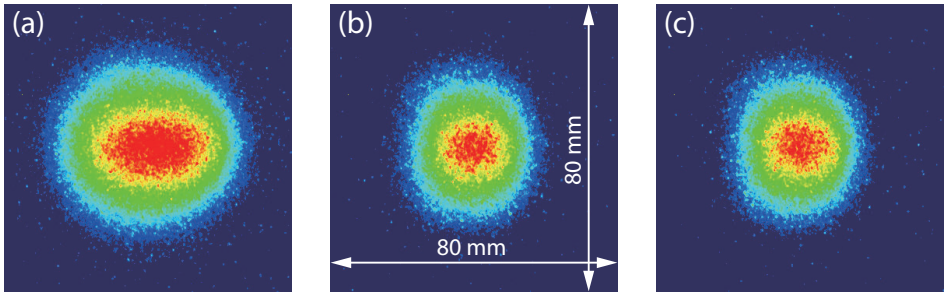

Figure 1. Muon beam profiles observed at area S1 with (a) beamline slits wide open, (b) after significant tailoring by narrowing down the slits, and (c) same condition as in (b) but using the electric kicker SK12 (1313-mode) instead of the switchyard magnet SSY12.

Negative muon beam commissioning was realized by using cloud-negative muons at S1. Muon asymmetry was measured in a highly oriented pyrolytic graphite (HOPG) sample with size 50 × 50 mm^2 in an open geometry with beam slits fully open (see Fig. 2). In contrast to the surface muons that are 100% polarized, cloud muons are produced by the lowest energy pions emitted from the muon target (cloud like) from a mixture of backward and forward decay, leading to a negative muon beam with lower polarization. The measured negative muon polarization was 0.38(1) at 28 MeV/c, and decreased with increasing muon momentum and intensity. A figure of merit, calculated by multiplying the asymmetry by the square-root of the spectrometer coincidence rate, showed that a momentum of ~32 MeV/c (maximum at S-line) is better as a measurement condition for μ^-SR, as only a data acquisition 30 times longer is needed to achieve a precision comparable to that of μ^+SR. This figure of merit depends on the negative muon residual polarization in the sample [5], and needs to be adjusted to other elements. For carbon, it is slightly higher (~20%) compared to most other elements (~16%).

The ARTEMIS spectrometer [2] is equipped with sample environment (SE) and autoruns. We have prepared: (1) flypast chamber to reduce the background signal originating from the muons stopped anywhere outside of the sample [3], (2) flash-lamp light illumination setup and pulse-wise light on/off histogram recording (red/green mode) of data acquisition, (3) micro transverse-field coil (μTC) with an inner bore of 130 mm, which can apply 50 mT horizontal field perpendicular to the beam and muon spin with a minimum shifting of the muon beam trajectory. Figure 3 shows a commissioning result of the photo-induced muon spin relaxation of silicon [6], as reproduced at ARTEMIS.

In Fig. 4a, the μTC setup and vertical helium flow cryostat as installed in ARTEMIS are shown. In order to measure the anisotropy of the hyperfine parameter of the shallow hydrogen-like state of muons, such as in

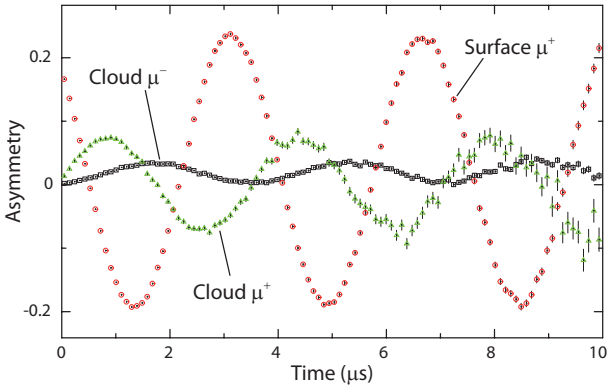

Figure 2. Negative muon commissioning at area S1 showing muon asymmetry measured in a HOPG sample with 28 MeV/c cloud μ^- (black square), and compared to 28 MeV/c surface μ^+ (red circle) and 32 MeV/c cloud μ^+ (green triangle), respectively.

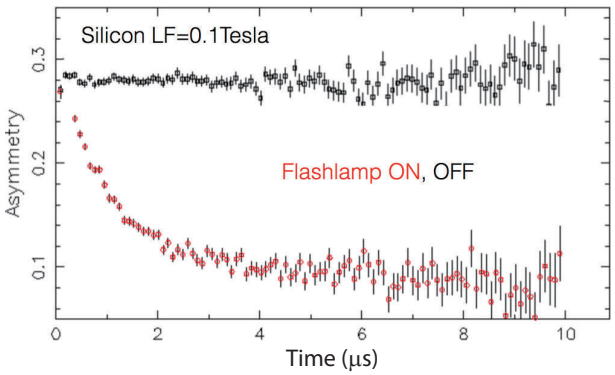

Figure 3. Photo induced relaxation of Silicon as reproduced at the light illumination attachment of ARTEMIS.

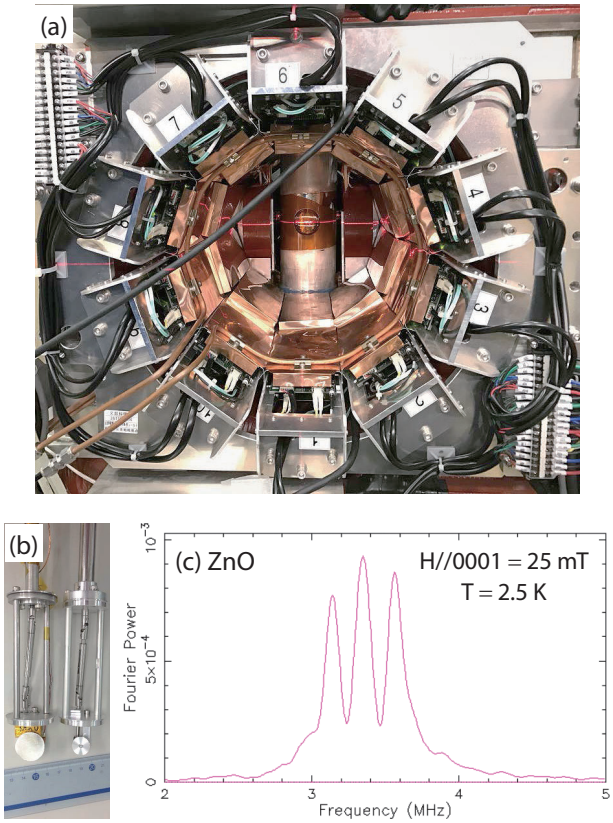

Figure 4. (a) Micro transverse-field coil (μTC) together with vertical helium flow cryostat installed in ARTEMIS. (b) Rotating samples rods: the rod with the smaller disk is automated by a stepping motor, and is computer controlled. (c) Fast Fourier Transform spectrum of ZnO shallow muonium state as measured at ARTEMIS.

ZnO [7] and rutile TiO_2 [8], an automated sample rotating rod, with rotation axis parallel to the beam axis has been prepared (Fig. 4b); with the μTC and vertical helium flow cryostat, the angle dependence measurement of the hyperfine coupling parameter is now fully automated. An example of an FFT spectrum of the shallow state (side bands) in ZnO is shown in Fig. 4c.

Autorun sequence system to run a series of measurements, together with a remote monitoring system of the running measurement is incorporated with the IROHA2 system developed for MLF [9]. The histogram data of the μSR measurement are also available on a KEK server with a password protection for each set of experimental numbers. The histogram data files may be downloaded upon request from the histogram data viewer in a format readable by the major analysis programs, such as musrfit, msrfit and WiMDA.

Experimental area S1 has been opened to the user program since February 2017. With area D1 at the D-line, two experimental areas at MUSE are now available to μSR users to perform condensed matter physics experiments.

Acknowledgement

The development of the ARTEMIS spectrometer was financially supported by MEXT Elements Strategy Initiative to Form Core Research Center at Tokyo Institute of Technology.

References

[1] A. Koda *et al.,* KEK-MSL Report 2015, 16 (2016) and MLF annual report 2015; P. Strasser et al. to appear in JPS Conf. Ser. (2017).
[2] K. Kojima *et al.,* J. Phys: Conf. Ser., **551** (2014) 012063; MLF annual report 2015, 133 (2016); to appear in JPS Conf. Ser. (2017).
[3] T. U. Ito *et al.,* Nucl. Instr. Meth. A 754, 1 (2014).
[4] P. Strasser *et al.*, KEK-MSL Report 2013, 14 (2014).
[5] V. R. Akylas and P. Vogel, Hyperfine Interact. 3, 77 (1977).
[6] R. Kadono *et al.*, *Phys. Rev. Lett.*, 73, 2724, (1994).
[7] K. Shimomura *et al.*, *Phys. Rev. Lett.*, 89, 255505, (2002).
[8] K. Shimomura *et al.*, *Phys. Rev. B*92, 075203, (2015).
[9] T. Nakatani *et al.*, Proceedings of ICALEPCS2009, 676 (2009).

P. Strasser[1,2], A. Koda[1,2,6], K. M. Kojima[1,2,6], T. U. Ito[2,3], H. Fujimori[1,2], Y. Irie[1,2,4], M. Aoki[5], Y. Nakatsugawa[1,2], W. Higemoto[2,3], M. Hiraishi[1], H. Li[1,6], H. Okabe[1,2], S. Takeshita[1], K. Shimomura[1,2], N. Kawamura[1,2], R. Kadono[1,2], and Y. Miyake[1,2]

[1]Muon Science Laboratory, Institute of Materials Structure Science, High Energy Accelerator Research Organization (KEK); [2]Muon Science Section, Materials and Life Science Division, J-PARC center; [3]Advanced Science Research Center, Japan Atomic Energy Agency (JAEA) ; [4]Accelerator Laboratory, High Energy Accelerator Research Organization (KEK); [5]Graduate School of Science, Osaka University; [6]Open Source Consortium of Instrumentation (Open-It)

Present Status of the H-line

A brand-new beam line, H-line, is planned to be constructed as the fourth beam line in MUSE. The new beam line is designed to have a large acceptance, momentum tunability, as well as the ability to use a kicker magnet and a Wien filter. This beam line will provide an intense beam for experiments that require high statistics, and need to occupy the experimental areas for relatively long periods. Several experiments in the field of fundamental physics have been proposed pertaining to the H-line [2-4].

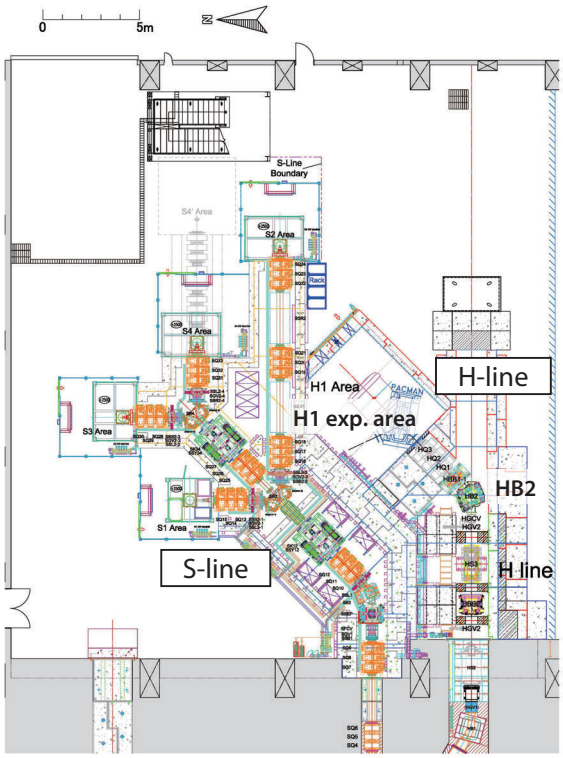

Figure 1. A layout plan of experimental hall #1 in the first phase of the H-line construction.

In the primary stage of the MUSE construction, only the D line and the front-end magnets in the S line were installed, then the front-end magnets in the U line were installed in 2009. In the H-line, temporary radiation-shield blocks were placed. J-PARC has been in operation since 2008, and thus the activation around the muon production target has become more serious with every passing year. According to the evaluation using a Monte-Carlo code [5], the dose rate near the target chamber was estimated to be close to 1 Sv/h, and the summer shutdown in 2012 was the actual deadline for installation of the front-end magnets in the H-line. Thus, the installation of the front-end devices was almost completed in 2012 and the remainder finished in 2014, as shown in Fig. 2.

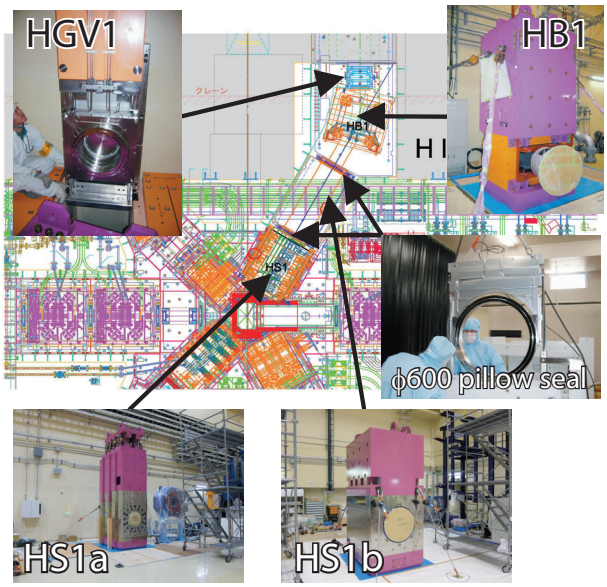

Figure 2. Installed front-end devices in the H-line.

In the other high-intensity beam line, the U line, we adopted only axial focusing magnets to obtain high-transmission efficiency [6]. However, in the H-line, the beam captured by an axial focusing large-aperture solenoid magnet is transported through bending magnets, although these non-axial focusing magnets increase the beam loss. To compensate for this and achieve a high transmission efficiency, large-aperture magnets and other devices are adopted in the H-line.

The conceptual design work for the major components in the experimental hall, i.e. magnets, vacuum components, etc., has been almost completed for the first phase of the H-line, where the beam-line was constructed up to the first experimental area, as shown in Fig. 1.

The design work for the radiation shield was performed in the same manner as in the other beam lines [5]. Along the beam-line, a few meters-thick concrete shield will be required to enclose the streaming neutrons and other radiation sources. Because large aperture devices were adopted, the effect of the streaming neutrons will be more serious than in the other beam lines. The evaluation of the streaming neutrons is important not only for radiation safety but also to determine its effect on the detectors and other devices in the experimental area. Figure 3 shows a typical result of the simulation. During the proton beam operation,

the dose rate in the experimental area is expected to reach 100 μSv/h, and no one can enter this area even if no muon beams are being delivered. By inserting a beam blocker made of a 40-cm thick copper block, the dose rate is decreased by about 1/10. Using the beam blocker as well as switching off the bending magnet, HB2, can guarantee radiation safety. Herewith, a personal protection interlock system can be introduced.

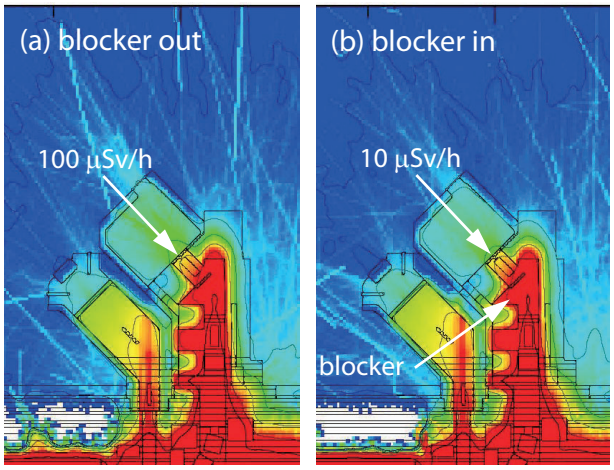

Figure 3. A typical simulated result of the radiation dose around the H-line.

In 2014JFY, supplemental budget was secured to reinforce the radiation shield against a 1-MW proton beam. A part of the H-line shield was designed and fabricated to unite the reinforcement shield in experimental hall #1. These shield blocks were delivered in the end of March 2015. Then, during this fiscal year, we assembled all of these blocks into the H-line up to the first experimental area, the H1 area, which is covered with deep blue shield blocks, as shown in Fig. 4. Although the assembly was completed about 10 days behind schedule, the work was done without any major problems.

The application for change in the shield was accepted by the regulatory agency after the inspection in early November, just after restarting the beam operation.

Early completion of the H-line construction is anticipated by the usercommunity. We aim to deliver the beam to the first experimental area in the first phase of the construction. After that, during the second phase, the H-line will be extended for g-2/EDM measurement and also for the transmission muon microscope, as shown in Fig. 5.

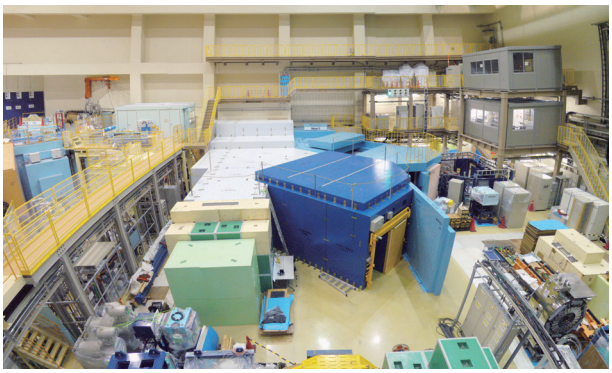

Figure 4. The radiation shield of the H-line assembled in experimental hall #1.

Figure 5. Beamline layout in the second phase.

[1] N. Kawamura *et al. 2013 Journal of Physics: Conference Series* **408** 012072.
[2] K. Shimomura *et al. ibid.*
[3] N. Saito *et al. ibid.*
[4] S. Mihara *et al. ibid.*
[5] N. Kawamura *et al.* 2009 *NIM A* **600** 114.
[6] K. Nakahara *et al.* 2010 AIP Conf. Proc. **1222** 420.

N. Kawamura[1,2], MuHFS collab., DeeMe collab., and g-2/EDM collab.
[1]*Muon Science Laboratory, Institute of Materials Structure Science, High Energy Accelerator Research Organization (KEK);* [2]*Muon Science Section, Materials and Life Science Division, J-PARC center*

MLF Safety

Research Safety

1. Radiation safety

(Adopting "low-surface contamination area" at the MLF Experimental halls)

To prepare for the upcoming high-beam-power operation of MLF, a new classification of the radiation-controlled-area at the MLF experimental halls, "low-surface contamination area", was adopted in November 2016. Its purpose is to avoid surface-contamination problems caused by a sample, an environmental atmosphere, contamination and so on, and to expand the flexibility of the experimental conducted at MLF.

The low-surface contamination area is defined in the local radiation protection rule of J-PARC and is included in the 1st-class radiation-controlled area. In the area, a concentration of surface contamination equal to or lower than the standard value (0.04 Bq/cm^2 for alpha-emitting radioisotopes and 0.4 Bq/cm^2 for non-alpha-emitting radioisotopes) should be kept. If the contamination in the area exceeds the standard value, it should be removed immediately. An operation with any surface contamination in the area can't be planned. However, any accidental contamination is acceptable (and of course, it should be removed immediately). The limitation of gas and liquid used in the experiment is mitigated. And challenging experiments can be conducted more easily. The low-surface contamination area is not applied to the BL11 experimental room and the 3rd experiment preparation room because the contamination is assumed during the experiment or the operation.

To introduce the low-surface contamination, a monitor for take-out articles and 2 hand-foot-clothes monitors were installed. More than 20 survey meters were prepared and can be used at each neutron instrument due to easy operation by users and staffs. Lockers were prepared in the locker room to reduce the number of articles brought to the experimental halls. Users and staffs can always take an article out of the radiation controlled-area, excluding irradiated articles and sample because of the installed monitor for articles that are being taken out. Periodic survey service (once a day) to take out large articles also started. In the summer maintenance period, the classification of the radiation-controlled area at the experimental halls temporarily changes to 2nd class to make it easy to maintain the instruments.

(Radiological License Upgrade)

The two applications for radiological license upgrades in FY2016 were approved on September 27, 2016, and February 2, 2017.

Updated items on September 27, 2016:

(1) Change of the contamination survey areas for preparation to apply the 1st-class radiation-controlled area in the MLF experimental halls
(2) Added storage and usage of several sealed radioisotopes (6 Cs-137)
(3) Preparation of the H-line installation of Muon beam line (change of shield structures)
(4) Change of the drainage equipment for radioactive liquid waste (position change of the connection to the tank lorry)

Updated item on February 2, 2017:

(1) Added gas folders in the off-gas system.

2. Chemical safety

The usual chemical safety checks of user-brought chemical materials, such as specimen and reagents, to evaluate their toxicity and the stability of their actual physical state – powder, solid, liquid or gas, were performed successfully by the chemical-safety team, along with approval of the actual materials for use by individual beamline staffs. As a result, the experiments were performed without serious problems. Figure 1 shows a trend for the number of chemical materials for safety check. As for the form of the sample, solid was used most frequently, then powder, liquid, and gas. From the viewpoint of organic or inorganic matter, inorganic matter was used more frequently. In 2016, because of stably available beam time (approximately 153 days), the total number of chemical materials was increased, compared with 2015 (approximately 62 days), that was the highest number ever.

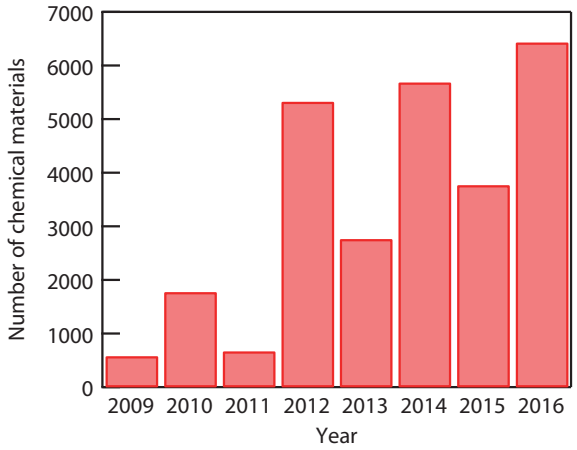

Figure 1. Trend of chemical materials for chemical safety check.

A Deuteration laboratory of P1 class has been under construction for several years. Currently, the rules for safety use are discussed, and it is scheduled for test operation from the next fiscal year.

3. Alarm indication system for instrument condition monitoring

We started installing alarm indication systems on individual beamlines in experimental halls. This system consists of signal line of equipment to monitor, connection box, controller, signal light and PC via J-LAN. The schematic of the system is shown in Fig. 2. The status of the equipment of an individual beamline, collectively monitored, is displayed at a monitoring room by using this system.

One of the purposes of the system is to ensure an unattended operation of various kinds of sample environment equipment, for example, cryo-furnace, by observation in the monitor room. Therefore, the burden on the users is alleviated for some of the equipment. On the other hand, an application possibility of the system for unattended operation of the high temperature furnace under maximum temperature of more than 1273 K is being discussed now. This year, the systems were installed at BL01, BL02, BL14 and BL22. Figure 3 shows the systems installed at BL01 and BL02.

The top red light indicates status of warning or normal-operation by blinking or by lighting, respectively at any time. The orange light in the middle indicates status of caution of equipment, when the equipment signals potential malfunction, the light glows. The bottom light indicates the operation status, when the equipment is working in unattended operation mode, the light is blue and when it is working in remote operation mode via IROHA2, which is the standard computational environment in MLF, the light turns green. A buzzer sounds when the status requires a warning.

Next year, the systems will be installed sequentially at other beamlines, including the muon beamline.

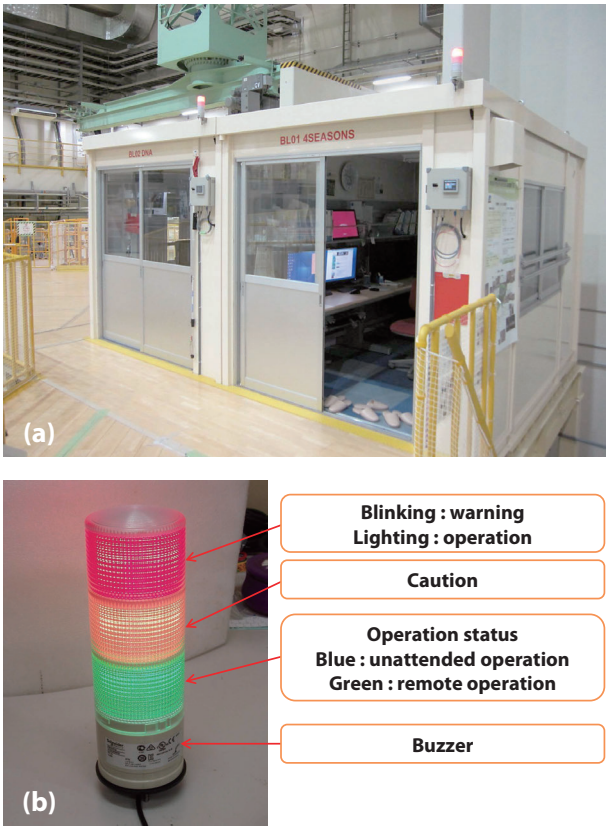

Figure 3. (a) alarm indication system at BL01 and BL02, (b) signal light.

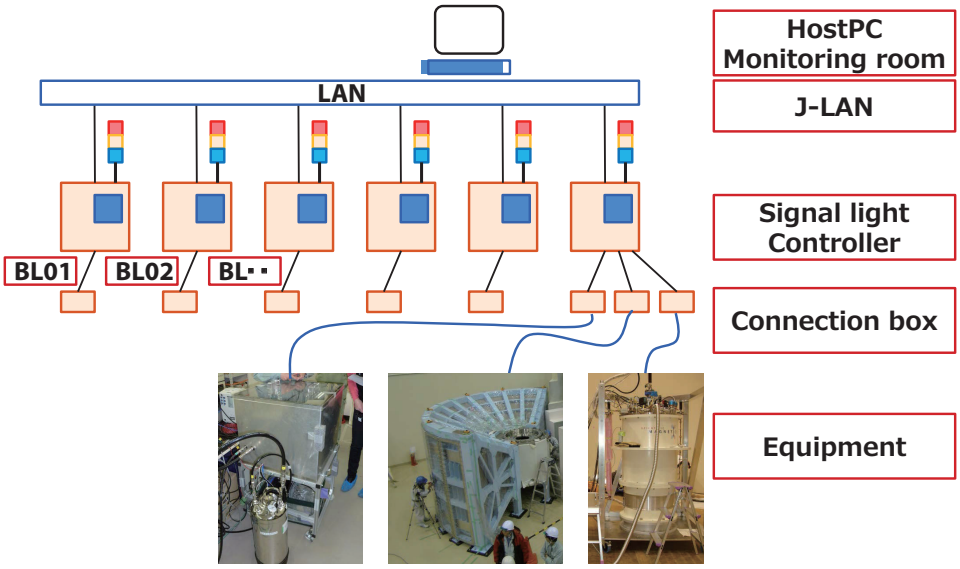

Figure 2. Schematic of the alarm indication system.

4. Crane safety

There are 2 cranes in each experimental hall (experimental hall No.1 and experimental hall No.2). These cranes are used to change the experimental setup during beam time and to perform summer maintenance by the technical staffs or constructors. Figure 3 shows the statistics of the total crane usage in both experimental halls as a function of every month. There was a total of 241 cases of use. The statistics for 2015 indicated high use in December and March, because of the performance of many experi-ments, based on the stable beam operation.

As usual, the safety measures and the effective schedules of crane usage were planned by the crane safety team. Also, the crane safety team checked monthly the mechanical sling, lifting sling, etc. and replaced the old ones with new ones when necessary. Furthermore, a crane operator, who wants to use the cranes in the experimental halls, needs to attend hands-on training by the crane safety team staff before the actual operation. As of the work team, according to the rules, it must include a crane operator, slinging operator, and observer.

As a result, there were no serious problems with the crane operations.

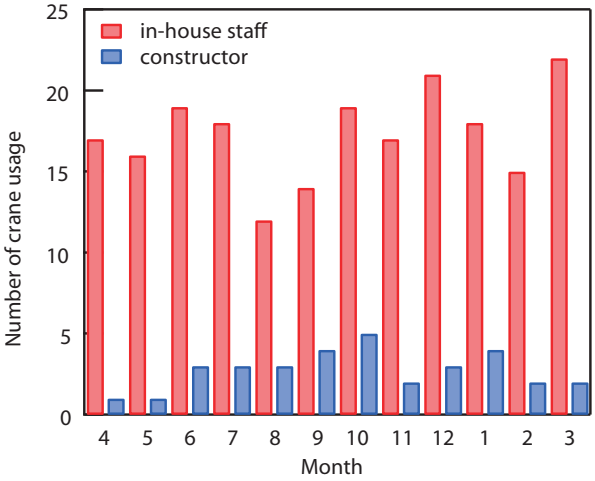

Figure 4. Trend of the total crane usage in one year.

M. Harada[1], M. Ooi[1], M. Sekijima[1], K. Kawakami[2], K. Aizawa[2], A. Hori[2], N. Kubo[2], W. Kambara[2], M. Sawabe[2], K. Suzuya[3], N. Kawamura[4], Y. Sakaguchi[5], Y. Yamaguchi[5], and K. Soyama[6]

[1]Neutron Source Section Materials and Life Science Division, J-PARC Center; [2]Technology Development Section, Materials and Life Science Division, J-PARC center; [3]Neutron Science Section, Materials and Life Science Division, J-PARC center; [4]Muon Science Section, Materials and Life Science Division, J-PARC Center; [5]Neutron R&D Division, CROSS-Tokai; [6]Materials and Life Science Division, J-PARC center

MLF Operations in 2016

Beam Operation Status at MLF

In Japanese Fiscal Year (JFY) 2016, the beam operation was planned to start on April 11, after the refreshment of the cryogenic for the neutron moderator, which was performed from April 4 to 10. On April 4, a beam collimator placed at 3-GeV synchrotron malfunctioned causing a leak into the vacuum of the beam duct. It took until April 13 to fix the issue, then the beam operation for JFY 2016 started. Like in the previous fiscal year, the beam power was maintained at 200 kW to avoid damage to the mercury target. In February 2016, we replaced the target with a new one (Target #2). Since this target was not equipped with a helium bubbler to mitigate cavitation erosion at the target vessel, the beam power was lowered below 200 kW. The use of such beam power was decided in the previous plan, according to which we had to replace the target during outage period from June to October 2016. However, because the design and fabrication of next robust target, which can withstand a high-power operation, took longer than expected, the target could not be changed in the summer as scheduled. To maintain the beam operation without the failure of Target #2, we decided to reduce the beam power to 150 kW for an expanded annual service from November to June 2017.

Table 1 shows the scheduled time and availability in JFY 2016 with a subtotal of records for the periods of 2016A and 2016B, which are switched on January 30. In JFY 2016, there were no severe failures, so the achieved availability was high at 90%. One of the reasons for such a high availability was the reduction of the beam power. The availability was very low in JFY 2015 due to the failure of the target on two occasions. These records show that the development of a target with robustness to accept high-power beams is crucial to achieving such high availability. Another reason for that achievement was that the cryogenic of the moderator was successfully cleaned up during the summer maintenance period. Figure 1 shows the trend of the beam power and its availability during JFY 2016. A significant failure was the malfunction of the timing system on June 21, which took a few days to fix and resume the operation. Due to this failure, the daily availability was limited at the end of June. Since this failure occurred shortly after radiation inspection of the beam to extend the usage of the facility, this failure did not affect the schedule of radiation inspection. After November 2016, very stable beam operation was achieved.

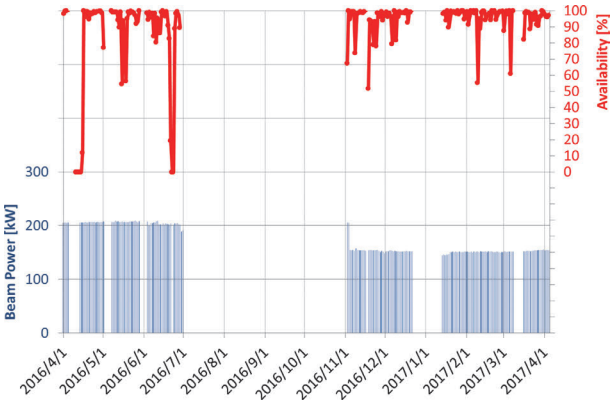

Figure 1. Beam power trend (shown in blue line) at MLF and availability per day (shown in red line).

Table 1. Run cycle, scheduled time and availability.

Run	Duration	Scheduled time (h)	Actual time (h)	Availability (%)
68	Apr 10 – May 28	891	744.3	83.5
69	Jun 3 – Jun 29	564	458.6	81.3
70	Nov 1 – Nov 16	322	307.2	95.4
71	Nov 18 – Dec 21	708	671.3	94.8
72A	Jan 14 – Jan 30	363	355.8	98.0
2016A[*1]	Apr 10 – Jan 30	2848	2537.2	89.1
72B	Jan 30 – Mar 30	802	766.7	95.6
73	Mar 16 – Mar 30	312	297.8	95.4
74	Mar 31 – Apr 1	12	11.73	97.8
2016B[*2]	Jan 30 – Apr 1	1126	1086.2	95.6
Overall	Apr 10 – Apr 1 2017	3974	3613.5	90.9

[*1] : Subtotal record for 2016A
[*2] : Subtotal record for 2016B

Users at the MLF

In the fiscal year 2016, the beam power was reduced to150 kW, but was steadily delivered all through the period.

The stable operation of MLF regained the number of users to the level of FY2014 and higher, as summarized in Table 1.

Table 1. The number of domestic and foreign users in the period of fiscal year.

	FY2008		FY2009		FY2010		FY2011		FY2012		FY2013	
	Domestic Users	Foreign Users	Domestic Users	Foreign Users	Domestic Users	Foreign Users	Domestic Users	Foreign Users	Domestic Users	Foreign Users	Domestic Users	Foreign Users
Neutron	107		317		476		259		708		449	
	95	12	303	14	432	44	238	21	628	80	399	50
Muon	18		40		50		23		56		61	
	18	0	38	2	42	8	21	2	46	10	50	11

	FY2014		FY2015		FY2016	
	Domestic Users	Foreign Users	Domestic Users	Foreign Users	Domestic Users	Foreign Users
Neutron	824		559		852	
	711	113	476	83	744	108
Muon	91		69		99	
	78	13	59	10	83	16

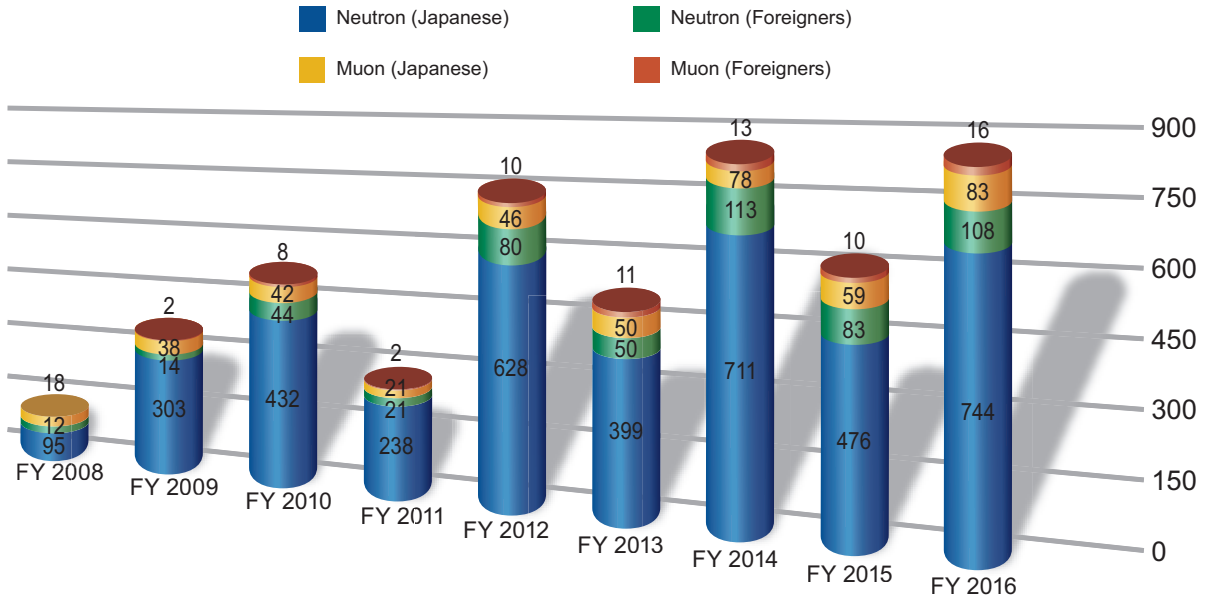

Figure 1. The number of domestic and foreign users in the period of fiscal year.

MLF Proposals Summary – FY2016

Table 1. Breakdown of Proposals Numbers for the 2016 Rounds.

Beam-line	Instrument		2016A		2016A		Full Year					
			Submitted	Approved	Submitted	Approved	Submitted			Approved		
			GU	GU	GU	GU	PU/S	IU	ES	PU/S	IU	ES
BL01	4D-Space Access Neutron Spectrometer - ***4SEASONS***		11(1)	5(1)	15(0)	5(0)	3	1	2	3	1	2
BL02	Biomolecular Dynamics Spectrometer - ***DNA***		16(1)	7(1)	19(1)	8(1)	2	1	0	2	1	0
BL03	Ibaraki Biological Crystal Diffractometer - ***iBIX***	(100-β)‡	8	1	6	0	0	0	0	0	0	0
		(β)†	2	2	0	0	18	0	0	18	0	0
BL04	Accurate Neutron-Nucleus Reaction Measurement Instrument - ***ANNRI***		9	3	12	3	2	1	0	2	1	0
BL05	Neutron Optics and Physics - ***NOP***		6	2	2	2	1	0	0	1	0	0
BL06	Neutron Resonance Spin Echo Spectrometers - ***VIN ROSE***		0	0	0	0	1	0	0	1	0	0
BL08	Super High Resolution Powder Diffractometer - ***S-HRPD***		11	3	12	6(0)	1	0	0	1	0	0
BL09	Special Environment Neutron Power Diffractometer - ***SPICA***		0	0	0	0	1	0	0	1	0	0
BL10	Neutron Beamline for Observation and Research Use - ***NOBORU***		11	5	8	7	3	1	0	3	1	0
BL11	High-Pressure Neutron Diffractometer - ***PLANET***		12(0)	8(0)	12(0)	8	0	1	0	0	1	0
BL12	High Resolution Chopper Spectrometer - ***HRC***		12	4	9	3	1	0	0	1	0	0
BL14	Cold-neutron Disk-chopper Spectrometer - ***AMATERAS***		28	4	22	6	4	1	1	4	1	1
BL15	Small and Wide Angle Neutron Scattering Instrument - ***TAIKAN***		29(3)	9(3)	17(2)	9(2)	4	3	1	4	3	1
BL16	High-Performance Neutron Reflectometer with a horizontal Sample Geometry - ***SOFIA***		19	10	7	7	0	0	0	0	0	0
BL17	Polarized Neutron Reflectometer - ***SHARAKU***		18(2)	8(2)	10(1)	4(1)	1	1	1	1	1	1
BL18	Extreme Environment Single Crystal Neutron Diffractometer - ***SENJU***		23(1)	4(1)	16(0)	5(0)	2	3	1	2	3	1
BL19	Engineering Diffractometer - ***TAKUMI***		23	5	25	7	3	1	2	3	1	2
BL20	Ibaraki Materials Design Diffractometer - ***iMATERIA***	(100-β)‡	13	4	19	4	0	0	0	0	0	0
		(β)†	44	24	20	20	15	0	0	15	0	0
BL21	High Intensity Total Diffractometer - ***NOVA***		19	7	17	7	1	0	0	1	0	0
BL22	Energy Resolved Neutron Imaging System - ***RADEN***		18	6(0)	11(0)	7(0)	2	2	0	2	2	0
BL23	Polarization Analysis Neutron Spectrometer - ***POLANO***		0	0	0	0	1	0	0	1	0	0
D1	Muon Spectrometer for Materials and Life Science Experiments - ***D1***		17(0)	6(0)	18(0)	1(1)	3	1	0	3	1	0
D2	Muon Spectrometer for Basic Science Experiments - ***D2***		13	6	15	7	1	1	0	1	1	0
U	Muon U		0	0	0	0	0	0	0	0	0	0
Total			**362**	**133**	**291**	**125**	**69**	**18**	**8**	**69**	**18**	**8**

GU : General Use **PU :** Project Use or Ibaraki Pref. Project Use **S :** S-type Proposals
IU : Instrument Group Use **ES :** Element Strategy
† : Ibaraki Pref. Exclusive Use Beamtime (β = 80% in FY2016)
‡ : J-PARC Center General Use Beamtime (100–β = 20% in FY2016)
( ) : Proposal Numbers under Trial Use Access System or P-type proposals (D1,D2) in GU

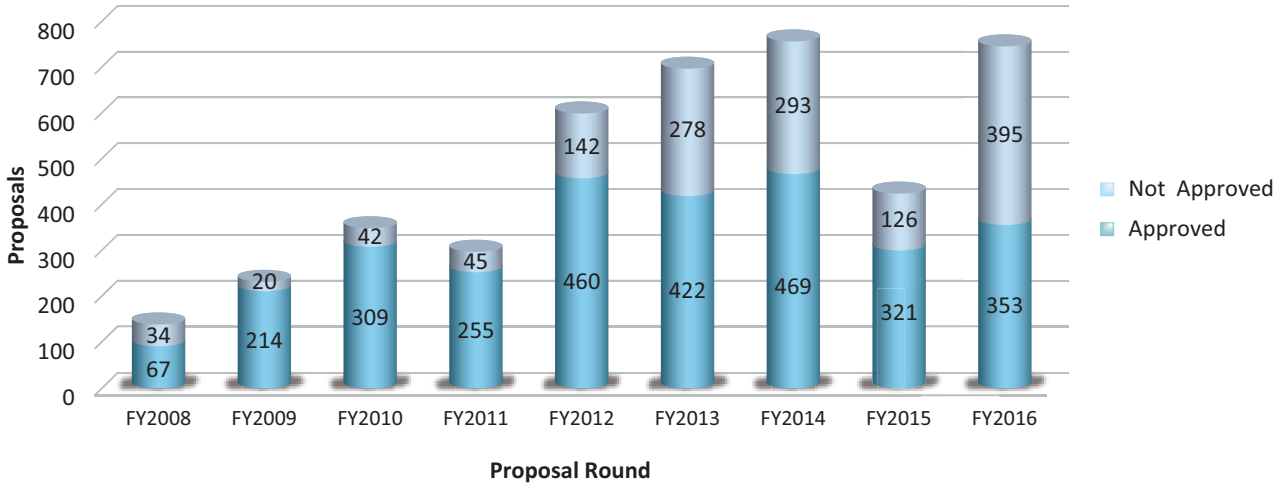

Figure 1. MLF Proposal Numbers over Time.

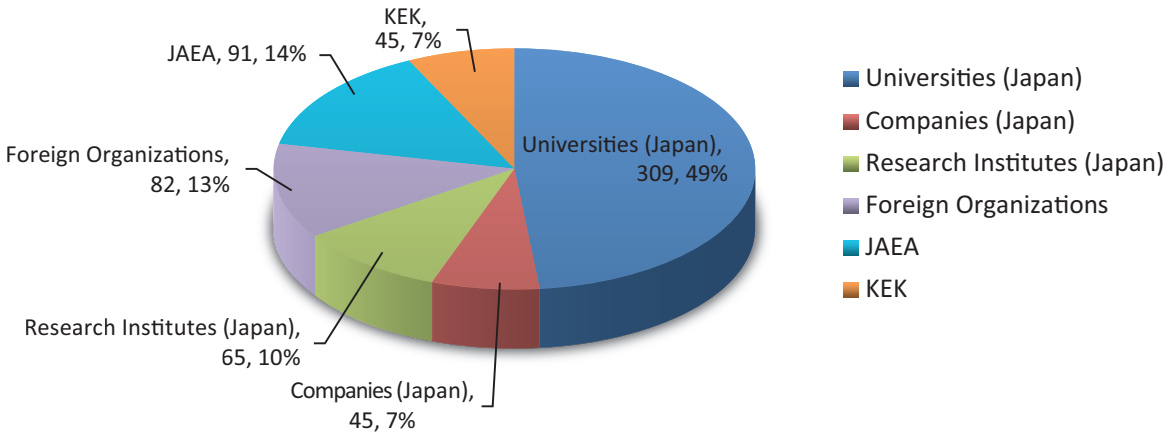

Figure 2. Origin of Submitted Proposals by affiliation - FY2016.

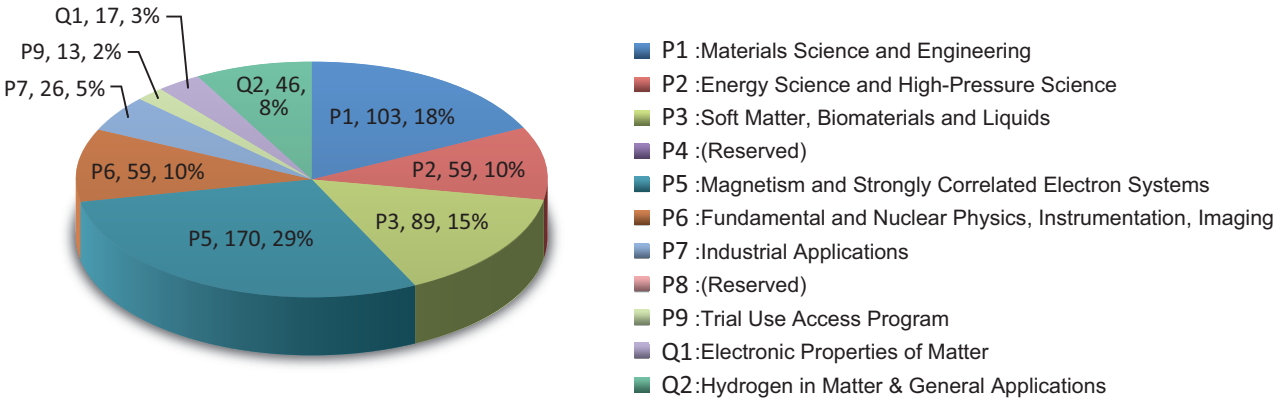

Figure 3. Submitted Proposals by Sub-committee/Expert Panel – FY2016.

MLF Division Staff 2016

Head	**Toshiji Kanaya**
Deputy Head	**Hideki Seto**
	Kazuhiko Soyama

Neutron Source Section

*: additional duties

<JAEA>

Hiroshi Takada (Leader)
Katsuhiro Haga (Sub-Leader)
Katsuhiro Aoyagi
Tomokazu Aso
Shinpei Fukuda
Kouhei Hanano
Masahide Harada
Shoichi Hasegawa *
Mitsunori Hirane
Miyuki Hoshino
Masato Ida
Kenji Imahashi
Tetsuya Kai *
Yuko Kato
Tomoyuki Kawasakii
Yoshinori Kikuchi
Hidetaka Kinoshita
Hiroyuki Kogawa
Kazuma Maekawa
Shin-ichiro Meigo
Hideki Muto
Takashi Naoe
Norio Narui
Masaaki Nishikawa
Kazutaka Nomura
Motoki Ohi
Ken-ichi Oikawa *
Kenji Sakai
Masakazu Seki
Mitsuaki Sekijima
Motonori Takagi
Makoto Teshigawara
Toshitsugu Uchida
Hiroyuki Uehara
Eiichi Wakai
Takashi Wakui
Zhihong Xiong
Shizuka Yoshinari

Neutron Science Section

*: additional duties

<JAEA>

Kenji Nakajima (Leader)
Yukinobu Kawakita (Sub-Leader)
Motoyasu Adachi * (QST)
Kazuya Aizawa *
Hiroyuki Aoki
Kazuhiro Aoyama
Satoru Fujiwara * (QST)
Hideo Harada *
Masahide Harada *
Takeshi Harada
Stefanus Harjo
Takanori Hattori
Yuu Hirano * (QST)
Kousuke Hiroi
Miho Igarashi
Yasuhiro Inamura
Hideaki Isozaki
Tetsuya Kai
Ryoichi Kajimoto
Wataru Kambara *
Kouji Kaneko *
Chiho Katagiri
Seiko Kawamura
Takuro Kawasaki
Naoko Kawase
Tatsuya Kikuchi
Atsushi Kimura *
Ryoji Kiyanagi
Maiko Kofu
Fumiaki Kono * (QST)
Masato Kubota *
Kazuo Kurihara *
Bing Li
Tatsuhito Matsuo * (QST)
Satoshi Morooka *
Naoki Murai
Hiroshi Nakagawa *
Shoji Nakamura *
Mitsutaka Nakamura
Takashi Ohhara
Mariko Ohtake
Kenichi Oikawa
Asami Sano
Mariko Segawa *
Yoshichika Seki

Kaoru Shibata
Naoko Shimizu
Rumi Shimizu * (QST)
Takenao Shinohara
Yuhua Su
Hiroshi Suzuki *
Kentaro Suzuya
Shin-ichi Takata
Tarou Tamada * (QST)
Itaru Tamura *
Katsuaki Tomoyori *
Yousuke Tou *
Wakana Ueno
Masao Watanabe *
Dai Yamazaki *

<KEK>

Shinichi Ito (Sub-Leader)
Hideki Seto
Hitoshi Endo
Takashi Honda
Kazutaka Ikeda
Takashi Ino
Takashi Kamiyama
Naokatsu Kaneko
Kenji Mishima
Fumiya Nemoto
Hidetoshi Oshita
Toshiya Otomo
Kaoru Taketani
Shuki Torii
Norifumi Yamada
Testuya Yokoo
Masao Yonemura

Technology Development Section

*: additional duties

<JAEA>

Kazuya Aizawa (Leader)
Takayuki Oku (Sub-Leader)
Tomokazu Aso *
Chikako Doda
Wu Gong
Katsuhiro Haga *
Masahide Harada *
Yuu Hirano * (QST)
Yasuhiro Inamura *
Tetsuya Kai *
Wataru Kambara
Kazuhiro Kawakami
Hiroyuki Kogawa *
Naoya Kubo
Kazuo Kurihara * (QST)
Mitsutaka Nakamura *
Tatsuya Nakamura *
Takeshi Nakatani
Motoki Ohi *
Kenji Sakai *
Kaoru Sakasai *
Masaki Sawabe
Kentaro Suzuya *
Ryuta Takahashi
Shin-ichi Takata *
Tarou Tamada * (QST)
Kazue Tanaka
Katsuaki Tomoyori * (QST)
Masao Watanabe

<KEK>

Masataka Sakaguchi
Hiroshi Fujimori *
Takashi Ino *
Naokatsu Kaneko *
Naritoshi Kawamura *
Kenji Kojima *
Shunsuke Makimura *
Setsuo Sato
Tomohiro Seya
Kaoru Taketani *
Shuki Torii *
Testuya Yokoo *

Neutron Instrumentation Section

*: additional duties

<JAEA>

Kaoru Sakasai (Leader)
Noriko Amezawa
Masumi Ebine *
Ryuji Maruyama
Tatsuya Nakamura
Kentaro Toh
Noriaki Tsutsui
Dai Yamazaki

Muon Science Section

*: additional duties

<KEK>

Ryosuke Kadono (Leader)
Naritoshi Kawamura (Sub-Leader)
Taihei Adachi
Pant Amba Datt
Hiroshi Fujimori
Koji Hamada
Masatoshi Hiraishi
Li Hua
Yutaka Ikedo
Yasuo Kobayashi
Akihiro Koda
Kenji Kojima
Shunsuke Makimura
Shiro Matoba
Yasuhiro Miyake
Junpei Nakamura
Yohei Nakatsugawa
Yasuhisa Nemoto
Yu Oishi
Hirotaka Okabe
Koichiro Shimomura
Patrick Strasser
Masato Tabe
Soshi Takeshita
Yutaka Taniguchi
Motonobu Tanpo
Shogo Doiuchi
Tatsuhiko Tachibana

<JAEA>

Wataru Higemoto *
Takashi Ito *

CROSS Staff 2016

Director **Hideaki Yokomizo**

Science Coordinators

Kazuhisa Kakurai
Makoto Hayashi
Yoshiaki Fukushima

Research & Development Division

*: additional duties

Jun-ichi Suzuki (Head)
Kenichi Funakoshi (Deputy Head)

<BL01 Group>
Kazuya Kamazawa (Leader)
Kazuhiko Ikeuchi
Kazuki Iida

<BL02 Group>
Masato Matsuura (Leader)
Takeshi Yamada
Taiki Tominaga

<BL11 Group>
Kenichi Funakoshi *(Leader)
Jun Abe
Shinichi Machida

<BL15 Group>
Kazuki Ohishi (Leader)
Jun-ichi Suzuki *
Hiroki Iwase

<BL17 Group>
Jun-ichi Suzuki *(Leader)
Noboru Miyata (Sub-Leader)
Kazuhiro Akutsu
Takayasu Hanashima

<BL18 Group>
Akiko Nakao (Leader)
Koji Munakata
Taketo Moyoshi

<BL22 Group>
Hirotoshi Hayashida (Leader)
Joseph Don Parker
Yoshihiro Matsumoto
Shuoyuan Zhang

<Technical Support Group>
Koji Kiriyama (Leader)
Takayoshi Ito (Sub-Leader)
Yoshifumi Sakaguchi
Yukihiko Kawamura
Hiroshi Kira
Motoyuki Ishikado
Nobuo Okazaki
Makoto Kobayashi
Satoshi Kasai
Toshiaki Morikawa
Hideyuki Hiramatsu
Yutaka Ebara
Kentaro Moriyama
Tetsuya Kuroda
Keiichi Ohuchi
Masae Sahara
Tazuko Mizusawa *

Health and Safety Division

*: additional duties

Yasuhiro Yamaguchi (Head)
Koji Kiriyama *
Yukihiko Kawamura *
Rei Ohuchi *

Utilization Promotion Division

*: additional duties

Junichi Sato (Head)
Tsukasa Miyazaki (Deputy Head)
Kenichi Funakoshi *(Deputy Head)
Junko Ohta
Toshiki Asai
Megumi Kawakami
Asuko Ariga
Tazuko Mizusawa
Atsuko Irie
Rie Suzuki
Sayaka Suzuki
Miho Kawato
Rei Ohuchi

Administration and Finance Division

Michihiko Murasawa (Head)
Yoshitaka Yasu
Takashi Hikita
Mika Gunji
Mutsumi Shiraishi

Proposals Review System, Committees and Meetings

Proposal Review System

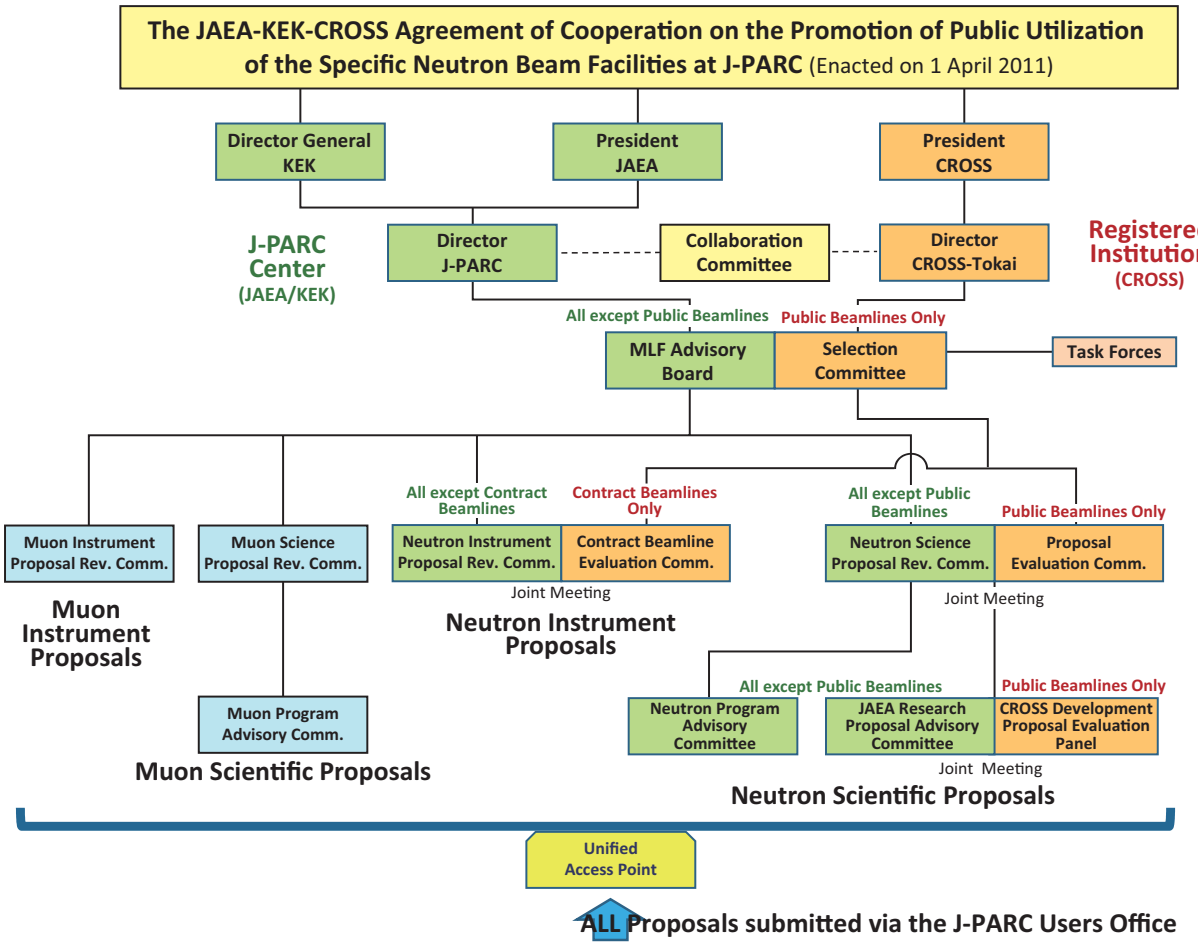

Figure 1. Proposals Review System Framework.

Materials and Life Science Facility Advisory Board

Kazuya Aizawa	Japan Atomic Energy Agency, Japan
Jun Akimitsu	Okayama University, Japan / Hiroshima University, Japan
Hiroshi Amitsuka	Hokkaido University, Japan
Masaki Fujita	Tohoku University, Japan
Michihiro Furusaka	Hokkaido University, Japan
Masatoshi Futakawa	Japan Atomic Energy Agency, Japan
Ryosuke Kadono	High Energy Accelerator Research Organization, Japan
Takashi Kamiyama	High Energy Accelerator Research Organization, Japan
Toshiji Kanaya	High Energy Accelerator Research Organization, Japan
Yuji Kawabata	Kyoto University, Japan
Yukinobu Kawakita	Japan Atomic Energy Agency, Japan
Yoshiaki Kiyanagi	Nagoya University, Japan
Kenya Kubo	International Christian University, Japan
Tetsurou Minemura	Ibaraki Prefecture, Japan
Yasuhiro Miyake	High Energy Accelerator Research Organization, Japan
Atsushi Nakagawa	Osaka University, Japan
Kenji Nakajima	Japan Atomic Energy Agency, Japan
Toshiya Otomo	High Energy Accelerator Research Organization, Japan
Hideki Seto	High Energy Accelerator Research Organization, Japan
Mitsuhiro Shibayama	The University of Tokyo, Japan
Kazuhiko Soyama	Japan Atomic Energy Agency, Japan
Jun Sugiyama	Toyota Central R&D Labs., Inc., Japan
Jun-Ichi Suzuki	Comprehensive Research Organization for Science and Society, Japan

Masayasu Takeda	Japan Atomic Energy Agency, Japan
Toshio Yamaguchi (Chair)	Fukuoka University, Japan

Term: through March 31, 2017

Neutron Instrument Proposal Review Committee

Masatoshi Futakawa	Japan Atomic Energy Agency, Japan
Toru Ishigaki	Ibaraki University, Japan
Takashi Kamiyama	High Energy Accelerator Research Organization, Japan
Hiroyuki Kimura	Tohoku University, Japan
Yoshiaki Kiyanagi	Nagoya University, Japan
Yukio Morii	Radiation Application Development Association, Japan
Kenji Nakajima	Japan Atomic Energy Agency, Japan
Toshiya Otomo	High Energy Accelerator Research Organization, Japan
Yasuhiro Sakemi	Tohoku University, Japan
Konoe Sato	Yokohama City University, Japan
Hideki Seto	High Energy Accelerator Research Organization, Japan
Kazuhiko Soyama	Japan Atomic Energy Agency, Japan
Masaaki Sugiyama	Kyoto University, Japan
Jun-Ichi Suzuki	Comprehensive Research Organization for Science and Society, Japan
Ichiro Tanaka	Ibaraki University, Japan
Naoya Torikai	Mie University, Japan
Hideki Yoshizawa	The University of Tokyo, Japan

Term: through March 31, 2017

Neutron Science Proposal Review Committee

Koichi Akita	Japan Atomic Energy Agency, Japan
Ken Andersen	European Spallation Source, Sweden
Takahisa Arima	The University of Tokyo, Japan
Samrath Chaplot	Bhabha Atomic Research Centre, India
Yoshiaki Fukushima	Comprehensive Research Organization for Science and Society, Japan
Michihiro Furusaka (Chair)	Hokkaido University, Japan
Makoto Hayashi	Ibaraki Prefecture, Japan
Shinichi Itoh	High Energy Accelerator Research Organization, Japan
Kazuaki Iwasa	Ibaraki University, Japan
Michael James	Australian Synchrotron, Australia
Ryosuke Kadono	High Energy Accelerator Research Organization, Japan
Hiroyuki Kagi	The University of Tokyo, Japan
Takashi Kamiyama	High Energy Accelerator Research Organization, Japan
Toshiji Kanaya	High Energy Accelerator Research Organization, Japan
Ryoji Kanno	Tokyo Institute of Technology, Japan
Yukinobu Kawakita	Japan Atomic Energy Agency, Japan
Stephen King	Rutherford Appleton Laboratory, U.K.
Seung-Hun Lee	University of Virginia, U.S.A.
Masaaki Matsuda	Oak Ridge National Laboratory, U.S.A.
Tetsurou Minemura	Ibaraki Prefecture, Japan
Yukio Morii	Radiation Application Development Association, Japan
Atsushi Nakagawa	Osaka University, Japan
Kenji Nakajima	Japan Atomic Energy Agency, Japan
Yukio Noda	Tohoku University, Japan
Toshiya Otomo	High Energy Accelerator Research Organization, Japan
Anna Paradowska	Australian Nuclear Science and Technology Organization, Australia
Je-Geun Park	Seoul National University, Korea
Vanessa Peterson	Australian Nuclear Science and Technology Organization, Australia
Hideki Seto	High Energy Accelerator Research Organization, Japan
Shinichi Shamoto	Japan Atomic Energy Agency, Japan
Hirohiko Shimizu	Nagoya University, Japan
Masaaki Sugiyama	Kyoto University, Japan
Jun-Ichi Suzuki	Comprehensive Research Organization for Science and Society, Japan
Keiji Tanaka	Faculty of Engineering, Kyushu University, Japan
Yo Tomota	Research Center for Strategic Materials, Japan
Albert Young	North Carolina State University, U.S.A.

Term: through March 31, 2017

Neutron Program Advisory Committee

Shinichi Adachi	High Energy Accelerator Research Organization, Japan
Masaki Azuma	Tokyo Institute of Technology, Japan
Hazuki Furukawa	Ochanomizu University, Japan
Masatoshi Futakawa	Japan Atomic Energy Agency, Japan
Yasushi Idemoto	Tokyo University of Science, Japan
Shinichi Itoh	High Energy Accelerator Research Organization, Japan
Takashi Kamiyama	High Energy Accelerator Research Organization, Japan

Toshiji Kanaya	High Energy Accelerator Research Organization, Japan
Mikio Kataoka	Nara Institute of Science and Technology, Japan
Yukinobu Kawakita	Japan Atomic Energy Agency, Japan
Yasuhiro Miyake	High Energy Accelerator Research Organization, Japan
Yutaka Moritomo	University of Tsukuba, Japan
Youichi Murakami	High Energy Accelerator Research Organization, Japan
Masato Ohnuma	Hokkaido University, Japan
Toshiya Otomo (Chair)	High Energy Accelerator Research Organization, Japan
Yasuhiro Sakwmi	Tohoku University, Japan
Taku Sato	Tohoku University, Japan
Hideki Seto	High Energy Accelerator Research Organization, Japan
Mitsuhiro Shibayama	The University of Tokyo, Japan
Hirohiko Shimizu	Nagoya University, Japan
Masaaki Sugiyama	Kyoto University, Japan
Toshio Yamaguchi	Fukuoka University, Japan

Term: through March 31, 2017

Muon Instrument Proposal Review Committee

Kazuya Aizawa	Japan Atomic Energy Agency, Japan
Koichiro Asahi	Tokyo Institute of Technology, Japan
Masatoshi Futakawa	Japan Atomic Energy Agency, Japan
Wataru Higemoto	High Energy Accelerator Research Organization, Japan
Masahiko Iwasaki	RIKEN, Japan
Ryosuke Kadono	High Energy Accelerator Research Organization, Japan
Toshiji Kanaya	High Energy Accelerator Research Organization, Japan
Kenji Kojima	High Energy Accelerator Research Organization, Japan
Kenya Kubo	International Christian University, Japan
Yoshitaka Kuno	Osaka University, Japan
Yasuhiro Miyake	High Energy Accelerator Research Organization, Japan
Nobuhiko Nishida	Toyota Physical and Chemical Research Institute, Japan
Hiroyuki Nojiri	Tohoku University, Japan
Toru Ogitsu	High Energy Accelerator Research Organization, Japan
Koichiro Shimomura	High Energy Accelerator Research Organization, Japan
Kazuhiko Soyama	Japan Atomic Energy Agency, Japan
Yasunori Yamazaki	RIKEN, Japan

Term: through March 31, 2017

Muon Science Proposal Review Committee

Kenta Amemiya	High Energy Accelerator Research Organization, Japan
Hiroshi Amitsuka	Hokkaido University, Japan
Masaharu Aoki	Osaka University, Japan
Alan Drew	University of London, U.K.
Masatoshi Futakawa	Japan Atomic Energy Agency, Japan
Takayuki Goto	Sophia University, Japan
Wataru Higemoto	High Energy Accelerator Research Organization, Japan
Ryosuke Kadono	High Energy Accelerator Research Organization, Japan
Toshiji Kanaya	High Energy Accelerator Research Organization, Japan
Yoji Koike	Tohoku University, Japan
Kenji Kojima	High Energy Accelerator Research Organization, Japan
Kenya Kubo (Chair)	International Christian University, Japan
Roderick Macrae	Marian University, U.S.A.
Yasuyuki Matsuda	The University of Tokyo, Japan
Takashi Miyake	National Institute of Advanced Industrial Science and Technology, Japan
Yasuhiro Miyake	High Energy Accelerator Research Organization, Japan
Seiji Miyashita	The University of Tokyo, Japan
Yuichiro Nagame	Japan Atomic Energy Agency, Japan
Kenji Nakajima	Japan Atomic Energy Agency, Japan
Yasuo Nozue	Osaka University, Japan
Chihiro Ohmori	High Energy Accelerator Research Organization, Japan
Toshiya Otomo	High Energy Accelerator Research Organization, Japan
Hideki Seto	High Energy Accelerator Research Organization, Japan
Tatsushi Shima	Osaka University, Japan
Koichiro Shimomura	High Energy Accelerator Research Organization, Japan
Yoko Sugawara	Kitazato University, Japan
Yoichi Yanase	Kyoto University, Japan
Kazuyoshi Yoshimura	Kyoto University, Japan

Term: through March 31, 2017

Muon Program Advisory Committee

Kenta Amemiya	High Energy Accelerator Research Organization, Japan
Hiroshi Amitsuka	Hokkaido University, Japan
Masaharu Aoki	Osaka University, Japan
Masatoshi Futakawa	Japan Atomic Energy Agency, Japan
Takayuki Goto	Sophia University, Japan

Wataru Higemoto	High Energy Accelerator Research Organization, Japan
Ryosuke Kadono	High Energy Accelerator Research Organization, Japan
Toshiji Kanaya	High Energy Accelerator Research Organization, Japan
Yoji Koike	Tohoku University, Japan
Kenji Kojima	High Energy Accelerator Research Organization, Japan
Kenya Kubo	International Christian University, Japan
Yasuyuki Matsuda	The University of Tokyo, Japan
Takashi Miyake	National Institute of Advanced Industrial Science and Technology, Japan
Yasuhiro Miyake (Chair)	High Energy Accelerator Research Organization, Japan
Seiji Miyashita	The University of Tokyo, Japan
Yasuo Nozue	Osaka University, Japan
Chihiro Ohmori	High Energy Accelerator Research Organization, Japan
Toshiya Otomo	High Energy Accelerator Research Organization, Japan
Hideki Seto	High Energy Accelerator Research Organization, Japan
Tatsushi Shima	Osaka University, Japan
Koichiro Shimomura	High Energy Accelerator Research Organization, Japan
Yoko Sugawara	Kitazato University, Japan
Yoichi Yanase	Kyoto University, Japan
Kazuyoshi Yoshimura	Kyoto University, Japan

Term: through March 31, 2017

Selection Committee (CROSS)

Jun Akimitsu	Okayama University, Japan / Hiroshima University, Japan
Masaki Fujita	Tohoku University, Japan
Michihiro Furusaka	Hokkaido University, Japan
Yasuhiro Iye (Chair)	Japan Society for Promotion of Science, Japan
Yuji Kawabata	Kyoto University, Japan
Hiroyuki Kishimoto	Sumitomo Rubber Industries, LTD., Japan
Naoki Kishimoto	Research Center for Strategic Materials, Japan
Yoshiaki Kiyanagi	Nagoya University, Japan
Tetsurou Minemura	Ibaraki Prefecture, Japan
Atsushi Nakagawa	Osaka University, Japan
Mitsuhiro Shibayama	The University of Tokyo, Japan
Jun Sugiyama	Toyota Central R&D Labs., Inc., Japan
Shinji Tsuneyuki	The University of Tokyo, Japan
Toshio Yamaguchi	Fukuoka University, Japan

Term: through March 31, 2017

Proposal Evaluation Committee (CROSS)

Ken Andersen	European Spallation Source, Sweden
Takahisa Arima	The University of Tokyo, Japan
Samrath Chaplot	Bhabha Atomic Research Centre, India
Yoshiaki Fukushima	Comprehensive Research Organization for Science and Society, Japan
Michihiro Furusaka (Chair)	Hokkaido University, Japan
Makoto Hayashi	Comprehensive Research Organization for Science and Society, Japan
Kazuaki Iwasa	Ibaraki University, Japan
Michael James	Australian Synchrotron, Australia
Hiroyuki Kagi	The University of Tokyo, Japan
Ryoji Kanno	Tokyo Institute of Technology, Japan
Stephen King	Rutherford Appleton Laboratory, U.K.
Seung-Hun Lee	University of Virginia, U.S.A.
Masaaki Matsuda	Oak Ridge National Laboratory, U.S.A.
Tetsurou Minemura	Ibaraki Prefecture, Japan
Yukio Morii	Radiation Application Development Association, Japan
Atsushi Nakagawa	Osaka University, Japan
Yukio Noda	Tohoku University, Japan
Anna Paradowska	Australian Nuclear Science and Technology Organization, Australia
Je-Geun Park	Seoul National University, Korea
Vanessa Peterson	Australian Nuclear Science and Technology Organization, Australia
Hirohiko Shimizu	Nagoya University, Japan
Masaaki Sugiyama	Kyoto University, Japan
Jun-Ichi Suzuki	Comprehensive Research Organization for Science and Society, Japan
Keiji Tanaka	Faculty of Engineering, Kyushu University, Japan
Yo Tomota	Research Center for Strategic Materials, Japan
Albert Young	North Carolina State University, U.S.A.

Term: through March 31, 2017

Neutron Advisory Committee (NAC)

NAC convened 20-21 February, 2017 at the J-PARC Research Building, Tokai

Group photo of NAC

Neutron Advisory Committee (20-21 Feb. 2017)

Robert McGreevy (chair)	Rutherford Appleton Laboratory
Bertrand Blau	Paul Scherrer Institute
Mark Wendel	Oak Ridge National Laboratory
Yoshiaki Kiyanagi	Nagoya University
Christiane Alba-Simionesco	Laboratoire Léon Brillouin
Jamie Schulz	Australian Nuclear Science and Technology Organisation
Dimitri Argyriou	European Spallation Source
Chang Hee Lee	Korea Atomic Energy Research Institute
Mitsuhiro Shibayama	The University of Tokyo
Masaaki Sugiyama	Kyoto University

Muon Advisory Committee (MAC)

MAC convened 22-23 February, 2017 at the KEK Tokai Campus, Tokai

Group photo of MAC

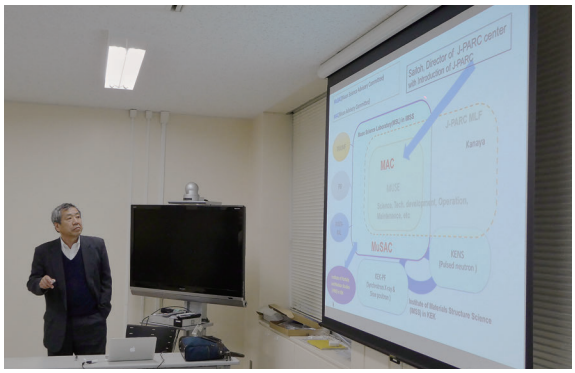

Muon Advisory Committee (22-23 Feb. 2017)

Francis Pratt (Chair)	Rutherford Appleton Laboratory
Toshiyuki Azuma	RIKEN
Klaus Jungmann	University of Groningen
Kenya Kubo	International Christian University
Andrew MacFarlane	The University of British Columbia
Yasuo Nozue	Osaka University
Prokscha Thomas	Paul Scherrer Institute
Jun Sugiyama	Toyota Central R & D Labs. Inc.

Workshops, Conferences, Seminars and Schools in 2016

Conferences held jointly by J-PARC MLF and CROSS

2016 Meeting on J-PARC MLF Industrial Use
21-22 July 2016, Akihabara Convention Hall, Tokyo


Photo of the 2016 Meeting on J-PARC MLF Industrial Use

2016 Quantum Beam Science Festival (The 8th MLF Symposium and The 34th PF Symposium)
14-15 Mar. 2017, Tsukuba International Congress Center, Ibaraki

Group photo of the 2016 Quantum Beam Science Festival

Workshops held by KEK

7th Progress Report Meeting of J-PARC MUSE
29 May 2016, KEK Tokai Campus, Ibaraki

Joint Workshop for CMRC and TRIMN
8 July 2016, KEK Tokai Campus, Ibaraki

Workshop for Negative Muon Research
11 July 2016, KEK Tokai Campus, Ibaraki

Workshop for Neutron Optics and Physics (BL05)
9 Aug. 2016, Nagoya University, Aichi

Workshop for Neutron Inelastic Scattering (BL12)
14 Nov. 2016, KEK Tokai Campus, Ibaraki

Workshop for Polarized Neutron Scattering (BL23)
15 Nov. 2016, KEK Tsukuba Campus, Ibaraki

Workshop for Neutron Total Scattering (BL21)
21 Nov. 2016, KEK Tokai Campus, Ibaraki

7th Workshop for Muon and Accelerator Research
5-7 Jan. 2017, RIKEN, Saitama

Workshops held by CROSS

The 18th CROSSroads Workshop
"Polarized Targets and Neutron Polarization Techiques"
15 June 2016, IBARAKI Quantum Beam Research Center, Ibaraki

Group photo of CROSSroads 18

The 19th CROSSroads Workshop
"Neutrons and Muons for Interface Investigations"
13 Feb. 2017, IBARAKI Quantum Beam Research Center, Ibaraki

Group photo of CROSSroads 19

Workshops and Seminars held by CROSS and other organizations

Potential of Neutrons in Interfacial Nano Electron Chemistry
15 July 2016, KANTO KAGAKU, Tokyo

2016 1st Workshop on Residual Stress and Strain
22 Aug. 2016, KENKYUSHA EIGO Center, Tokyo

3rd Symposium on the Collaborative Use of Large Research Institutions and the KEI Super Computer 2016
1 Sep. 2016, Akihabara UDX, Tokyo


Photo of the 3rd Symposium on the Collaborative Use of Large Research Institutions and the KEI Super Computer 2016

2016 1st Workshop on Structural Biology
2 Sep. 2016, KENKYUSHA EIGO Center, Tokyo

13th Seminar on Industrial Applications at SPring-8
7-8 Sep. 2016, Hyogo Arts & Culture Association, Hyogo

2016 Workshop on Surfaces and Interfaces
28 Sep. 2016, KENKYUSHA EIGO Center, Tokyo

2016 Workshop on Materials Science
29 Sep. 2016, Essam Kanda Hall, Tokyo

2016 Workshop on Analytical Methods In Small Angle Scattering
1 Nov. 2016, Essam Kanda Hall, Tokyo

2016 Workshop on Metallographic Structure
11 Nov. 2016, Essam Kanda Hall, Tokyo

Ibaraki Society for the Promotion of the Use of Neutrons
"2016 Meeting on Magnetic Materials"
14 Nov. 2016, Essam Kanda Hall, Tokyo

2016 Workshop on Soft Matter Neutron Scattering
17 Nov. 2016, Essam Kanda Hall, Tokyo

Seminar on Industrial Applications of Neutrons in Saitama
11 Dec. 2016, Cultural Center "Sanazeria", Saitama

2016 Workshop on Neutron Science
14 Dec. 2016, Essam Kanda Hall, Tokyo

1st Workshop on the Collaborative Use of Large Research Institutions and the KEI Super Computer 2017
10 Jan. 2017, RIST, Hyogo


Photo of the 1st Workshop of the Collaborative Use of Large Research Institutions and the KEI Super Computer 2017

2016 Workshop on Magnetic Materials
19 Jan. 2017, Essam Kanda Hall, Tokyo

2016 Workshop on Battery Materials
25 Jan. 2017, KENKYUSHA EIGO Center, Tokyo

2016 Workshop on Non-destructive Visualization and Analysis Methods
15 Feb. 2017, KENKYUSHA EIGO Center, Tokyo

3rd Seminar on the Complementary Use of Synchrotron Radiation and Neutrons
17 Feb. 2017, KENKYUSHA EIGO Center, Tokyo


Photo of the 3rd Seminar on the Complementary Use of Synchrotron Radiation and Neutrons

2016 Z-Code Training Course
27-28 Feb. 2017, LMJ Tokyo, Tokyo

2016 2nd Workshop on Residual Stress and Strain
8 Mar. 2017, KENKYUSHA EIGO Center, Tokyo

2016 Workshop on Liquids and Amorphous Materials
13 Mar. 2017, Essam Kanda Hall, Tokyo

2016 2nd Workshop on Structural Biology
29 Mar. 2017, KENKYUSHA EIGO Center, Tokyo

Schools in 2016

KEK-Summer Challenge Beam Experiment
12-13 Nov. 2016, J-PARC Center and KEK Tokai Campus, Ibaraki

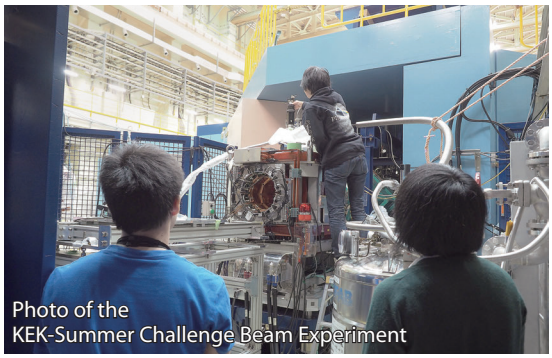
Photo of the
KEK-Summer Challenge Beam Experiment

The Neutron and Muon School
22-26 Nov. 2016, J-PARC Center, Ibaraki

Group photo of the Neutron and Muon School

Hello Science from J-PARC: Chocolate Science
21 Jan. 2017, Food court at AEON Tokai, Ibaraki

Photo of Hello Science from J-PARC:
Chocolate Science

Award List

AESJ Best Paper Award (Atomic Energy Society of Japan)
Development of microbubble generator for suppression of pressure waves in mercury target of spallation source
H. Kogawa, T. Naoe, and H. Kyotoh (2017-03-28)

Young Scientist Award of Societry of Muon and Meson Science of Japan
Research of Iron-based superconductors using muon spin rotation and relaxation
M. Hiraishi (2017-03-19)

Scientist Award of Societry of Muon and Meson Science of Japan
Research of spin-orbit coupling induced Mott insulators and their superconductivity using muon spin rotation and relaxation
H. Okabe (2017-03-19)

Tire Technology of the Year
Advanced 4D Nano Design
Sumitomo Rubber Industries (2017-02)

JAEA President's Awards 2016, Research and Development Prizes
Completion of design, construction and leading research of Engineering Materials Diffractometer in J-PARC
S. Harjo, A. Moriai, T. Kawasaki, K. Sakasai, T. Nakamura, T. Ito, J. Abe, H. Arima, W. Gong, T. Iwahashi, and K. Aizawa (October 2016)

The 11th Young Scientist Award of the Physical Society of Japan, Beam Physics Region
Pulsed ultra-cold neutron production using a Doppler shifter at J-PARC
S. Imajo (2016-10-16)

The Japan Institute of Metals and Materials The Best Paper Award
Relation between Vickers Hardness and Bragg-Edge Broadening in Quenched Steel Rods Observed by Pulsed Neutron Transmission Imaging
H. Sato, T. Sato, Y. Shioda, T. Kamiyama, A.S. Tremsin, M. Ohnuma and Y. Kiyanagi (2016-09-21)

The Society of Polymer Science Research Award
Conformational analysis of single polymer chains by super-resolution optical microscopy
H. Aoki (2016-09-15)

Fellowship of the Royal Society of Chemistry
A. Takahara (2016-07)

The 28th Award from The Society of Rubber Science and Technology, Japan
Combined analysis of Rubber material using SPring-8, J-PARC, K-Computer
H. Kishimoto, Y. Masui, F. Kaneko, Y. Shinohara, and Y. Masubuchi (2016-05)

Science Technology Award of MEXT in FY2016
Advance in Neutron Resonance Spectroscopy and Application Researches
S. Harada, A. Kimura, and Y. Toh (2016-04-20)

The 10th Young Scientist Award of the Physical Society of Japan, Magnetism (Region 3)
M. Soda (2016-03-21)

MLF Publication 2016

1 H. Kawaura, M. Harada, Y. Kondo, H. Kondo, Y. Suganuma, N. Takahashi, J. Sugiyama, Y. Seno, and N. L. Yamada
Operando Measurement of Solid Electrolyte Interphase Formation at Working Electrode of Li-ion Battery by Time-slicing Neutron Reflectometry
ACS Appl. Mater. Interfaces **8** 9540-9544 (2016)

2 S. Tsukui, F. Kimura, K. Kusaka, S. Baba, N. Mizuno, and T. Kimura
Neutron and X-ray single-crystal diffraction from protein microcrystals via magnetically oriented microcrystal arrays in gels
Acta Crystallographica Section D-Biological Crystallography **72** 823-829 (2016)

3 H.-J. Jhuo, S.-H. Liao, Y.-L. Li, P.-N. Yeh, S.-A. Chen, W.-R. Wu, C.-J. Su, J.-J. Lee, N. L. Yamada, and U-S. Jeng
New Processing Route with a Novel Additive 1-Naphthalenethiol for Efficiency Enhancement of Polymer Solar Cells
Adv. Funct. Mater. **26** 3094-3104 (2016)

4 O. A. Louchev, N. Saito, Y. Oishi, K. Miyazaki, K. Okamura, J. Nakamura, M. Iwasaki, and S. Wada
Photoionization pathways and thresholds in generation of Lyman-α radiation by resonant four-wave mixing in Kr-Ar mixture
AIP Advances **6** 95018 (2016)

5 T. Matsuo, T. Arata, T. Oda, K. Nakajima, S. Ohira-Kawamura, T. Kikuchi, and S. Fujiwara
Difference in the hydration water mobility around F-actin and myosin subfragment-1 studied by quasielastic neutron scattering
Biochemistry and Biophysics Reports **6** 220-225 (2016)

6 S. Nishimura, Y. Suzuki, J. Lu, S. Torii, T. Kamiyama, and A. Yamada
High-Temperature Neutron and X-ray Diffraction Study of Fast Sodium Transport in Alluaudite-type Sodium Iron Sulfate
Chemistry of Materials **28** 2393–2399 (2016)

7 T. Matsunaga, H. Komatsu, K. Shimoda, T. Minato, M. Yonemura, T. Kamiyama, S. Kobayashi, T. Kato, T. Hirayama, Y. Ikuhara, H. Arai, Y. Ukyo, Y. Uchimoto, and Z. Ogumi
Dependence of Structural Defects in Li2MnO3 on Synthesis Temperature
Chemistry of Materials **28** 4143-4150 (2016)

8 Y. Tsuchiya, K. Takanashi, T. Nishinobo, A. Hokura, M. Yonemura, T. Matsukawa, T. Ishigaki, and N. Yabuuchi
Layered NaxCrxTi1-xO2 as Bi-Functional Electrode Materials for Rechargeable Sodium Batteries
Chemistry of Materials **28** 7006–7016 (2016)

9 T. Niizeki, S. Nagayama, Y. Hasegawa, N. Miyata, M. Sahara, and K. Akutsu
Structural Study of Silica Coating Thin Layers Prepared from Perhydropolysilazane: Substrate Dependence and Water Penetration Structure
Coatings **6** 64 (2016)

10 T. Masuda, J. Arase, Y. Inagaki, M. Kawahata, K. Yamaguchi, T. Ohhara, A. Nakao, H. Momma, E. Kwon, and W. Setaka
Molecular Gyrotops with a Five-Membered Heteroaromatic Ring: Synthesis, Temperature-Dependent Orientation of Dipolar Rotors inside the Crystal, and its Birefringence Change
Crystal Growth & Design **16** 4392-4401 (2016)

11 Y. Idemoto, A. Horie, N. Ishida, and N. Kitamura
Crystal Structure Analysis in the Charge and Discharge Process of Li-ion Battery Cathode-material LiNi0.8Co0.2O2
Electrochemistry **84** 802-807 (2016)

12 K. Sasaki, T. Mizutani, M. Iio, T. Mibe, T. Ogitsu, N. Saito, K. Shimomura, and T. Obata
Study of Magnetic Field Measurement System for g-2/EDM Experiment at J-PARC
IEEE Trans. Appl. Supercond. **26** 0605604 (2016)

13 T. Matsukawa, H. Hoshima, A. Hoshikawa, C. Otani, and T. Ishigaki
Temperature Dependence of Crystal Structure and THz Absorption Spectra of Organic Nonlinear Optical Stilbazolium Material for High-Output THz-Wave Generation
Infrared Milli. Terahertz Waves **37** 540-550 (2016)

14 M. Inukai, S. Horike, T. Itakura, R. Shinozaki, R. Ogiwara, D. Umeyama, S. Nagarkar, Y. Nishiyama, M. Malon, A. Hayashi, T. Ohhara, R. Kiyanagi, and S. Kitagawa
Encapsulating Mobile Proton Carriers into Structural Defects in Coordination Polymer Crystals: High Anhydrous Proton Conduction and Fuel Cell Application
J. Am. Chem. Soc. **136** 8505-8511 (2016)

15 H. Akiba, M. Kofu, H. Kobayashi, H. Kitagawa, K. Ikeda, T. Otomo, and O. Yamamuro
Nanometer-Size Effect on Hydrogen Sites in Palladium Lattice
J. Am. Chem. Soc. **138** 10238-10243 (2016)

16 A. S. Tremsin, S. Ganguly, S. M. Meco, G. R. Pardal, T. Shinohara, and W. B. Feller
Investigation of dissimilar metal welds by energyresolved neutron imaging
J. Appl. Cryst. **49** 1130-1140 (2016)

17 T. Ohhara, R. Kiyanagi, K. Oikawa, K. Kaneko, T. Kawasaki, et al.
SENJU: A new time-of-flight single-crystal neutron diffractometer at J-PARC
J. Appl. Cryst. **49** 120-127 (2016)

18 Y. Onuki, A. Hoshikawa, S. Sato, P. Xu, T. Ishigaki, Y. Saito, H. Todoroki, and M. Hayashi
Rapid measurement scheme for texture in cubic metallic materials using time-of-flight neutron diffraction at iMATERIA
J. Appl. Cryst. **49** 1579-1584 (2016)

19 Y. Oba, S. Morooka, K. Ohishi, N. Sato, R. Inoue, N. Adachi, J. Suzuki, T. Tsuchiyama, E. P. Gilbert, and M. Sugiyama
Magnetic Scattering in the Simultaneous Measurement of Small-Angle Neutron Scattering and Bragg Edge Transmission from Steel
J. Appl. Cryst. **49** 1659-1664 (2016)

20 Y. Noda, S. Koizumi, T. Masui, R. Mashita, H. Kishimoto, D. Yamaguchi, T. Kumada, S. Takata, K. Ohishi, and J. Suzuki
Contrast variation by dynamic nuclear polarization and time-of-flight small-angle neutron scattering. I. Application to industrial multi-component nano composites
J. Appl. Cryst. **49** 2036-2045 (2016)

21 K. Akutsu, T. Niizeki, S. Nagayama, N. Miyata, M. Sahara, A. Shimomura, M. Yoshii, and Y. Hasegawa
Investigation of structure of a thin SiO2 layer as an antifouling and corrosion-resistant coating
J. Ceram. Soc. Jpn. **124** 172-176 (2016)

22 N. Kitamura, K. Kaneko, H. Kamagata, N. Ishida, and Y. Idemoto
Hydrothermal synthesis of lanthanum silicate nanopowder and film preparation by electrophoretic deposition method

J. Ceram. Soc. Jpn. **124** 29-33 (2016)

23 M. Hirayama, T. Shibusawa, R. Yamaguchi, K.-S. Kim, S. Taminato, N. L. Yamada, M. Yonemura, K. Suzuki, and R. Kanno
Neutron reflectometry analysis of Li4Ti5O12/organic electrolyte interfaces: characterization of surface structure changes and lithium intercalation properties
J. Mater. Res. **31** 3142-3150 (2016)

24 Y. Sekine, H. Endo, H. Iwase, S. Takeda, S. Mukai, H. Fukazawa, K. C. Littrell, Y. Sasaki, and K. Akiyoshi
Nanoscopic structural investigation of physically crosslinked nanogels formed from self-associating polymers
J. Phys. Chem. B **120 (46)** 11996–12002 (2016)

25 Y. Kameda, S. Ebina, Y. Amo, T. Usuki, and T. Otomo
Microscopic Structure of Contact Ion Pairs in Concentrated LiCl- and LiClO4-Tetrahydrofuran Solutions Studied by Low-Frequency Isotropic Raman Scattering and Neutron Diffraction with (6)Li/(7)Li Isotopic Substitution Methods
J. Phys. Chem. B **120** 4668-4678 (2016)

26 T. Minato, H. Kawaura, M. Hirayama, S. Taminato, K. Suzuki, N. L. Yamada, H. Sugaya, K. Yamamoto, K. Nakanishi, Y. Orikasa, H. Tanida, R. Kanno, H. Arai, Y. Uchimoto, and Z. Ogumi
Dynamic Behavior at the Interface between Lithium Cobalt Oxide and an Organic Electrolyte Monitored by Neutron Reflectivity Measurements
J. Phys. Chem. C **120** 20082–20088 (2016)

27 K. Miwa, T. Sato, M. Matsuo, K. Ikeda, T. Otomo, S. Deledda, B.C. Hauback, G. Li, S. Takagi, and S.-I. Orimo
Metallic Intermediate Hydride Phase of LaMg2Ni with Ni–H Covalent Bonding: Precursor State for Complex Hydride Formation
J. Phys. Chem. C **120** 5926-5931 (2016)

28 T. Matsunaga, H. Komatsu, K. Shimoda, T. Minato, M. Yonemura, T. Kamiyama, S. Kobayashi, T. Kato, T. Hirayama, Y. Ikuhara, H. Arai, Y. Ukyo, Y. Uchimoto, and Z. Ogumi
Structural Understanding of Superior Battery Properties of Partially Ni-Doped Li2MnO3 as Cathode Material
J. Phys. Chem. Lett. **7** 2063-2067 (2016)

29 S. Saito, H. Watanabe, Y. Hayashi, M. Matsugami, S. Tsuzuki, S. Seki, J. N. C. Lopes, R. Atkin, K. Ueno, K. Dokko, M. Watanabe, Y. Kameda, and Y. Umebayashi
Li(+) Local Structure in Li-Tetraglyme Solvate Ionic Liquid Revealed by Neutron Total Scattering Experiments with the (6/7)Li Isotopic Substitution Technique
J. Phys. Chem. Lett. **7** 2832-2837 (2016)

30 Y. Ikeda, S. Suzuki, T. Nakabayashi, H. Yoshizawa, T. Yokoo, and S. Itoh
Inelastic Neutron-Scattering Study of Stripe and Over-Doped Checkerboard Ordering in Layered Nickel Oxide Nd2-xSrxNiO4
J. Phys. Soc. Jpn. **85** 023701 (5 pages) (2016)

31 T. Haku, M. Soda, M. Sera, K. Kimura, S. Itoh, T. Yokoo, and T. Masuda
Crystal Field Excitations in Breathing Pyrochlore Antiferromagnet Ba3Yb2Zn5O11
J. Phys. Soc. Jpn. **85** 034721 (2016)

32 W. Higemoto, Y. Aoki, and D. E. MacLaughlin
Spin and time-reversal symmetries of superconducting electron pairs probed by the muon spin rotation and relaxation technique
J. Phys. Soc. Jpn. **85** 091007 (2016)

33 J. Sugiyama
Study on Hydrogen Storage Materials
J. Phys. Soc. Jpn. **85** 091012 (2016)

34 K. Shimomura and T. U. Ito
Electronic Structure of Hydrogen Donors in Semiconductors and Insulators Probed by Muon Spin Rotation
J. Phys. Soc. Jpn. **85** 091013 (2016)

35 T. Okuda, H. Hata, T. Eto, S. Sobaru, R. Oda, H. Kaji, K. Nishina, H. Kuwahara, M. Nakamura, and R. Kajimoto
Effects of Mn Substitution on the Thermoelectric Properties and Thermal Excitations of the Electrondoped Perovskite Sr1-xLaxTiO3
J. Phys. Soc. Jpn. **85** 094717 (2016)

36 Y. Togawa, Y. Kousaka, K. Inoue, and J. Kishine
Symmetry, structure, and dynamics of monoaxial chiral magnets
J. Phys. Soc. Jpn. **85** 112001/1-37 (2016)

37 T. Kawasaki, K. Kaneko, A. Nakamura, N. Aso, M. Hedo, T. Nakama, T. Ohhara, R. Kiyanagi, K. Oikawa, I. Tamura, A. Nakao, K. Munakata, T. Hanashima, and Y. Ōnuki
Magnetic Structure of Divalent Europium Compound EuGa4 Studied by Single-Crystal Time-of-Flight Neutron Diffraction
J. Phys. Soc. Jpn. **85** 114711 (2016)

38 T. Adachi, A. Takahashi, K. M. Suzuki, M. A. Baqiya, T. Konno, T. Takamatsu, M. Kato, I. Watanabe, A. Koda, M. Miyazaki, R. Kadono, and Y. Koike
Strong electron correlation behind the superconductivity in Ce-free and Ce-underdoped high-Tc T′-cuprates
J. Phys. Soc. Jpn. **85** 114716 (2016)

39 K. Iwasa, R. Higashinaka, Y. Aoki, S. Ohira-Kawamura, and K. Nakajima
Broad Excitation Spectra between Crystalline-Electric-Field Levels Associated with Non-Kramers Doublet Ground State of f Electrons in PrNb2Al20
J. Phys. Soc. Jpn. **85** 123704 (2016)

40 M. Soda, Y. Honma, S. Takamizawa, S. Ohira-Kawamura, K. Nakajima, and T. Masuda
Spin Model of O2-based Magnet in a Nanoporous Metal Complex
J. Phys. Soc. Jpn. **85** 34717 (2016)

41 M. Miyazaki, I. Yamauchi, and R. Kadono
Quest for the Origin of Heavy Fermion Behavior in d-Electron Systems
J. Phys. Soc. Jpn. **85** 91009 (2016)

42 K. Kodama, K. Ikeda, M. Isobe, H. Takeda, M. Itoh, Y. Ueda, S.-I. Shamoto, and T. Otomo
Local Structural Analysis of Half-Metallic Ferromagnet CrO2
J. Phys. Soc. Jpn. **85** 94709 (2016)

43 H. Hazama, S. Tajima, Y. Masuoka, and R. Asahi
Transport properties of the Cu2ZnSnS4 bulk systems: Effects of nonstoichiometry and defect formation
Journal of Alloys and Compounds **657** 179–183 (2016)

44 A. F. Gubkin, E. P. Proskurina, Y. Kousaka, E. M. Sherokalova, N. V. Selezneva, P. Miao, S. Lee, J. Zhang, Y. Ishikawa, S. Torii, T. Kamiyama, J. Campo, J. Akimitsu, and N. V. Baranov
Crystal and magnetic structures of Cr1/3NbSe2 from neutron diffraction
Journal of Applied Physics **119** 13903 (2016)

45 Y. Sakaguchi, H. Asaoka, Y. Uozumi, K. Kondo, D. Yamazaki, K. Soyama, M. Ailavajhala, and M. Mitkova
Silver photo-diffusion and photo-induced macroscopic surface deformation of Ge33S67/Ag/Si substrate
Journal of Applied Physics **120** 55103 (2016)

46 K. Yoshida, T. Yamaguchia, T. Yokoo, and S. Itoh
Collective dynamics measurement of liquid methanol by inelastic neutron scattering
Journal of Molecular Liquids **222** 395 (2016)

47 T. Naoe, H. Kogawa, T. Wakui, K. Haga, M. Teshigawara, H. Kinoshita, H.Takada, and M. Futakawa
Cavitation damage prediction for the JSNS mercury target vessel
Journal of Nuclear Materials **468** 313-320 (2016)

48 T. Naoe, X. Zhihong, and M. Futakawa
Gigacycle fatigue behaviour of austenitic stainless steels used for mercury target vessels
Journal of Nuclear Materials **468** 331-338 (2016)

49 M. Tabuchi, H. Kageyama, K. Kubota, H. Shibuya, K. Doumae, and R. Kanno
Structural change during charge–discharge for iron substituted lithium manganese oxide
Journal of Power Sources **318** 18–25 (2016)

50 S. Shiotani, T. Naka, M. Morishima, M. Yonemura, T. Kamiyama, Y. Ishikawa, Y. Ukyo, Y. Uchimoto, and Z. Ogumi
Degradation analysis of 18650-type lithium-ion cells by operando neutron diffraction
Journal of Power Sources **325** 404-409 (2016)

51 K. Ninomiya , M. Inagaki, M. K. Kubo, T. Nagatomo, W. Higemoto, N. Kawamura, P. Strasser, K. Shimomura, Y. Miyake, S. Sakamoto, A. Shinohara, and T. Saito
Negative muon induced elemental analysis by muonic X-ray and prompt gamma-ray measurements
Journal of Radioanalytical and Nuclear Chemistry **309** 65-69 (2016)

52 D. Habu, Y. Masubuchi, S. Torii, T. Kamiyama, and S. Kikkawa
Crystal structure study of dielectric oxynitride perovskites La1-xSrxTiO2+xN1-x (x = 0, 0.2)
Journal of Solid State Chemistry **237** 254–257 (2016)

53 S. Takahashi, N. L. Yamada, K. Ito, and H. Yokoyama
Inclusion Complex of α-Cyclodextrin with Poly(ethylene glycol) Brush
Macromolecules **49** 6947-6952 (2016)

54 A. Zarei-Hanzaki, M. A. Mohtadi-Bonab, Y. Onuki, R. Basu, A. Asghari, and J. A. Szpunar
Grain-orientation-dependent of γ–ε–α′ transformation and twinning in a super-high-strength, high ductility austenitic Mn-steel
Materials Science and Engineering A **674** 514-528 (2016)

55 Y. Su, K. Oikawa, S. Harjo, T. Shinohara, T. Kai, M. Harada, K. Hiroi, S. Zhang, J. D. Parker, H. Sato, Y. Shiota, Y. Kiyanagi, and Y. Tomota
Time-of-flight neutron Bragg-edge transmission imaging of microstructures in bent steel plates
Materials Science and Engineering A **675** 19-31 (2016)

56 Y. Wang, Y. Tomota, S. Harjo, W. Gong, and T. Ohmura
In-situ neutron diffraction during tension-compression cyclic deformation of a pearlite steel
Materials Science and Engineering: A **676** 522-530 (2016)

57 K. Fukuda, Y. Tomota, S. Harjo, W. Gong, W. Woo, B. S. Seong, Y. Kuwahara, and F. Ikuta
Residual stresses in steel rod with collar formed by partial diameter-enlarging technique
Materials Science and Technology **33** 172-180 (2016)

58 H. Nishijima, Y. Tomota, Y. Su, W. Gong, and J. Suzuki
Monitoring of Bainite Transformation Using in Situ Neutron Scattering
Metals **6(1)** 16 (2016)

59 S. Nakano, S. Konno, N. Tomita, G. Matsuba, T. Tominaga, and S. Takata
Gelation process of polyacrylonitrile solutions as studied using small-angle neutron scattering techniques
Microsystem Technologies **22** 57-63 (2016)

60 J. Oh, M. D. Le, H.-H. Nahm, H. Sim, J. Jeong, T. G. Perring, H. Woo, K. Nakajima, S. Ohira-Kawamura, Z. Yamani, Y. Yoshida, H. Eisaki, S.-W. Cheong, A. L. Chernyshev, and J.-G. Park
Spontaneous decays of magneto-elastic excitations in noncollinear antiferromagnet (Y,Lu)MnO3
Nature Communication **7** 13146 (2016)

61 S. Itoh, Y. Endoh, T. Yokoo, J.-G. Park, Y. Kaneko, K. S. Takahashi, Y. Tokura, and N. Nagaosa
Weyl fermions and spin dynamics of metallic ferromagnet SrRuO3
Nature Communications **7** 11788 (2016)

62 Q. Wang, Y. Shen, B. Pan, X. Zhang, K. Ikeuchi, K. Iida, A. D. Christianson, H. C. Walker, D. T. Adroja, M. Abdel-Hafiez, X. Chen, D. A. Chareev, A. N. Vasiliev, and J. Zhao
Magnetic ground state of FeSe
Nature Communications **7** 12182 (2016)

63 N. Yabuuchi, M. Nakayama, M. Takeuchi, S. Komaba, Y. Hashimoto, T. Mukai, H. Shiiba, K. Sato, Y. Kobayashi, A. Nakao, M. Yonemura, K. Yamanaka, K. Mitsuhara, and T. Ohta
Origin of stabilization and destabilization in solid-state redox reaction of oxide ions for lithium-ion batteries
Nature Communications **7** 13814 (2016)

64 Y. Kato, S. Hori, T. Saito, K. Suzuki, M. Hirayama, A. Mitsui, M. Yonemura, H. Iba, and R. Kanno
High-power all-solid-state batteries using sulfide superionic conductors
Nature Energy **1** 16030 (2016)

65 R. Maruyama, T. Bigault, A. R. Wildes, C. D. Dewhurst, K. Soyama, and P. Courtois
Study of the in-plane magnetic structure of a layered system using polarized neutron scattering under grazing incidence geometry
Nucl. Instrum. Methods Phys. Res. A **819** 37-53 (2016)

66 T. Fujiwara, U. Bautista, Y. Mitsuya, H. Takahashi, N. L. Yamada, Y. Otake, A. Taketani, M. Uesaka, and H. Toyokawa
Microstructured boron foil scintillating G-GEM detector for neutron imaging
Nucl. Instrum. Methods Phys. Res. A **838** 124-128 (2016)

67 S. Takeda, Y. Yamagata, N. L. Yamada, M. Hino, T. Hosobata, J. Guo, S. Morita, T. Oda, and M. Furusaka
Development of a large plano-elliptical neutron-focusing supermirror with metallic substrates
Opt. Express **24** 12478-12488 (2016)

68 N. Saito, Y. Oishi, K. Miyazaki, K. Okamura, J. Nakamura, O. A. Louchev, M. Iwasaki, and S. Wada
High-efficiency generation of pulsed Lyman-α radiation by resonant laser wave mixing in low pressure Kr-Ar mixture
Opt. Express **24** 7566 (2016)

69 N. D. Khanh, N. Abe, H. Sagayama, A. Nakao, T. Hanashima, R. Kiyanagi, Y. Tokunaga, and T. Arima
Magnetoelectric coupling in the honeycomb antiferromagnet Co4Nb2O9
Phys. Rev. B **93** 075117 (2016)

70 S. Torigoe, Y. Ishimoto, Y. Aoishi, H. Murakawa, D. Matsumura, K. Yoshii, Y. Yoneda, Y. Nishihata, K. Kodama, K. Tomiyasu, K. Ikeda, H. Nakao, Y. Nogami, N. Ikeda, T. Otomo, and N. Hanasaki
Observation of all-in type tetrahedral displacements in nonmagnetic pyrochlore niobates
Phys. Rev. B **93** 085109 (2016)

71 M. Hiraishi, K. M. Kojima, M. Miyazaki, I. Yamauchi, H. Okabe, A. Koda, R. Kadono, S. Matsuishi, and H. Hosono
Cage electron-hydroxyl complex state as electron donor in mayenite
Phys. Rev. B **93** 121201(R) (2016)

72 M. Ruminy, M. Núñez Valdez, B. Wehinger, A. Bosak, D. T. Adroja, U. Stuhr, K. Iida, K. Kamazawa, E. Pomjakushina, D. Prabakharan, M. K. Haas, L. Bovo, D. Sheptyakov, A. Cervellino, R. J. Cava, M. Kenzelmann, N. A. Spaldin, and T. Fennell
First-principles calculation and experimental investigation of lattice dynamics in the rare-earth pyrochlores R2Ti2O7 (R=Tb,Dy,Ho)
Phys. Rev. B **93** 214308 (2016)

73 S. Lee, Y. Ishikawa, P. Miao, S. Torii, T. Ishigaki, and T. Kamiyama
Novel magnetoelastic coupling forbidden by timereversal symmetry: Spin-direction-dependent magnetoelastic coupling on MnO, CoO, and NiO
Phys. Rev. B **93** 64429 (2016)

74 M. Ruminy, E. Pomjakushina, K. Iida, K. Kamazawa, D. T. Adroja, U. Stuhr, and T. Fennell
Crystal-field parameters of the rare-earth pyrochlores R2Ti2O7 (R = Tb, Dy, and Ho)
Phys. Rev. B **94** 024430 (2016)

75 D. Hu, Z. Yin, W. Zhang, R. A. Ewings, K. Ikeuchi, M. Nakamura, B. Roessli, Y. Wei, L. Zhao, G. Chen, S. Li, H. Luo, K. Haule, G. Kotliar, and P. Dai
Spin excitations in optimally P-doped BaFe2(As0.7P0.3)2 superconductor
Phys. Rev. B **94** 094504 (2016)

76 H. Sim, S. Lee, K.-P. Hong, J. Jeong, J. R. Zhang, T. Kamiyama, D. T. Adroja, C. A. Murray, S. P. Thompson, F. Iga, S. Ji, D. Khomskii, and J.-G. Park
Spontaneous structural distortion of the metallic Shastry-Sutherland system DyB4 by quadrupole-spinlattice coupling
Phys. Rev. B **94** 195128 (2016)

77 T. Hayakawa, Y. Toh, M. Huang, T. Shizuma, A. Kimura, S. Nakamura, H. Harada, N. Iwamoto, S. Chiba, and T. Kajino
Measurement of the isomer production ratio for the 112Cd(n,γ)113Cd reaction using neutron beams at JPARC
Phys. Rev. C **94** 055803-1-6 (2016)

78 Y. Sakaguchi, H. Asaoka, Y. Uozumi, Y. Kawakita, T. Ito, M. Kubota, D. Yamazaki, K. Soyama, G. Sheoran, and M. Mitkova
Processes of silver photodiffusion into Ge-chalcogenide probed by neutron reflectivity technique
Physica Status Solidi (a) Applications and Materials Science **213** 1894-1903 (2016)

79 N. Tomioka, T. Okuchi, N. Purevjav, J. Abe, and S. Harjo
Hydrogen sites in the dense hydrous magnesian silicate phase E: a pulsed neutron powder diffraction study
Physics and Chemistry of Minerals **43** 267-275 (2016)

80 S. Fujiwara, K. Araki, T. Matsuo, H. Yagi, T. Yamada, K. Shibata, and H. Mochizuki
Dynamical Behavior of Human α-Synuclein Studied by Quasielastic Neutron Scattering
PLoS ONE **11(4)** e0151447 (2016)

81 A. Izumi, Y. Shudo, T. Nakao, and M. Shibayama
Cross-link Inhomogeneity in Phenolic Resins at the Initial Stage of Curing Studied by 1H-pulse NMR Spectroscopy and Complementary SAXS/WAXS and SANS/WANS with a Solvent-swelling Technique
Polymer **103** 152-162 (2016)

82 R. Mashita, H. Kishimoto, R. Inoue, A. Koda, R. Kadono, and T. Kanaya
Dynamics of polybutadiene reinforced with unsaturated carboxylate studied by muon spin relaxation (mSR)
Polymer **105** 510-515 (2016)

83 S. Shimomura, M. Inutsuka, N. L. Yamada, and K. Tanaka
Unswollen layer of cross-linked polyisoprene at the solid interface
Polymer **105** 526-531 (2016)

84 S. Imajo, K. Mishima, M. Kitaguchi, Y. Iwashia, N. L. Yamada, M. Hino, T. Oda, T. Ino, H. M. Shimizu, S. Yamashita, and R. Katayama
Pulsed UCN Production using a Doppler Shifter at JPARC
Prog. Theor. Exp. Phys. **2016** 013C02 (2016)

85 A. Mukunoki, T. Chiba, Y. Benino, and T. Sakuragi
Microscopic structural analysis of lead borate-based glass
Progress in Nuclear Energy **91** 339–344 (2016)

86 G. Yoshida, K. Ninomiya, M. Inagaki, W. Higemoto, N. Kawamura, K. Shimomura, Y. Miyake, T. Miura, M. K. Kubo, and A. Shinohara
Chemical environmental effects on muon transfer process in low-pressure H2+CO and H2+CO2 gases
RADIOISOTOPES **65** 113-118 (2016)

87 Y. Matsuda, Y. Itami, K. Hayamizu, T. Ishigaki, M. Matsuia, Y. Takeda, O. Yamamoto, and N. Imanishi
Phase relation, structure and ionic conductivity of Li7-x-3yAlyLa3Zr2-xTaxO12
RSC Adv. **6** 78210-78218 (2016)

88 A. S. Tremsin, Y. Gao, L. C. Dial, F. Grazzi, and T. Shinohara
Investigation of microstructure in additive manufactured Inconel 625 by spatially resolved neutron transmission spectroscopy
Sci. Technol. Adv. Mater. **17** 326 (2016)

89 G. Kobayashi, Y. Hinuma, S. Matsuoka, A. Watanabe, M. Iqbal, M. Hirayama, M. Yonemura, T. Kamiyama, I. Tanaka, and R. Kanno
Pure H– conduction in oxyhydrides
Science **351** 1314-1317 (2016)

90 K. Komatsu, N. Noritake, S. Machida, A. Sano-Furukawa, T. Hattori, R. Yamane, and H. Kagi
Partially ordered state of ice XV
Scientfic Reports **6** 28920 (2016)

91 S. Klotz, K. Komatsu, F. Pietrucci, H. Kagi, A.–A. Ludl, S. Machida, T. Hattori, A. Sano-Furukawa, and L. E. Bove
Ice VII from aqueous salt solutions: From a glass to a crystal with broken H-bonds
Scientfic Reports **6** 32040 (2016)

92 S. Taminato, M. Yonemura, S. Shiotani, T. Kamiyama, S. Torii, M. Nagao, Y. Ishikawa, K. Mori, T. Fukunaga, Y. Onodera, T. Naka, M. Morishima, Y. Ukyo, D. S. Adipranoto, H. Arai, Y. Uchimoto, Z. Ogumi, K. Suzuki, M. Hirayama, and R. Kanno
Real-time observations of lithium battery reactions—operando neutron diffraction analysis during
Scientific Reports **6** 28843 (2016)

93 K. Horigane, K. Kihou, K. Fujita, R. Kajimoto, K. Ikeuchi, S. Ji, J. Akimitsu, and C. H. Lee
Spin excitations in hole-overdoped iron-based superconductors
Scientific Reports **6** 33303 (2016)

94 N. Yano, T. Yamada, T. Hosoya, T. Ohhara, I. Tanaka, and K. Kusaka
Application of profile fitting method to neutron time-of-flight protein single crystal diffraction data collected at the iBIX
Scientific Reports **6** 36628 (2016)

95 H. Takahashi
New phase transition in superprotonic phase of Cs2(HSO4)(H2PO4)
Materials Science and Engineering A 674 514-528 (2016)
Solid State Ionics **285** 155-159 (2016)

96 D. Chen, D. Habu, Y. Masubuchi, S. Torii, T. Kamiyama, and S. Kikkawa
Partial nitrogen loss in SrTaO2N and LaTiO2N oxynitride perovskites
Solid State Sciences **54** 2-6 (2016)

Editorial Board - MLF Annual Report 2016

J-PARC

JAPAN PROTON ACCELERATOR RESEARCH COMPLEX

High Energy Accelerator Research Organization (KEK)
Japan Atomic Energy Agency (JAEA)

http://j-parc.jp/

Materials and Life Science Division
J-PARC Center

http://j-parc.jp/MatLife/

CROSS

Comprehensive Research Organization for Science and Society

http://www.cross-tokai.jp/

J-PARC 17-07